SPACECRAFT FORMATIONS USING RELATIVE ORBITAL ELEMENTS AND ARTIFICIAL POTENTIAL FUNCTIONS

A Dissertation

Submitted to the Faculty

of

Purdue University

by

Sylvain Renevey

In Partial Fulfillment of the

Requirements for the Degree

of

Doctor of Philosophy

May 2020

Purdue University

West Lafayette, Indiana

THE PURDUE UNIVERSITY GRADUATE SCHOOL
STATEMENT OF DISSERTATION APPROVAL

Dr. David A. Spencer, Chair

School of Aeronautics and Astronautics

Dr. Carolin Frueh

School of Aeronautics and Astronautics

Dr. Kathleen C. Howell

School of Aeronautics and Astronautics

Dr. Inseok Hwang

School of Aeronautics and Astronautics

Approved by:

Dr. Gregory A. Blaisdell

Professor and Associate Head of Gambaro Graduate Program of Aeronautics and Astronautics

To my family and my wife Floriane.

ACKNOWLEDGMENTS

The completion of my dissertation would not have been possible without the support and nurturing of Dr. David A. Spencer. The research ideas he has provided through his extensive knowledge of spacecraft formations and proximity operations were invaluable in writing this dissertation. I wish to express my deepest gratitude to my committee, Drs. Carolin Frueh, Kathleen C. Howell, and Inseok Hwang. I very much appreciate the time spent to review my dissertation and their insightful comments and suggestions. I would like to thank my colleagues and friends from the Space Flight Projects Laboratory, and in particular Jannuel Cabrera, Tom Cunningham, Rohan Deshmukh, and Justin Mansell for the interesting discussions we had. Their support helped me successfully go through this endeavor. Last but not least, I'd like to thank my family and my wife, Floriane, for their unwavering support throughout the years.

TABLE OF CONTENTS

Page

LIST OF TABLES

Table Page

LIST OF FIGURES

Figure Page

SYMBOLS

γ	constant phase angle
$\boldsymbol{\Delta V}$	delta-V vector in the LVLH reference frame
ΔV_{max}	maximum amplitude of the delta-V
ΔV_{min}	minimum amplitude of the delta-V
$\boldsymbol{\rho}$	vector containing a set of relative orbital elements
$\boldsymbol{\rho}_t$	vector containing a set of target relative orbital elements
σ	slant
σ_θ	standard deviation of the thrust pointing error
σ_M	standard deviation of the thrust magnitude error
σ_x	standard deviation of the state uncertainties in the radial direction
σ_y	standard deviation of the state uncertainties in the along-track direction
σ_z	standard deviation of the state uncertainties in the cross-track direction
Υ	colatitude of the sinilaterating node
υ	ratio between the major and minor axes of the repulsive ellipsoid
$\boldsymbol{\Phi}$	state transition matrix
ϕ	artificial potential function
ϕ_a	attractive artificial potential function
ϕ_r	repulsive artificial potential function
ψ	phase angle in the cross-track projection
ω	argument of pericenter or angular velocity
a	semi-major axis of the instantaneous relative orbit
a_r	semi-major axis of the projected instantaneous relative orbit

A_z	amplitude of the cross-track motion of the relative orbit
c	central anomaly
E_r	relative eccentric anomaly
I_{sp}	specific impulse
k_a	scaling parameter of the attractive artificial potential function
k_r	scaling parameter of the repulsive artificial potential function
m	mass
n	mean motion of the chief
$\mathbf{Q}_a$	shaping matrix of the attractive artificial potential function
$\mathbf{Q}_r$	shaping matrix of the repulsive artificial potential function
$\boldsymbol{r}$	relative position expressed in rectangular coordinates in the LVLH reference frame
${}^I\boldsymbol{r}$	absolute position in the Earth Centered Inertial frame
$\dot{\boldsymbol{r}}$	relative velocity expressed in rectangular coordinates in the LVLH reference frame
${}^I\dot{\boldsymbol{r}}$	inertial velocity in the Earth Centered Inertial frame
r_s	radius of the sphere circumscribing the obstacle
r_{SOI}	radius of the sphere of influence of the obstacle
$\boldsymbol{s}$	relative state expressed in rectangular coordinates in the LVLH reference frame
T_c	time interval between two collision checks
T_m	time of flight between two attractive maneuvers
$\hat{\boldsymbol{x}}$	unit vector along the radius vector pointing away from the central body and defining the LVLH reference frame
x	radial component of the relative position
$\dot{x}$	radial component of the relative velocity
x_c	coordinate of the instantaneous center of motion in the radial direction (GROE notation)

x_r	coordinate of the instantaneous center of motion in the radial direction (ROE notation)
$\hat{\boldsymbol{y}}$	unit vector in the along-track direction defining the LVLH reference frame
y	along-track component of the relative position
$\dot{y}$	along-track component of the relative velocity
y_c	coordinate of the instantaneous center of motion in the along-track direction (GROE notation)
y_r	coordinate of the instantaneous center of motion in the along-track direction (ROE notation)
$\hat{\boldsymbol{z}}$	unit vector along the orbital angular momentum vector defining the LVLH reference frame
z	cross-track component of the relative position
$\dot{z}$	cross-track component of the relative velocity

ABBREVIATIONS

APF	artificial potential function
CAM	collision avoidance maneuver
CRO	circular relative orbit
CW	Clohessy-Wiltshire
GRACE	Gravity Recovery and Climate Experiment
GROE	geometric relative orbital element
LVLH	local-vertical, local-horizontal
MMS	Magnetospheric Multiscale Spacecraft
NAIF	Navigation and Ancillary Information Facility
NASA	National Aeronautics and Space Administration
PRISMA	Prototype Research Instruments and Space Mission technology Advancement
ROE	relative orbital element
STM	state transition matrix
TDB	temps dynamique barycentrique or barycentric dynamical time
TanDEM-X	TerraSAR-X add-on for Digital Elevation Measurement

ABSTRACT

Renevey, Sylvain Ph.D., Purdue University, May 2020. Spacecraft Formations Using Relative Orbital Elements and Artificial Potential Functions. Major Professor: David A. Spencer.

A control methodology to design and establish spacecraft formations is presented. The intuitive design of complex spacecraft formation geometry is achieved by utilizing two different sets of relative orbital elements derived from a linearization of the dynamics. These sets provide strong insights into the shape, size, and orientation of the relative trajectory and facilitate the design of relative orbits in addition to relative positions. An artificial potential function (APF) composed of an attractive potential for goal seeking and a repulsive potential for obstacle avoidance is constructed. The derivation of a control law from this APF results in a computationally efficient algorithm able to fully control the relative position and velocity of the spacecraft and therefore to establish spacecraft formations. The autonomous selection of some of the design parameters of the model based on fuel minimization considerations is described. An assessment of the formation establishment accuracy is conducted for different orbital perturbation as well as various degrees of thrust errors and state uncertainties. Then, the performance of the control algorithm is demonstrated with the numerical simulation of four different scenarios. The first scenario is the design and establishment of a 10-spacecraft triangular lattice, followed by the establishment of a 37-spacecraft formation composed of two hexagonal lattices on two different relative planes. The control method is used to illustrate proximity operations with the visual inspection of an on-orbit structure in the third scenario. Finally, a formation composed of four spacecraft arranged in a tetrahedron is presented.

1. INTRODUCTION

Decentralized space architectures are enabling mission concepts that replace the functionalities of a large monolithic spacecraft by the cooperative behavior of a group of smaller spacecraft. The broad interest that these architectures have gained over recent years is in part due to their lower cost, distributed risk among several entities, and versatility. The implementation of these distributed systems has been successfully demonstrated with the deployment of large scale architectures such as the GPS and Iridium constellations for instance, and megaconstellations composed of hundreds to thousands of satellites are being planned and deployed by SpaceX and OneWeb. On a smaller scale, spacecraft formations composed of a few agents offer resilience for orbital applications including remote sensing, astronomy and astrophysics, and deep space exploration. A few missions have been flown using this concept: The Gravity Recovery and Climate Experiment (GRACE) mission composed of two spacecraft maps variations in Earth's gravity field with high accuracy. Scientific application has also been demonstrated with the Magnetospheric Multiscale Spacecraft (MMS) in which four spacecraft arranged in a tetrahedron geometry study a phenomenon known as magnetic reconnection between the Earth's and Sun's magnetic fields. The synthetic aperture radar embarked onboard the two satellites of the TanDEM-X mission allowed to create a digital elevation model of the Earth, and technology for autonomous operations has been demonstrated with the PRISMA mission composed of two spacecraft.

The operation of several satellites in close proximity adds additional challenges as compared to a single spacecraft. The dynamics of the relative motion of a deputy spacecraft with respect to a chief spacecraft must be well understood in order to design trajectories which result in the desired relative motion. Orbital perturbations, which will tend to disturb the geometry of the formation, must be accounted for

to obtain precise positioning. Several models have been developed to describe the relative motion for a wide range of conditions ranging from circular orbits to highly eccentric ones, inter-spacecraft distances from a few meters to several kilometers, and presence or absence of various perturbations. The description of the relative motion using traditional Cartesian coordinates is challenging due to the nonlinear nature of the system. Different sets of parameters have been developed to provide quantities which allow the intuitive understanding of the natural evolution of the system and therefore facilitate the design of relative trajectories. These elements are somewhat comparable to the classical orbital elements utilized for the description of the absolute motion and are of great use to design relative orbits as opposed to relative positions.

In addition to these challenges, the risk of collision that comes with operating spacecraft in close proximity drives the need for real-time collision monitoring and avoidance systems. The guidance of a group of spacecraft is traditionally based on numerically integrating the trajectories of the agents and using optimal control to compute maneuvers to maintain the spacecraft on their nominal orbits. These computationally demanding processes are usually performed on computers on the ground and the maneuver commands are then uplinked to the spacecraft. In the case of a close proximity spacecraft formation, the time delay between collision risk detection and avoidance maneuver incurred by this ground-in-the-loop process can have catastrophic outcomes. An increased degree of autonomy is thus desired, with the deployment of computationally efficient guidance algorithms able to monitor collisions in near real-time directly on-board the spacecraft. The artificial potential function methodology is a computationally lightweight control method which can incorporate collision avoidance in its formulation. Its analytic nature and modularity makes it an ideal candidate for space applications.

In this dissertation, the design and precise control of spacecraft formations is investigated. The challenges mentioned previously are addressed by introducing a novel algorithm based on relative orbital elements and artificial potential functions. The methodology enables the intuitive design of geometrically complex formations

and the safe formation establishment by continuous monitoring for collision risks. The effects of nonlinearities and orbital perturbations on the performance of the control methodology are analyzed and the performance and limitations of the control algorithm are illustrated with the design and numerical simulation of four spacecraft formations.

In the following sections, the definitions of the different distributed space systems is provided followed by the state-of-the-art in spacecraft relative motion, relative orbital elements, and artificial potential functions. The contributions made by this dissertation are then detailed.

1.1 Distributed Space Systems

A distributed space system (DSS) is defined as a group of spacecraft that cooperate to achieve a common objective. These systems can be implemented using different distributed architectures including: constellations, clusters, swarms, fractionated spacecraft, and federated spacecraft. No global consensus of the exact properties of each of these architectures exists in the community, yet these terms are widely used in the literature. Le Moigne [1] defines a constellation as: "A reference to a space mission that, beginning with its inception, is composed of two or more spacecraft that are placed into specific orbit(s) for the purpose of serving a common objective [...]". Poghosyan et al. [2] describe the architecture as "a traditional approach, when sporadically distributed satellites are used for maximizing the coverage". Typical examples of constellations include the GPS constellation, Iridium, and Planet constellation. Recent years have seen a trend in the development of so called megaconstellations involving hundreds to thousands of satellites. SpaceX's Starlink and OneWeb are two examples of such megaconstellations.

A spacecraft formation is defined as: "Two or more spacecraft that conduct a mission such that relative distances and 3D spatial relationships [...] are controlled through direct sensing by one spacecraft of at least one other spacecraft state [...]"

in [1]. A similar definition is given by Scharf et al. [3]: "a set of more than one spacecraft whose dynamic states are coupled through a common control law", which is also adopted by Alfriend et al. [4]. Poghosyan et al. [2] define formation flight as "involving some form of tight flight control compared to constellations [...]". They also define clusters as "an implementation of the distributed space system featuring two or more satellites flying in a close formation. Spacecraft in a cluster require accurate formation knowledge and control [...]" and swarms as "roughly comparable to clusters except they involve a much larger number of usually smaller and cheaper satellites [and] do not have as stringent attitude determination and control requirements as the clusters." The authors further elaborate that swarms are usually envisioned as groups of hundreds to thousands nano- to femtosatellites weighting a few grams and having limited capabilities. These definitions imply that both clusters and swarms can be classified as spacecraft formations.

Fractionated and federated systems are distributed architectures that have been proposed more recently. A fractionated architecture consists in disaggregating the subsystems of a single monolithic spacecraft into several smaller satellites that communicate wirelessly [5]. In a federated system, the spacecraft share some of their resources with other members in the federation [6]. A large spacecraft could, for instance, store data on behalf of a smaller, less capable satellite.

Based on these definitions, the groups of spacecraft that will be considered in this research can be classified as spacecraft formations and are composed of up to a few tens of members.

1.2 Spacecraft Relative Motion

One of the earliest models describing the relative motion between two spacecraft, still extensively used today, is the one developed by Clohessy and Wiltshire in 1960 [7]. This model makes the assumptions that the reference spacecraft is on a circular orbit and that the two vehicles are close to each other in order to linearize the dynamics.

One of the advantages of this model is that a closed-form solution can be derived under certain assumptions, thus avoiding the need of numerically integrating the equations of motion. A few years later, De Vries [8] introduces a model to describe the relative motion for elliptical orbits. The solution is expressed as a power series of the eccentricity of the chief's orbit. Tschauner and Hempel [9] generalize the model introduced by Clohessy and Wiltshire and provide differential equations describing the relative motion for a chief on an elliptical orbit with any eccentricity. Lawden, who derived the same equations independently albeit describing the primer vector rather than the spacecraft [10], proposes a solution with the introduction of an integral term expressed as a function of the true anomaly of the chief [11]. This integral, however, is singular whenever the true anomaly is a multiple of π. A modification of this integral is proposed by Carter [12] to remove the singularity. The independent variable of the integral term is transformed from true anomaly to eccentric anomaly for elliptical orbits and hyperbolic anomaly for hyperbolic orbits. The integral can be directly evaluated for parabolic orbits and has therefore no singularity. The introduction of eccentric anomaly and hyperbolic anomaly, however, makes the evaluation of this integral impractical. In the early 2000s, Yamanaka and Ankersen [13] develop a new solution where the integral term is based on the constant of angular momentum that can be calculated directly. The authors then propose a state transition matrix that can be used to compute the state at any time given the initial state without the need of numerical integration.

All of the solutions mentioned so far are based on the assumption that the relative position is small with respect to the chief's orbital radius, thus allowing linearization of the gravitational potential using a Taylor series truncated to the first order. London [14] presents a second-order solution obtained by retaining the second-order gravitational terms in the differential equations of relative motion. The closed-form solution is a function of time and provides significant improvement of the numerical accuracy. Anthony et al. [15] use perturbation techniques to derive a solution that contains second-order terms in the relative distance and is valid for nearly circular

orbits. Vaddi et al. [16] study the effect of nonzero eccentricity and nonlinearity perturbations. They first derive a model with a quadratic term for the gravitational force and a model with eccentricity. The solutions to the two models are then combined into a global solution which is used to generate a set of initial conditions to mitigate the drift in the along-track direction and keep the relative motion bounded. More recently, Willis et al. [17] have proposed a model where the second order term in the Taylor series is kept. The analytical solution that they present extends the range of validity to larger relative distances while still being valid for any eccentricity.

The effects of orbital perturbations on the relative motion is discussed by Alfriend et al. [18]. They consider the effect of a nonspherical gravitational potential in addition to nonlinearity and nonzero eccentricity and express the state of the deputy as the addition of small changes to the chief's orbital elements. Humi and Carter [19] introduce a model that incorporates linear drag. The differential equations they derive can, under certain assumptions, be solved in terms of integrals, thus enabling representation of the solution of the problem with a state-transition matrix. In [20], Carter and Humi modify the Clohessy-Wiltshire equations to include quadratic drag. The differential equations obtained with this additional perturbation can be solved analytically for specific values of the drag coefficient and geometry of the spacecraft. Schweighart and Sedwick [21, 22] introduce a linear model that accounts for second order geopotential perturbations using the time average of the gradient of the J2 potential. The linear differential equations can be solved analytically to describe the position of the deputy with respect to the chief. A comparison with numerical simulations shows good agreement between the linear model and the difference between the absolute states with maximum modeling errors of 0.4%. Vadali [23] develops a model based on the secular drift and short-period variations of the chief's orbital elements to incorporate local perturbations and avoid the need of using the time average of the gradient of the J2 potential. The J2 perturbation affects the orbital elements with secular drift and short and long period motion, causing the relative motion to vary as described by Schaub and Alfriend [24]. The authors propose a method to establish

J2 invariant relative orbits by selecting neighboring orbits which have a similar drift rate of the longitude of the ascending node. The short-period variations are mitigated by using the mean orbit elements. Morgan et al. [25] develop a model that account for J2 and atmospheric drag perturbations and propose guidance strategies to control spacecraft swarms.

Most of the approaches mentioned above rely on the use of rectangular coordinates to describe the relative state of one spacecraft with respect to the other, yet the description of relative trajectories in terms of such coordinates is not intuitive. In order to remedy these difficulties, several sets of elements providing more insights into the geometry of the relative motion have been developed and are presented in the next section.

1.3 Relative Orbital Elements

Several sets of relative orbital elements have been introduced over the past decades. Schaub and Alfriend [26] present a control strategy where the desired orbit is described in terms of orbital element differences and the actual position is given in terms of Cartesian coordinates. A linear transformation to go from Cartesian coordinates to orbital element differences is derived. Lovell and Tragesser [27] introduce a set of six elements based on the solution to the Clohessy-Wiltshire equations. These elements are defined for the projection of the relative trajectory on the Hill frame and provide strong geometrical insights into the relative motion. Schaub [28] introduces a method to describe the relative orbit in terms of a set of orbit element differences. The parametrization is valid for any eccentricity and is based on the assumption that the relative position is much smaller than the chief's radius vector. The linear mapping between these elements and the Cartesian coordinates in the Hill frame breaks down when this assumption is violated. Kasdin et al. [29] use Hamiltonian mechanics to derive a parametrization of the relative motion in terms of epicyclic elements. J2-induced perturbations of the relative motion are studied

using these elements and a method to find J2-invariant orbits is described. D'Amico and Montenbruck [30] extend the concept of eccentricity/inclination vector separation originally developed for geostationary spacecraft [31] to spacecraft formations on low Earth orbits. The spacecraft are assumed to be on near-circular orbits and to have a close relative distance. The authors provide a control method to target desired separation vectors which can be used to ensure collision free maneuvring and illustrate the control methodology with a reconfiguration of the TanDEM-X/TerraSAR-X formation. The method has been used to switch positions of the two spacecraft in the GRACE formation [32]. These elements have also been used in the control algorithm of the PRISMA formation [33]. Wang and Nakasuka [34] use these vector separations to present a method to design fuel-optimal cluster flight orbits. Two constrained optimization problems including maximum relative distance and passive safety are introduced and solved using a genetic algorithm. He and Han [35] derive a set similar to the one derived by D'Amico and Montenbruck in [30] and present a velocity impulse control law to control these elements. Han and Yin [36] extend the vector separation method to eccentric orbits using spherical trigonometry. Yin and Han [37] compute the state transition matrix for this set of relative orbit elements and present a method to control formations on elliptical orbits. Lee [38] describes the unperturbed relative motion with parametric equations of cycloids and trochoids. The method is applicable to large-scale relative motion such as the GPS constellation and is well suited to describe constellations having rosette (flowerlike) orbital patterns (see for instance [39]). Yao et al. [40] use the set of elements introduced in [27] and derive a new parametric angle to describe the relative inclination. The authors then describe relative trajectories design strategies taking the Sun illumination into account. Bevilacqua and Lovell [41] develop an on-off thrust guidance methodology based on the elements developed in [27]. They present an analytic solution to the time evolution of the relative orbital elements when on-off thrust is applied and is particularly applicable to small spacecraft such as CubeSats. Lovell and Spencer [42] and Spencer [43] present a modern derivation of the elements first introduced in [27]. The

time evolution of these elements is given and the authors study the characteristics of the unforced motion. Transformations to map relative orbital elements to Cartesian coordinates are provided. Spencer and Lovell [44] introduce maneuver strategies to target specific sets of the relative orbital elements developed in [42]. The strategies are illustrated with several close proximity operations scenarios. Sinclair et al. [45] provide a geometric interpretation of the Tschauner-Hempel equations. The six independent fundamental solutions to the differential equations are combined to form general solutions to the linearized equations. The amplitudes of the fundamental solutions are used as parameters to describe the relative motion and a simple maneuver scheme to target arbitrary amplitudes is presented. Gaias et al. [46] develop a relative navigation tool based on angles measurements only where the deputy measures the azimuth and elevation of the chief in the camera reference frame. Healy and Henshaw [47] introduce a set of eight elements which have a strong analogy with the classical orbital elements. This set is based on the solution to the equations derived by Clohessy and Wiltshire and has some similitudes with the formulation of Lovell and Tragesser. Bennett and Schaub [48] address the singularities for the two phase angles in the Lovell and Tragesser formulation that arise in specific relative configurations. The new formulation is based on the use of trigonometric identities to remove these singularities. The authors then present variational equations for this new set and study the effect of drag on the relative motion. A comprehensive survey of the different relative motion dynamics models as well as relative elements sets can be found in [49].

1.4 Artificial Potential Functions

First introduced by Khatib [50] in the 1970s to control robotic arm manipulators, artificial potential function (APF) methodology quickly gained broad attention from the robotics community [51–53]. The methodology is based on the definition of a potential field that admits a minimum at the location of a desired goal. Obstacles

can be accounted for by adding a repulsive component to the potential. A controller is then designed to follow the direction of steepest descent which, under certain assumptions, will bring the robot to the goal while avoiding obstacles. The analytical nature of the methodology results in a low computational cost and makes it attractive for real-time, on-board applications. Since their first applications, artificial potential functions have been used in a variety of fields including autonomous car driving [54], camera motion tracking [55], or UAV path planning [56].

The first application of APF to spacecraft relative motion can probably be attributed to McInnes [57] in 1993. In [58], the same author uses the control methodology to establish a planar ring formation. Lopez and McInnes [59] consider the terminal rendezvous guidance between a deputy and a chief. A quadratic potential field is defined for the attractive part and static obstacles are accounted for with the inclusion of a Gaussian repulsive potential. The linear combination of attractive and repulsive potential fields might lead to the emergence of local minima. Lopez and McInnes state that for simple configurations these minima are unstable saddle points and the spacecraft will therefore converge towards the goal. McQuade and McInnes [60] use the methodology to do autonomous on-orbit assembly by multiple robots. They present a control strategy to assemble a large number of beams into a truss structure by utilizing a potential function that incorporate collision avoidance between the free-flyers and connection constraints between the beams. Sato [61] introduces a method to compute a potential function based on the solution to the Laplace equation. A mesh is defined on the state space and the potential is computed at each mesh node. A linear interpolation method is then used to compute the potential on the entire space. This Laplace artificial potential function is guaranteed to have a global minimum and no local minimum. In [62], Roger and McInnes use this Laplace potential to compute the collision-free trajectory of a free-flyer near the International Space Station (ISS). The method guarantees convergence towards the goal; however, the iterative algorithm used to compute the potential is computationally expensive and makes the method unsuitable for real-time applications.

Most of the preliminary work on APFs focused on static target and obstacles. Ge and Cui [63] study the case of moving targets and moving obstacles assuming constant velocities. They define an APF where both the attractive and repulsive components depend on the position and velocity of the targets and obstacles and discuss strategies to avoid local minima. Tatsch and Fitz-Coy [64] and Tatsch [65] extend the method to targets and obstacles with time-varying velocities and augment the repulsive potential with a priority index weighting scheme, allowing to account for several obstacles simultaneously. The authors illustrate their algorithm with autonomous on-orbit servicing simulations. Tatsch [65] also derives an APF to control the attitude of the spacecraft. The combination of APF and sliding mode control has been used for terrestrial applications. Gazi [66] and Saaj et al. [67] investigate the applicability of this method to the guidance and navigation of spacecraft swarms. Their method is shown to be robust to disturbances. St. John-Olcayto et al. [68] investigate the use of APF based control for the autonomous operations of a free-flier near the ISS. They look in particular at the autonomous rendezvous and docking of the European Automated Transfer Vehicle (ATV) and the Japanese HII Transfer Vehicle (HTV) and show that the method is robust to perturbations such as residual atmospheric drag and spacecraft thrust imperfections. In [69], Badawy and McInnes use a quadratic field which depends on position, velocity, orientation, and angular velocity for the attractive component of the APF and a superquadric function for the repulsive component. The superquadric function enables the description of complex obstacle geometries and the authors illustrate the control law with the autonomous on-orbit assembly of beams. In [70], they change the attractive field of the APF from quadratic to hyperbolic to reduce the control intervention and the control method is applied to the establishment of a spacecraft formation. Another investigation of local minima is proposed by Mabrouk and McInnes [71] where they introduce internal dynamic agent states which manipulate the potential to change stable equilibrium points into unstable equilibrium points, enabling the spacecraft to escape. In his PhD dissertation, Muñoz [72] develops adaptive artificial potential functions (AAPFs) which

adapt their coefficients based on the solution to a two points boundary value problem (TPBVP). A performance index is introduced in the APF formulation that accounts for the dynamics of the system. The weights of the attractive potential are updated such that the negative gradient of the potential adapts to the velocity profile of the TPBVP solution, thus lowering the required control effort. Nag and Summerer [73] use an APF control methodology to study the gathering and scattering behavior of a swarm in the presence of an incoming kinetic impacter. In [74], Wahl and Howell introduce a guidance strategy based on an AAPF using the Yamanaka-Ankersen state transition matrix along with an auction algorithm for the initial target assignment. In Wahl [75] and Wahl and Howell [76] a model predictive control (MPC) guidance scheme is presented along the APF guidance and auction algorithm. Spencer [43, 77] introduces an APF formulation based on the relative orbital elements developed by Lovell and Tragesser. The methodology allows to target four elements, thus enabling the targeting of specific relative orbits but not a precise position on that orbit. Static obstacles are considered with a Gaussian repulsive potential field. Sun et al. [78] present a control method based on APF and bifurcation theory. The authors design a static hyperbolic-exponential potential function which presents certain bifurcation and stability properties and asses the stability of the controller analytically. Wang et al. [79] use a set of eight dimensionless relative orbital elements derived from the solution to the Tschauner-Hempel equations to formulate quadratic reconfiguration and dispersion APFs. The reconfiguration function is used to drive the spacecraft toward the goal while the dispersion function ensures an even distribution of the spacecraft on the relative orbit.

1.5 Contributions

The present investigation extends the method first introduced by Spencer with the formulation of a control algorithm based on relative orbital elements and artificial potential functions. The algorithm presented in this dissertation allows full

control of the relative position and velocity of a spacecraft in order to design and establish spacecraft formations and is able to monitor and prevent collisions between the formation's agents. This work extends the state of the art with the following contributions:

I. Definition of an artificial potential function control method based on relative orbital elements.

An artificial potential function is formulated in terms of relative orbital elements. Two methodologies are proposed: the first one is based on the Lovell and Tragesser [27] formulation and the second one uses the Healy and Henshaw [47] formulation. In both cases, all elements of the set are taken into account allowing the precise positioning of the spacecraft on a given relative orbit. The APF is constructed with an attractive quadratic potential field for goal seeking and an ellipsoidal repulsive field to ensure collision avoidance during the reconfiguration. The repulsive portion of the APF is only considered when a collision risk criterion is met. This decoupling between attractive maneuvers and collision avoidance mitigates the risk of the deputy being trapped in a local minima. The control law is obtained by following the steepest descent of the APF in the orbital elements domain to generate a reference trajectory which is then transformed into Cartesian coordinates and tracked using impulsive burns.

II. Autonomous selection of the APF parameters.

The construction of APFs involves several parameters to scale and shape the potentials which are, traditionally, manually selected. Strategies to automatically select some of these parameters are presented. A sensitivity analysis of the relative orbital elements with respect to changes in the relative velocity is conducted and used to select some shaping coefficients of the attractive potential. The shaping coefficients of the repulsive potential are automatically computed based on the relative velocity

between the spacecraft and the obstacle. Fuel consumption being strongly impacted by the scale of the APF, a method to select the scaling coefficient resulting in the smallest cumulative delta-V while satisfying some maneuvers' constraints is discussed.

III. Validation of the proposed algorithm in a high-fidelity simulation environment.

The performance of the control algorithm is evaluated with the numerical simulation of different formation establishments. The simulations are carried out in a high fidelity six degrees of freedom simulation environment which has originally been developed for LightSail. This simulator uses a nonlinear model of the dynamics and accounts for several orbital perturbations. The robustness and limitations of the control algorithm are assessed.

The three aforementioned contributions have led to conference papers and presentations at the 29th AAS/AIAA Space Flight Mechanics Meeting [80] and 2019 AAS/AIAA Astrodynamics Specialist Conference [81] as well as a publication in Acta Astronautica [82].

2. MATHEMATICAL MODEL

In this chapter, the mathematical model of the control algorithm is developed. A derivation of the model used to describe the dynamics of the relative motion is first presented followed by a description of the two sets of relative orbital elements used in this work. These sets are the Relative Orbital Elements (ROEs) first introduced by Lovell and Tragesser [27] and the Geometric Relative Orbital Elements (GROEs) introduced by Healy and Henshaw [47]. The construction of the artificial potential function is introduced with the definition of the attractive and repulsive portions. The APF and relative orbital elements methodologies are then merged to build the control algorithm. Several methods to automatically select the parameters of the APF are presented and the effects of orbital dynamics on the accuracy of the controller are studied.

2.1 Relative Motion

We consider two spacecraft in orbit about a central body and we want to describe the relative motion of one of them, the deputy, with respect to a non-maneuvring chief. In some cases, a virtual chief will be considered, where there is not a physical spacecraft at the chief location. The absolute position and velocity of the spacecraft are described in a body-centered inertial frame with the $\hat{\boldsymbol{i}}$ axis pointing toward the vernal equinox, the $\hat{\boldsymbol{k}}$ axis normal to the mean equator of date at epoch J2000 TDB, and the $\hat{\boldsymbol{j}}$ axis completing the triad and such that $\hat{\boldsymbol{j}} = \hat{\boldsymbol{k}} \times \hat{\boldsymbol{i}}$. This frame is commonly referred to as J2000 or EME2000 [83, 84]. The second reference frame which is extensively used throughout this work is the local-vertical, local-horizontal (LVLH) reference frame, also called Hill frame. This frame is centered on the chief and is defined with $\hat{\boldsymbol{x}}$ pointing away from the central body along the radius vector, $\hat{\boldsymbol{z}}$ along the

angular momentum vector, and $\hat{\boldsymbol{y}}$ in the along-track direction such that $\hat{\boldsymbol{y}} = \hat{\boldsymbol{z}} \times \hat{\boldsymbol{x}}$. In the case of a circular orbit, $\hat{\boldsymbol{y}}$ is aligned with the velocity vector of the chief. Note that the definition of this frame is not globally agreed upon and various definitions can be found in the literature (see for instance [83], [4], and [85]). The Earth-centered inertial frame and LVLH frame are illustrated on Fig. 2.1.

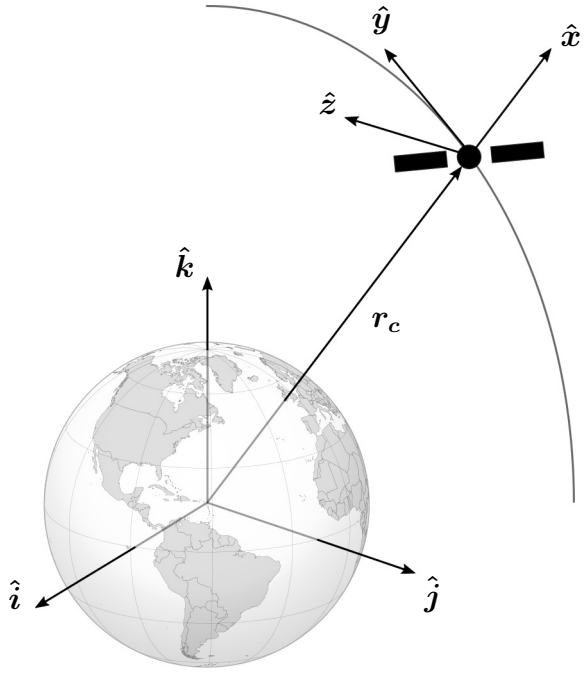

Figure 2.1: Earth-centered inertial and LVLH reference frames.

Given the inertial position $\boldsymbol{r}_c$ and velocity $\dot{\boldsymbol{r}}_c$ of the chief, the LVLH frame can be computed as

$$\hat{\boldsymbol{x}} = \frac{\boldsymbol{r}_c}{\|\boldsymbol{r}_c\|} \tag{2.1}$$

$$\hat{\boldsymbol{z}} = \frac{\boldsymbol{r}_c \times \dot{\boldsymbol{r}}_c}{\|\boldsymbol{r}_c \times \dot{\boldsymbol{r}}_c\|} \tag{2.2}$$

$$\hat{\boldsymbol{y}} = \hat{\boldsymbol{z}} \times \hat{\boldsymbol{x}} \tag{2.3}$$

The relative position of a deputy spacecraft with respect to the chief can be expressed as

$$\boldsymbol{r} = \boldsymbol{r}_d - \boldsymbol{r}_c \tag{2.4}$$

where $\boldsymbol{r}_d$ is the absolute position of the deputy in the inertial frame (Fig. 2.2).

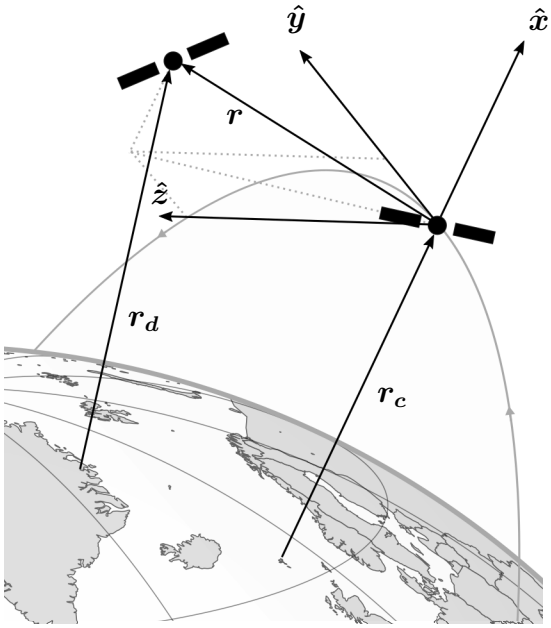

Figure 2.2: Relative position of the deputy and chief's LVLH reference frame.

Taking the time derivative of Eq. (2.4) twice in the inertial frame results in the relative acceleration of the deputy spacecraft:

$$^I\ddot{\boldsymbol{r}} = {}^I\ddot{\boldsymbol{r}}_d - {}^I\ddot{\boldsymbol{r}}_c \tag{2.5}$$

where superscript I indicates quantities in the inertial frame. In order to describe the relative motion in the LVLH frame, we need to compute the relative acceleration in that frame. Let

$$\boldsymbol{r} = x\hat{\boldsymbol{x}} + y\hat{\boldsymbol{y}} + z\hat{\boldsymbol{z}} \tag{2.6}$$

the relative position of the deputy with respect to the chief in the LVLH frame. The velocity in the inertial frame is given by

$$ {}^{I}\dot{\boldsymbol{r}} = {}^{I}\frac{d}{dt}\boldsymbol{r} = {}^{R}\frac{d}{dt}\boldsymbol{r} + {}^{I}\boldsymbol{\omega}^{R} \times \boldsymbol{r} \tag{2.7} $$

where superscript R indicates that the derivative is computed in the rotating LVLH frame and ${}^{I}\boldsymbol{\omega}^{R} = \omega\hat{\boldsymbol{z}}$ is the angular velocity of the LVLH frame with respect to the inertial one. The acceleration in the inertial frame can be computed by taking the time derivative of the above equation:

$$ \begin{aligned} {}^{I}\ddot{\boldsymbol{r}} &= {}^{I}\frac{d}{dt}\left({}^{I}\dot{\boldsymbol{r}}\right) = {}^{R}\frac{d}{dt}\left({}^{I}\dot{\boldsymbol{r}}\right) + {}^{I}\boldsymbol{\omega}^{R} \times \left({}^{I}\dot{\boldsymbol{r}}\right) \\ &= {}^{R}\frac{d^2}{dt^2}\boldsymbol{r} + {}^{R}\frac{d}{dt}{}^{I}\boldsymbol{\omega}^{R} \times \boldsymbol{r} + {}^{I}\boldsymbol{\omega}^{R} \times {}^{R}\frac{d}{dt}\boldsymbol{r} + {}^{I}\boldsymbol{\omega}^{R} \times \left({}^{R}\frac{d}{dt}\boldsymbol{r} + {}^{I}\boldsymbol{\omega}^{R} \times \boldsymbol{r}\right) \\ &= {}^{R}\frac{d^2}{dt^2}\boldsymbol{r} + {}^{R}\frac{d}{dt}{}^{I}\boldsymbol{\omega}^{R} \times \boldsymbol{r} + 2{}^{I}\boldsymbol{\omega}^{R} \times {}^{R}\frac{d}{dt}\boldsymbol{r} + {}^{I}\boldsymbol{\omega}^{R} \times \left({}^{I}\boldsymbol{\omega}^{R} \times \boldsymbol{r}\right) \end{aligned} \tag{2.8} $$

where the different cross products yield

$$ {}^{R}\frac{d}{dt}{}^{I}\boldsymbol{\omega}^{R} \times \boldsymbol{r} = \begin{bmatrix} -\dot{\omega}y \\ \dot{\omega}x \\ 0 \end{bmatrix} \tag{2.9} $$

$$ {}^{I}\boldsymbol{\omega}^{R} \times {}^{R}\frac{d}{dt}\boldsymbol{r} = \begin{bmatrix} -\omega\dot{y} \\ \omega\dot{x} \\ 0 \end{bmatrix} \tag{2.10} $$

$$ {}^{I}\boldsymbol{\omega}^{R} \times \left({}^{I}\boldsymbol{\omega}^{R} \times \boldsymbol{r}\right) = \begin{bmatrix} -\omega^2 x \\ -\omega^2 y \\ 0 \end{bmatrix} \tag{2.11} $$

Therefore, the relative acceleration can be expressed as

$$ {}^{I}\ddot{\boldsymbol{r}} = \begin{bmatrix} \ddot{x} - \dot{\omega}y - 2\omega\dot{y} - \omega^2 x \\ \ddot{y} + \dot{\omega}x + 2\omega\dot{x} - \omega^2 y \\ \ddot{z} \end{bmatrix} \tag{2.12} $$

Using Newton's second law

$$ \sum_i \boldsymbol{F}_i = m\,{}^{I}\ddot{\boldsymbol{r}}_{c,d} \tag{2.13} $$

we can compute the acceleration of the chief and the deputy respectively. In the two-body, unperturbed problem, the only force acting on the chief is the gravitational force

$$ \boldsymbol{F}_g(\boldsymbol{r}_c) = -\mu\frac{m_c}{r_c^3}\boldsymbol{r}_c \tag{2.14} $$

where μ is the standard gravitational parameter of the central body and $r_c = \|\boldsymbol{r}_c\|$. The acceleration of the chief is thus

$$ {}^{I}\ddot{\boldsymbol{r}}_c = \boldsymbol{f}_g(\boldsymbol{r}_c) = -\frac{\mu}{r_c^3}\boldsymbol{r}_c \tag{2.15} $$

where lowercase $\boldsymbol{f}$ denotes force per unit mass. For the deputy spacecraft, however, additional external forces such as thrust must be considered. The total force applied on that spacecraft is

$$ \boldsymbol{F}_g(\boldsymbol{r}_d) + \boldsymbol{F}_{ext} = -\mu\frac{m_d}{r_d^3}\boldsymbol{r}_d + \boldsymbol{F}_{ext} \tag{2.16} $$

where $r_d = \|\boldsymbol{r}_d\|$, resulting in an acceleration

$$ {}^{I}\ddot{\boldsymbol{r}}_d = \boldsymbol{f}_g(\boldsymbol{r}_d) + \boldsymbol{f}_{ext} = -\frac{\mu}{r_d^3}\boldsymbol{r}_d + \boldsymbol{f}_{ext} \tag{2.17} $$

The relative acceleration in the inertial frame (Eq. 2.5) can therefore be expressed in terms of force per unit mass as follows:

$$ {}^{I}\ddot{\boldsymbol{r}} = \boldsymbol{f}_g(\boldsymbol{r}_d) - \boldsymbol{f}_g(\boldsymbol{r}_c) + \boldsymbol{f}_{ext} \tag{2.18} $$

If we now express the position of the chief and the deputy in the LVLH frame as

$$\boldsymbol{r}_c = r_c\hat{\boldsymbol{x}} \tag{2.19}$$

$$\boldsymbol{r}_d = \boldsymbol{r}_c + \boldsymbol{r} = (r_c + x)\hat{\boldsymbol{x}} + y\hat{\boldsymbol{y}} + z\hat{\boldsymbol{z}} \tag{2.20}$$

Eq. (2.18) can be rewritten using Eqs. (2.15) (2.17) as:

$${}^{I}\ddot{\boldsymbol{r}} = \begin{bmatrix} -\frac{\mu}{r_d^3}(r_c + x) + \frac{\mu}{r_c^2} + f_x \\ -\frac{\mu}{r_d^3}y + f_y \\ -\frac{\mu}{r_d^3}z + f_z \end{bmatrix} \tag{2.21}$$

Finally, equating Eq. (2.12) with Eq. (2.21) results in

$$\ddot{x} - \dot{\omega}y - 2\omega\dot{y} - \omega^2 x = -\frac{\mu}{r_d^3}(r_c + x) + \frac{\mu}{r_c^2} + f_x \tag{2.22}$$

$$\ddot{y} + \dot{\omega}x + 2\omega\dot{x} - \omega^2 y = -\frac{\mu}{r_d^3}y + f_y \tag{2.23}$$

$$\ddot{z} = -\frac{\mu}{r_d^3}z + f_z \tag{2.24}$$

This system of equations describes the exact relative motion of the deputy with respect to the chief in the LVLH reference frame when considering a two-body, unperturbed system. These nonlinear equations cannot be solved analytically and numerical methods must be used instead. In order to derive a close-form solution describing the relative motion, the following assumptions which allow linearization of the system are made:

1. The chief is on a circular orbit.

2. The distance between the deputy spacecraft and the chief is much smaller than the distance between the central body and the chief: $\|\boldsymbol{r}\| \ll \|\boldsymbol{r}_c\|$.

The first assumption implies that the orbital velocity of the chief is constant. Since the LVLH frame is fixed to the chief, its angular rate will also be constant and thus

$$\dot{\omega} = 0 \tag{2.25}$$

Furthermore, for a circular orbit, the angular velocity corresponds to the mean motion and we have

$$\omega = n = \frac{2\pi}{P_c} = \sqrt{\frac{\mu}{a_c^3}} = \sqrt{\frac{\mu}{r_c^3}} \tag{2.26}$$

where P_c is the orbital period of the chief and a_c the semi-major axis of its orbit. These two equations allow simplification of Eq. (2.12) to

$${}^{I}\ddot{\boldsymbol{r}} = \begin{bmatrix} \ddot{x} - 2n\dot{y} - n^2 x \\ \ddot{y} + 2n\dot{x} - n^2 y \\ \ddot{z} \end{bmatrix} \tag{2.27}$$

We now express the gravitational force on the deputy spacecraft as a function of the relative position. Since $\boldsymbol{r}_d = \boldsymbol{r}_c + \boldsymbol{r}$, $\boldsymbol{f}_g(\boldsymbol{r}_d)$ becomes

$$\boldsymbol{f}_g(\boldsymbol{r}_d) = \boldsymbol{f}_g(\boldsymbol{r}_c + \boldsymbol{r}) = -\frac{\mu}{[(r_c + x)^2 + y^2 + z^2]^{3/2}} \begin{bmatrix} r_c + x \\ y \\ z \end{bmatrix} \tag{2.28}$$

The second assumption made previously allows us to expand this expression into a Taylor series about $\boldsymbol{r} = \boldsymbol{0}$:

$$\boldsymbol{f}_g(\boldsymbol{r}_d) = \boldsymbol{f}_g(\boldsymbol{r}_c) + \mathbf{J}|_{\boldsymbol{r}=\boldsymbol{0}}\, \boldsymbol{r} + \mathcal{O}(2) \tag{2.29}$$

where $\mathbf{J}$ is the Jacobian matrix of $\boldsymbol{f}_g$ and $\mathcal{O}(2)$ denotes higher order terms. The Jacobian matrix can be computed as

$$\mathbf{J}_{i,j} = \frac{\partial f_i}{\partial x_j} = \begin{cases} \frac{3\mu x_i^2}{[(r_c+x)^2+y^2+z^2]^{5/2}} - \frac{\mu}{[(r_c+x)^2+y^2+z^2]^{3/2}} & \text{if } i = j \\ \frac{3\mu x_i x_j}{[(r_c+x)^2+y^2+z^2]^{5/2}} & \text{if } i \neq j \end{cases} \tag{2.30}$$

which, when evaluated at $\boldsymbol{r} = \mathbf{0}$, becomes

$$\mathbf{J}|_{\boldsymbol{r}=\mathbf{0}} = \begin{bmatrix} \frac{2\mu}{r_c^3} & 0 & 0 \\ 0 & -\frac{\mu}{r_c^3} & 0 \\ 0 & 0 & -\frac{\mu}{r_c^3} \end{bmatrix} \tag{2.31}$$

When plugging this expression back into Eq. (2.29) and neglecting the higher order terms, we get

$$\boldsymbol{f}_g(\boldsymbol{r}_d) = \begin{bmatrix} -\frac{\mu}{r_c^2} + \frac{2\mu x}{r_c^3} \\ -\frac{\mu y}{r_c^3} \\ -\frac{\mu z}{r_c^3} \end{bmatrix} \tag{2.32}$$

This equation along with Eqs. (2.15) and (2.27) is used in Eq. (2.18) which, after rearranging, finally becomes [7]:

$$\ddot{x} - 2n\dot{y} - 3n^2 x = f_x \tag{2.33}$$

$$\ddot{y} + 2n\dot{x} = f_y \tag{2.34}$$

$$\ddot{z} + n^2 z = f_z \tag{2.35}$$

These equations are known as the Clohessy-Wiltshire (CW) or Hill-Clohessy-Wiltshire (HCW) equations and are a linear approximation of the exact equations of relative motion described by Eqs. (2.22) - (2.24). A closed-form, analytical solution to these equations can be derived if we assume that no external force aside from gravity acts

on the system, i.e. $f_{x,y,z} = 0$. If we take the Laplace transform of Eqs. (2.33)-(2.35) with this assumption, we obtain

$$\mathcal{L}\{\ddot{x}\} - 2n\mathcal{L}\{\dot{y}\} - 3n^2\mathcal{L}\{x\} = 0 \tag{2.36}$$

$$\mathcal{L}\{\ddot{y}\} + 2n\mathcal{L}\{\dot{x}\} = 0 \tag{2.37}$$

$$\mathcal{L}\{\ddot{z}\} + n^2\mathcal{L}\{z\} = 0 \tag{2.38}$$

where we used the linearity of the Laplace transform. Moreover, the transforms of the first and second order derivatives of a function satisfy [86]:

$$\mathcal{L}\{f'\} = s\mathcal{L}\{f\} - f(0) \tag{2.39}$$

$$\mathcal{L}\{f''\} = s^2\mathcal{L}\{f\} - sf(0) - f'(0) \tag{2.40}$$

With these properties, Eqs. (2.36)-(2.38) can be rewritten as

$$s^2\mathcal{L}\{x\} - sx_0 - \dot{x}_0 - 2ns\mathcal{L}\{y\} + 2ny_0 - 3n^2\mathcal{L}\{x\} = 0 \tag{2.41}$$

$$s^2\mathcal{L}\{y\} - sy_0 - \dot{y}_0 + 2ns\mathcal{L}\{x\} - 2nx_0 = 0 \tag{2.42}$$

$$s^2\mathcal{L}\{z\} - sz_0 - \dot{z}_0 + n^2\mathcal{L}\{z\} = 0 \tag{2.43}$$

where 0 subscripts indicate initial values at time t_0. This linear system of equations can be solved to get

$$\mathcal{L}\{x\} = \left(4x_0 + \frac{2\dot{y}_0}{n}\right)\frac{1}{s} - \left(3x_0 + \frac{2\dot{y}_0}{n}\right)\frac{s}{s^2+n^2} + \frac{\dot{x}_0}{n}\frac{n}{s^2+n^2} \tag{2.44}$$

$$\begin{aligned}\mathcal{L}\{y\} = &\left(y_0 - \frac{2\dot{x}_0}{n}\right)\frac{1}{s} - (6nx_0 + 3\dot{y}_0)\frac{1}{s^2} + \frac{2\dot{x}_0}{n}\frac{s}{s^2+n^2} \\ &+ \left(6x_0 + \frac{4\dot{y}_0}{n}\right)\frac{n}{s^2+n^2}\end{aligned} \tag{2.45}$$

$$\mathcal{L}\{z\} = z_0\frac{s}{s^2+n^2} + \frac{\dot{z}_0}{n}\frac{n}{s^2+n^2} \tag{2.46}$$

Applying an inverse Laplace transform on these equations finally results in [4]:

$$x(t) = \left(4x_0 + \frac{2\dot{y}_0}{n}\right) - \left(3x_0 + \frac{2\dot{y}_0}{n}\right)\cos[n(t-t_0)] + \frac{\dot{x}_0}{n}\sin[n(t-t_0)] \tag{2.47}$$

$$\begin{aligned} y(t) = y_0 - \frac{2\dot{x}_0}{n} - (6nx_0 + 3\dot{y}_0)(t-t_0) + \frac{2\dot{x}_0}{n}\cos[n(t-t_0)] \\ + \left(6x_0 + \frac{4\dot{y}_0}{n}\right)\sin[n(t-t_0)] \end{aligned} \tag{2.48}$$

$$z(t) = z_0\cos[n(t-t_0)] + \frac{\dot{z}_0}{n}\sin[n(t-t_0)] \tag{2.49}$$

Similar equations for the relative velocity can be obtained by taking the first derivative of these equations:

$$\dot{x}(t) = (3nx_0 + 2\dot{y}_0)\sin[n(t-t_0)] + \dot{x}_0\cos[n(t-t_0)] \tag{2.50}$$

$$\dot{y}(t) = -(6nx_0 + 3\dot{y}_0) - 2\dot{x}_0\sin[n(t-t_0)] + (6nx_0 + 4\dot{y}_0)\cos[n(t-t_0)] \tag{2.51}$$

$$\dot{z}(t) = -nz_0\sin[n(t-t_0)] + \dot{z}_0\cos[n(t-t_0)] \tag{2.52}$$

These equations describe the relative position and velocity of the deputy at any time t given the initial relative position and velocity of the spacecraft at time t_0 under the assumptions that the chief is on a circular orbit and that the deputy is close to the chief.

2.1.1 Accuracy of the Clohessy-Wiltshire Equations

In order to assess the range of validity of the CW equations, a comparison between the linearized model and the exact one is made for different chief's eccentricities and different distances between the deputy and the chief. It is assumed that the deputy has an initial relative position

$$\boldsymbol{r} = \begin{bmatrix} 50 & -200 & -30 \end{bmatrix}^T \text{ m}$$

and velocity

$$\dot{\boldsymbol{r}} = \begin{bmatrix} 0.4 & -0.1 & 0.5 \end{bmatrix}^T \text{ m/s}$$

with respect to the chief and that the chief is on an orbit with semi-major axis

$$a = R_\oplus + 700 \text{ km} = 7078.1366 \text{ km}$$

The exact relative motion, $\boldsymbol{r}_{\text{exact}}$, is obtained by numerically integrating the equations describing the absolute motion of both spacecraft, computing the difference, and rotating the relative position into the LVLH reference frame, i.e. $\boldsymbol{r}_{\text{exact}} = \mathcal{R}(\boldsymbol{r}_d - \boldsymbol{r}_c)$ with $\mathcal{R}$ the rotation matrix from J2000 to LVLH. The linear approximation of the motion is computed using the CW equations (Eqs. (2.47)-(2.52)) and the error between the two models is given by

$$\mathbf{err} = \boldsymbol{r}_{\text{CW}} - \boldsymbol{r}_{\text{exact}} \tag{2.53}$$

Fig. 2.3 shows the time evolution of the error in the x, y, and z directions of the LVLH frame between the linearized relative motion and the exact relative motion for different eccentricities of the chief's orbit. As can be seen on this figure, the error is reasonably small for small eccentricities but grows as the eccentricity grows. We see that the amplitude of the error grows with time in the x and y directions but stays more or less constant in the z direction. Periodic oscillations in the positive and negative directions are visible for x and z and a steady increase is observed for y. These results show that if the chief is on an eccentric orbit with $e = 0.1$ for instance, and the CW equations are used to describe the relative motion of a deputy, then after 4.5 hours an error of about 200 meters will have accumulated in the x direction, 1 kilometers in the y direction, and -50 meters in the z direction. In order to relate these eccentricities to injection errors, we compute the differences between the apsides for a given eccentricity and the radius of a circular orbit. We assume that the semi-major axis of the elliptic orbit corresponds to the radius of the desired circular orbit. With

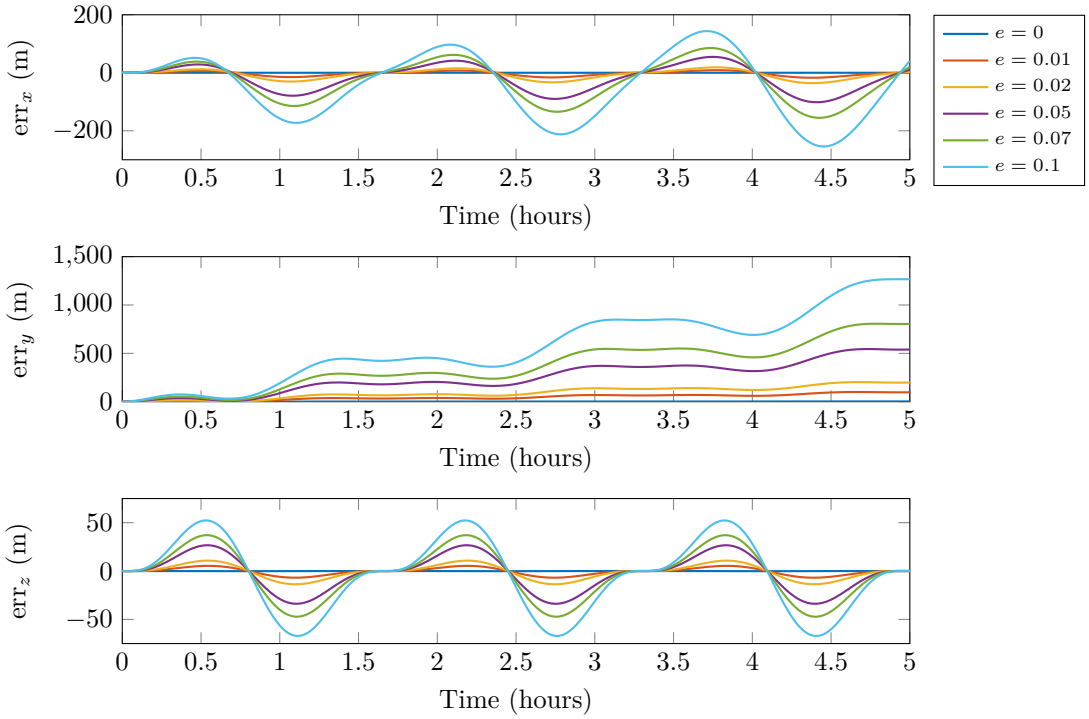

Figure 2.3: Error introduced by the linearization for different chief's eccentricity along the x, y, and z directions of the LVLH frame.

this assumption, the difference between both apsides will be the same as illustrated in Fig. 2.4.

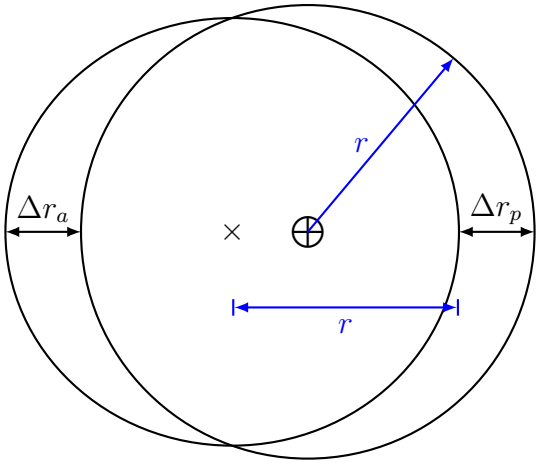

Figure 2.4: Circular and elliptic orbits.

For a given semi-major axis a and eccentricity e, the distance of the apoapsis and periapsis from the central body are respectively

$$r_a = a(1+e) \tag{2.54}$$

$$r_p = a(1-e) \tag{2.55}$$

Hence, if the desired radius of the circular orbit is $r = a$, the difference between the radius and the apoapsis and periapsis is

$$\Delta r_a = |r - r_a| \tag{2.56}$$

$$\Delta r_p = |r - r_p| \tag{2.57}$$

Since $\Delta r \coloneqq \Delta r_a = \Delta r_p$, we have

$$\Delta r = |a - r_p| = |a - a(1-e)| = |ae| = ae \tag{2.58}$$

which corresponds to half the distance between the two focii. This quantity allows us to compute the eccentricity of the orbit after an injection error of Δr, assuming that the elliptical orbit has a semi-major axis corresponding to the radius of the circular orbit. Similarly, given an eccentricity, we can compute the injection error that would result in such an orbit under the same assumption. Table 2.1 shows the injection errors resulting in elliptic orbits with eccentricities presented in Fig. 2.3 for a targeted 700 km altitude circular orbit.

These results show that in order to achieve a perfectly circular orbit, a perfect injection is required. We then see that even a large injection error of about 70 kilometers results in a relatively small eccentricity of 0.01. Note that the elliptical orbit with $e = 0.1$ would have a perigee below the Earth surface for this specific case. Some launch vehicles have an injection accuracy that falls within a few kilometers for LEO. The Delta IV launch vehicle, for instance, has a 3-σ accuracy of ± 11 km for the perigee altitude and ± 12 km for the apogee altitude for a 500 km circular orbit at 90°

Table 2.1: Injection errors resulting in the specified eccentricities.

Eccentricity	**Error (km)**
0	0
0.01	70.78
0.02	141.56
0.05	353.91
0.07	495.97
0.1	707.81

inclination [87]. These errors could result in an maximum eccentricity of $e = 0.0017$. This level of accuracy would allow to inject a chief spacecraft on an orbit for which the eccentricity would be in close agreement with the circular orbit assumption used in the derivation of the CW equations.

We now look at how the distance between the deputy and the chief affects the accuracy of the linear model. Let us consider a deputy spacecraft slightly ahead of the chief, on the same orbit. In the linear model, the relative position can be expressed in the LVLH frame as

$$\boldsymbol{r}_{\text{LVLH}} = \begin{bmatrix} 0 & y_{\text{LVLH}} & 0 \end{bmatrix}^T \tag{2.59}$$

In reality, due to the curvature of the orbit, the true relative position of the deputy expressed in the LVLH frame is

$$\boldsymbol{r}_{\text{true}} = \begin{bmatrix} x_{\text{true}} & y_{\text{true}} & 0 \end{bmatrix}^T \tag{2.60}$$

Fig. 2.5 illustrates the errors introduced by the linearization on both the x and y directions for a chief spacecraft on a circular orbit with radius r. The length of the blue segment and the length of the blue arc are identical. Since the length of the arc is given by $r\theta$, we have

$$r\theta = y_{\text{LVLH}} \tag{2.61}$$

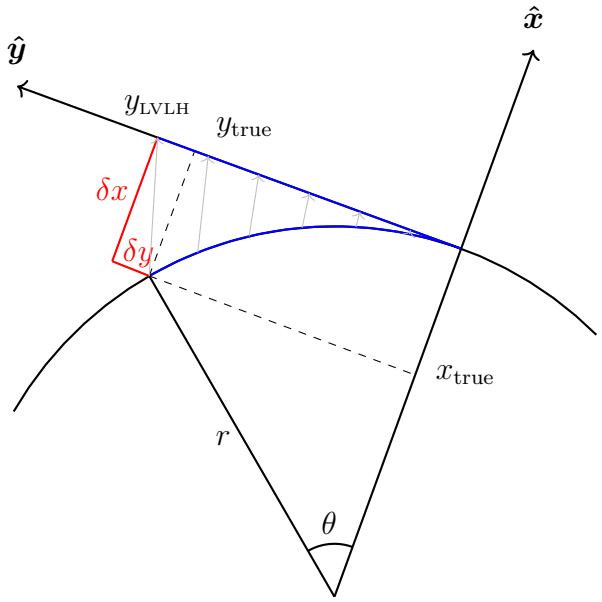

Figure 2.5: Error between the true position and the LVLH position.

and therefore

$$\theta = \frac{y_{\text{LVLH}}}{r} \tag{2.62}$$

The true position of the spacecraft can thus be computed as

$$x_{\text{true}} = -(r - r\cos\theta) = -r\left(1 - \cos\frac{y_{\text{LVLH}}}{r}\right) \tag{2.63}$$

$$y_{\text{true}} = r\sin\theta = r\sin\frac{y_{\text{LVLH}}}{r} \tag{2.64}$$

The errors correspond to the difference between the true position and the linear approximation and yield

$$\delta x = |x_{\text{true}} - x_{\text{LVLH}}| = \left|-r\left(1 - \cos\frac{y_{\text{LVLH}}}{r}\right)\right| \tag{2.65}$$

$$\delta y = |y_{\text{true}} - y_{\text{LVLH}}| = \left|r\sin\frac{y_{\text{LVLH}}}{r} - y_{\text{LVLH}}\right| \tag{2.66}$$

Table 2.2 below shows the errors for different relative distances between the deputy and the chief for a 700 km altitude orbit about the Earth.

Table 2.2: Errors for different relative distances in the along-track direction.

$\boldsymbol{y}_{\text{LVLH}}$ (m)	$\boldsymbol{\delta x}$ (m)	$\boldsymbol{\delta y}$ (m)
10	7.06e-6	3.33e-12
100	7.06e-4	3.33e-9
500	1.77e-2	4.16e-7
1,000	7.06e-2	3.33e-6
5,000	1.77	4.16e-4
10,000	7.06	3.33e-3
50,000	176.60	0.42

We see from this table that the errors stay reasonably small for small y_{LVLH} and then significantly grow when y_{LVLH} reaches distances in the order of several kilometers. We can also observe that the error in the x direction is much larger than the one in the y direction. For instance, at a distance of 1 km, the error in the x direction is 7.06 cm whereas the error in the y direction is 3.33 μm. These results show that at that altitude, the linear approximation of the relative motion can be used for spacecraft formations with a baseline of a few hundred meters but care must be taken when designing more distributed formations. For a given relative distance, the errors will become less significant at higher altitudes and more significant at lower altitudes.

The LVLH Cartesian coordinates used with the CW equations do not offer much intuition into the relative trajectory followed by the deputy. In order to gain a better understanding of the time evolution of the deputy spacecraft's relative motion, several sets of elements have been developed over the past decades. Two different formulations which are used in this work are described in the following sections.

2.1.2 Lovell and Tragesser Formulation

The first set of relative orbital elements used in this work has first been introduced by Lovell and Tragesser [27]. The set consists of six elements derived from the solution to the CW equations which represent quantities associated with the projection of the

instantaneous relative orbit in the x-y plane and x-z plane. The first four elements are defined with respect to the projection of the instantaneous relative orbit in the chief's orbital plane, that is in the x-y plane of the LVLH frame. The relative motion in that plane is given by Eqs. (2.47)-(2.49). We see from Eq. (2.47) that the motion along the x axis is described by the harmonic motion about a constant center. The position of this center is given by

$$x_r = 4x_0 + \frac{2\dot{y}_0}{n} \tag{2.67}$$

The motion along the y axis is described by the combination of a constant, a secular term, and trigonometric terms as can be seen in Eq. (2.48). The combination of these expressions result in an harmonic motion about a center which has a secular drift. The position of that center is given by

$$y_r(t) = y_0 - \frac{2\dot{x}_0}{n} - (6nx_0 + 3\dot{y}_0)(t - t_0) \tag{2.68}$$

These two quantities define the first two ROEs and describe the position of the instantaneous center of motion of the relative orbit. After some trigonometric manipulations and rearranging, Eqs. (2.47) and (2.48) can be combined into

$$\frac{(x - x_r)^2}{\left(3x_0 + \frac{2\dot{y}_0}{n}\right)^2 + \left(\frac{\dot{x}_0}{n}\right)^2} + \frac{(y - y_r)^2}{4\left[\left(3x_0 + \frac{2\dot{y}_0}{n}\right)^2 + \left(\frac{\dot{x}_0}{n}\right)^2\right]} = 1 \tag{2.69}$$

which can be readily identified as the equation of an ellipse. This ellipse has a semi-minor axis

$$A_x = \sqrt{\left(3x_0 + \frac{2\dot{y}_0}{n}\right)^2 + \left(\frac{\dot{x}_0}{n}\right)^2} \tag{2.70}$$

and semi-major axis

$$A_y = 2\sqrt{\left(3x_0 + \frac{2\dot{y}_0}{n}\right)^2 + \left(\frac{\dot{x}_0}{n}\right)^2} \tag{2.71}$$

It follows from these quantities that the semi-major axis of an unforced relative orbit will always have a length twice that of the semi-minor axis, and therefore a single quantity can be defined to describe the shape of the ellipse. Hence, the third ROE is the relative semi-major axis defined as

$$a_r = \sqrt{\left(6x_0 + \frac{4\dot{y}_0}{n}\right)^2 + \left(\frac{2\dot{x}_0}{n}\right)^2} \tag{2.72}$$

If the Harmonic Addition Theorem [88] is now applied to Eqs. (2.47) and (2.48), and x_r, y_r, and a_r are substituted back, we get

$$x(t) = x_r - \frac{1}{2}a_r \cos\left[n(t-t_0) + \text{atan2}\left(\frac{2\dot{x}_0}{n}, 6x_0 + \frac{4\dot{y}_0}{n}\right)\right] \tag{2.73}$$

$$y(t) = y_r(t) + a_r \sin\left[n(t-t_0) + \text{atan2}\left(\frac{2\dot{x}_0}{n}, 6x_0 + \frac{4\dot{y}_0}{n}\right)\right] \tag{2.74}$$

where atan2 is the 2-argument arctangent and returns a value in the range $(-\pi, \pi]$. The argument of the sine and cosine being identical, the fourth ROE is defined as

$$E_r(t) = n(t-t_0) + E_{r0} \tag{2.75}$$

with

$$E_{r0} = \text{atan2}\left(\frac{2\dot{x}_0}{n}, 6x_0 + \frac{4\dot{y}_0}{n}\right) \tag{2.76}$$

This element is called the relative eccentric anomaly and describes the position of the deputy spacecraft on the relative orbit. It is a measure of the angle from the position of the periapsis to the projection of the spacecraft on an auxiliary circle of radius a_r. A geometric interpretation of these four ROEs is shown in Fig. 2.6.

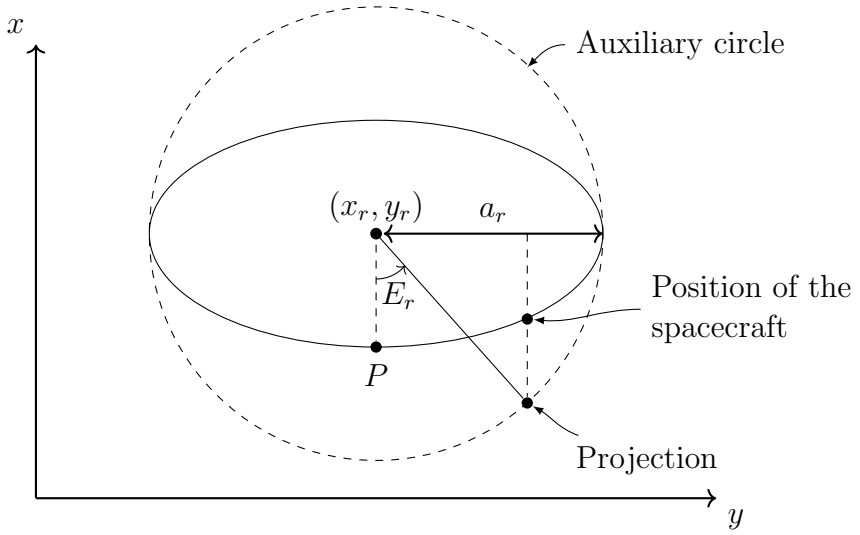

Figure 2.6: Projection of the relative trajectory in the x-y plane of the LVLH frame. P denotes the position of the periapsis. Reproduced from [42].

Using these four ROEs, the relative position and velocity of the deputy spacecraft in the x-y plane can be expressed as

$$x(t) = x_r - \frac{1}{2}a_r \cos E_r(t) \tag{2.77}$$

$$y(t) = y_r(t) + a_r \sin E_r(t) \tag{2.78}$$

and

$$\dot{x}(t) = \frac{n}{2}a_r \sin E_r(t) \tag{2.79}$$

$$\dot{y}(t) = -\frac{3}{2}nx_r + na_r \cos E_r(t) \tag{2.80}$$

The last two elements are defined in the projection on the x-z plane. Applying the Harmonic Addition Theorem to Eq. (2.49) results in

$$z(t) = \sqrt{z_0^2 + \left(\frac{\dot{z}_0^2}{n}\right)^2} \sin\left[n(t - t_0) + \text{atan2}\left(z_0, \frac{\dot{z}_0}{n}\right)\right] \tag{2.81}$$

We see from this equation that the amplitude of the relative cross-track motion of the spacecraft is

$$A_z = \sqrt{z_0^2 + \left(\frac{\dot{z}_0}{n}\right)^2} \tag{2.82}$$

which defines a fifth ROE. Additionally, the argument of the sine in Eq. (2.81) provides a sixth element defined as the phase angle of the cross-track motion

$$\psi(t) = n(t - t_0) + \psi_0 \tag{2.83}$$

with

$$\psi_0 = \text{atan2}\left(z_0, \frac{\dot{z}_0}{n}\right) \tag{2.84}$$

This phase angle is measured from the negative x direction to the projection of the spacecraft on an auxiliary circle of radius A_z. Fig. 2.7 shows the projection of the relative trajectory together with the two ROEs in the cross-track plane.

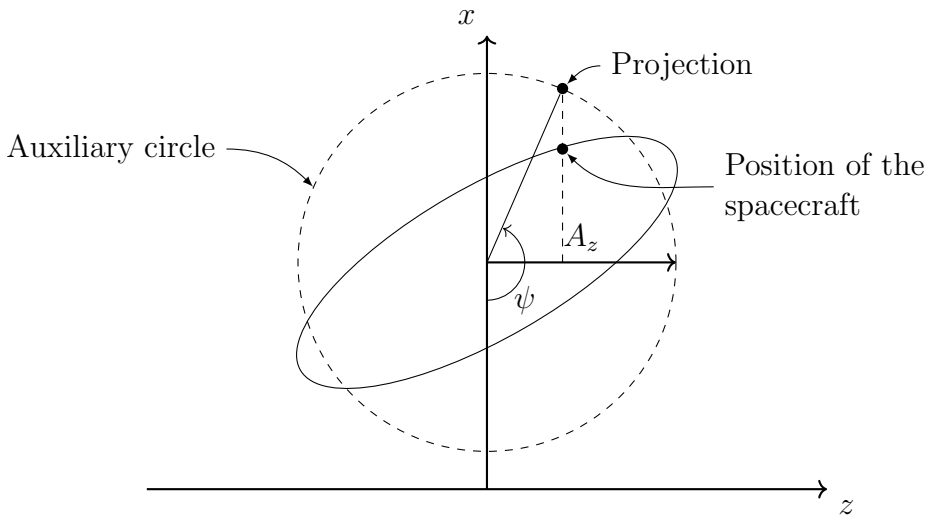

Figure 2.7: Projection of the relative trajectory in the x-z plane of the LVLH frame. Reproduced from [42].

With the definition of these two ROEs, the position along the z axis can be expressed as

$$z(t) = A_z \sin\psi(t) \tag{2.85}$$

and the velocity

$$\dot{z}(t) = nA_z \cos\psi(t) \tag{2.86}$$

It follows from the definition of the ROEs that three elements, y_r, E_r, and ψ are time-dependent. In order to replace one of them with a constant value, the difference between the phase angle in the cross-track projection and the relative eccentric anomaly is defined and is used instead of ψ:

$$\gamma = \psi(t) - E_r(t) \tag{2.87}$$

The set of ROEs thus becomes $\{x_r \quad y_r \quad a_r \quad E_r \quad A_z \quad \gamma\}$ and fully describes the relative position and velocity of the deputy spacecraft with respect to the chief. With the definition of γ, Eqs. (2.85) and (2.86) become

$$z(t) = A_z \sin(E_r(t) + \gamma) \tag{2.88}$$

$$\dot{z}(t) = nA_z \cos(E_r(t) + \gamma) \tag{2.89}$$

The equations describing the ROEs derived so far involve knowledge of the initial condition of the deputy spacecraft. It is sometimes convenient to compute the ROEs in terms of instantaneous LVLH Cartesian coordinates rather than initial conditions. This can be achieved with the following set of equations [42]:

$$x_r = 4x + \frac{2\dot{y}}{n} \tag{2.90}$$

$$y_r = y - \frac{2\dot{x}}{n} \tag{2.91}$$

$$a_r = \sqrt{\left(6x + \frac{4\dot{y}}{n}\right)^2 + \left(\frac{2\dot{x}}{n}\right)^2} \tag{2.92}$$

$$E_r = \text{atan2}\left(\frac{2\dot{x}}{n}, 6x + \frac{4\dot{y}}{n}\right) \tag{2.93}$$

$$A_z = \sqrt{z^2 + \left(\frac{\dot{z}}{n}\right)^2} \tag{2.94}$$

$$\gamma = \text{atan2}\left(z, \frac{\dot{z}}{n}\right) - \text{atan2}\left(\frac{2\dot{x}}{n}, 6x + \frac{4\dot{y}}{n}\right) \tag{2.95}$$

Finally, these equations can be inverted to express the LVLH coordinates in terms of ROEs as:

$$x(t) = x_r - \frac{1}{2}a_r \cos E_r(t) \tag{2.96}$$

$$y(t) = y_r(t) + a_r \sin E_r(t) \tag{2.97}$$

$$z(t) = A_z \sin(E_r(t) + \gamma) \tag{2.98}$$

$$\dot{x}(t) = \frac{n}{2}a_r \sin E_r(t) \tag{2.99}$$

$$\dot{y}(t) = -\frac{3}{2}nx_r + na_r \cos E_r(t) \tag{2.100}$$

$$\dot{z}(t) = nA_z \cos(E_r(t) + \gamma) \tag{2.101}$$

2.1.3 Healy and Henshaw Formulation

Another set of relative orbital elements called geometric relative orbital elements (GROEs) has been derived by Healy and Henshaw [47]. This set, also based on the solution to the CW equations, comprises eight parameters and is the geometric analog to the classical orbital elements for relative orbits. The derivation of this set is based on the observation that Eqs. (2.47)-(2.52) can be rewritten in terms of six parameters:

$$x = x_c + \kappa \sin\tau \tag{2.102}$$

$$y = y_c - \frac{3}{2}x_c(\tau - \tau_0) + 2\kappa \cos\tau \tag{2.103}$$

$$z = \kappa\eta \sin(\Xi + \tau) \tag{2.104}$$

$$\dot{x} = n\kappa \cos\tau \tag{2.105}$$

$$\dot{y} = -\frac{3}{2}nx_c - 2n\kappa \sin\tau \tag{2.106}$$

$$\dot{z} = n\kappa\eta \cos(\Xi + \tau) \tag{2.107}$$

where

$$\Xi = \text{atan2}(nz, \dot{z}) - \text{atan2}(-3nx - 2\dot{y}, \dot{x}) \tag{2.108}$$

$$\eta = \sqrt{\frac{n^2 z^2 + \dot{z}^2}{\dot{x}^2 + (3nx + 2\dot{y})^2}} \tag{2.109}$$

$$\kappa = \frac{1}{n}\sqrt{\dot{x}^2 + (3nx + 2\dot{y})^2} \tag{2.110}$$

$$x_c = 4x + \frac{2\dot{y}}{n} \tag{2.111}$$

$$y_c = y - \frac{2\dot{x}}{n} + \frac{3}{2}x_c(\tau - \tau_0) \tag{2.112}$$

$$\tau = \text{atan2}(-3nx - 2\dot{y}, \dot{x}) \tag{2.113}$$

The first parameter, Ξ, represents a phase angle and is the difference between the phase in the cross-track plane and in the fundamental plane. The second parameter, η, corresponds to the ratio of the amplitudes of the cross-track and in-plane motions. κ describes the semi-minor axis of the projected ellipse in the x-y plane. The fourth and fifth parameters describe the location of the center of motion of the instantaneous relative orbit. Finally, τ is a phase angle in the x-y plane that evolves according to $\tau = \tau_0 + nt$ where τ_0 is the value of τ at $t = 0$. Out of these six parameters, y_c and τ are time-varying whereas the other ones are constant. These parameters are closely related to the ROEs and can be transformed with the following equations:

$$\Xi = \gamma - \frac{\pi}{2} \qquad \eta = \frac{2A_z}{a_r} \qquad \kappa = \frac{a_r}{2} \qquad x_c = x_r \qquad y_c = y_r \qquad \tau = E_r + \frac{\pi}{2}$$

The eight GROEs are based on these parameters. Similarly to the ROEs, the first two GROEs, x_c and y_c, describe the position of the instantaneous center of motion. Using

these two elements, the time-varying position and velocity of the center of motion in the LVLH frame can be defined:

$$\boldsymbol{\rho}_c = \begin{bmatrix} x_c \\ y_c - \frac{3}{2}ntx_c \\ 0 \end{bmatrix} \tag{2.114}$$

$$\dot{\boldsymbol{\rho}}_c = \begin{bmatrix} 0 \\ -\frac{3}{2}nx_c \\ 0 \end{bmatrix} \tag{2.115}$$

which correspond to the constant and secular terms in Eqs. (2.102)-(2.104). The relative position and velocity of the deputy can then be shifted with respect to the position and velocity of the center of motion to obtain the relative state in what is defined as the centered LVLH or cLVLH frame:

$$\boldsymbol{s}_{\text{cLVLH}} = \boldsymbol{r} - \boldsymbol{\rho}_c = \kappa \begin{bmatrix} \sin\tau \\ 2\cos\tau \\ \eta\sin(\Xi+\tau) \end{bmatrix}_{\text{cLVLH}} \tag{2.116}$$

$$\dot{\boldsymbol{s}}_{\text{cLVLH}} = \dot{\boldsymbol{r}} - \dot{\boldsymbol{\rho}}_c = n\kappa \begin{bmatrix} \cos\tau \\ -2\sin\tau \\ \eta\cos(\Xi+\tau) \end{bmatrix}_{\text{cLVLH}} \tag{2.117}$$

A new coordinate system, the apocentral coordinates, is now defined with two of its axes lying in the plane of the relative orbit. The $\hat{\boldsymbol{X}}$ axis is defined as the direction of maximum excursion of the deputy in the half-plane with $y \geq 0$. The $\hat{\boldsymbol{Z}}$ axis is defined along the relative orbit's plane normal. The third axis, $\hat{\boldsymbol{Y}}$, is chosen to be orthogonal to the first two axes and completes the triad: $\hat{\boldsymbol{Y}} = \hat{\boldsymbol{Z}} \times \hat{\boldsymbol{X}}$. Fig. 2.8 illustrates the apocentral coordinates system in the LVLH frame.

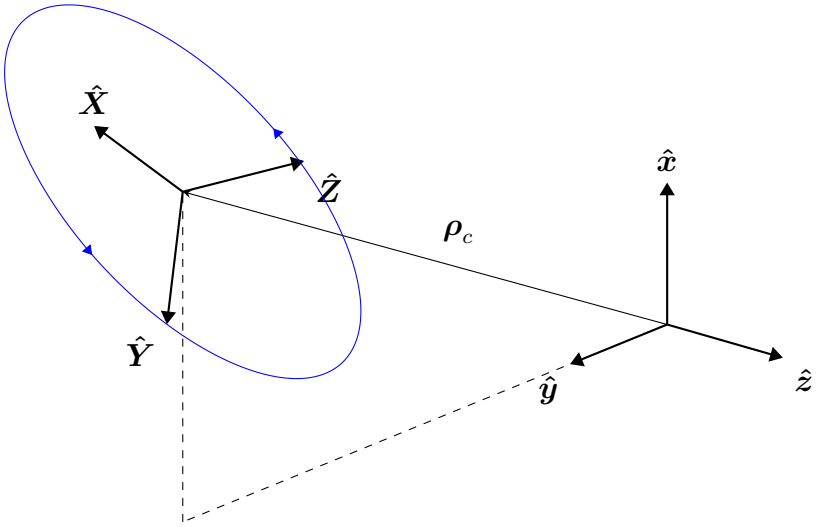

Figure 2.8: Apocentral coordinates and LVLH frame.

The rotation matrix to go from apocentral to cLVLH can be computed as:

$$\mathcal{R} = \begin{bmatrix} \frac{X\sin\varpi}{Z} & \frac{X\cos\varpi}{Z} & \frac{2\eta\cos\Xi}{Z} \\ \frac{2\cos\varpi}{X} - \frac{\eta^2\sin 2\Xi\sin\varpi}{XZ} & -\frac{2\sin\varpi}{X} - \frac{\eta^2\sin 2\Xi\cos\varpi}{XZ} & \frac{\eta\sin\Xi}{z} \\ \frac{4\eta\cos\Xi\sin\varpi}{XZ} + \frac{\eta\sin\Xi\cos\varpi}{X} & \frac{4\eta\cos\Xi\cos\varpi}{XZ} - \frac{\eta\sin\Xi\sin\varpi}{X} & -\frac{2}{Z} \end{bmatrix} \tag{2.118}$$

with

$$X = \sqrt{4 + \eta^2\sin^2\Xi} \tag{2.119}$$

$$Z = \sqrt{4 + \eta^2(1 + 3\cos^2\Xi)} \tag{2.120}$$

$$\varpi = \arctan\left(\frac{Z\sin\tau_a}{X^2\cos\tau_a + \eta^2\sin\Xi\cos\Xi\sin\tau_a}\right) \tag{2.121}$$

$$\tau_a = \begin{cases} \tau_{\text{ext}} & \text{if } \eta^2\cos 2(\Xi + \tau_{\text{ext}}) \leq 3\cos 2\tau_{\text{ext}} \\ \tau_{\text{ext}} + \frac{\pi}{2} & \text{otherwise} \end{cases} \tag{2.122}$$

$$\tau_{\text{ext}} = \frac{1}{2}\,\text{atan2}(\eta^2\sin 2\Xi, 3 - \eta^2\cos 2\Xi) \tag{2.123}$$

A derivation of these equations is presented in [47]. The relative position in apocentral coordinates can be obtained by multiplying Eq. (2.116) by $\mathcal{R}^T$

$$\boldsymbol{s}_{\text{apoc}} = \mathcal{R}^T \boldsymbol{s}_{\text{cLVLH}} \tag{2.124}$$

Since the instantaneous relative orbit is an ellipse, we can also express $\boldsymbol{s}_{\text{apoc}}$ as

$$\boldsymbol{s}_{\text{apoc}} = \begin{bmatrix} a\cos c \\ b\sin c \\ 0 \end{bmatrix}_{\text{apoc}} \tag{2.125}$$

where a is the semi-major axis of the ellipse, b the semi-minor axis, and $c = \tau - \tau_a$ the central anomaly measured from $\hat{\boldsymbol{X}}$ to the projection of the deputy on an auxiliary circle of radius a. If we compute the first component of Eq. (2.124) and evaluate at $\tau = \tau_a$, we get

$$a = \frac{\kappa}{X}([4\cos\tau_a + \eta^2 + \sin\Xi\sin(\Xi+\tau_a)]\cos\varpi + Z\sin\tau_a\sin\varpi) \tag{2.126}$$

and similarly for the second component evaluated at $\tau = \tau_a + \pi/2$

$$b = \frac{\kappa}{X}([4\sin\tau_a - \eta^2\sin\Xi\cos(\Xi+\tau_a)]\sin\varpi + Z\cos\tau_a\cos\varpi) \tag{2.127}$$

The eccentricity of the relative orbit can then be computed as

$$e = \sqrt{1 - \left(\frac{b}{a}\right)^2} \tag{2.128}$$

The semi-major axis of the relative orbit, a, and its eccentricity, e, are used as third and fourth GROEs. The fifth element is the central anomaly, c, that describes the in-plane motion of the deputy. These three elements describe the size and shape of the ellipse as well as the location of the spacecraft. The last three ones describe the

orientation of the relative orbit in the LVLH frame. The slant, σ, is the analog to the inclination and is defined as the angle from $\hat{\boldsymbol{z}}$ to $\hat{\boldsymbol{Z}}$:

$$\sigma = \arccos\left(-\frac{2}{Z}\right) \tag{2.129}$$

Since $Z \geq 0$, the slant is defined within $[\frac{\pi}{2}, \pi]$. Similar to the ascending node, the sinilaterating node is defined as the point where the relative orbit crosses the chief's orbital plane in the direction from $-\hat{\boldsymbol{z}}$ to $\hat{\boldsymbol{z}}$. The angle between the sinilaterating node direction $\hat{\boldsymbol{n}}$ and the positive x direction is denoted Υ and is called the colatitude of the sinilaterating node:

$$\Upsilon = \text{atan2}(2\cos\Xi, -\sin\Xi) \tag{2.130}$$

Finally, the last element of the set is the argument of pericenter, ω, which is an angle measured from the direction of the sinilaterating node to the $\hat{\boldsymbol{X}}$ axis and is the analog of the argument of periapsis:

$$\omega = \varpi + \text{atan2}(Z\sin\Xi, 4\cos\Xi) \tag{2.131}$$

This element completes the set of eight GROEs:

$$\{x_c \quad y_c \quad a \quad e \quad c \quad \sigma \quad \Upsilon \quad \omega\} \tag{2.132}$$

Fig. 2.9 illustrates the GROEs in the chief's LVLH frame.

The equations described so far allow to transform from LVLH Cartesian coordinates to GROEs. The inverse transformation from GROEs to LVLH coordinates is obtained by first computing the phase difference

$$\Xi = \text{atan2}(-2\cos\Upsilon, \sin\Upsilon) \tag{2.133}$$

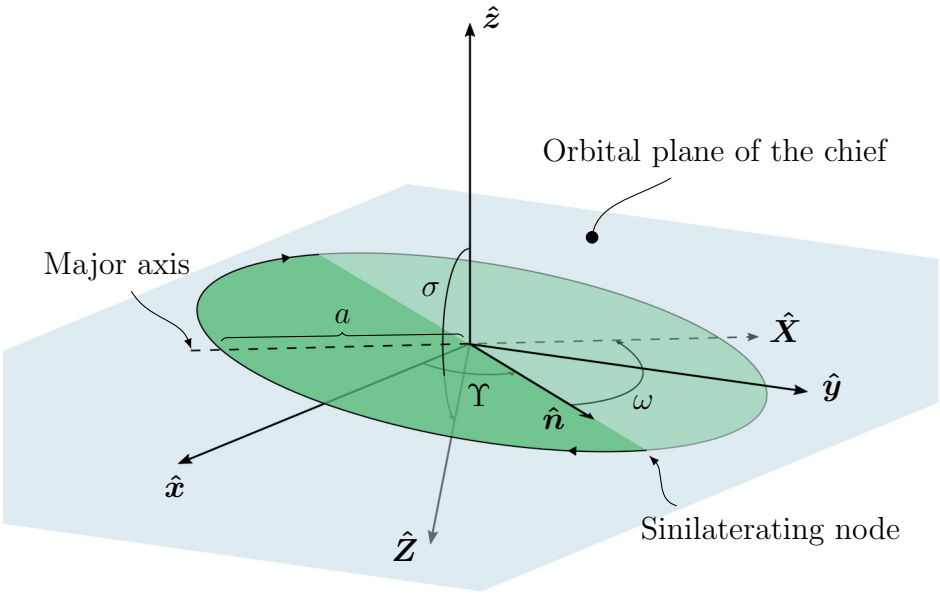

Figure 2.9: Representation of the geometric relative orbital elements (GROEs).

and the relative amplitude

$$\eta = -\frac{2\tan\sigma}{\sqrt{1+3\cos^2\Xi}} = -\sqrt{1+3\cos^2\Upsilon}\tan\sigma \tag{2.134}$$

These quantities allow us to compute Eqs. (2.119)-(2.123) and the rotation matrix $\mathcal{R}$. The relative position and velocity in LVLH Cartesian coordinates can then be computed as

$$\boldsymbol{r} = \boldsymbol{\rho}_c + \mathcal{R}\begin{bmatrix} a\cos(c_0+nt) \\ b\sin(c_0+nt) \\ 0 \end{bmatrix}_{\text{apoc}} \tag{2.135}$$

$$\dot{\boldsymbol{r}} = \dot{\boldsymbol{\rho}}_c + n\mathcal{R}\begin{bmatrix} -a\sin(c_0+nt) \\ b\cos(c_0+nt) \\ 0 \end{bmatrix}_{\text{apoc}} \tag{2.136}$$

where $\boldsymbol{\rho}_c$ and $\dot{\boldsymbol{\rho}}_c$ are given by Eqs. (2.114) and (2.115). Note that if the GROEs are known, the rotation matrix $\mathcal{R}$ can be obtained from the composition of rotations of $-\omega$ about $\hat{\boldsymbol{z}}$, $-\sigma$ about $\hat{\boldsymbol{x}}$, and $-\Upsilon$ about $\hat{\boldsymbol{z}}$, that is

$$\mathcal{R} = \mathcal{R}_z(-\Upsilon)\mathcal{R}_x(-\sigma)\mathcal{R}_z(-\omega) \tag{2.137}$$

where $\mathcal{R}_x$ and $\mathcal{R}_z$ are the standard rotation matrices along the 1st and 3rd dimensions.

It is important to note that since the GROEs are derived from six parameters, the eight elements are not independent. In fact, σ, Υ, and ω, are parameterized by the phase difference Ξ and the relative amplitude η. In addition to these two parameters, a and e also depend on κ. This means that all combinations of GROEs are not valid representations of relative orbits and fixing σ, Υ, and τ for instance will determine ω, a, and e.

2.1.4 Circular Relative Orbits

Circular relative orbits (CROs) are of particular interest to design specific geometries that will be illustrated in Chapter 3. In this sub-section, the sets of ROEs and GROEs describing a CRO are derived. The derivation is first conducted for the ROEs and is based on the assumption that the distance between the spacecraft and the instantaneous center of relative motion is constant. This distance can be expressed as

$$d(t) = \sqrt{(x(t) - x_r(t))^2 + (y(t) - y_r(t))^2 + z(t)^2} \tag{2.138}$$

or similarly as

$$d(t)^2 = (x(t) - x_r(t))^2 + (y(t) - y_r(t))^2 + z(t)^2 \tag{2.139}$$

where the rectangular coordinates (x, y, z) denote the relative position of the spacecraft in the LVLH frame at time t and the first two ROEs, $x_r(t)$ and $y_r(t)$, describe

the position of the center of motion. For a CRO of radius r, this distance is constant and therefore

$$(x(t) - x_r(t))^2 + (y(t) - y_r(t))^2 + z(t)^2 = r^2 \tag{2.140}$$

Using Eqs. (2.96) and (2.98), the rectangular coordinates can be expressed in terms of ROEs which yields

$$\left[-\frac{1}{2}a_r(t)\cos E_r(t)\right]^2 + [a_r(t)\sin E_r(t)]^2 + [A_z(t)\sin(E_r(t)+\gamma(t))]^2 = r^2 \tag{2.141}$$

Replacing the time dependant terms by

$$a_r(t) = a_{r0} \tag{2.142}$$

$$E_r(t) = E_{r0} + n(t - t_0) \tag{2.143}$$

$$A_z(t) = A_{z0} \tag{2.144}$$

$$\gamma(t) = \gamma_0 \tag{2.145}$$

we get

$$\frac{1}{4}a_{r0}^2\cos^2(E_{r0}+n(t-t_0)) + a_{r0}^2\sin^2(E_{r0}+n(t-t_0)) + A_{z0}^2\sin^2(E_{r0}+n(t-t_0)+\gamma_0) = r^2 \tag{2.146}$$

Let $\varphi(t) = n(t - t_0)$ and substitute in the above equation:

$$\frac{1}{4}a_{r0}^2\cos^2(E_{r0}+\varphi(t)) + a_{r0}^2\sin^2(E_{r0}+\varphi(t)) + A_{z0}^2\sin^2(E_{r0}+\varphi(t)+\gamma_0) = r^2 \tag{2.147}$$

This expression is now evaluated at three distinct times such that $\varphi(t_1) = \frac{\pi}{2} - E_{r0}$, $\varphi(t_2) = -E_{r0}$, and $\varphi(t_3) = -E_{r0} - \gamma_0$ which results in, respectively

$$a_{r0}^2 + A_{z0}^2\cos^2\gamma_0 = r^2 \tag{2.148}$$

$$\frac{1}{4}a_{r0}^2 + A_{z0}^2\sin^2\gamma_0 = r^2 \tag{2.149}$$

$$\frac{1}{4}a_{r0}^2\cos^2\gamma_0 + a_{r0}^2\sin^2\gamma_0 = r^2 \tag{2.150}$$

where $\sin(\theta + \frac{\pi}{2}) = \cos(\theta)$ has been used in Eq. (2.148). Subtracting Eq. (2.149) from Eq. (2.148) yields

$$\frac{3}{4}a_{r0}^2 + A_{z0}^2 \cos(2\gamma_0) = 0 \tag{2.151}$$

Since the relative semi-major axis a_{r0} and the amplitude of the cross-track motion A_{z0} are non negative values, the phase angle must satisfy $\cos(2\gamma_0) \leq 0$ and therefore

$$\frac{\pi}{4} \leq \gamma_0 \leq \frac{3\pi}{2} \tag{2.152}$$

Eq. (2.150) is now substituted in Eqs. (2.148) and (2.149) to eliminate r^2, which gives

$$a_{r0}^2 + A_{z0}^2 \cos^2\gamma_0 = \frac{1}{4}a_{r0}^2 \cos^2\gamma_0 + a_{r0}^2 \sin^2\gamma_0 \tag{2.153}$$

$$\frac{1}{4}a_{r0}^2 + A_{z0}^2 \sin^2\gamma_0 = \frac{1}{4}a_{r0}^2 \cos^2\gamma_0 + a_{r0}^2 \sin^2\gamma_0 \tag{2.154}$$

Summing and subtracting these two equations yields respectively

$$\frac{5}{4}a_{r0}^2 + A_{z0}^2 = \frac{1}{2}a_{r0}^2 \cos^2\gamma_0 + 2a_{r0}^2 \sin^2\gamma_0 \tag{2.155}$$

$$\frac{3}{4}a_{r0}^2 + A_{z0}^2(2\cos^2\gamma_0 - 1) = 0 \tag{2.156}$$

Solving for A_{z0} in Eq. (2.155) and plugging back into Eq. (2.156) results in

$$\frac{3}{4}a_{r0}^2 + \left[\frac{1}{2}a_{r0}^2 \cos^2\gamma_0 + 2a_{r0}^2 \sin^2\gamma_0 - \frac{5}{4}a_{r0}^2\right][2\cos^2\gamma_0 - 1] = 0 \tag{2.157}$$

which can be reduced to

$$3a_{r0}^2 \cos^2\gamma_0(1 - \cos^2\gamma_0) = 0 \tag{2.158}$$

Since the relative semi-major axis a_{r0} is strictly positive, it follows that

$$\cos^2\gamma_0(1 - \cos^2\gamma_0) = 0 \tag{2.159}$$

which admits $\gamma_0 = 0$, $\gamma_0 = \frac{\pi}{2}$, $\gamma_0 = \pi$, and $\gamma_0 = \frac{3\pi}{2}$. It has been found however that $\frac{\pi}{4} \leq \gamma_0 \leq \frac{3\pi}{2}$ (Eq. (2.152)) and therefore a CRO is characterized by

$$\gamma_0 = \pm\frac{\pi}{2} \tag{2.160}$$

If this value is plugged back into Eq. (2.151), the amplitude of the cross-track motion becomes

$$A_{z0} = \frac{\sqrt{3}}{2} a_{r0} \tag{2.161}$$

Finally, substituting Eqs. (2.160) and (2.161) into Eq. (2.148) results in

$$a_{r0} = r \tag{2.162}$$

These results indicate that for the unforced motion and for any given radius, only two circular relative orbits exist in the linear approximation of the unperturbed relative motion. Fig. 2.10 illustrates these two orbits in the LVLH reference frame.

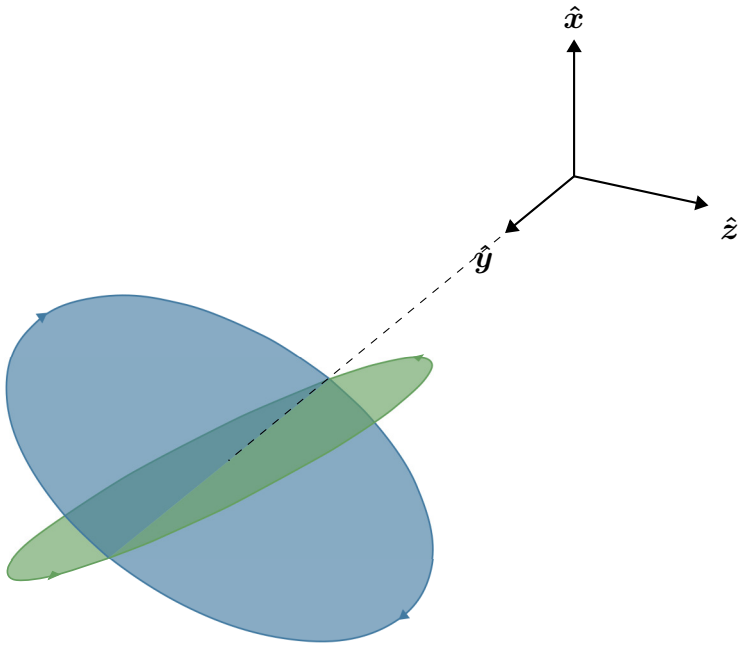

Figure 2.10: Circular relative orbits in the LVLH reference frame. The orientation of the relative orbits planes is defined by $\gamma = 90°$ (green) and $\gamma = -90°$ (blue).

The natural motion of the deputy on these CROs is determined by the orbital velocity of the spacecraft. When the deputy is at a higher altitude, its velocity will be smaller than the velocity of the chief, thus resulting in the deputy drifting in the negative y direction. When on a lower orbit, the deputy will have a larger velocity than the chief, resulting in a drift in the positive y direction.

If $\hat{\boldsymbol{n}}_r$ is the unit vector normal to the relative orbit plane along the relative angular momentum vector, an additional element, the relative inclination, can be defined as the angle between $\hat{\boldsymbol{z}}$ and $\hat{\boldsymbol{n}}_{\boldsymbol{r}}$ [42]:

$$i_r = \cos^{-1}\left(\frac{-a_r}{\sqrt{4A_z^2\sin^2\gamma + A_z^2\cos^2\gamma + a_r^2}}\right) \tag{2.163}$$

This value is identical to the slant σ defined in the context of GROEs. For a CRO, the relative inclination is found by substituting Eqs. (2.160) and (2.161) into Eq. (2.163) and yields

$$i_r = \frac{2\pi}{3} \text{ or } 120^\circ \tag{2.164}$$

This angle is illustrated in Fig. 2.11.

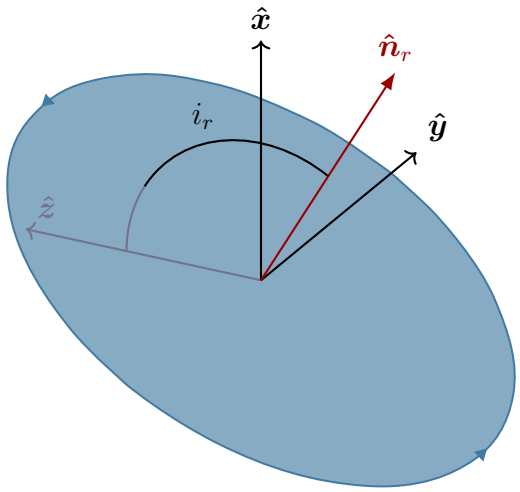

Figure 2.11: Relative inclination angle for a circular relative orbit.

We now show that for a CRO, an angular separation of ν in the orbital plane corresponds to a relative eccentric anomaly difference of ν in the $x-y$ plane. This relation will be used in Chapter 3 to design formation geometries where the spacecraft are equally distributed on the CRO. Fig. 2.12 shows the portion of relative orbit swept out by an angle ν in the relative orbit plane along with the projection on the x-y plane.

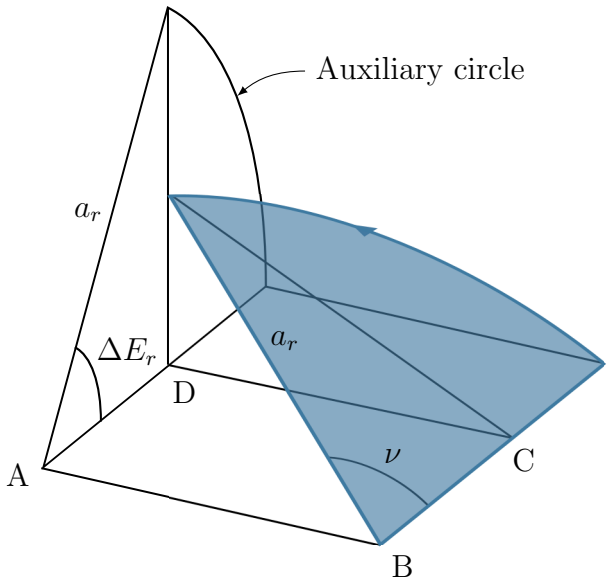

Figure 2.12: Relation between the angular separation in the relative orbit plane ν and the relative eccentric anomaly ΔE_r.

As can be seen in Fig. 2.12, the segment BC can be computed by trigonometry as

$$BC = a_r \cos\nu \tag{2.165}$$

Noting that $AD = BC$, we have

$$\cos\Delta E_r = \frac{AD}{a_r} = \cos\nu \tag{2.166}$$

and therefore, for a CRO, an angular separation of ν in the relative orbit plane corresponds to an angular separation $\Delta E_r = \nu$ in relative eccentric anomaly.

The set of GROEs leading to a CRO is now derived. The relations between the intermediate parameters used in the derivation of the GROEs and the ROEs are used to describe these elements. Based on the values of the ROEs describing a CRO, these parameters become

$$\Xi = 0, \pi \qquad \eta = \sqrt{3} \qquad \kappa = \frac{r}{2}$$

These quantities allow to compute X and Z (Eqs. (2.119) and (2.120)):

$$X = \pm 2 \qquad Z = \pm 4$$

It follows that the slant is

$$\sigma = \cos^{-1}\left(-\frac{2}{Z}\right) = \cos^{-1}\left(\pm\frac{1}{2}\right) = \frac{\pi}{3} \text{ or } \frac{2\pi}{3} \tag{2.167}$$

and since its value is defined within $[\frac{\pi}{2}, \pi]$, the slant must be

$$\sigma = \frac{2\pi}{3} \tag{2.168}$$

The colatitude of the sinilaterating node becomes

$$\Upsilon = \text{atan2}(2\cos\Xi, -\sin\Xi) = \begin{cases} \text{atan2}(2,0) & \text{if } \Xi = 0 \\ \text{atan2}(-2,0) & \text{if } \Xi = \pi \end{cases} \tag{2.169}$$

Hence,

$$\Upsilon = \pm\frac{\pi}{2} \tag{2.170}$$

Also, $\tau_{ext} = 0$, $\tau_a = 0$, and ϖ is undefined if the the relative motion is circular. With these expressions, the relative semi-major and semi-minor axes are

$$a = b = r \tag{2.171}$$

and finally the eccentricity is

$$e = \sqrt{1 - \left(\frac{b}{\bar{b}}\right)^2} = 0 \tag{2.172}$$

The argument of apocenter ω is undefined for circular relative orbits. In the case of GROEs, an angular separation ν in the orbital plane corresponds to an angular separation Δc of the central anomaly for CROs.

2.2 Artificial Potential Function

The APF methodology consists in defining a scalar potential field on the phase space that admits a minimum at the location of a desired goal and design a controller to follow the steepest descent of the gradient of the potential. In order for the method to converge, candidate functions must satisfy Lyapunov's second method for stability. That is, for a scalar potential function $\phi(\boldsymbol{x})$ such that $\phi(\mathbf{0}) = 0$, if

$$\phi(\boldsymbol{x}) > 0, \quad \forall \boldsymbol{x} \neq \mathbf{0} \tag{2.173}$$

$$\phi(\boldsymbol{x}) \to \infty, \quad \text{as } \boldsymbol{x} \to \infty \tag{2.174}$$

$$\dot{\phi}(\boldsymbol{x}) < 0, \quad \forall \boldsymbol{x} \neq \mathbf{0} \tag{2.175}$$

then the origin is an equilibrium point and is globally attractive. If the potential is constructed such that it satisfies the first two conditions and the third one is enforced by the definition of a suitable control law, then the spacecraft will converge to the global minimum and thus to the goal. A typical control definition found in the literature consists in following the steepest descent of the gradient of the potential (see for instance [59, 68, 77]):

$$\Delta \boldsymbol{V} = \begin{cases} -\nabla_{\boldsymbol{x}} \phi - \dot{\boldsymbol{x}} & \text{if } \dot{\phi} \geq 0 \\ 0 & \text{if } \dot{\phi} < 0 \end{cases} \tag{2.176}$$

Obstacles present in the state space can be accounted for by constructing a repulsive potential which admits local maxima at the position of each obstacle. The total artificial potential is then the linear combination of the attractive and repulsive portions. This superposition may give rise to local minima which may create convergence issues as discussed in Chapter 1, as well as shift the location of the goal. A strategy to mitigate these issues will be discussed in Section 2.3.

2.2.1 Attractive Potential Field

The attractive potential field used in this work is a quadratic function of the form

$$\phi_a(\boldsymbol{x}) = \frac{1}{2} k_a \boldsymbol{x}^T \mathbf{Q}_a \boldsymbol{x} \tag{2.177}$$

where k_a is a scaling parameter which determines the height of the potential and $\mathbf{Q}_a$ is a shaping matrix. Fig. 2.13 shows quadratic potentials of two variables with a global minimum at the origin for different shaping matrices and $k_a = 10^{-4}$. The first potential, Fig. 2.13a, has a symmetric shaping matrix $\mathbf{Q}_a = \left[\begin{smallmatrix} 1 & 0 \\ 0 & 1 \end{smallmatrix}\right]$. In that case, the convergence rate of a controller following the steepest descent of the gradient along the x and y coordinates will be identical. The second potential, Fig. 2.13b, has a shaping matrix $\mathbf{Q}_a = \left[\begin{smallmatrix} 2 & 0 \\ 0 & 10 \end{smallmatrix}\right]$ leading to a faster convergence rate along the y coordinate than the x coordinate. Adding off-diagonal terms in the shaping matrix leads to a distortion of the potential as illustrated in Fig. 2.13c. This potential has been obtained with $\mathbf{Q}_a = \left[\begin{smallmatrix} 3 & -2 \\ -3 & 6 \end{smallmatrix}\right]$.

The APF is now defined in terms of element sets rather than Cartesian coordinates. If $\boldsymbol{\rho}$ is the set of ROEs or GROEs and $\boldsymbol{\rho}_t$ the set of target elements, then the attractive potential field is

$$\phi_a(\boldsymbol{\rho}) = \frac{1}{2} k_a (\boldsymbol{\rho} - \boldsymbol{\rho}_t)^T \mathbf{Q}_a (\boldsymbol{\rho} - \boldsymbol{\rho}_t) \tag{2.178}$$

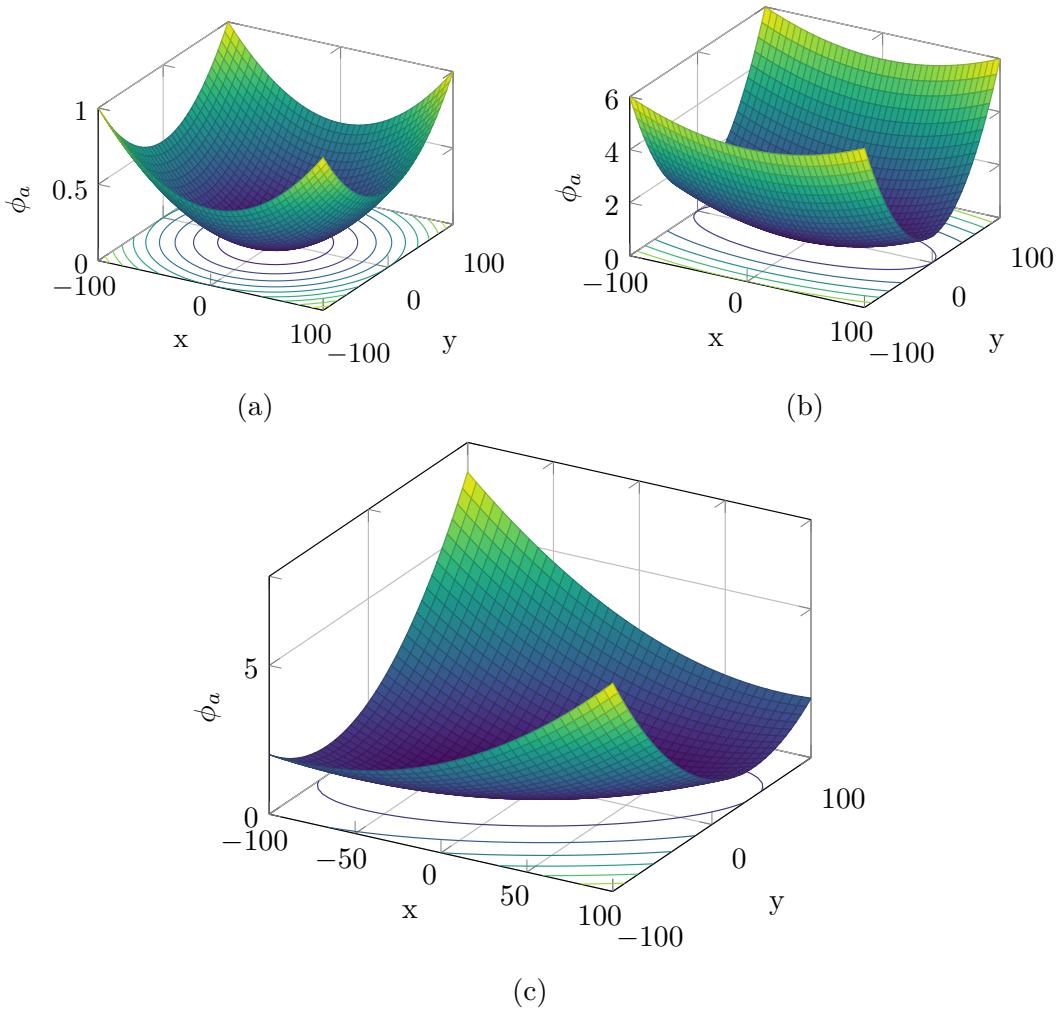

Figure 2.13: Quadratic attractive potential for different shaping matrices.

This potential will take a minimum value of zero whenever the set of elements has reached the target. If we assume that the shaping matrix is diagonal and if we expand Eq. (2.178) for the ROEs, we get

$$\begin{aligned}\phi_a(\boldsymbol{\rho}^{\text{ROEs}}) =& \frac{1}{2}k_a[Q_{a1}(x_r - x_{rt})^2 + Q_{a2}(y_r - y_{rt})^2 + Q_{a3}(a_r - a_{rt})^2 \\ &+ Q_{a4}(E_r - E_{rt})^2 + Q_{a5}(A_z - A_{zt})^2 + Q_{a6}(\gamma - \gamma_t)^2]\end{aligned} \tag{2.179}$$

where subscript t denotes targeted quantities. Similarly, for the GROEs, we obtain

$$\begin{aligned}\phi_a(\boldsymbol{\rho}^{\text{GROEs}}) =& \frac{1}{2}k_a[Q_{a1}(x_c - x_{ct})^2 + Q_{a2}(y_c - y_{ct})^2 + Q_{a3}(a - a_t)^2 \\ &+ Q_{a4}(e - e_t)^2 + Q_{a5}(c - c_t)^2 + Q_{a6}(\sigma - \sigma_t)^2 \\ &+ Q_{a7}(\Upsilon - \Upsilon)^2 + Q_{a8}(\omega - \omega_t)^2]\end{aligned} \tag{2.180}$$

Based on the definition of the ROEs, targeting a constant value of the relative eccentric anomaly, E_r, would require continuous actuation in order to counter its natural motion. Therefore, it is more practical to target an angular separation with respect to a moving reference, referred to as a virtual leader. If we assume that this virtual leader has a relative eccentric anomaly given by

$$E_r^{'}(t) = E_{r0}^{'} + n(t - t_0) \tag{2.181}$$

where $E_{r0}^{'}$ is the initial value at t_0, then the angular separation between a deputy and that leader is

$$\Delta E_r = E_r(t) - E_r^{'}(t) \tag{2.182}$$

Hence, if we target a fixed angular separation ΔE_{rt}, the targeted relative eccentric anomaly at time t is

$$E_{rt}(t) = \Delta E_{rt} + E_{r0}^{'} + n(t - t_0) \tag{2.183}$$

A similar computation for the central anomaly leads to

$$c_t(t) = \Delta c_t + c_0^{'} + n(t - t_0) \tag{2.184}$$

The use of a virtual leader instead of an actual spacecraft is based on fuel considerations. If the deputy were to follow an actual spacecraft, whenever that leader maneuvers to move toward its target or performs a collision avoidance maneuver, the follower will react by performing a maneuver to adjust its relative eccentric anomaly. By uti-

lizing a virtual leader instead, no collision avoidance maneuver will be performed by the leader and therefore a chain reaction is avoided, thus saving propellant.

The APF defined in Eq. (2.179) is used to generate a reference trajectory by following the steepest descent of the gradient. Let $\boldsymbol{\rho_0}$ the initial set of ROEs or GROEs and $\tilde{\boldsymbol{\rho}}$ the reference such that $\tilde{\boldsymbol{\rho}}(t_0) = \boldsymbol{\rho_0}$. The reference trajectory is then generated according to the update rule

$$\tilde{\boldsymbol{\rho}}(t_{i+1}) = \tilde{\boldsymbol{\rho}}(t_i) - \nabla_{\boldsymbol{\rho}}\phi_a|_{\tilde{\boldsymbol{\rho}}}(t_{i+1} - t_i) \tag{2.185}$$

where it is assumed that $t_{i+1} - t_i$ is small. That is, at each time step, the reference trajectory is updated by taking a small step in the direction of steepest descent of the gradient of the attractive potential. For the quadratic potential defined in Eq. (2.178), the gradient is given by

$$\nabla_{\boldsymbol{\rho}}\phi_a = k_a \mathbf{Q}_a(\boldsymbol{\rho} - \boldsymbol{\rho}_t) \tag{2.186}$$

If we develop the expression of Eq. (2.185) for the ROEs, we get

$$\tilde{x}_r(t_{i+1}) = \tilde{x}_r(t_i) - \left.\frac{\partial \phi_a}{\partial x_r}\right|_{\tilde{x}_r}(t_{i+1} - t_i) \tag{2.187}$$

$$\tilde{y}_r(t_{i+1}) = \tilde{y}_r(t_i) - \left.\frac{\partial \phi_a}{\partial y_r}\right|_{\tilde{y}_r}(t_{i+1} - t_i) \tag{2.188}$$

$$\tilde{a}_r(t_{i+1}) = \tilde{a}_r(t_i) - \left.\frac{\partial \phi_a}{\partial a_r}\right|_{\tilde{a}_r}(t_{i+1} - t_i) \tag{2.189}$$

$$\tilde{E}_r(t_{i+1}) = \tilde{E}_r(t_i) + n(t_{i+1} - t_i) - \left.\frac{\partial \phi_a}{\partial E_r}\right|_{\tilde{E}_r}(t_{i+1} - t_i) \tag{2.190}$$

$$\tilde{A}_z(t_{i+1}) = \tilde{A}_z(t_i) - \left.\frac{\partial \phi_a}{\partial A_z}\right|_{\tilde{A}_z}(t_{i+1} - t_i) \tag{2.191}$$

$$\tilde{\gamma}(t_{i+1}) = \tilde{\gamma}(t_i) - \left.\frac{\partial \phi_a}{\partial \gamma}\right|_{\tilde{\gamma}}(t_{i+1} - t_i) \tag{2.192}$$

The additional term in Eq. (2.190) comes from the fact that an angular separation is targeted. The update rule for ΔE_r would be

$$\Delta\tilde{E}_r(t_{i+1}) = \Delta\tilde{E}_r(t_i) - \frac{\partial\phi_a}{\partial\Delta E_r}(t_{i+1} - t_i) \tag{2.193}$$

Using Eqs. (2.181) and (2.182), this equation can be expanded into

$$\tilde{E}_r(t_{i+1}) - \tilde{E}_r'(t_{i+1}) = \tilde{E}_r(t_i) - \tilde{E}_r'(t_i) - \frac{\partial\phi_a}{\partial\Delta E_r}(t_{i+1} - t_i) \tag{2.194}$$

$$\tilde{E}_r(t_{i+1}) - (\tilde{E}_r'(t_i) + n(t_{i+1} - t_i)) = \tilde{E}_r(t_i) - \tilde{E}_r'(t_i) - \frac{\partial\phi_a}{\partial\Delta E_r}(t_{i+1} - t_i) \tag{2.195}$$

$$\tilde{E}_r(t_{i+1}) = \tilde{E}_r(t_i) + n(t_{i+1} - t_i) - \frac{\partial\phi_a}{\partial\Delta E_r}(t_{i+1} - t_i) \tag{2.196}$$

From Eq. (2.182), $\frac{\partial E_r}{\partial\Delta E_r} = 1$. Hence,

$$\frac{\partial\phi_a}{\partial\Delta E_r} = \frac{\partial\phi_a}{\partial E_r}\frac{\partial E_r}{\partial\Delta E_r} = \frac{\partial\phi_a}{\partial E_r} \tag{2.197}$$

and

$$\tilde{E}_r(t_{i+1}) = \tilde{E}_r(t_i) + n(t_{i+1} - t_i) - \left.\frac{\partial\phi_a}{\partial E_r}\right|_{\tilde{E}_r}(t_{i+1} - t_i) \tag{2.198}$$

Computing the partial derivatives of Eq. (2.179) and replacing into Eqs. (2.187)-(2.192) finally results in

$$\tilde{x}_r(t_{i+1}) = \tilde{x}_r(t_i) - k_a Q_{a1}(\tilde{x}_r(t_i) - x_{rt})(t_{i+1} - t_i) \tag{2.199}$$

$$\tilde{y}_r(t_{i+1}) = \tilde{y}_r(t_i) - k_a Q_{a2}(\tilde{y}_r(t_i) - y_{rt})(t_{i+1} - t_i) \tag{2.200}$$

$$\tilde{a}_r(t_{i+1}) = \tilde{a}_r(t_i) - k_a Q_{a3}(\tilde{a}_r(t_i) - a_{rt})(t_{i+1} - t_i) \tag{2.201}$$

$$\tilde{E}_r(t_{i+1}) = \tilde{E}_r(t_i) + n(t_{i+1} - t_i) - k_a Q_{a4}(\tilde{E}_r(t_i) - E_{rt}(t_i))(t_{i+1} - t_i) \tag{2.202}$$

$$\tilde{A}_z(t_{i+1}) = \tilde{A}_z(t_i) - k_a Q_{a5}(\tilde{A}_z(t_i) - A_{zt})(t_{i+1} - t_i) \tag{2.203}$$

$$\tilde{\gamma}(t_{i+1}) = \tilde{\gamma}(t_i) - k_a Q_{a6}(\tilde{\gamma}(t_i) - \gamma_t)(t_{i+1} - t_i) \tag{2.204}$$

These equations allow the definition of waypoints which converge to the minimum of the potential. Once the reference trajectory is computed in terms of ROEs, it is transformed into LVLH Cartesian coordinates using Eqs. (2.96)-(2.101). The computation of reference waypoints leading to a CRO is illustrated in Fig. 2.14. The initial set of ROEs is

$$\boldsymbol{\rho}_0 = \begin{bmatrix} 30 \text{ m} & 600 \text{ m} & 400 \text{ m} & 210^\circ & 40 \text{ m} & 30^\circ \end{bmatrix}^T$$

and the target set

$$\boldsymbol{\rho}_t = \begin{bmatrix} 0 \text{ m} & 0 \text{ m} & 50 \text{ m} & \text{n/a} & 43.30 \text{ m} & -90^\circ \end{bmatrix}^T$$

where the relative eccentric anomaly is not targeted in this example. The value for the scaling parameter of the potential is $k_a = 10^{-3}$ and the shaping matrix is the identity matrix $\mathbf{Q}_a = \mathbf{I}_5$. Each waypoint of the trajectory is separated by 180 seconds (i.e. $t_{i+1} - t_i = 180$) and the reference trajectory is propagated for 4 hours. The mean motion of the chief is assumed to be $n = 0.0011$ rad/s.

A similar derivation can be carried on for the GROEs and results in the following equations:

$$\tilde{x}_c(t_{i+1}) = \tilde{x}_c(t_i) - k_a Q_{a1}(\tilde{x}_c(t_i) - x_{ct})(t_{i+1} - t_i) \tag{2.205}$$

$$\tilde{y}_c(t_{i+1}) = \tilde{y}_c(t_i) - k_a Q_{a2}(\tilde{y}_c(t_i) - y_{ct})(t_{i+1} - t_i) \tag{2.206}$$

$$\tilde{a}(t_{i+1}) = \tilde{a}(t_i) - k_a Q_{a3}(\tilde{a}(t_i) - a_t)(t_{i+1} - t_i) \tag{2.207}$$

$$\tilde{e}(t_{i+1}) = \tilde{e}(t_i) - k_a Q_{a4}(\tilde{e}(t_i) - e_t)(t_{i+1} - t_i) \tag{2.208}$$

$$\tilde{c}(t_{i+1}) = \tilde{c}(t_i) + n(t_{i+1} - t_i) - k_a Q_{a5}(\tilde{c}(t_i) - c_t(t_i))(t_{i+1} - t_i) \tag{2.209}$$

$$\tilde{\sigma}(t_{i+1}) = \tilde{\sigma}(t_i) - k_a Q_{a6}(\tilde{\sigma}(t_i) - \sigma_t)(t_{i+1} - t_i) \tag{2.210}$$

$$\tilde{\Upsilon}(t_{i+1}) = \tilde{\Upsilon}(t_i) - k_a Q_{a7}(\tilde{\Upsilon}(t_i) - \Upsilon_t)(t_{i+1} - t_i) \tag{2.211}$$

$$\tilde{\omega}(t_{i+1}) = \tilde{\omega}(t_i) - k_a Q_{a8}(\tilde{\omega}(t_i) - \omega_t)(t_{i+1} - t_i) \tag{2.212}$$

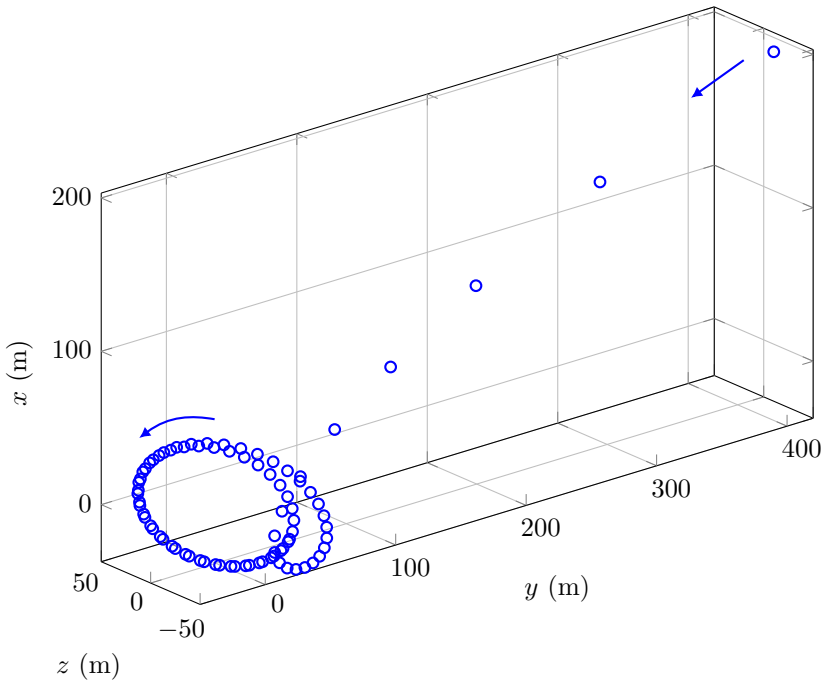

Figure 2.14: Reference waypoints computed using the attractive APF based on the ROEs.

These update equations are used to compute the reference waypoints shown in Fig. 2.15. The initial set of GROEs is

$$\boldsymbol{\rho}_0 = \begin{bmatrix} -50 \text{ m} & -1200 \text{ m} & 2100 \text{ m} & 0.02 & 60^\circ & 120^\circ & 45^\circ & 70^\circ \end{bmatrix}^T$$

and the target set

$$\boldsymbol{\rho}_t = \begin{bmatrix} 0 \text{ m} & 0 \text{ m} & 800 \text{ m} & 0.7 & \text{n/a} & 130^\circ & 75^\circ & 90^\circ \end{bmatrix}^T$$

The central anomaly is not targeted in this example and the same values for the parameters of the APF as in the ROEs example are used.

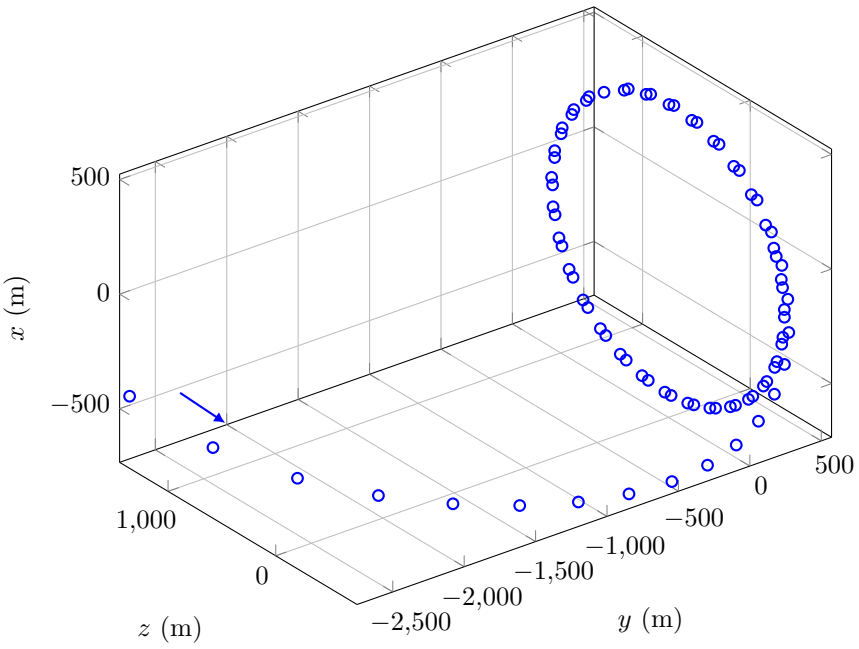

Figure 2.15: Reference waypoints computed using the attractive APF based on the GROEs.

2.2.2 Repulsive Potential Field

Obstacle avoidance is enforced by defining a repulsive potential function that admits local maxima at the locations of the obstacles. A common choice for the repulsive APF is a Gaussian function of the form

$$\phi_r(\boldsymbol{x}) = k_r \exp\left(-\frac{(\boldsymbol{x}-\boldsymbol{x}^{\text{obs}})^T \mathbf{Q}_r (\boldsymbol{x}-\boldsymbol{x}^{\text{obs}})}{\sigma^2}\right) \tag{2.213}$$

where k_r is the scaling parameter, $\mathbf{Q}_r$ the shaping matrix, σ the standard deviation of the Gaussian, and $\boldsymbol{x}^{\text{obs}}$ the position of the obstacle. If several obstacles are present in the phase space, the linear combination of the repulsive potentials is constructed. For N obstacles, this function becomes

$$\phi_r(\boldsymbol{x}) = \sum_{i=1}^{N} k_r \exp\left(-\frac{(\boldsymbol{x}-\boldsymbol{x}_i^{\text{obs}})^T \mathbf{Q}_{ri} (\boldsymbol{x}-\boldsymbol{x}_i^{\text{obs}})}{\sigma_i^2}\right) \tag{2.214}$$

where each parameter can be specific to the obstacle. Fig. 2.16 shows the Gaussian repulsive potential for two obstacles located at $[50, -20]$ and $[-15, 50]$. The first repulsive potential (Fig. 2.16a) has a standard deviation $\sigma = 10$ and the second one (Fig. 2.16b) $\sigma = 25$. The scaling parameter for both potentials is $k_r = 0.8$ and the shaping matrix is the identity matrix, $\mathbf{Q}_r = \mathbf{I}_2$.

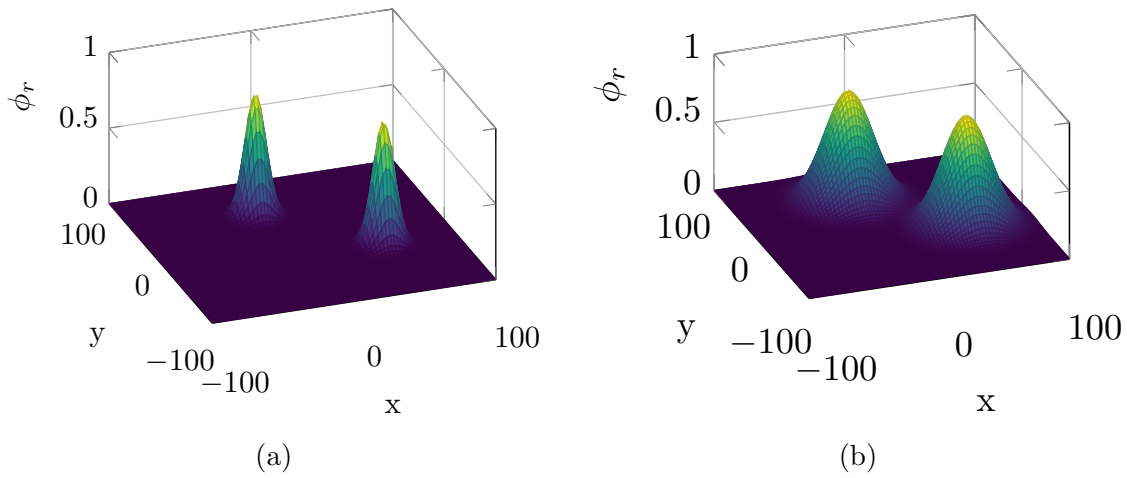

Figure 2.16: Gaussian repulsive potential fields of different widths for two obstacles.

The gradient of the Gaussian repulsive potential is

$$\nabla_{\boldsymbol{x}}\phi_r(\boldsymbol{x}) = \sum_{i=1}^{N} k_r \left(-\frac{2\mathbf{Q}_{ri}(\boldsymbol{x} - \boldsymbol{x}_i^{\text{obs}})}{\sigma_i^2}\right) \exp\left(-\frac{(\boldsymbol{x} - \boldsymbol{x}_i^{\text{obs}})^T \mathbf{Q}_{ri}(\boldsymbol{x} - \boldsymbol{x}_i^{\text{obs}})}{\sigma_i^2}\right) \quad (2.215)$$

It can be seen from this equation that when the spacecraft is at the exact position of an obstacle, the contribution of that obstacle to the gradient of the total repulsive potential field will be zero. In the situation where the spacecraft is very close to the obstacle, following the direction of steepest descent of the gradient will result in the spacecraft moving away very slowly since the slope of the gradient will be relatively gentle near the obstacle. In order to remedy this potentially risky situation, a new ellipsoidal repulsive potential field is introduced:

$$\phi_r(r) = \frac{\alpha}{r^\beta} \quad (2.216)$$

where r is the distance between the spacecraft and the obstacle, α the value of the potential at $r = 1$, and β the negative of the inverse of the slope evaluated at $r = 1$ when $\alpha = 1$. Fig. 2.17a shows the influence of α on the potential for a fixed value of $\beta = 0.5$ and Fig. 2.17b the influence of β on a potential with fixed $\alpha = 1$.

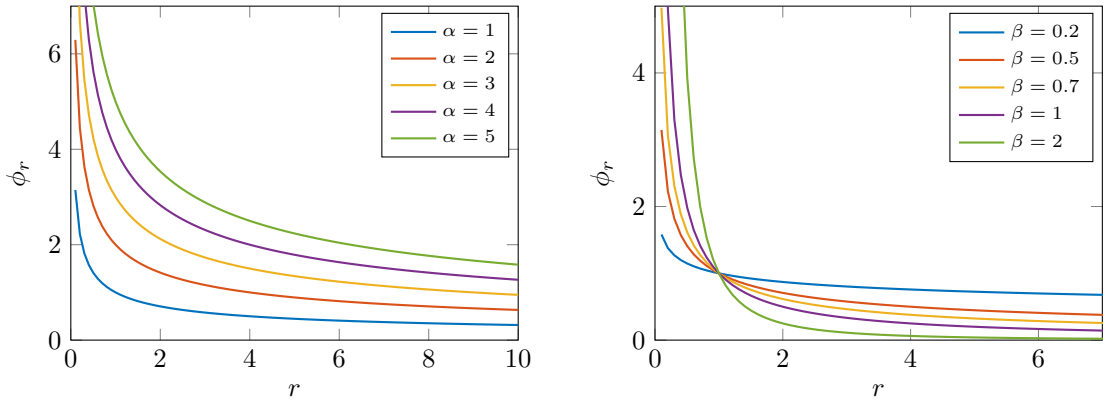

(a) Fixed $\beta = 0.5$.

(b) Fixed $\alpha = 1$.

Figure 2.17: Shape of the ellipsoidal potential for different values of α and β.

As can be seen on these Figures, the potential goes to infinity as the distance between the spacecraft and the obstacle approaches zero. The derivative of the potential will tend toward negative infinity in the vicinity of the obstacle and the controller will thus move the spacecraft away from the obstacle.

The two parameters α and β can be computed by selecting four quantities associated with the obstacle. The first two quantities are the radius of a sphere that encompasses the obstacle and which can be seen as the surface of the obstacle, r_s, and the value of the potential on that surface, k_r. Then, the radius of the sphere of influence around the obstacle is defined, r_{SOI}, as well as the value of the potential at that distance expressed as a ratio p of k_r. Fig. 2.18 illustrates these four quantities.

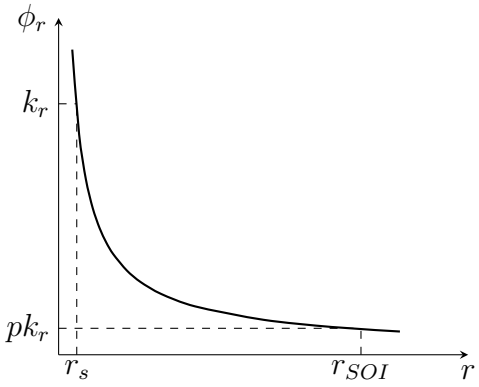

Figure 2.18: Shape of the repulsive potential used for collision avoidance.

The relation between α, β and these four quantities can be derived from Eq. (2.216). Evaluating the potential at r_s and r_{SOI} yields

$$\phi_r(r_s) = k_r \tag{2.217}$$

$$\phi_r(r_{\mathrm{SOI}}) = pk_r \tag{2.218}$$

and using Eq. (2.216), the coefficients α and β can be computed:

$$\beta = \frac{\log_{10} p}{\log_{10}\left(\frac{r_s}{r_{\mathrm{SOI}}}\right)} \tag{2.219}$$

$$\alpha = r_s^{\beta} k_r \tag{2.220}$$

If the function is expanded to three dimensions and when N obstacles are in the neighborhood of the spacecraft, the repulsive potential becomes

$$\phi_r(\boldsymbol{x}) = \sum_{i=1}^{N} \frac{\alpha_i}{\left[(\boldsymbol{x} - \boldsymbol{x}_i^{\mathrm{obs}})^T \mathbf{Q}_{ri} (\boldsymbol{x} - \boldsymbol{x}_i^{\mathrm{obs}})\right]^{\beta_i/2}} \tag{2.221}$$

where α_i and β_i are specific to each obstacle and are computed using Eqs. (2.220) and (2.219), and $\mathbf{Q}_{ri}$ is a shaping matrix. Fig. 2.19 shows four isosurfaces of a three-dimensional ellipsoidal potential for an obstacle located at the origin of the frame.

The obstacle is characterized by a radius $r_s = 1$ m, a sphere of influence $r_{\text{SOI}} = 15$ m,

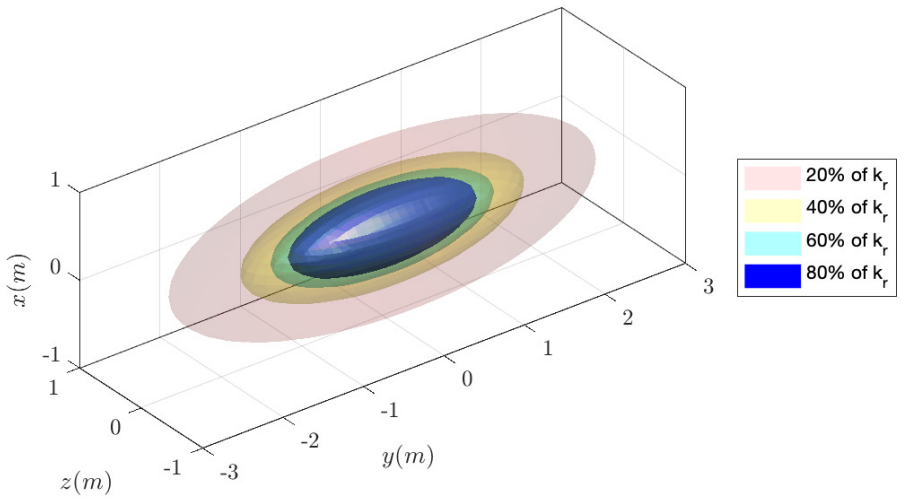

Figure 2.19: Isosurfaces of the three-dimensional ellipsoidal potential.

a potential value at the surface $k_r = 10^{-4}$, and a fraction $p = 0.01$ of k_r at the surface of the sphere of influence, resulting in $\alpha = 10^{-4}$ and $\beta = 1.7005$. The shaping matrix is chosen such that the ellipsoid is an ellipsoid of revolution, or spheroid, with minor axes of one third the length of the major axis, and oriented such that the major axis is along the y axis:

$$\mathbf{Q}_r = \begin{bmatrix} 9 & 0 & 0 \\ 0 & 1 & 0 \\ 0 & 0 & 9 \end{bmatrix}$$

In Fig. 2.20, the two-dimensional ellipsoidal potential fields created by two obstacles located at $[50, -20]$ and $[-10, 50]$ for two sets of parameters are illustrated. Both obstacles in Fig. 2.20a are assumed to have a radius of $r_s = 1$, a sphere of influence of $r_{\text{SOI}} = 30$, a potential value at the surface of $k_r = 1$, and a fraction $p = 0.01$ of k_r at the surface of the sphere of influence. These parameters lead to $\alpha = 1$ and $\beta = 1.3540$. The potential field in Fig. 2.20b is obtained with $r_s = 3$, $r_{\text{SOI}} = 50$, $k_r = 1$, and $p = 0.05$ resulting in $\alpha = 3.2214$, and $\beta = 1.0648$. It is assumed that the shaping matrix is the identity matrix, $\mathbf{Q}_{ri} = \mathbf{I}_2$ in both examples. We see in this

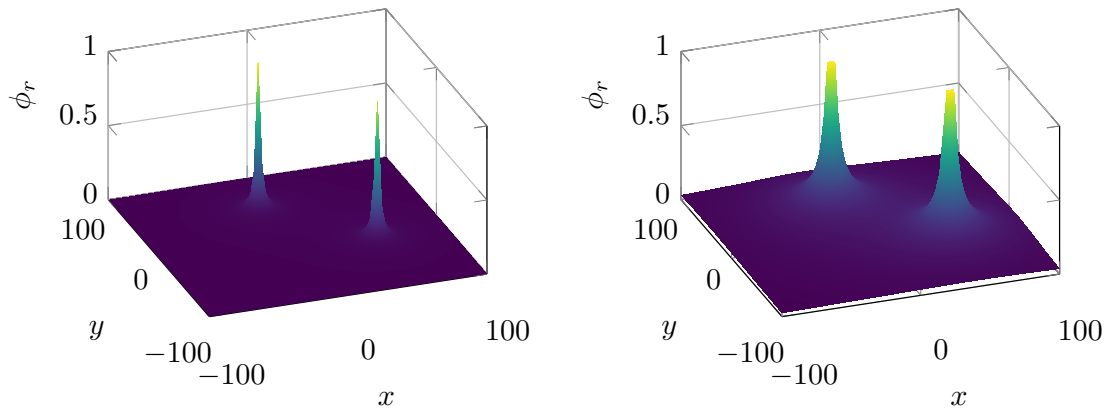

Figure 2.20: Repulsive ellipsoidal potential fields for two obstacles.

figure that the slope of the repulsive potential increases as the distance to the obstacle decreases and the potential goes to infinity at the exact location of the obstacle.

The gradient of the ellipsoidal repulsive potential can be computed as

$$\nabla_{\boldsymbol{x}}\phi_r(\boldsymbol{x}) = \sum_{i=1}^{N} -\frac{\alpha_i\beta_i}{2}\frac{\mathbf{Q}_{ri}(\boldsymbol{x}-\boldsymbol{x}_i^{\text{obs}})}{[(\boldsymbol{x}-\boldsymbol{x}_i^{\text{obs}})^T\mathbf{Q}_{ri}(\boldsymbol{x}-\boldsymbol{x}_i^{\text{obs}})]^{\frac{\beta_i+2}{2}}} \tag{2.222}$$

In order to assess how the gradient of the repulsive potential behaves at the location of an obstacle j, the limit when $\boldsymbol{x}$ goes to $\boldsymbol{x}_j$ is computed for each component of the gradient individually. For the x coordinate and assuming that $\mathbf{Q}_{rj}$ is diagonal, this limit is

$$\lim_{(x,y,z)\to(x_j,y_j,z_j)} -\frac{\alpha_j\beta_j}{2}\frac{Q_{rj1}(x-x_j)}{[Q_{rj1}(x-x_j)^2+Q_{rj2}(y-y_j)^2+Q_{rj3}(z-z_j)^2]^{\frac{\beta_j+2}{2}}} \tag{2.223}$$

Even though this limit takes on an indeterminate form and cannot be evaluated directly, since $p < 1$ and $r_{\text{SOI}} > r_s$, it follows that $\log_{10} p < 0$ and $\log_{10}\frac{r_s}{r_{\text{SOI}}} < 0$. From Eq. (2.219), the beta coefficient must be strictly positive, $\beta > 0$, and therefore $\frac{\beta}{2}+1 > 1$. The degree of the polynomial on the numerator is thus lower than the degree of the polynomial on the denominator and consequently this limit will go

toward $-\infty$ when the spacecraft approaches the obstacle. This reasoning also applies to the y and z coordinates of the gradient. Hence, for an ellipsoidal potential and contrarily to the Gaussian potential, the gradient will become infinitely negative as the spacecraft approaches the obstacle and thus preventing it from being "trapped" at the location of the obstacle.

The control algorithm presented in the next section uses a combination of this repulsive potential with the attractive potential. It is therefore necessary to express the gradient of this potential in terms of relative orbital elements. The partial derivatives of the ellipsoidal repulsive potential with respect to the ROEs can be computed for each obstacle using the chain rule and are given by:

$$\frac{\partial \phi_r}{\partial x_r} = \frac{\partial \phi_r}{\partial x} \tag{2.224}$$

$$\frac{\partial \phi_r}{\partial y_r} = \frac{\partial \phi_r}{\partial y} \tag{2.225}$$

$$\frac{\partial \phi_r}{\partial a_r} = -\frac{1}{2}\cos E_r \frac{\partial \phi_r}{\partial x} + \sin E_r \frac{\partial \phi_r}{\partial y} \tag{2.226}$$

$$\frac{\partial \phi_r}{\partial E_r} = \frac{1}{2} a_r \sin E_r \frac{\partial \phi_r}{\partial x} + a_r \cos E_r \frac{\partial \phi_r}{\partial y} + A_z \cos(\gamma + E_r) \frac{\partial \phi_r}{\partial z} \tag{2.227}$$

$$\frac{\partial \phi_r}{\partial A_z} = \sin(\gamma + E_r) \frac{\partial \phi_r}{\partial z} \tag{2.228}$$

$$\frac{\partial \phi_r}{\partial \gamma} = A_z \cos(\gamma + E_r) \frac{\partial \phi_r}{\partial z} \tag{2.229}$$

where the partial derivatives with respect to the Cartesian coordinates are obtained from Eq. (2.222). The derivatives of the repulsive potential with respect to the GROEs can be computed in a similar way using the chain rule and Eqs (2.135) and (2.137).

2.3 Control Methodology

The traditional formulation of an APF-based control algorithm relies on the definition of a total APF that linearly combines both attractive and repulsive potential functions together with the derivation of a control law from the gradient of this APF.

This approach has two disadvantages: the superposition of the two potentials leads to a shift of the location of the targeted minimum and local minima may arise. In the presence of local minima, the spacecraft can become trapped at an undesired position and if this local minima requires constant actuation from the spacecraft, its resources will eventually deplete and uncontrolled behavior will ensue. The combination of the quadratic attractive potential illustrated in Fig. 2.13a with the repulsive ellipsoidal potential in Fig. 2.20a is shown in Fig. 2.21.

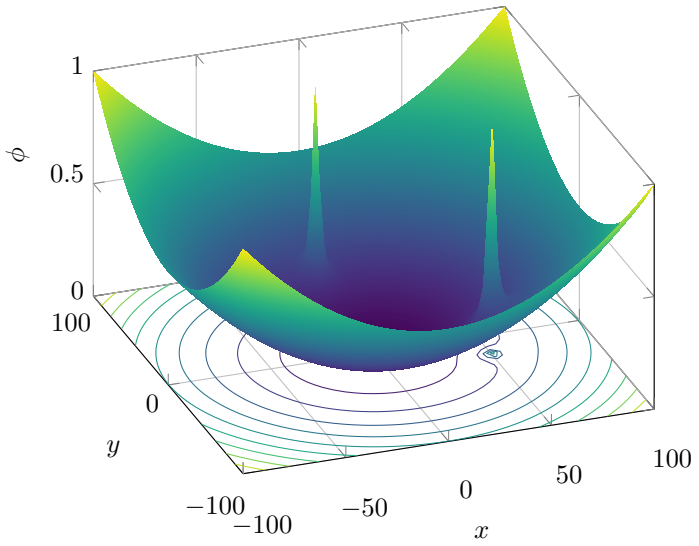

Figure 2.21: Combination of the quadratic attractive and ellipsoidal repulsive potentials.

The total potential does not have any local minima in that specific case but two saddle points emerge near the locations of the obstacles. As can be seen from a top-down view of this potential, Fig. 2.22, the addition of the two repulsive APFs to the quadratic potential results in the global minimum being slightly shifted from [0 0] (white dot in Fig. 2.22) to $[-0.82 \ -0.84]$ (red dot in Fig. 2.22). This shift means that even though the origin is specified as the target location, the algorithm, by following the steepest descent of the gradient, will eventually converge toward the shifted global minimum thus resulting in an error with respect to the target. The amplitude of the error depends on the parameters of the repulsive potential as well

as the location of the obstacles: the closer to the global minimum they are, the larger the error will be.

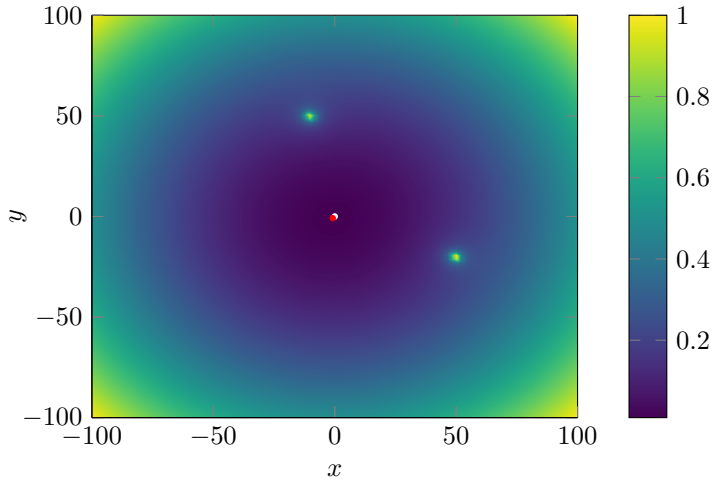

Figure 2.22: Surface plot of the total potential. The global minimum is shifted from the origin (white dot) to the lower left quadrant (red dot) in the presence of two obstacles (bright dots).

In order to mitigate this shift, the repulsive potential can be ignored if the spacecraft satisfies some safety conditions with respect to collision risk. The algorithm proposed in this work thus decouples the attractive and repulsive maneuvers computations.

2.3.1 Maneuvers Decoupling

The control algorithm is based on the attractive quadratic potential of Eq. (2.178) and the repulsive ellipsoidal potential of Eq. (2.221). In order to decouple their computation, two parameters are defined: T_m corresponds to the time interval between two maneuvers, or time of flight, computed using the attractive portion only and typically ranges from a few minutes to a few hours, and T_c corresponds to the time interval between two collision checks typically of the order of a few seconds. These two parameters determine the frequency at which a maneuver is performed to target an attractive waypoint, that is a waypoint generated using the attractive potential

only, and a repulsive waypoint, that is a waypoint generated using a combination of attractive and repulsive APFs.

The control algorithm is initialized by computing the initial value of the reference trajectory as the current state of the deputy expressed in terms of ROEs or GROEs: $\tilde{\boldsymbol{\rho}}(t_0) = \boldsymbol{\rho}_0$. The control loop is then started and operates with a frequency of $1/T_c$ (it is assumed that $T_c < T_m$). At the beginning of the loop, the risk of collision with another agent in the formation is assessed. A spacecraft is considered at risk when its distance to the obstacle is less than the sphere of influence of the obstacle, r_{SOI}. The risk of collision is assessed with respect to all other agents in the formation and if a risk is detected, a collision avoidance maneuver (CAM) is initiated. A collision avoidance waypoint is first computed using a combination of the repulsive potential and the attractive one. This combination is used to ensure that the spacecraft will move away from the obstacle while at the same time converge toward the target. A proper selection of the APFs parameters ensures that collision avoidance is prioritized over goal targeting and will be discussed in section 2.3.4. The repulsive waypoints are computed using the following equation:

$$\tilde{\boldsymbol{\rho}}(t_i + T_c) = \boldsymbol{\rho}(t_i) - \left(\nabla_{\boldsymbol{\rho}} \phi_a|_{\boldsymbol{\rho}} + \frac{1}{N} \sum_{i=1}^{N} \nabla_{\boldsymbol{\rho}} \phi_{ri}|_{\boldsymbol{\rho}} \right) T_c \tag{2.230}$$

where $\boldsymbol{\rho}$ is the set of elements corresponding to the current relative state and N is the number of obstacles presenting a risk of collision. The gradient of the attractive potential is computed using Eq. (2.185) and is evaluated at the current state, and the gradient of the repulsive potential is obtained with Eqs. (2.224)-(2.229) for the ROEs or as described in section 2.2.2 for the GROEs. The sum of the gradients of the repulsive potentials is scaled by the number of obstacles contributing to the CAM to get the mean magnitude. This is done to prevent having excessively large avoidance maneuvers if several spacecraft contribute to the repulsive potential. The impulsive burn required to track this waypoint is then computed using a linear targeter that will be introduced in section 2.3.3. When a CAM has been performed and if the spacecraft

is no longer at risk of collision, the distances to the previous obstacles are computed. If each of these distances is larger than a threshold, a maneuver is executed to put the spacecraft back on a trajectory that intercepts the next attractive waypoint. This check is carried out to avoid having the spacecraft be at risk right after a CAM just occurred. If the recovery maneuver saturates, the process is repeated in the next control iteration, until the magnitude of the desired delta-V falls within the allowed bounds, which indicates that the next attractive waypoint has been successfully targeted. Fig. 2.23 shows the flow chart of the spacecraft mode and maneuvers when a collision avoidance maneuver occurs.

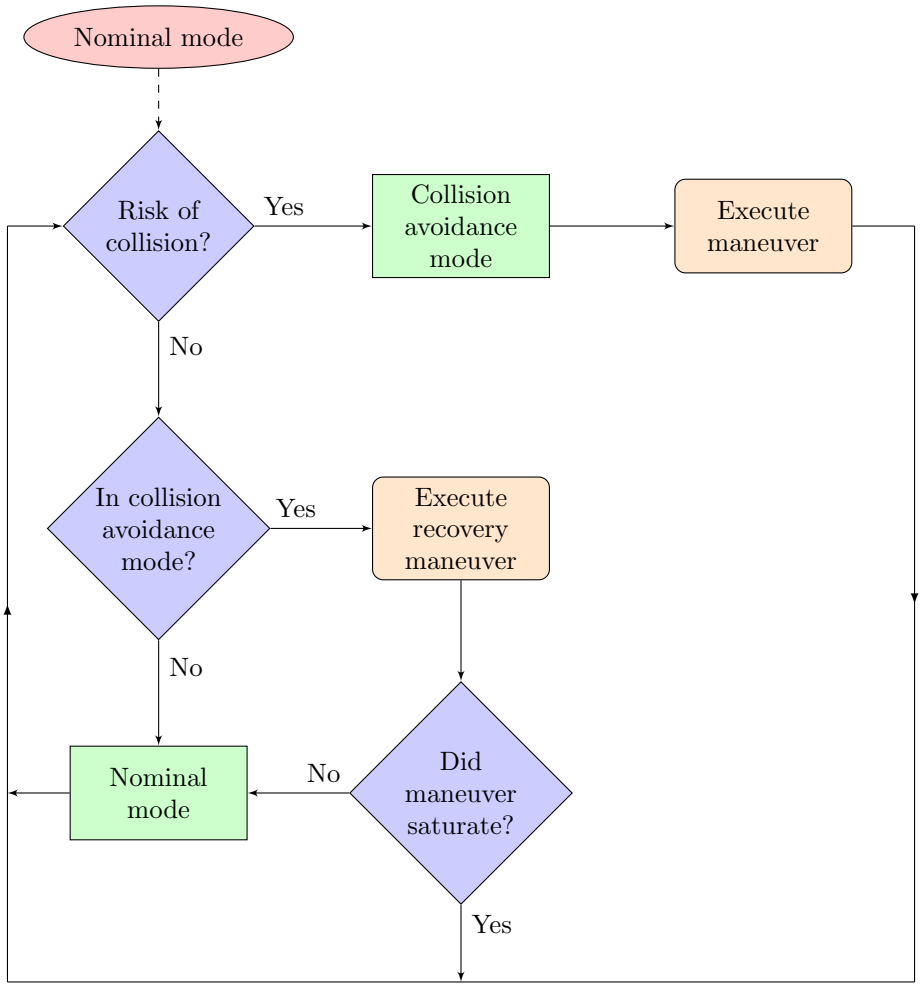

Figure 2.23: Flow chart of the collision avoidance maneuver and recovery control logic.

If, at the beginning of the control loop, no risk of collision is detected and if a duration of T_m has elapsed since the last attractive waypoint has been computed, then the next waypoint is computed using the attractive potential. These waypoints are computed using Eqs. (2.199)-(2.204) for the ROEs or Eqs. (2.205)-(2.212) for the GROEs. Lastly, the maneuver to track this waypoint is computed and executed. The control algorithm is summarized in Algorithm 1 below.

Algorithm 1: APF-based control algorithm.

Input : current time, T_m, T_c, last reference waypoint

Output: desired delta-V

```
check for collisions;
if risk of collision then
    compute next collision avoidance waypoint;
    compute delta-V to target that point;
else if no risk of collision and CAM occurred at previous time step or
  previous recovery maneuver saturated then
    check distances with previous obstacles;
    if distances > threshold then
        if current time greater than last computed attractive waypoint then
            compute next attractive waypoint;
        end
        compute delta-V to target the next attractive waypoint;
    end
else if no risk of collision and T_m has elapsed since the last attractive
  waypoint targeting then
    compute next attractive waypoint;
    compute delta-V to target the next waypoint;
end
```

When the attractive reference trajectory is computed in the control loop, the partial derivatives of the attractive potential ϕ_a with respect to the ROEs or GROEs

are evaluated. Partial derivatives being local quantities, the step taken in the direction of steepest descent, i.e. T_m, must be small in order for the attractive waypoints to converge to the target. If the step is too large, the reference trajectory will take longer to converge or will even diverge. Fig. 2.24 illustrates the convergence of the reference value $\tilde{a}_r$ computed using the attractive potential to a target value $a_{rt} = 0.2$ km starting from $\tilde{a}_r = 1.5$ km for different time steps T_m.

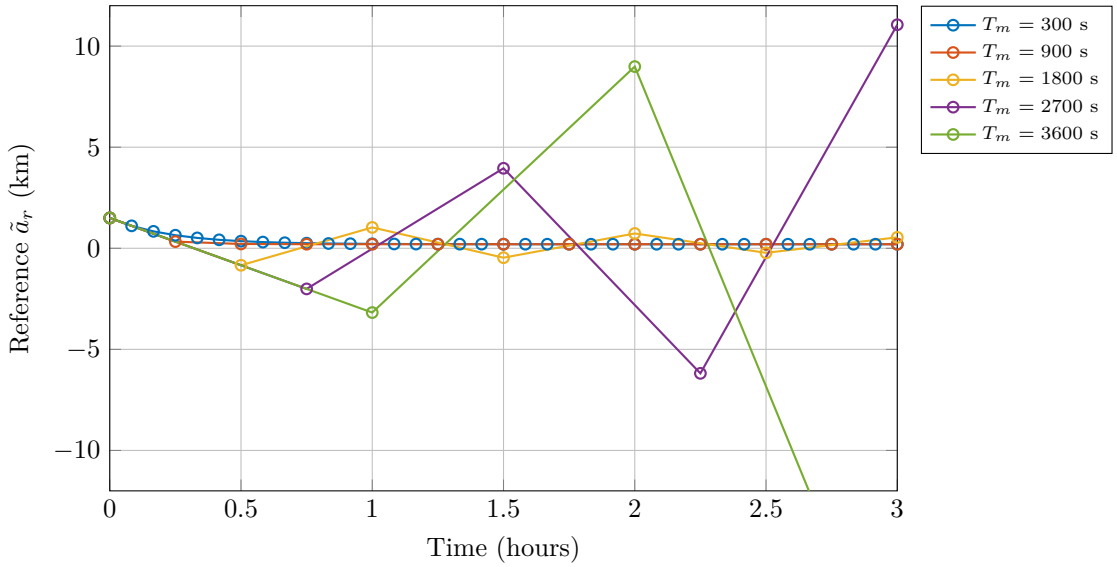

Figure 2.24: Convergence properties of the reference relative semi-major axis toward a target value $a_{rt} = 0.2$ km for different time steps.

As can be seen in Fig. 2.24, the attractive waypoints converge toward the target value when the step size is relatively small. The reference value starts to diverge when the time step is somewhere between 1800 s and 2700 s in this example. We also see that the larger the time step is, the longer it takes for the reference value to stabilize at the minimum. Therefore, if the time interval between two maneuvers, T_m, is large, the next attractive waypoint can not be computed in a single step but must be computed iteratively instead, using a smaller time step. This iterative process incurs an additional computational cost that can be avoided by deriving a set of recursive relations.

2.3.2 Recursive Relations

When updating the reference trajectory using the update equations, the step taken in the direction of steepest descent must be small for the algorithm to converge, as seen in the previous section. One way of doing this is to split T_m into smaller time intervals and iteratively compute the waypoint at t_0+T_m. Algorithm 2 below describes the steps required to iteratively compute the attractive waypoint in terms of ROEs at time $t_0 + T_m$ given the current reference waypoint $\tilde{\boldsymbol{\rho}}(t_0)$, the target elements set, and the parameters of the quadratic potential.

Algorithm 2: Iterative computation of the attractive waypoint at $t_0 + T_m$

Input : $\tilde{\boldsymbol{\rho}}(t_0)$, $\boldsymbol{\rho}_t$, t_0, T_m, k_a, $\mathbf{Q}_a$, n

Output: $\tilde{\boldsymbol{\rho}}(t_0 + T_m)$

1 $dt \leftarrow \min(10, T_m)$;

2 $k \leftarrow \lceil T_m/dt \rceil$; `// number of iterations`

3 $\tilde{\boldsymbol{\rho}} \leftarrow \tilde{\boldsymbol{\rho}}(t_0)$;

4 **for** $i \leftarrow 1$ **to** k **do**

5 $\quad E_{rt} \leftarrow \Delta E_{rt} + E'_{r0} + n(t_0 + idt)$; `// update the targeted` E_r

6 $\quad \tilde{x}_r \leftarrow \tilde{x}_r - k_a Q_{a1}(\tilde{x}_r - x_{rt})dt$;

7 $\quad \tilde{y}_r \leftarrow \tilde{y}_r - k_a Q_{a2}(\tilde{y}_r - y_{rt})dt$;

8 $\quad \tilde{a}_r \leftarrow \tilde{a}_r - k_a Q_{a3}(\tilde{a}_r - a_{rt})dt$;

9 $\quad \tilde{E}_r \leftarrow \tilde{E}_r + ndt - k_a Q_{a4}(\tilde{E}_r - E_{rt})dt$;

10 $\quad \tilde{A}_z \leftarrow \tilde{A}_z - k_a Q_{a5}(\tilde{A}_z - A_{zt})dt$;

11 $\quad \tilde{\gamma} \leftarrow \tilde{\gamma} - k_a Q_{a6}(\tilde{\gamma} - \gamma_t)dt$;

12 **end**

13 $\tilde{\boldsymbol{\rho}} \leftarrow [\tilde{x}_r, \tilde{y}_r, \tilde{a}_r, \tilde{E}_r, \tilde{A}_z, \tilde{\gamma}]$;

14 **return** $\tilde{\boldsymbol{\rho}}$

As can be seen on line 1, the time step used to update the reference is the minimum between T_m and 10 seconds. Based on Fig. 2.24, 10 seconds is small enough for the algorithm to converge. Since the targeted angular element, (E_{rt} for the ROEs or c_t

for the GROEs), is time-varying, it needs to be updated at each iteration, before the reference is computed (line 5). Many mathematical operations are involved in this algorithm making it computationally inefficient. In order to improve the computation speed, a set of recursive relations which can be evaluated in a single step is derived.

The following derivation is carried out for the ROEs but similar equations can be obtained for the GROEs. From the definition of the attractive APF, the equation used to update the first ROE has been defined as (Eq. (2.199)):

$$\tilde{x}_r(t_{i+1}) = \tilde{x}_r(t_i) - k_a Q_{a1}(\tilde{x}_r(t_i) - x_{rt})(t_{i+1} - t_i) \tag{2.231}$$

which can be rewritten as

$$\tilde{x}_r(k+1) = \tilde{x}_r(k) - k_a Q_{a1}(\tilde{x}_r(k) - x_{rt})dt \tag{2.232}$$

where dt is the time interval between step k and $k+1$. This equation can be rearranged into

$$\tilde{x}_r(k+1) = \tilde{x}_r(k)(1 - k_a Q_{a1} dt) + k_a Q_{a1} x_{rt} dt \tag{2.233}$$

Evaluating this expression at $k = 0$ and $k = 1$ results in

$$\tilde{x}_r(1) = \tilde{x}_r(0)(1 - k_a Q_{a1} dt) + k_a Q_{a1} x_{rt} dt \tag{2.234}$$

and

$$\tilde{x}_r(2) = \tilde{x}_r(1)(1 - k_a Q_{a1} dt) + k_a Q_{a1} x_{rt} dt \tag{2.235}$$

Substituting Eq. (2.234) into Eq. (2.235) yields

$$\tilde{x}_r(2) = \tilde{x}_r(0)(1 - k_a Q_{a1} dt)^2 + k_a Q_{a1} x_{rt} dt \left[(1 - k_a Q_{a1} dt) + 1\right] \tag{2.236}$$

Hence, by recursion:

$$\tilde{x}_r(1) = \tilde{x}_r(0)(1 - k_a Q_{a1} dt) + k_a Q_{a1} x_{rt} dt \tag{2.237}$$

$$\tilde{x}_r(2) = \tilde{x}_r(0)(1 - k_a Q_{a1} dt)^2 + k_a Q_{a1} x_{rt} dt \left[(1 - k_a Q_{a1} dt) + 1\right] \tag{2.238}$$

$$\tilde{x}_r(3) = \tilde{x}_r(0)(1 - k_a Q_{a1} dt)^3 + k_a Q_{a1} x_{rt} dt \left[(1 - k_a Q_{a1} dt)^2 + (1 - k_a Q_{a1} dt) + 1\right] \tag{2.239}$$

$$\begin{aligned} \tilde{x}_r(4) = \tilde{x}_r(0)(1 - k_a Q_{a1} dt)^4 + k_a Q_{a1} x_{rt} dt \left[(1 - k_a Q_{a1} dt)^3 + (1 - k_a Q_{a1} dt)^2 \right. \\ \left. + (1 - k_a Q_{a1} dt) + 1\right] \end{aligned} \tag{2.240}$$

$$\vdots$$

$$\tilde{x}_r(k) = \tilde{x}_r(0)(1 - k_a Q_{a1} dt)^k + k_a Q_{a1} x_{rt} dt \sum_{i=0}^{k-1} (1 - k_a Q_{a1} dt)^i \tag{2.241}$$

The sum in the last equation can be identified as a geometric sum and can be simplified to

$$\sum_{i=0}^{k-1} (1 - k_a Q_{a1} dt)^i = \frac{1 - (1 - k_a Q_{a1} dt)^k}{1 - (1 - k_a Q_{a1} dt)} = \frac{1 - (1 - k_a Q_{a1} dt)^k}{k_a Q_{a1} dt} \tag{2.242}$$

Substituting in Eq. (2.241) yields

$$\tilde{x}_r(k) = \tilde{x}_r(0)(1 - k_a Q_{a1} dt)^k + x_{rt} \left[1 - (1 - k_a Q_{a1} dt)^k\right] \tag{2.243}$$

which, after rearranging, becomes

$$\tilde{x}_r(k) = (\tilde{x}_r(0) - x_{rt})(1 - k_a Q_{a1} dt)^k + x_{rt} \tag{2.244}$$

Similar equations can be derived for the other ROEs except for E_r which needs more considerations. From Eq. (2.202), the relation used to update this element is

$$\tilde{E}_r(t_{i+1}) = \tilde{E}_r(t_i) + n(t_{i+1} - t_i) - k_a Q_{a4} (\tilde{E}_r(t_i) - E_{rt}(t_i))(t_{i+1} - t_i) \tag{2.245}$$

which can be rewritten as

$$\tilde{E}_r(k+1) = \tilde{E}_r(k) + n dt - k_a Q_{a4} (\tilde{E}_r(k) - E_{rt}(k)) dt \tag{2.246}$$

Since an angular separation rather than a fixed relative eccentric anomaly is targeted, E_{rt} is time-varying. At step k, the targeted relative eccentric anomaly is thus:

$$E_{rt}(k) = \Delta E_{rt} + E_{r0}^{'} + n(t_0 + kdt) \tag{2.247}$$

Plugging Eq. (2.247) into Eq. (2.246) yields

$$\begin{aligned}\tilde{E}_r(k+1) &= \tilde{E}_r(k) - k_a Q_{a4}\left[\tilde{E}_r(k) - (\Delta E_{rt} + E_{r0}^{'} + n(t_0 + kdt))\right] dt + ndt \\ &= \tilde{E}_r(k)(1 - k_a Q_{a4} dt) + k_a Q_{a4}\left[\Delta E_{rt} + E_{r0}^{'} + n(t_0 + kdt)\right] dt + ndt\end{aligned} \tag{2.248}$$

and by recursion

$$\tilde{E}_r(1) = \tilde{E}_r(0)(1 - k_a Q_{a4} dt) + k_a Q_{a4}\left[\Delta E_{rt} + E_{r0}^{'} + nt_0\right] dt + ndt \tag{2.249}$$

$$\begin{aligned}\tilde{E}_r(2) =& \tilde{E}_r(0)(1 - k_a Q_{a4} dt)^2 \\ &+ \left[k_a Q_{a4}(\Delta E_{rt} + E_{r0}^{'} + nt_0)dt + ndt\right](1 - k_a Q_{a4} dt) \\ &+ k_a Q_{a4}\left[\Delta E_{rt} + E_{r0}^{'} + n(t_0 + dt)\right] dt + ndt\end{aligned} \tag{2.250}$$

$$\begin{aligned}\tilde{E}_r(3) =& \tilde{E}_r(0)(1 - k_a Q_{a4} dt)^3 \\ &+ \left[k_a Q_{a4}(\Delta E_{rt} + E_{r0}^{'} + nt_0)dt + ndt\right](1 - k_a Q_{a4} dt)^2 \\ &+ \left[k_a Q_{a4}(\Delta E_{rt} + E_{r0}^{'} + n(t_0 + dt))dt + ndt\right](1 - k_a Q_{a4} dt) \\ &+ k_a Q_{a4}\left[\Delta E_{rt} + E_{r0}^{'} + n(t_0 + 2dt)\right] dt + ndt \\ &\vdots\end{aligned} \tag{2.251}$$

$$\begin{aligned}\tilde{E}_r(k) =&\tilde{E}_r(0)(1-k_aQ_{a4}dt)^k+\sum_{i=0}^{k-1}\Big[k_aQ_{a4}(\Delta E_{rt}+E_{r0}^{'}+n(t_0+(k-1-i)dt))dt\\&+ndt\Big]\left[1-k_aQ_{a4}dt\right]^i\\=&\tilde{E}_r(0)(1-k_aQ_{a4}dt)^k+\Big[k_aQ_{a4}(\Delta E_{rt}+E_{r0}^{'}+n(t_0-dt))dt+ndt\Big]\\&\sum_{i=0}^{k-1}(1-k_aQ_{a4}dt)^i+k_aQ_{a4}ndt^2\sum_{i=0}^{k-1}(k-i)(1-k_aQ_{a4}dt)^i\end{aligned}\tag{2.252}$$

The two sums in Eq. (2.252) are geometric sums and can be rewritten as

$$\sum_{i=0}^{k-1}(1-k_aQ_{a4}dt)^i=\frac{1-(1-k_aQ_{a4}dt)^k}{1-(1-k_aQ_{a4}dt)}=\frac{1-(1-k_aQ_{a4}dt)^k}{k_aQ_{a4}dt}\tag{2.253}$$

$$\sum_{i=0}^{k-1}(k-i)(1-k_aQ_{a4}dt)^i=\frac{(1-k_aQ_{a4}dt)^{k+1}-(1-k_aQ_{a4}dt)+kk_aQ_{a4}dt}{(k_aQ_{a4}dt)^2}\tag{2.254}$$

Hence, substituting into Eq. (2.252) results in

$$\begin{aligned}\tilde{E}_r(k)=&\tilde{E}_r(0)(1-k_aQ_{a4}dt)^k\\&+\Big[k_aQ_{a4}(\Delta E_{rt}+E_{r0}^{'}+n(t_0-dt))+n\Big]\frac{1-(1-k_aQ_{a4}dt)^k}{k_aQ_{a4}}\\&+n\frac{(1-k_aQ_{a4}dt)^{k+1}-(1-k_aQ_{a4}dt)+kk_aQ_{a4}dt}{k_aQ_{a4}}\end{aligned}\tag{2.255}$$

and after simplification, it follows that

$$\begin{aligned}\tilde{E}_r(k)=&\left[\tilde{E}_r(0)-(\Delta E_{rt}+E_{r0}^{'}+n(t_0-dt))-\frac{n}{k_aQ_{a4}}\right]\left[1-k_aQ_{a4}dt\right]^k\\&+(\Delta E_{rt}+E_{r0}^{'}+n(t_0-dt))\\&+\frac{n}{k_aQ_{a4}}\left[(1-k_aQ_{a4}dt)^{k+1}+(k+1)k_aQ_{a4}dt\right]\end{aligned}\tag{2.256}$$

This equation along with equations similar to Eq. (2.244) for the other ROEs allows to compute the attractive waypoint at time t_0+T_m in a single evaluation. The

computation of the attractive waypoint at time $t_0 + T_m$ using the recursive relations is described in Algorithm 3.

Algorithm 3: Recursive computation of the attractive waypoint at $t_0 + T_m$

Input : $\tilde{\boldsymbol{\rho}}(t_0)$, $\boldsymbol{\rho}_t$, t_0, T_m, k_a, $\mathbf{Q}_a$, n

Output: $\tilde{\boldsymbol{\rho}}(t_0 + T_m)$

$dt \leftarrow \min(10, T_m)$;

$k \leftarrow \lceil T_m/dt \rceil$; `// number of steps`

$\tilde{\boldsymbol{\rho}} \leftarrow \tilde{\boldsymbol{\rho}}(t_0)$;

$\tilde{x}_r \leftarrow (\tilde{x}_r - x_{rt})(1 - k_a Q_{a1} dt)^k + x_{rt}$;

$\tilde{y}_r \leftarrow (\tilde{y}_r - y_{rt})(1 - k_a Q_{a2} dt)^k + y_{rt}$;

$\tilde{a}_r \leftarrow (\tilde{a}_r - a_{rt})(1 - k_a Q_{a3} dt)^k + a_{rt}$;

$\tilde{E}_r \leftarrow$ Eq. (2.256);

$\tilde{A}_z \leftarrow (\tilde{A}_z - A_{zt})(1 - k_a Q_{a5} dt)^k + A_{zt}$;

$\tilde{\gamma} \leftarrow (\tilde{\gamma} - \gamma_t)(1 - k_a Q_{a6} dt)^k + \gamma_t$;

$\tilde{\boldsymbol{\rho}} \leftarrow [\tilde{x}_r, \tilde{y}_r, \tilde{a}_r, \tilde{E}_r, \tilde{A}_z, \tilde{\gamma}]$;

return $\tilde{\boldsymbol{\rho}}$

In contrast to Algorithm 2, this algorithm does not contain any iterative loop and the amount of elementary mathematical operations is therefore greatly reduced which results in a significant speed up, especially for large values of T_m. The computational efficiency of the recursive method is compared to the iterative method in Fig. 2.25.

The elapsed real time presented in that figure is the average of 5000 runs for each T_m. The computations have been done on an 2.6 GHz 6-Core Intel Core i7 in Matlab. We see in that figure that for small T_m, the elapsed real time is roughly similar for both methods. When T_m increases, the difference becomes significant: for $T_m = 7200$s, the recursive method is about 660 times faster than the iterative one with an elapsed real time of 0.58 ms for the iterative method and 0.87 μs for the recursive method. An important observation is that the algorithm using the recursive method has a constant time complexity ($O(1)$) whereas the algorithm using

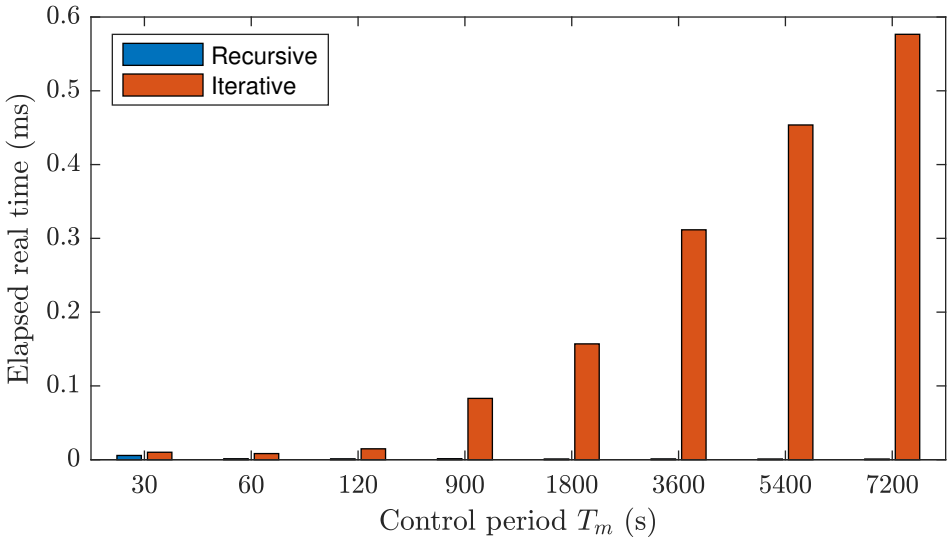

Figure 2.25: Comparison of the computation time between the iterative and recursive methods.

the iterative method has a linear time complexity (O(n)). The recursive equations therefore allow to compute the attractive waypoints using an arbitrarily large T_m efficiently. In general, the time interval between two collision checks, T_c, is of the order of a few seconds and therefore the computation of the repulsive waypoints does not need to rely on recursive relations but can be computed directly.

When the reference waypoint has been generated, an impulsive maneuver is executed to track it. The linear targeter designed to compute the maneuver is presented next.

2.3.3 Reference Tracking

So far, the reference trajectory is computed in terms of relative orbital elements. In order to track it, it is first converted into LVLH Cartesian coordinates using Eqs. (2.96)-(2.101) for the ROEs or the procedure described in section 2.1.3 for the GROEs:

$$\tilde{\boldsymbol{\rho}} \rightarrow \tilde{\boldsymbol{s}} = \begin{bmatrix} \tilde{\boldsymbol{r}} \\ \dot{\tilde{\boldsymbol{r}}} \end{bmatrix} \tag{2.257}$$

Once the reference is expressed in terms of LVLH coordinates, a linear targeter is designed using the CW equations. From Eqs. (2.47)-(2.52), the time evolution of the LVLH state is

$$\boldsymbol{s}(t) = \mathbf{A}(t, t_0)\boldsymbol{s}_0 \tag{2.258}$$

with

$$\mathbf{A}(t, t_0) = \begin{bmatrix} 4 - 3c_{n\tau} & 0 & 0 & \frac{1}{n}s_{n\tau} & \frac{2}{n}(1 - c_{n\tau}) & 0 \\ -6n\tau + 6s_{n\tau} & 1 & 0 & \frac{2}{n}(c_{n\tau} - 1) & -3\tau + \frac{4}{n}s_{n\tau} & 0 \\ 0 & 0 & c_{n\tau} & 0 & 0 & \frac{1}{n}s_{n\tau} \\ 3ns_{n\tau} & 0 & 0 & c_{n\tau} & 2s_{n\tau} & 0 \\ 6n(1 - c_{n\tau}) & 0 & 0 & -2s_{n\tau} & -3 + 4c_{n\tau} & 0 \\ 0 & 0 & -ns_{n\tau} & 0 & 0 & c_{n\tau} \end{bmatrix} \tag{2.259}$$

where $\tau = t - t_0$, $c_{n\tau} = \cos(n(t - t_0))$, and $s_{n\tau} = \sin(n(t - t_0))$. If the current time is t_0 and the next reference waypoint has been computed for time t_1, then the error between the reference $\tilde{\boldsymbol{s}}(t_1)$ and the relative position of the deputy resulting from the unforced relative motion at time t_1, $\boldsymbol{s}(t_1)$, will be

$$\boldsymbol{e}(t_1) = \tilde{\boldsymbol{s}}(t_1) - \boldsymbol{s}(t_1) \tag{2.260}$$

The targeter is based on the computation of a small perturbation, $\delta\boldsymbol{s}_0$, which, when added to the initial conditions at t_0, cancels out this error and results in the spacecraft

reaching the reference state at time t_1. That is, a perturbation term $\delta \boldsymbol{s}_0$ is computed such that

$$\mathbf{A}(t_1, t_0)(\boldsymbol{s}_0 + \delta \boldsymbol{s}_0) = \tilde{\boldsymbol{s}}(t_1) \tag{2.261}$$

Developing this equation gives

$$\mathbf{A}(t_1, t_0)\boldsymbol{s}_0 + \mathbf{A}(t_1, t_0)\delta \boldsymbol{s}_0 = \tilde{\boldsymbol{s}}(t_1) \tag{2.262}$$

$$\boldsymbol{s}(t_1) + \mathbf{A}(t_1, t_0)\delta \boldsymbol{s}_0 = \tilde{\boldsymbol{s}}(t_1) \tag{2.263}$$

$$\mathbf{A}(t_1, t_0)\delta \boldsymbol{s}_0 = \tilde{\boldsymbol{s}}(t_1) - \boldsymbol{s}(t_1) \tag{2.264}$$

$$\mathbf{A}(t_1, t_0)\delta \boldsymbol{s}_0 = \boldsymbol{e}(t_1) \tag{2.265}$$

$$\delta \boldsymbol{s}_0 = \mathbf{A}^{-1}(t_1, t_0)\boldsymbol{e}(t_1) \tag{2.266}$$

Since the initial position is fixed and assuming that only the relative position is targeted, the initial perturbation becomes

$$\delta \dot{\boldsymbol{r}}_0 = \mathbf{A}_{12}^{-1}(t_1, t_0)(\tilde{\boldsymbol{r}}(t_1) - \boldsymbol{r}(t_1)) \tag{2.267}$$

where $\mathbf{A}_{12}^{-1}(t_1, t_0)$ is the inverse of the top right block of matrix $\mathbf{A}(t, t_0)$ evaluated at t_1 given by

$$\mathbf{A}_{12}^{-1}(t_1, t_0) = \begin{bmatrix} \frac{3n^2\tau - 4ns_{n\tau}}{8(c_{n\tau}-1)+3n\tau s_{n\tau}} & \frac{2n(1-c_{n\tau})}{8(c_{n\tau}-1)+3n\tau s_{n\tau}} & 0 \\ \frac{2n(c_{n\tau}-1)}{8(c_{n\tau}-1)+3n\tau s_{n\tau}} & \frac{-ns_{n\tau}}{8(c_{n\tau}-1)+3n\tau s_{n\tau}} & 0 \\ 0 & 0 & \frac{n}{s_{n\tau}} \end{bmatrix} \tag{2.268}$$

This perturbation in initial velocity is created by applying a delta-V of the same magnitude, assuming an impulsive burn:

$$\Delta \boldsymbol{V}_1 = \mathbf{A}_{12}^{-1}(t_1, t_0)(\tilde{\boldsymbol{r}}(t_1) - \boldsymbol{r}(t_1)) \tag{2.269}$$

Applying this delta-V will bring the spacecraft to the position of the waypoint at time t_1. In order to align the relative velocity with the reference velocity, a second delta-V can be applied at time t_1. This second maneuver can be computed with:

$$\Delta \boldsymbol{V}_2 = \dot{\tilde{\boldsymbol{r}}}(t_1) - \dot{\boldsymbol{r}}^-(t_1) \tag{2.270}$$

where $\dot{\boldsymbol{r}}^-(t_1)$ is the velocity that the spacecraft will have when it reaches the reference relative position $\tilde{\boldsymbol{r}}(t_1)$. The velocity at that position is given by

$$\dot{\boldsymbol{r}}^-(t_1) = \mathbf{A}^*(t_1, t_0) \left(\boldsymbol{s}_0 + \begin{bmatrix} \mathbf{0} \\ \Delta \boldsymbol{V}_1 \end{bmatrix} \right) \tag{2.271}$$

where $\mathbf{A}^*(t_1, t_0)$ is the lower half of $\mathbf{A}(t, t_0)$ evaluated at t_1. Fig. 2.26 illustrates the two-burn scheme used to target a relative state. The blue quantities are associated with the targeting of the relative position and the orange quantities with the targeting of the relative velocity. The first maneuver, $\Delta \boldsymbol{V}_1$ is performed at time t_0 and the second one, $\Delta \boldsymbol{V}_2$ at time t_1. The dashed blue arc corresponds the the natural motion of the deputy and the solid blue arc corresponds to the trajectory after the first burn has been applied.

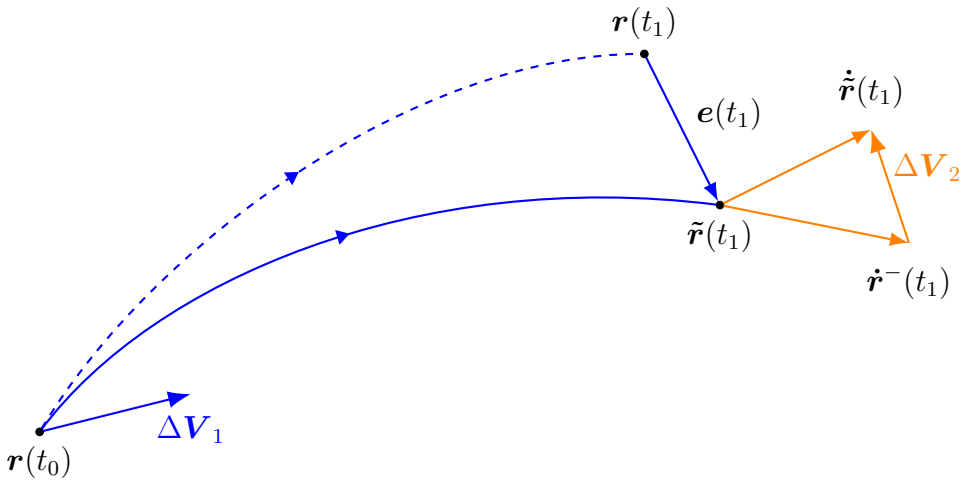

Figure 2.26: Two-burn scheme used to target a reference waypoint.

In practice, the second burn is not applied. Since at time t_1 a new delta-V will be computed to target the reference position at time t_2, applying both $\Delta\boldsymbol{V}_2^{(1)}$ and $\Delta\boldsymbol{V}_1^{(2)}$, where superscript i denotes quantities associated with the targeting sequence i, might result in an overlap between the two maneuvers effectively cancelling parts of each other and therefore wasting propellant. Fig. 2.27 illustrates the combination of the two maneuvers into a single one, resulting in a lower fuel consumption. We see on that figure that applying the second maneuver of the first targeting sequence $\Delta\boldsymbol{V}_2^{(1)}$ and then the first maneuver of the second targeting sequence $\Delta\boldsymbol{V}_1^{(2)}$ might result in a larger delta-V than applying the combination of both in one burn, $\Delta\boldsymbol{V}^{(2)}$.

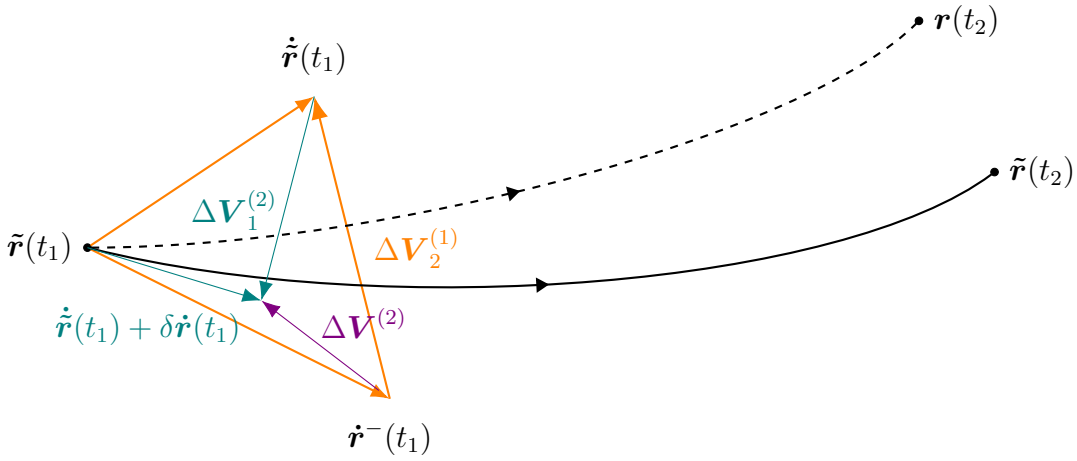

Figure 2.27: Combination of two subsequent maneuvers into a single one.

A consequence of this control scheme is that even though the spacecraft will follow the reference relative position, the relative velocity will not be tracked. Computing the ROEs or GROEs from a measurement of the relative state at time t will therefore result in a different elements set than the reference waypoint at that time. For this reason, it is important to store the reference trajectory into memory and compute the next waypoint from that trajectory rather than a measure of the relative state to ensure convergence of the reference waypoints toward the target.

The magnitude of delta-V that a spacecraft can deliver is limited by the physical properties of the propulsion system. Accordingly, the impulsive maneuvers computed

using the linear targeter are bounded between a minimum ΔV_{min} and maximum ΔV_{max} value. These bounds are enforced by discarding the computed maneuver if it is smaller than ΔV_{min}, and rescaling it if it is larger than ΔV_{max}. That is, the desired delta-V is

$$\Delta \boldsymbol{V}_d = \begin{cases} \mathbf{0} & \text{if } \|\Delta \boldsymbol{V}\| < \Delta V_{min} \\ \Delta \boldsymbol{V} & \text{if } \Delta V_{min} \leq \|\Delta \boldsymbol{V}\| \leq \Delta V_{max} \\ \frac{\Delta \boldsymbol{V}}{\|\Delta \boldsymbol{V}\|} \Delta V_{max} & \text{if } \|\Delta \boldsymbol{V}\| > \Delta V_{max} \end{cases} \tag{2.272}$$

When the magnitude of the maneuvers is trimmed, the targeter might not be able to follow the reference trajectory and therefore the algorithm might fail to converge to the target relative orbit. One way to mitigate this risk is by choosing a small scaling factor k_a for the quadratic potential such that the attractive waypoints can be tracked without violating the delta-V's upper limit. A method to automatically select this parameter will be presented in the next section.

Fig. 2.28 shows the tracking of a reference trajectory composed of attractive reference waypoints which have been generated using different T_m values. The initial LVLV Cartesian state used for this example is

$$\boldsymbol{s}_0 = \begin{bmatrix} -200 \text{ m} & 1500 \text{ m} & -1200 \text{ m} & 0.2 \text{ m/s} & 0.2 \text{ m/s} & 0.1 \text{ m/s} \end{bmatrix}$$

and the set of target ROEs is

$$\boldsymbol{\rho}_t = \begin{bmatrix} 0 \text{ m} & -100 \text{ m} & 200 \text{ m} & 0^\circ & 100 \text{ m} & 60^\circ \end{bmatrix}$$

An angular separation of $\Delta E_{rt} = 0^\circ$ with respect to a virtual leader with $E'_{r0} = 0^\circ$ is targeted. The reference trajectories have been generated using a scaling factor $k_a = 10^{-3}$ and a shaping matrix $\mathbf{Q}_a = \mathbf{I}_6$. The amplitude of the maneuvers used to track the reference are bounded between 2 cm/s and 5 m/s. We see on Fig. 2.28a that for $T_m = 1$ minute, the reference waypoints are very close to each other. The spacecraft follows the steepest slope of the gradient very closely and needs a lot of

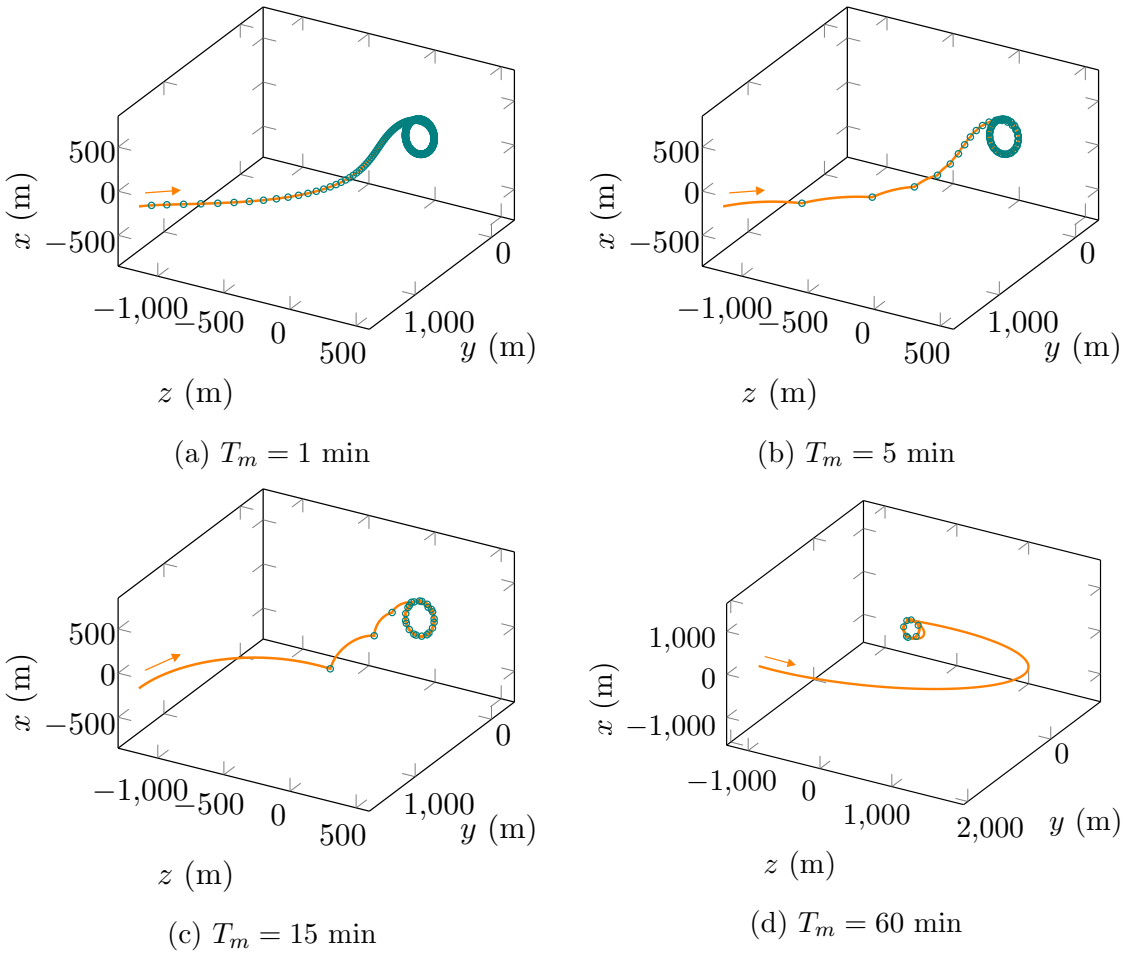

Figure 2.28: Reference waypoints tracking for different T_m.

maneuvers to reach the target relative orbit. The total delta-V required to track the reference in this case is 6.50 m/s. In Fig. 2.28b, a time interval of 5 minutes between each maneuver is used. The deputy follows the reference trajectory slightly more loosely and less maneuvers are required to reach the target. The total delta-V in this case is 5.98 m/s. The trajectory in Fig. 2.28c uses a T_m of 15 minutes resulting in a delta-V of 4.24 m/s. Finally, a time interval of 60 minutes is used in Fig. 2.28d. In this last case, a single maneuver brings the spacecraft directly on the desired relative orbit and subsequent maneuvers ensure that it stays on it. The total delta-V is 4.14 m/s.

This example shows that the time interval between two maneuvers has an impact on the total delta-V required to reach a desired relative orbit. As can be seen in Fig. 2.29, some values of T_m yield a lower total delta-V than others. We also see that the targeter fails to track the reference trajectory when T_m is close to 3000 s and 6000 s as indicated by the very high total delta-V. In these specific cases, the initial maneuver executed to track the first reference waypoint results in a trajectory which goes very far away from the origin in the cross-track direction. When the spacecraft reaches the first waypoint, its very large velocity in the z direction must be countered and results in a delta-V that exceeds the maximum delta-V, ΔV_{max}. This trend of having a very large excursion in the cross-track direction when T_m is close to 3000 s can already be observed in Fig. 2.28d above. In this case the targeter is still able to track the reference.

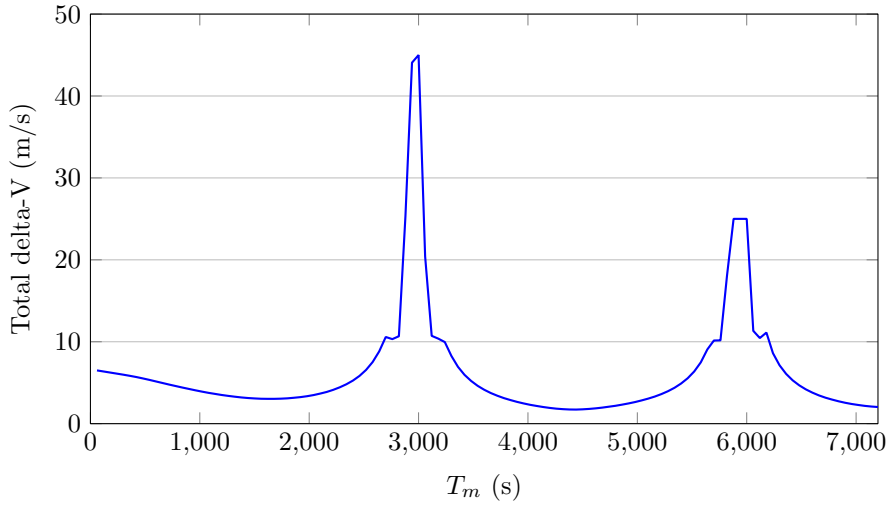

Figure 2.29: Total delta-V required to track the reference as a function of the time interval between two maneuvers.

Even though the total delta-V has periodic local minima, a longer T_m generally results in a lower targeting accuracy as will be shown in section 3.1.3. The convergence properties of this linear targeter in the perturbed, nonlinear environment will be assessed in section 2.4.2.

2.3.4 Autonomous Coefficients Selection

The definitions of the attractive and repulsive potentials introduced some parameters that must be manually selected. A summary of these parameters is presented in Table 2.3.

Table 2.3: Summary of the parameters of the attractive and repulsive potentials.

Attractive potential	**Repulsive potential**
k_a: scaling parameter	r_s: radius of a sphere circumscribing the obstacle
$\mathbf{Q}_a$: diagonal shaping matrix	r_{SOI}: radius of the sphere of influence
	k_r: value of the potential at r_s
	p: potential at r_{SOI} as a fraction of k_r
	$\mathbf{Q}_r$: diagonal shaping matrix

The shaping matrix $\mathbf{Q}_a$ will contain six elements for the ROEs and eight for the GROEs. Hence, a minimum of fourteen parameters are required for the ROEs and sixteen for the GROEs. If the repulsive field of each obstacle is characterized by different parameters, then many more parameters may be required. In order to reduce the number of parameters that must be manually tuned, some considerations on the fuel minimization leading to the autonomous selection of some of these coefficients are presented.

The selection of the coefficients of the shaping matrix $\mathbf{Q}_a$ is first considered. These coefficients define the shape of the attractive potential and therefore impact the convergence rate of each element. Since the slope of the gradient affects the total delta-V required to bring a spacecraft to the target, a judicious choice of the shaping coefficients might lead to a reduction of the total delta-V and therefore a reduction of the fuel consumption. The following analysis is done for the ROEs but a similar approach can be followed for the GROEs. A relation between a maneuver expressed in terms

of LVLH Cartesian coordinates and a change of ROEs is sought. Looking at a small perturbation in the LVLH frame, this relation can be expressed as

$$\delta\boldsymbol{\rho}(t) = \Phi(t, t_0)\delta\boldsymbol{s}_0 \tag{2.273}$$

where $\Phi(t, t_0)$ is the state transition matrix given by

$$\Phi(t,t_0) = \begin{bmatrix} \frac{\partial x_r}{\partial x_0} & \frac{\partial x_r}{\partial y_0} & \frac{\partial x_r}{\partial z_0} & \frac{\partial x_r}{\partial \dot{x}_0} & \frac{\partial x_r}{\partial \dot{y}_0} & \frac{\partial x_r}{\partial \dot{z}_0} \\ \frac{\partial y_r}{\partial x_0} & \frac{\partial y_r}{\partial y_0} & \frac{\partial y_r}{\partial z_0} & \frac{\partial y_r}{\partial \dot{x}_0} & \frac{\partial y_r}{\partial \dot{y}_0} & \frac{\partial y_r}{\partial \dot{z}_0} \\ \frac{\partial a_r}{\partial x_0} & \frac{\partial a_r}{\partial y_0} & \frac{\partial a_r}{\partial z_0} & \frac{\partial a_r}{\partial \dot{x}_0} & \frac{\partial a_r}{\partial \dot{y}_0} & \frac{\partial a_r}{\partial \dot{z}_0} \\ \frac{\partial E_r}{\partial x_0} & \frac{\partial E_r}{\partial y_0} & \frac{\partial E_r}{\partial z_0} & \frac{\partial E_r}{\partial \dot{x}_0} & \frac{\partial E_r}{\partial \dot{y}_0} & \frac{\partial E_r}{\partial \dot{z}_0} \\ \frac{\partial A_z}{\partial x_0} & \frac{\partial A_z}{\partial y_0} & \frac{\partial A_z}{\partial z_0} & \frac{\partial A_z}{\partial \dot{x}_0} & \frac{\partial A_z}{\partial \dot{y}_0} & \frac{\partial A_z}{\partial \dot{z}_0} \\ \frac{\partial \gamma}{\partial x_0} & \frac{\partial \gamma}{\partial y_0} & \frac{\partial \gamma}{\partial z_0} & \frac{\partial \gamma}{\partial \dot{x}_0} & \frac{\partial \gamma}{\partial \dot{y}_0} & \frac{\partial \gamma}{\partial \dot{z}_0} \end{bmatrix} \tag{2.274}$$

and describes the sensitivity of the ROEs to a perturbation in the LVLH coordinates. The partial derivatives can be computed using the definitions of the ROEs in terms of initial conditions given in section 2.1.2, resulting in

$$\Phi = \begin{bmatrix} 4 & 0 & 0 & 0 & \frac{2}{n} & 0 \\ -6n(t-t_0) & 1 & 0 & -\frac{2}{n} & 0 & 0 \\ \frac{6(6x_0+4\dot{y}_0/n)}{a_r} & 0 & 0 & \frac{4\dot{x}_0}{n^2 a_r} & \frac{4(6x_0+4\dot{y}_0/n)}{n a_r} & 0 \\ \frac{-12nx_0}{(6nx_0+4\dot{y}_0)^2+(2\dot{x}_0)^2} & 0 & 0 & \frac{12nx_0+8\dot{y}_0}{(6nx_0+4\dot{y}_0)^2+(2\dot{x}_0)^2} & \frac{-8\dot{x}_0}{(6nx_0+4\dot{y}_0)^2+(2\dot{x}_0)^2} & 0 \\ 0 & 0 & \frac{z_0}{\sqrt{z_0^2+(\dot{z}_0/n)^2}} & 0 & 0 & \frac{\dot{z}_0/n^2}{\sqrt{z_0^2+(\dot{z}_0/n)^2}} \\ \frac{12n\dot{x}_0}{(6nx_0+4\dot{y}_0)^2+4\dot{x}_0^2} & 0 & \frac{n\dot{z}_0}{\dot{z}_0^2+n^2 z_0^2} & \frac{-12nx_0-8\dot{y}_0}{(6nx_0+4\dot{y}_0)^2+4\dot{x}_0^2} & \frac{8\dot{x}_0}{(6nx_0+4\dot{y}_0)^2+4\dot{x}_0^2} & \frac{-nz_0}{\dot{z}_0^2+n^2 z_0^2} \end{bmatrix} \tag{2.275}$$

Since the impulsive maneuvers only perturb the initial velocity and not the position, the right-hand half of this matrix is considered and the Cartesian coordinates are substituted by their ROEs counterparts:

$$\Phi = \begin{bmatrix} 0 & \frac{2}{n} & 0 \\ -\frac{2}{n} & 0 & 0 \\ 2\sin E_r & \frac{4}{n}\cos E_r & 0 \\ \frac{2\cos E_r}{na_r} & -\frac{4\sin E_r}{na_r} & 0 \\ 0 & 0 & \frac{\cos(\gamma+E_r)}{n} \\ \frac{-2\cos E_r}{na_r} & \frac{4\sin E_r}{na_r} & -\frac{\sin(\gamma+E_r)}{nA_z} \end{bmatrix} \tag{2.276}$$

Hence, the response of the ROEs to a perturbation in the relative velocity in the LVLH frame can be expressed as:

$$\begin{pmatrix} \delta x_r \\ \delta y_r \\ \delta a_r \\ \delta E_r \\ \delta A_z \\ \delta\gamma \end{pmatrix} = \begin{bmatrix} 0 & \frac{2}{n} & 0 \\ -\frac{2}{n} & 0 & 0 \\ 2\sin E_r & \frac{4}{n}\cos E_r & 0 \\ \frac{2\cos E_r}{na_r} & -\frac{4\sin E_r}{na_r} & 0 \\ 0 & 0 & \frac{\cos(\gamma+E_r)}{n} \\ \frac{-2\cos E_r}{na_r} & \frac{4\sin E_r}{na_r} & -\frac{\sin(\gamma+E_r)}{nA_z} \end{bmatrix} \begin{pmatrix} \delta\dot{x}_0 \\ \delta\dot{y}_0 \\ \delta\dot{z}_0 \end{pmatrix} \tag{2.277}$$

Several observations can be made from this relation:

1. The response of the center of motion of the instantaneous relative orbit described by x_r and y_r is not sensitive to the location where the maneuver is applied. These two ROEs are only affected by maneuvers applied along the y and x directions respectively and the response is inversely proportional to the mean motion n of the chief.

2. The response of the relative semi-major axis a_r, depends on the position of the deputy on the relative orbit through the relative eccentric anomaly E_r. If the spacecraft has a relative eccentric anomaly close to $\pi/2$ or $3\pi/2$ a maneuver

along the x axis will be the most effective while a maneuver along the y axis will be most effective for a relative eccentric anomaly close to 0 or π. It is also interesting to note that, since $n \ll 1$ for LEOs, the response to a maneuver along the y axis will be much stronger than that to a maneuver along the x axis in general.

3. The relative eccentric anomaly is more sensitive to a variation along the x axis when E_r is close to 0 or π and to a variation along the y axis when E_r is close to $\pi/2$ or $3\pi/2$. Since the response of that element is inversely proportional to a_r, a maneuver performed when a_r is small will have a greater impact.

4. The amplitude of the cross-track motion only responds to a variation in the z direction. The response is stronger when $\gamma + E_r$ is close to 0 or π, which happens when the spacecraft is close to the x axis, i.e. $z \approx 0$.

5. Finally, γ is the only ROE sensitive to a perturbations in all directions. Its response to a perturbation along the x and y axis is opposite to the response of E_r. A perturbation along the z axis will have more effect if $\gamma + E_r$ is close to $\pi/2$ or $3\pi/2$ which happens when the spacecraft is furthest from the x axis. It is also inversely proportional to A_z.

The third observation tends to indicate that setting the value of Q_{a4} based on a_r could result in a lower fuel consumption. In order to minimize the cost of targeting a specified E_r, the weight associated with this ROE, Q_{a4}, can be automatically tuned based on the value of a_r. Since E_r is most sensitive to a maneuver when a_r is small, if the current relative semi-major axis is larger than the target value, it is best to wait until the actual a_r decreases before performing the maneuver. This behavior is obtained by defining Q_{a4} as an exponentially decaying function of a_r as shown in Fig. 2.30.

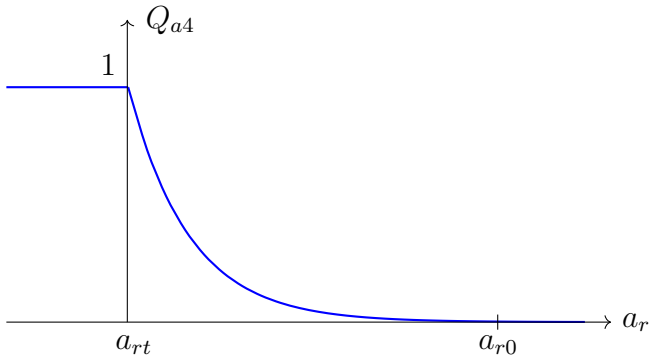

Figure 2.30: Desired behavior of Q_{a4}, assuming that the initial value of a_r is larger than the target value.

This function is obtained by defining:

$$Q_{a4}(a_r;\beta) = \begin{cases} \exp\left(-\beta \frac{a_r - a_{rt}}{|a_{r0} - a_{rt}|}\right), & \text{if } a_r > a_{rt} \\ 1, & \text{if } a_r \leq a_{rt} \end{cases} \tag{2.278}$$

where β is a parameter that defines the rate of the exponential decay. A large value of β means that the targeting of E_r will become significant only when a_r is very close to the target value a_{rt}.

In order to assess the efficiency of this autonomous tuning, a Monte Carlo simulation has been conducted. The initial state of the deputy is randomly generated with relative position within ± 1 km of the origin of the LVLH frame and velocity within ± 10 cm/s. A target relative orbit centered on the origin of the frame is created with a_{rt} and A_{zt} drawn from a uniform distribution bounded between 0 and 400 m, and ΔE_{rt} and γ from a uniform distribution bounded between $-\pi$ and π. The controller uses a time interval $T_m = 15$ min between two maneuvers and the scale of the attractive potential is $k_a = 10^{-3}$. For each pair of initial state and target orbit, the formation establishment is performed with $\beta = 0$ and $\beta = 5$ and the total delta-V's are compared. The process is repeated 50,000 times. Out of the 50,000 runs, 24,426 of them have a lower total delta-V with the adaptive Q_{a4} (i.e. when $\beta = 5$). For the 24,426 cases with lower delta-V, the mean of the total delta-V obtained with

constant coefficient $Q_{a4} = 1$ is 7.01 m/s and the mean with the adaptive coefficient is 5.56 m/s. That is, for these cases, the adaptive selection of Q_{a4} resulted in an average total delta-V which is 20.68% smaller than the total delta-V obtained with a fixed coefficient $Q_{a4} = 1$. The process has been repeated for different values of β to assess which value yields the best improvement. The results are presented in Fig. 2.31.

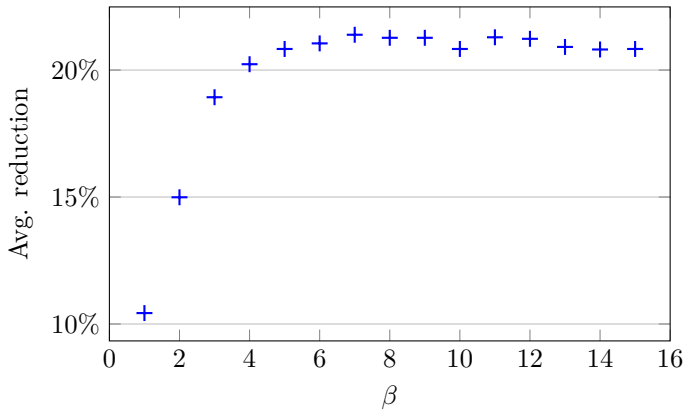

Figure 2.31: Average reduction of the total delta-V for different values of β.

We see in that figure that the reduction increases up to about 21% when β is larger than 3. The best improvement has been obtained for $\beta = 7$ with an average reduction of 21.39% as compared to a fixed Q_{a4} coefficient.

In order to identify when the autonomous selection results in a lower delta-V and when it doesn't, the correlations between the initial state and the target elements are computed. Figures 2.32 and 2.33 show the correlation coefficients between the LVLH initial coordinates and target ROEs for cases when a fixed Q_{a4}, respectively adaptive Q_{a4} result in a lower delta-V. These correlation matrices clearly show that there is a negative correlation between the targeted angular separation ΔE_{rt} and the initial x coordinate for fixed Q_{a4} and a positive correlation for adaptive Q_{a4}. We can also see a weaker correlation between ΔE_{rt} and y_0; however, after examination of the relation between these two coordinates and which method yields the lower total delta-V, no causality has been found.

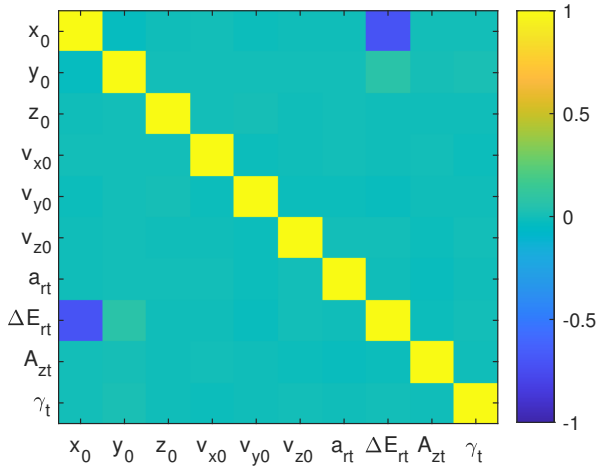

Figure 2.32: Correlation matrix for cases when a fixed Q_{a4} coefficient results in a lower total delta-V consumption.

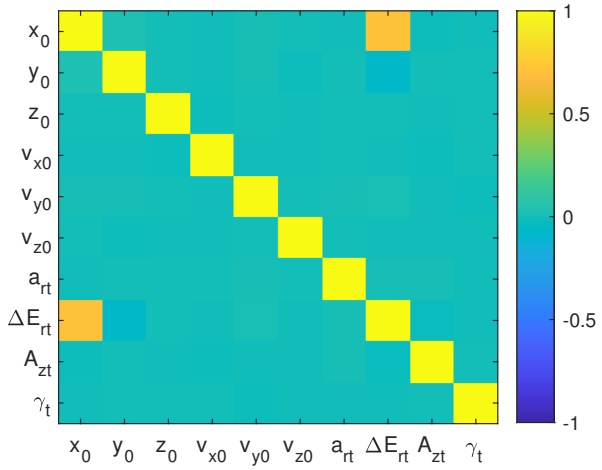

Figure 2.33: Correlation matrix for cases when an adaptive Q_{a4} coefficient results in a lower total delta-V consumption.

The correlations observed in the two figures suggest a relation between ΔE_{rt}, x_0, and whether the fixed or adaptive coefficient yields a lower delta-V. This relation is illustrated in Fig. 2.34. Blue dots corresponds to $(x_0, \Delta E_{rt})$ pairs for which the adaptive Q_{a4} results in a lower delta-V and red dots denote pairs for which the fixed Q_{a4} yields a lower delta-V. We see in this figure that the adaptive coefficient works

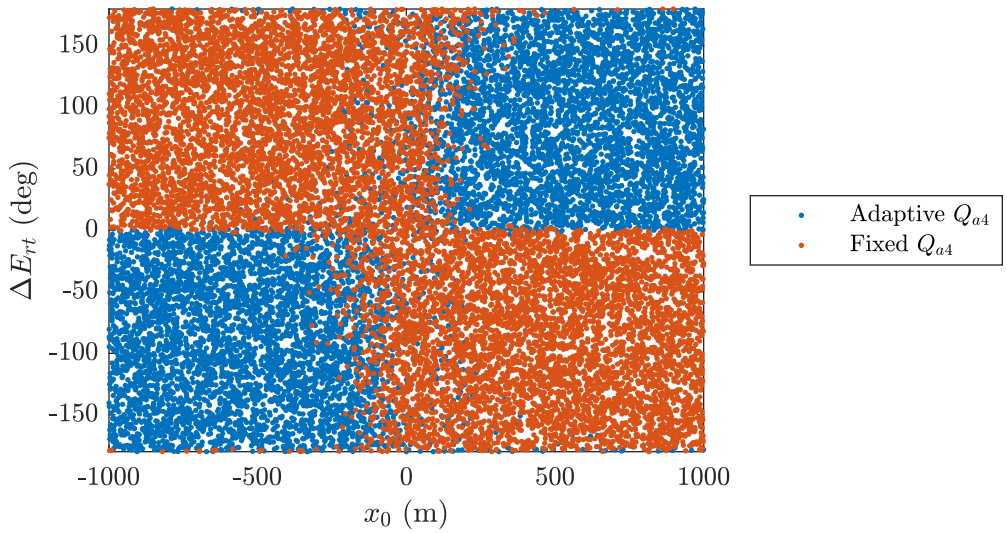

Figure 2.34: Relation between the initial x component and the targeted angular separation for the fixed and adaptive Q_{a4}. Blue dots denote pairs for which the adaptive method results in a lower cumulative delta-V and red dots pairs for which the fixed coefficient results in a lower delta-V.

best if the deputy is initially on a lower orbit than the chief and targets a negative angular separation or if it is above the chief and targets a positive angular separation. Similarly, a fixed coefficient results in a lower total delta-V if the spacecraft is under the chief and targets a positive angular separation or if it is above and targets a negative angular separation. The behavior is not well defined if the spacecraft is close to $x_0 = 0$. For this reason, the adaptive Q_{a4} defined by Eq. (2.278) is used with $\beta = 7$ if $x_0 < -150$ m and $\Delta E_{rt} < 0°$ or $x_0 > 150$ m and $\Delta E_{rt} > 0°$. If these conditions are not satisfied, a constant coefficient $Q_{a4} = 1$ is used instead. The other observations made from Eq. (2.277) do not lead to the straightforward derivation of autonomous coefficient selection methods for the other shaping parameters for the current formulation. For this reason, the other coefficients of the shaping matrix for the attractive potential are all set to one.

As seen in section 2.2.2, the selection of the shaping matrix $\mathbf{Q}_r$ for the repulsive potential determines the size and orientation of the ellipsoid. Since the imminence of a collision is higher if the relative velocity between the spacecraft and the obstacle

is high, the ellipsoid is oriented such that its main axis is aligned with the relative velocity vector. The relative velocity of the obstacle as seen by the spacecraft is

$$\delta\dot{\boldsymbol{r}} = \dot{\boldsymbol{r}}^{\text{obs}} - \dot{\boldsymbol{r}} \tag{2.279}$$

Assuming that the major axis of the ellipsoid is along the first dimension, the rotation axis is

$$\hat{\boldsymbol{a}} = \frac{\hat{\boldsymbol{e}}_1 \times \delta\dot{\boldsymbol{r}}}{\|\hat{\boldsymbol{e}}_1 \times \delta\dot{\boldsymbol{r}}\|} \tag{2.280}$$

with $\hat{\boldsymbol{e}}_1 = \begin{bmatrix} 1 & 0 & 0 \end{bmatrix}^T$, and the rotation angle is given by

$$\theta = \cos^{-1}\left(\frac{\delta\dot{\boldsymbol{r}} \cdot \hat{\boldsymbol{e}}_1}{\|\delta\dot{\boldsymbol{r}}\|}\right) \tag{2.281}$$

These two quantities allow to construct the rotation matrix

$$\mathbf{R} = \cos\theta\mathbf{I}_3 + \sin\theta[\hat{\boldsymbol{a}}]_\times + (1-\cos\theta)\hat{\boldsymbol{a}}\hat{\boldsymbol{a}}^T \tag{2.282}$$

where $\mathbf{I}_3$ is the 3-by-3 identity matrix and $[\hat{\boldsymbol{a}}]_\times$ is the cross-product matrix of $\hat{\boldsymbol{a}}$ given by

$$[\hat{\boldsymbol{a}}]_\times = \begin{bmatrix} 0 & -\hat{a}_3 & \hat{a}_2 \\ \hat{a}_3 & 0 & -\hat{a}_1 \\ -\hat{a}_2 & \hat{a}_1 & 0 \end{bmatrix} \tag{2.283}$$

If υ is the ratio between the major and minor axes, then the shaping matrix is computed as

$$\mathbf{Q}_r = \mathbf{R}\begin{bmatrix} 1 & 0 & 0 \\ 0 & \upsilon^2 & 0 \\ 0 & 0 & \upsilon^2 \end{bmatrix}\mathbf{R}^T \tag{2.284}$$

Fig. 2.35 illustrates the orientation of the repulsive ellipsoidal potential when a spacecraft encounters a static obstacle on its trajectory.

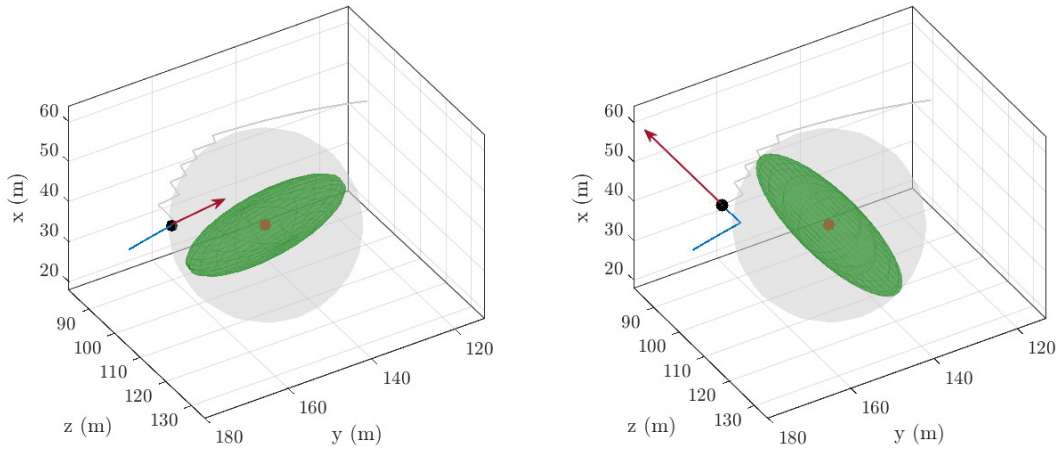

Figure 2.35: Orientation of the repulsive ellipsoidal potential based on the relative velocity between the spacecraft and the obstacle.

When the spacecraft first reaches the sphere of influence of the obstacle (gray sphere), the relative velocity (red arrow) is mostly in the direction of the negative y axis. After a first collision avoidance maneuver is performed, the relative velocity points in the positive x and negative z directions leading to a rotation of the repulsive ellipsoidal potential. The green ellipsoid in the figure has a semi-major axis $r_{\text{SOI}} = 20$ m and corresponds to an isosurface of $\phi_r = 10^{-5} k_r$. In this example, the spacecraft "bounces" on the sphere of influence. In the simulations that will be presented in Chapter 3, the threshold to trigger a recovery maneuver after a CAM has been performed is set to three times the sphere of influence, thus reducing the likelihood that the spacecraft will perform several CAMs in a row. This feature has been deactivated in this example for illustration purpose.

The motivation for the computation of k_a is to minimize fuel consumption while ensuring that the maneuvers will not exceed ΔV_{max}. For given sets of initial ROEs and target ROEs, an attractive potential function is constructed with a given k_a. The reference trajectory is created using this attractive potential only and the maneuver required to track the first waypoint is computed. The relative state of the spacecraft is then propagated for a duration T_m using the CW equations and this new state is used

to compute the maneuver to reach the next waypoint. The reference tracking is carried on for a given duration τ_c. Once this duration is reached, the total delta-V required to track the trajectory is recorded along the amplitude of the largest maneuver that occurred. The process is repeated for different values of k_a. Once these different values have been computed, the k_a value for which the maximum delta-V does not exceed ΔV_{max} and that results in the lowest total delta-V is selected. In addition to these constraints, the Euclidean distance between the final position of the spacecraft and the target position is calculated to ensure that the trajectory has converged and a k_a value such that this metric is smaller than a threshold d_c is chosen. If no value satisfies the constraint, a fallback value of 10^{-3} is used. Fig. 2.36 shows the output of the k_a search algorithm for a spacecraft with initial relative state

$$\boldsymbol{s}_0 = \begin{bmatrix} -70 \text{ m} & 800 \text{ m} & -300 \text{ m} & 0.09 \text{ m/s} & 0.08 \text{ m/s} & 0.08 \text{ m/s} \end{bmatrix}^T$$

and corresponding ROEs

$$\boldsymbol{\rho}_0 = \begin{bmatrix} -129.1 \text{ m} & 630.2 \text{ m} & 206.9 \text{ m} & 124.8^\circ & 309.3 \text{ m} & 159.3^\circ \end{bmatrix}^T$$

The targeted relative orbit is in the x-y plane and is described by

$$\boldsymbol{\rho}_t = \begin{bmatrix} 0 \text{ m} & -100 \text{ m} & 100 \text{ m} & 60^\circ & 0 \text{ m} & 0^\circ \end{bmatrix}^T$$

The controller uses a time interval of $T_m = 3600$ s between two maneuvers. In this example, the trajectory is propagated for a duration $\tau_c = 4.8$ hours and the search space for k_a contains 33 values ranging from 10^{-5} to 10^{-1} which are logarithmically spaced. We see in Fig. 2.36 that for small values of k_a the total delta-V (green line) required to track the reference trajectory is high. The high error (orange line) indicates that the trajectory did not converge at the end of the 4.8 hours. The shaded area corresponds to values of k_a for which the largest delta-V (blue line) is larger than the maximum delta-V allowed (red dashed line), set to 1 m/s in this example, and are

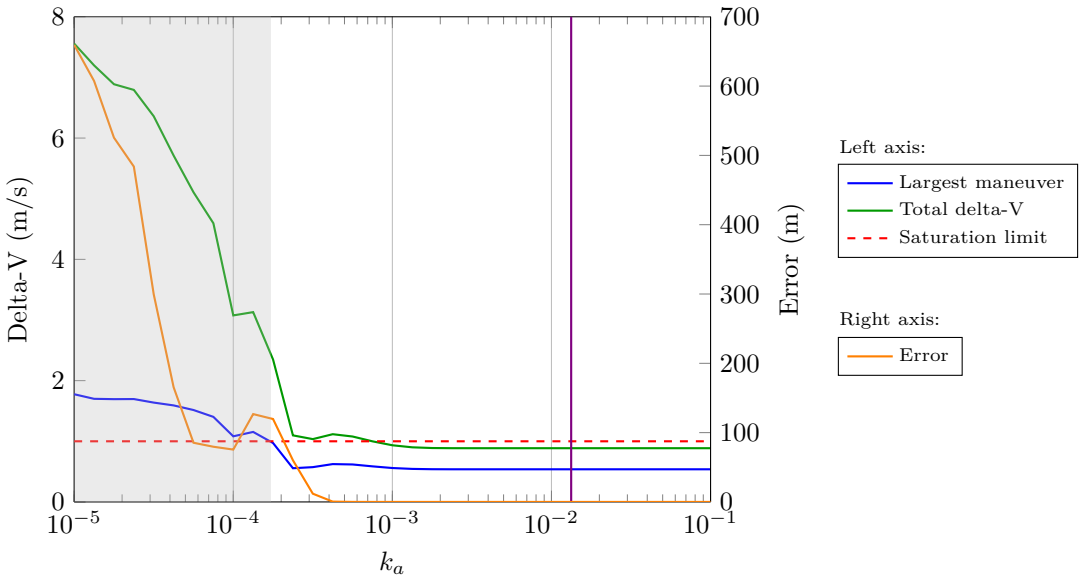

Figure 2.36: Autonomous computation of the optimal k_a value.

therefore not feasible. The minimum delta-V satisfying the constraints is $k_a = 0.0133$ as shown by the violet line. The threshold on the metric has been set to $d_c = 3$ meters for this example, that is, the algorithm has selected a value such that the spacecraft is at most 3 meters away from the target at the end of the 4.8 hours of propagation. Fig. 2.37 shows the trajectories for a selection of k_a values. If the value is too small, we see that the trajectory does not converge to the target relative orbit. The trajectory resulting from the selected k_a is shown in red. The two trajectories for larger values of k_a are superimposed with the optimal trajectory.

The amplitude of the repulsive potential, k_r, can also be selected automatically. Since the controller is based on the minimization of the potential field, the value of the attractive potential field monotonically decreases over time. Hence, if the spacecraft is initially not at risk of colliding with another agent, by the time a risk of collision is detected the value of the attractive potential will be lower than the initial value. Setting $k_r = \phi_a(t_0)$, that is, the value of the repulsive potential field at the surface of the obstacle corresponds to the initial value of the attractive potential, results in a potential at the surface of the obstacle higher than the current potential

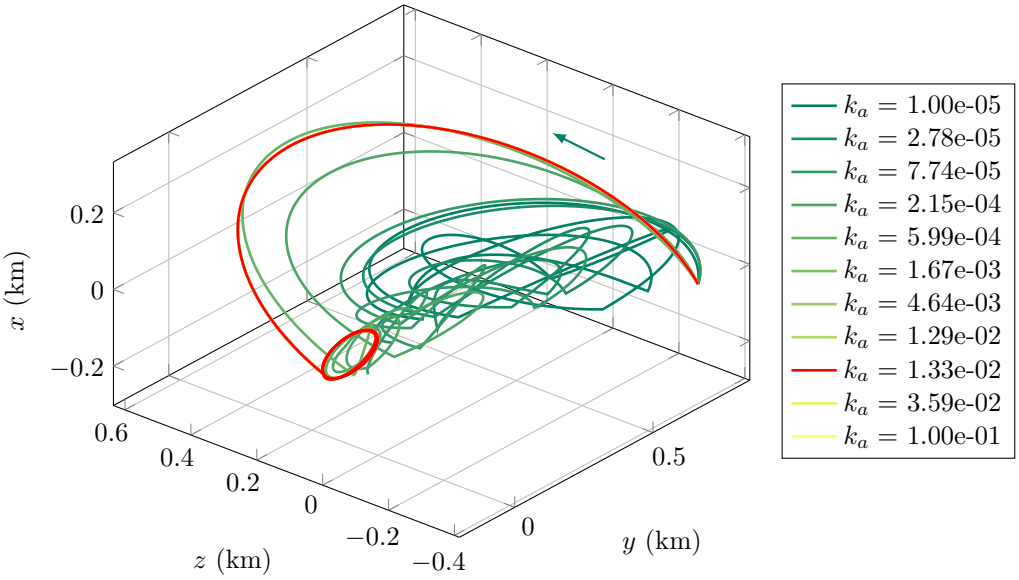

Figure 2.37: Trajectories for different values of k_a.

of the spacecraft. That way, by following the steepest descent of the gradient, the spacecraft will never reach the surface of the obstacle, assuming an appropriate time step between two control cycles has been chosen.

The different methods proposed in this section led to the automatic selection of several parameters of the APFs, thus reducing the number of parameters that must be manually tuned. The methods described to compute these parameters are based on fuel minimization considerations for some, while others are based on convergence considerations. Out of the fourteen parameters initially required when working with the ROEs, eleven of them can be automatically computed using methods based on the definition of three parameters which have an intuitive interpretation. Hence, the six parameters summarized in Table 2.4 need to be manually selected.

2.4 Orbital Dynamics

The space environment in which spacecraft evolve is nonlinear and several effects from physical phenomenon impact the translational and rotational motion of the vehicles. A common approach to numerically propagate spacecraft trajectories is to

Table 2.4: Summary of the parameters of the attractive and repulsive potentials that must be manually selected.

Attractive potential	**Repulsive potential**
τ_c: convergence time for the computation of k_a d_c: convergence threshold	r_s: radius of a sphere circumscribing the obstacle r_{SOI}: radius of the sphere of influence p: value of the potential at r_{SOI} as a fraction of k_r υ: ratio between the semi-major and semi-minor axes of the ellipsoid

consider a two-body system where a trajectory evolves due to the spherical potential created by a central body. Equations of motion describing the dynamics of the spacecraft are then derived from this spherical potential and numerically integrated. In order to obtain a higher fidelity model of the space environment, orbital perturbations must be accounted for. One way of doing this is to add them to the two-body acceleration:

$$\boldsymbol{a} = \boldsymbol{a}_{\text{2-body}} + \boldsymbol{a}_{\text{geo}} + \boldsymbol{a}_{\text{drag}} + \boldsymbol{a}_{\text{3-body}} + \boldsymbol{a}_{\text{SRP}} + \boldsymbol{a}_{\text{other}} \tag{2.285}$$

where $\boldsymbol{a}_{\text{2-body}}$ is the acceleration resulting from the spherical potential and the following terms are the perturbations created by the geopotential field, atmospheric drag, third-body effects, solar radiation pressure, and other sources respectively. The equations of motion are then formed with

$$^{I}\ddot{\boldsymbol{r}} = \boldsymbol{a}(t, \boldsymbol{r}, \dot{\boldsymbol{r}}) \tag{2.286}$$

and numerically integrated. This method is sometimes referred to as Cowell's formulation. In the following section, the trajectories have been propagated by integrating Eq. (2.286) using a Runge-Kutta-Fehlberg integrator of order 8 with error estimation of order 7. The absolute and relative tolerances have been both set to 10^{-12}. The

initial state of the chief in terms of classical orbital elements used for the propagation is

$$a = R_\oplus + 500 \text{ km} \qquad e = 0 \qquad i = 45^\circ \qquad \Omega = 0^\circ \qquad \omega = 0^\circ \qquad M = 0^\circ$$

and the initial state of the deputy in terms of ROEs is

$$\boldsymbol{\rho}_0 = \begin{bmatrix} 0 \text{ m} & 0 \text{ m} & 300 \text{ m} & 90^\circ & 100 \text{ m} & -45^\circ \end{bmatrix}^T$$

2.4.1 Perturbations

Several perturbations act on spacecraft in the vicinity of the Earth. Non-spherical potential, atmospheric drag, third-body perturbations, and solar radiation pressure are external forces that perturb the ideal orbit computed from the two-body approximation. The gravitational potential field generated by the uneven mass distribution within the Earth can be described using spherical harmonics [89]:

$$U(r) = \frac{\mu_\oplus}{r} \sum_{n=0}^{\infty} \sum_{m=0}^{n} \frac{R_\oplus^n}{r^n} \overline{P}_{nm}(\sin\phi)(\overline{C}_{nm}\cos(m\lambda) + \overline{S}_{nm}\sin(m\lambda)) \tag{2.287}$$

where $\mu_\oplus$ is the standard gravitational parameter of Earth, $R_\oplus$ the radius of the planet, $\overline{P}_{nm}(\cdot)$ the normalized associated Legendre polynomial of degree n and order m, ϕ the geocentric latitude, and λ the longitude. The normalized coefficients $\overline{C}_{nm}$ and $\overline{S}_{nm}$ are obtained from

$$\begin{Bmatrix} \overline{C}_{nm} \\ \overline{S}_{nm} \end{Bmatrix} = \sqrt{\frac{(n+m)!}{(2-\delta_{0m})(2n+1)(n-m)!}} \begin{Bmatrix} C_{nm} \\ S_{nm} \end{Bmatrix} \tag{2.288}$$

with

$$C_{nm} = \frac{2-\delta_{0m}}{M_\oplus}\frac{(n-m)!}{(n+m)!}\int \frac{s^n}{R_\oplus^n} P_{nm}(\sin\phi')\cos(m\lambda')\rho(\boldsymbol{s})d^3\boldsymbol{s} \tag{2.289}$$

$$S_{nm} = \frac{2-\delta_{0m}}{M_\oplus}\frac{(n-m)!}{(n+m)!}\int \frac{s^n}{R_\oplus^n} P_{nm}(\sin\phi')\sin(m\lambda')\rho(\boldsymbol{s})d^3\boldsymbol{s} \tag{2.290}$$

where δ is the Kronecker delta, $M_\oplus$ the mass of the Earth, $(\cdot)'$ denotes quantities associated with $\boldsymbol{s}$, and $\rho(\boldsymbol{s})$ is the mass density at $\boldsymbol{s}$. Coefficients with $m = 0$, $m < n$, and $m = n$ are called zonal, tesseral, and sectorial coefficients respectively. Since the precise mass distribution is not known, these coefficients can't be computed directly but have instead been measured from satellite tracking, surface gravimetry, and altimeter data [89]. If the mass distribution is assumed to be symmetric with respect to the axis of rotation, then only the zonal terms, commonly referred to as J_n terms, contribute to the geopotential. The acceleration due to the non-spherical potential is obtained from the gradient of Eq. (2.287):

$$\boldsymbol{a}_{\text{geo}} = \nabla U(r) \tag{2.291}$$

The effect of the geopotential on the inertial motion is a secular drift of the right ascension of the ascending node, argument of perigee, and mean anomaly [83]. For relative motion, this perturbation results in the rotation of the relative orbit as seen in the LVLH reference frame. Fig. 2.38 shows the relative orbit in the two-body approximation (blue) and in a perturbed environment with geopotential expansion up to degree six, i.e. including J_2 to J_6 (orange). The trajectory has been propagated for 48 hours.

We see in that figure that the relative orbit shifts along the y axis and is distorted. The magnitude of the geopotential perturbations averaged on one orbit of this simu-

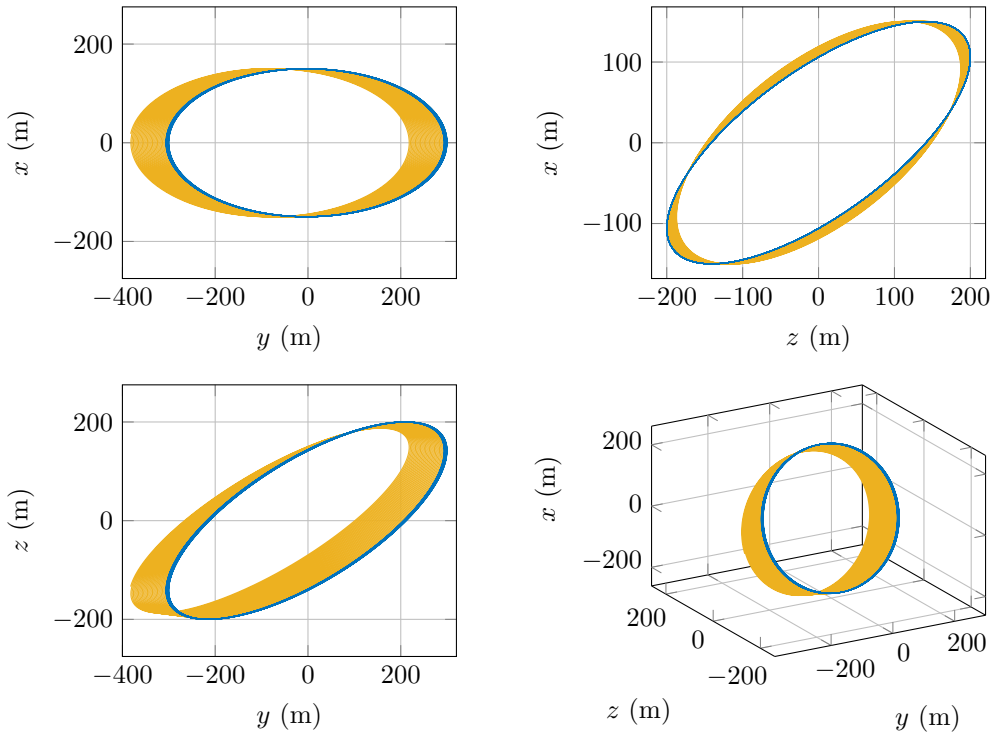

Figure 2.38: Relative orbit in the LVLH frame in the two-body approximation (blue) and under the influence of geopotential perturbations (orange).

lation is $a^c_{\text{geo}} = 1.158493 \cdot 10^{-5}$ km/s^2 for the chief and $a^d_{\text{geo}} = 1.158504 \cdot 10^{-5}$ km/s^2 for the deputy, leading to a differential acceleration of

$$\Delta a_{\text{geo}} = \left| a^d_{\text{geo}} - a^c_{\text{geo}} \right| = 1.0348 \cdot 10^{-10} \text{ km/s}^2 \tag{2.292}$$

Atmospheric drag results from the friction of air on the spacecraft's surfaces. This force acts in a direction opposite to the velocity vector relative to the rotating atmosphere. The acceleration induced by atmospheric drag is

$$\boldsymbol{a}_{\text{drag}} = -\frac{c_D A \rho}{2m} \|\boldsymbol{v}_{\text{rel}}\|^2 \frac{\boldsymbol{v}_{\text{rel}}}{\|\boldsymbol{v}_{\text{rel}}\|} \tag{2.293}$$

where m is the mass of the spacecraft, c_D the drag coefficient, A the exposed cross-sectional area, ρ the atmospheric density, and $\boldsymbol{v}_{\text{rel}}$ the relative velocity vector, computed with

$$\boldsymbol{v}_{\text{rel}} = {}^{I}\dot{\boldsymbol{r}} - \boldsymbol{\omega}_{\oplus} \times {}^{I}\boldsymbol{r} \tag{2.294}$$

where $\boldsymbol{\omega}_{\oplus}$ is the Earth angular velocity vector. The drag coefficient as well as the cross-sectional area depend on the geometry of the vehicle and precise values can only be obtained when a detailed CAD model of the spacecraft is available. Several models exist to estimate the atmospheric density. The exponential model is widely used for first order approximations due to its computational efficiency. This model assumes an exponentially decaying atmospheric density as altitude increases and provides tabulated data that can be used to retrieve the density at a specific altitude. More accurate models have been developed to account for time, temperature, solar activity, and geomagnetic activity such as GRAM and NRLMSIS-00 among others. Fig. 2.39 illustrates the effect of the drag on the relative orbit using EarthGRAM2016. For this example, both the leader and the deputy have the same physical properties. The spacecraft have a mass of 10 kg, a c_D of 2.2, and a cross-sectional area of 0.25 m^2. The trajectories have been propagated for 48 hours with no perturbation (blue) and with atmospheric drag (orange). It can be seen in that figure that the effect of the drag is purely in the along-track direction, resulting in the relative orbit drifting in the negative y direction. The total drift after 48 hours is about 6.6 meters. The magnitude of the perturbing acceleration from the atmospheric drag averaged on one orbit is $a^c_{\text{drag}} = 2.901504 \cdot 10^{-9}$ km/s^2 for the chief and $a^d_{\text{drag}} = 2.901510 \cdot 10^{-9}$ km/s^2 for the deputy, resulting in a differential acceleration of

$$\Delta a_{\text{drag}} = \left| a^d_{\text{drag}} - a^c_{\text{drag}} \right| = 5.9379 \cdot 10^{-15} \text{ km/s}^2 \tag{2.295}$$

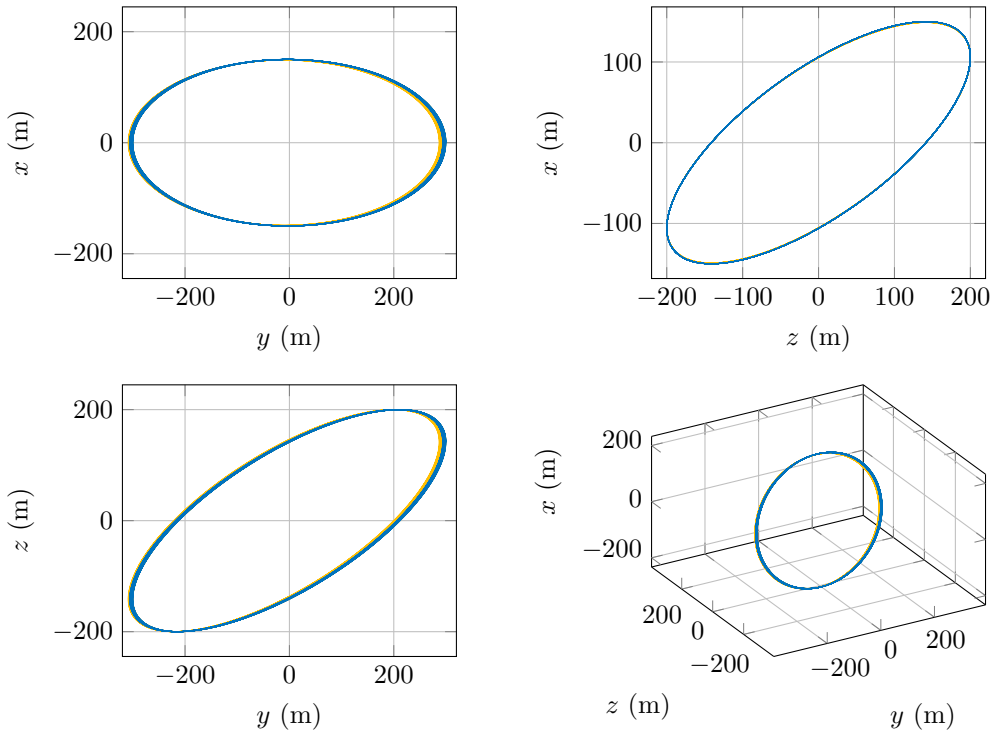

Figure 2.39: Relative orbit in the LVLH frame in the two-body approximation (blue) and under the effect of atmospheric drag (orange).

A third source of perturbations that act on the spacecraft is the third-body effect, caused by the gravitational field of celestial bodies other than the central body. For Earth-bound satellites, the acceleration induced by a third body is [83]:

$$\boldsymbol{a}_{\text{3-body}} = \mu_3 \left(\frac{\boldsymbol{r}_{\text{s/c-3}}}{\|\boldsymbol{r}_{\text{s/c-3}}\|^3} - \frac{\boldsymbol{r}_{\oplus\text{-3}}}{\|\boldsymbol{r}_{\oplus\text{-3}}\|^3} \right) \tag{2.296}$$

where μ_3 is the standard gravitational parameter of the third body, $\boldsymbol{r}_{\text{s/c-3}}$ the position vector from the spacecraft to the third body, and $\boldsymbol{r}_{\oplus\text{-3}}$ the position vector from the Earth to the third body. When $\boldsymbol{r}_{\text{s/c-3}} \approx \boldsymbol{r}_{\oplus\text{-3}}$, both terms on the right hand side of the equations will be very small and the difference will be even smaller. The precision required to accurately compute this difference might be very high and lead to rounding errors. To remedy this difficulty, several authors have proposed different

approximations of this equation. One of these approximations has been proposed by Long et al. [90] and uses Legendre functions:

$$\boldsymbol{a}_{\text{3-body}} = -\mu_3 \left(\frac{-\boldsymbol{r}_{\text{s/c-3}}(3B + 3B^2 + B^3) + \boldsymbol{r}_{\oplus\text{-s/c}}}{\|\boldsymbol{r}_{\oplus\text{-3}}\|^3} \right) \tag{2.297}$$

with

$$B = \sum_{j=1}^{\infty} P_j[\cos\zeta] h^j$$

where P_j are Legendre functions, $h = \|\boldsymbol{r}_{\oplus\text{-s/c}}\| / \|\boldsymbol{r}_{\oplus\text{-3}}\|$, and ζ is the angle between the third body and the satellite and can be computed with

$$\|\boldsymbol{r}_{\text{s/c-3}}\|^2 = \|\boldsymbol{r}_{\oplus\text{-s/c}}\|^2 + \|\boldsymbol{r}_{\oplus\text{-3}}\|^2 - 2\|\boldsymbol{r}_{\oplus\text{-s/c}}\|\|\boldsymbol{r}_{\oplus\text{-3}}\| \cos\zeta$$

Using Eq. (2.296), the magnitude of the perturbation from the Moon and the Sun on a spacecraft on a 500 km altitude circular orbit about the Earth can be estimated. It is assumed that the spacecraft is located between the Earth and the third body. The different position vectors used for the computation of the perturbation from the Moon are illustrated in Fig. 2.40.

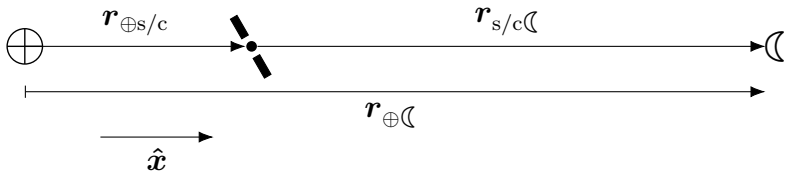

Figure 2.40: Position vectors between the Earth, the spacecraft, and the Moon.

The constant values for the different bodies and distances are shown in Table 2.5.

Table 2.6 shows the magnitude and direction of the different terms of Eq. (2.296) when considering the Moon and the Sun individually. The first term on the right hand side of the equation is the direct perturbing term, the second one is the indirect perturbing term, and the difference is the net perturbing acceleration. We see from

Table 2.5: Physical constants used for the computation of third-body perturbations [91–94].

$R_\oplus = 6378.1366$ km
$\mu_\leftmoon = 4902.800066$ km^3/s^2
$\mu_\odot = 132,712,440,041.939400$ km^3/s^2
$r_{\oplus\leftmoon} = 384,400$ km
$r_{\oplus\odot} = 149.6 \cdot 10^6$ km

Table 2.6: Direct, indirect, and net perturbations for the Moon and the Sun.

	Moon		Sun	
	Magnitude (km/s^2)	Direction	Magnitude (km/s^2)	Direction
Direct perturbation	$3.44 \cdot 10^{-8}$	$+\hat{\boldsymbol{x}}$	$5.9306 \cdot 10^{-6}$	$+\hat{\boldsymbol{x}}$
Indirect perturbation	$3.3180 \cdot 10^{-8}$	$-\hat{\boldsymbol{x}}$	$5.9301 \cdot 10^{-6}$	$-\hat{\boldsymbol{x}}$
Net perturbation	$1.22 \cdot 10^{-9}$	$+\hat{\boldsymbol{x}}$	$5.0000 \cdot 10^{-10}$	$+\hat{\boldsymbol{x}}$

this table that the direct perturbing acceleration is larger than the indirect term for both bodies, and the net perturbation from the Moon is one order of magnitude larger than that of the Sun. In both cases, the net perturbation is in the positive $\hat{x}$ direction, that is, pulling the spacecraft away from the Earth in this simplified situation.

Numerical simulations using JPL's ephemerides to retrieve the Moon and Sun position have been run for the same spacecraft physical properties as before. The average magnitude of the net perturbing acceleration from the Moon and the Sun acting on the chief is $a^c_{\text{3-body}} = 7.731217 \cdot 10^{-10}$ km/s^2 and the effect on the deputy is $a^d_{\text{3-body}} = 7.731230 \cdot 10^{-10}$ km/s^2 resulting in a differential acceleration of

$$\Delta a_{\text{3-body}} = \left| a^d_{\text{3-body}} - a^c_{\text{3-body}} \right| = 1.3626 \cdot 10^{-15} \text{ km/s}^2 \tag{2.298}$$

Lastly, the perturbation induced by the solar radiation pressure (SRP) are considered. The perturbing acceleration created by this pressure is [83]:

$$\boldsymbol{a}_{\text{SRP}} = -\frac{p_{\text{SRP}} C_R A_\odot}{m} \frac{\boldsymbol{r}_{\text{s/c}\odot}}{\|\boldsymbol{r}_{\text{s/c}\odot}\|} \tag{2.299}$$

where p_{SRP} is the solar pressure, C_R the radiation pressure coefficient, $A_\odot$ the area exposed to the Sun, m the mass of the spacecraft, and $\boldsymbol{r}_{\text{s/c}\odot}$ the position vector from the spacecraft to the Sun. In the vicinity of the Earth, the solar flux is approximately constant with $SF = 1367$ W/m^2 leading to a solar radiation pressure of $p_{\text{SRP}} = 4.57 \cdot 10^{-6}$ N/m^2. Thus, considering a spacecraft with $C_R = 1.5$, $A_\odot = 0.25$ m^2, and a mass $m = 10$ kg, the magnitude of the acceleration due to SRP is $a_{\text{SRP}} = 1.7138 \cdot 10^{-10}$ km/s^2. Since the solar flux varies very slowly at the distance of the Earth, it can be assumed constant for LEOs and therefore the differential SRP acceleration between a deputy and a chief with the same physical properties will be approximately zero, except when one of the two spacecraft enters or exits eclipse before the other one. The magnitude of the perturbing acceleration created by solar radiation pressure averaged on one orbit of the trajectory propagated using the initial conditions described before is $a^c_{\text{SRP}} = 1.354493 \cdot 10^{-10}$ km/s^2 for the chief and $a^d_{\text{SRP}} = 1.354486 \cdot 10^{-10}$ km/s^2 for the deputy. The difference between these two accelerations results in a differential acceleration of

$$\Delta a_{\text{SRP}} = \left| a^d_{\text{SRP}} - a^c_{\text{SRP}} \right| = 6.3870 \cdot 10^{-16} \text{ km/s}^2 \tag{2.300}$$

Table 2.7 summarizes the differential perturbing accelerations acting on the relative motion for a formation with the chief on a 500 km altitude circular orbit.

Table 2.7: Orders of magnitude of the perturbing accelerations.

Perturbation	**Differential acceleration (km/s^2)**
Geopotential	$1.0348 \cdot 10^{-10}$
Atmospheric drag	$5.9379 \cdot 10^{-15}$
Third-body	$1.3626 \cdot 10^{-15}$
Solar radiation pressure	$6.3870 \cdot 10^{-16}$

As can be seen in Table 2.7, the magnitude of the perturbations induced by the non-spherical geopotential is the largest by several orders of magnitude. The atmospheric drag, third-body, and SRP perturbations all contribute to a lesser extend to the perturbation of the relative motion of the deputy. Since the atmospheric drag

and solar radiation pressure depend on the physical properties of the spacecraft, having very different vehicles acting as chief and deputy might result in significantly higher differential accelerations for these two perturbing terms.

Other sources of orbital perturbations such as tides, the albedo, and the magnetic field exist but are not considered in this work due to their lower impact on relative motion. In the next section, the effect of nonlinear dynamics and orbital perturbations on the linear targeter is presented.

2.4.2 Accuracy of the Linear Targeter

The targeter derived in Section 2.3.3 is based on the CW equations which are derived from a linear approximation of the dynamics. Since spacecraft evolve in a nonlinear, perturbed environment, it is important to assess the convergence properties of the targeter when used in that environment. Being mostly interested in the effects of nonlinearity and orbital perturbations, the magnitude of the maneuvers is assumed to be unbounded in this section. The accuracy of the targeter is assessed by conducting Monte Carlo simulations. An initial position is randomly generated within a distance $\pm d$ from the chief and zero initial velocity is set. A target position is generated within that same distance and the maneuver required to reach it within a specified duration T_m is computed using the linear targeter. Once the delta-V has been computed, it is added to the initial LVLH state which is then converted into inertial coordinates. The absolute inertial states of the chief and the deputy are propagated using the Cowell formulation presented in section 2.4 with the four perturbing accelerations described previously. The final relative state is computed as the difference between the two inertial states and transformed into LVLH Cartesian coordinates. The norm of the difference between the target position and the final position is used as an indicator of the accuracy of the targeting. For these simulations, both spacecraft are assumed to have the same physical properties, summarized in Table 2.8. It is also assumed that the chief is on a circular orbit with a 30° inclination and

Table 2.8: Physical properties of the spacecraft

$m = 20$ kg
$c_D = 2.2$
$A = 0.16$ m^2
$C_r = 1.8$
$A_\odot = 0.16$ m^2

0° right ascension of the ascending node, argument of periapsis, and true anomaly. The simulations are performed for different chief's altitudes, distances d, and time of flight T_m to reach the target. For each case, 5000 runs have been performed and the mean, standard deviation, minimum, 25th percentile, 75th percentile, and maximum values of the error are computed. Table 2.9 presents the results of these simulations.

Several observations can be made from Table 2.9. In general, the error resulting from initial conditions and target which are far away is smaller when the chief is on a high altitude orbit than when it is on a low altitude orbit. Not surprisingly, for all three altitudes, the error is smaller when the initial conditions and target are close to each other, i.e. for small d values. A short duration also improves the accuracy of the targeter. For a short time interval, the spacecraft will travel in a more direct way than for a long time interval resulting in a shorter path and shorter exposure to perturbations and nonlinear effects thus leading to a higher targeting accuracy. These results indicate that the waypoints of the reference trajectory should be within a few hundred meters apart and the time interval between two of them should be reasonably small if a precise tracking is desired.

Table 2.9: Monte Carlo simulations of the targeter accuracy.

				Error					
Case	**alt** (km)	**d** (km)	$\boldsymbol{T}_m$ (min)	**mean** (m)	**std** (m)	**min** (m)	$\boldsymbol{p}_{25}$ (m)	$\boldsymbol{p}_{75}$ (m)	**max** (m)
1	300	1	15	1.70	0.73	0.04	1.12	2.20	4.40
2			30	7.31	3.56	0.28	4.58	9.51	22.23
3			60	19.67	9.18	0.47	12.90	24.90	61.72
4		5	15	8.57	3.90	0.72	5.57	10.97	23.26
5			30	38.36	19.82	0.98	23.57	49.54	134.87
6			60	104.55	53.19	4.89	65.74	134.10	373.73
7		10	15	18.05	8.77	0.96	11.53	23.23	57.16
8			30	84.31	49.47	2.02	49.12	108.21	365.60
9			60	246.60	140.46	3.19	144.61	320.48	918.18
10	500	1	15	1.46	0.63	0.05	0.98	1.88	3.78
11			30	6.20	2.94	0.17	3.90	8.13	17.52
12			60	18.71	9.07	0.69	11.90	24.21	58.87
13		5	15	7.36	3.37	0.56	4.81	9.49	20.90
14			30	32.25	16.27	1.63	19.80	41.96	110.39
15			60	99.85	55.02	3.25	60.52	126.09	415.94
16		10	15	15.61	7.64	0.47	10.03	19.73	50.34
17			30	71.14	40.43	2.31	42.01	92.27	279.15
18			60	242.81	152.18	8.99	136.43	311.97	1103.16
19	700	1	15	1.28	0.55	0.01	0.87	1.65	3.47
20			30	5.32	2.49	0.30	3.39	6.94	15.36
21			60	18.88	9.70	0.70	11.65	24.54	63.21
22		5	15	6.43	2.88	0.27	4.27	8.22	16.97
23			30	27.59	13.39	0.57	17.51	35.53	102.70
24			60	104.14	63.28	4.84	60.47	130.88	447.35
25		10	15	13.66	6.77	0.42	8.72	17.47	45.50
26			30	59.67	33.16	2.46	35.00	77.41	237.73
27			60	264.01	188.36	2.66	132.95	341.71	1342.48

3. NUMERICAL SIMULATIONS

In this chapter, the performance of the control algorithm is demonstrated through numerical simulations of the establishment of different formation geometries. The six degrees of freedom simulator is first introduced and uncertainties are described. An assessment of the accuracy of formation establishment followed by the results of the numerical simulation of four different scenarios are then presented.

3.1 Orbital Propagation

The numerical simulations presented in this chapter have been run using a six degrees of freedom Matlab/Simulink orbital propagator originally designed for LightSail [95,96]. The simulator has been modified to accommodate spacecraft formations. The orbital perturbations taken into account include non-spherical geopotential with expansion up to degree six, atmospheric drag using the 2001 United States Naval Research Laboratory Mass Spectrometer and Incoherent Scatter Radar Exosphere (NRLMSIS-00) atmospheric model, solar radiation pressure, third-body effects from the Moon and the Sun, and gravity gradient. The equations of motions are integrated using a fourth-order Runge-Kutta method with a fixed time step of one second. In the simulator, modifications of the translational motion are obtained by commanding the propulsion system to apply a specific force. In order to convert the commanded delta-V computed using the control algorithm into a force, the assumption that the force is delivered over one second is made. Hence, the commanded force is

$$\boldsymbol{F}_c = m\boldsymbol{a} = m\frac{\Delta \boldsymbol{V}_c}{\Delta t} = m\Delta \boldsymbol{V}_c \tag{3.1}$$

Using the rocket equation, the mass of the spacecraft after the maneuver is

$$m_f = m_0 \exp\left(-\frac{F_a}{m_0 I_{sp} g_0}\right) \tag{3.2}$$

where m_0 is the mass before the maneuver, F_a the amplitude of the actual force that is applied (i.e. the commanded force with the addition of errors), I_{sp} the specific impulse, and g_0 the gravitational constant. In order to increase the fidelity of the simulations, uncertainties in the relative state knowledge as well as thrust errors have been added to the model.

3.1.1 Relative State Estimation Uncertainties

Ferguson et al. [97] have studied the relative state estimation for the Orion-Emerald mission, a three-spacecraft formation flying mission originally planned in the early 2000s but later cancelled. The method is based on carrier-phase differential GPS which provides a direct measure of the relative states between the agents of the formation, and has been tested on the Formation Flying Testbed at NASA Goddard Space Flight Center. For a close range formation, the method achieves an accuracy of about 2 cm for the relative position determination and less than 0.5 mm/s for the relative velocity. The mean values and standard deviations for the position and velocity in the radial, along-track, and cross-track directions for a purely in-plane formation with a 1 km baseline is shown in Table 3.1.

Table 3.1: Relative state estimation accuracy for an in-plane formation with a 1 km baseline [97].

	Position (cm)		Velocity (mm/s)	
	Mean	Std	Mean	Std
Radial	0.25	0.45	0.032	0.156
Along-track	1.06	0.66	0.001	0.275
Cross-track	0.16	0.29	0.017	0.107

Similarly for an out-plane elliptic formation with a 1 km baseline, the maximum mean and standard deviation along the three directions is shown in Table 3.2. Based

Table 3.2: Relative state estimation accuracy for an out-plane formation with a 1 km baseline [97].

	Position (cm)		Velocity (mm/s)	
	Mean	Std	Mean	Std
Out-plane	1.03	0.54	0.04	0.34

on these results, the state estimation used to compute the maneuvers in the formation establishments presented in Section 3.2 assumes an accuracy characterized by the means and standard deviations shown in Table 3.3. The same values are used for the three dimensions.

Table 3.3: Relative state estimation accuracy used for the numerical simulations.

Position (cm)		Velocity (mm/s)	
Mean	Std	Mean	Std
1.1	0.7	0.04	0.4

3.1.2 Thrust Errors

The desired delta-V computed by the control algorithm described in Section 2.3.3 results, if applied with no perturbation, in the spacecraft moving to the next reference waypoint. When commanding an impulsive maneuver, however, the actual delta-V delivered by the thrusters will slightly differ from the commanded one due to errors in magnitude and direction coming from misalignment, time to ramp up and down, timing offsets, etc, therefore adding uncertainties to the model. This thrust error can be mitigated by using a method introduced by Chioma and Titus [98] to command a delta-V which is slightly different than the desired one. A summary of their analysis is provided hereafter.

The analysis of the thrust errors is computed in a reference frame where one of the axes is aligned with the commanded impulse. The V-frame is defined with

$$\hat{\boldsymbol{x}}_V = \frac{\Delta \boldsymbol{V}_c}{\|\Delta \boldsymbol{V}_c\|} \tag{3.3}$$

$$\hat{\boldsymbol{y}}_V = \frac{\hat{\boldsymbol{x}}_V \times \hat{\boldsymbol{e}}_3}{\|\hat{\boldsymbol{x}}_V \times \hat{\boldsymbol{e}}_3\|} \tag{3.4}$$

$$\hat{\boldsymbol{z}}_V = \hat{\boldsymbol{x}}_V \times \hat{\boldsymbol{y}}_V \tag{3.5}$$

where $\hat{\boldsymbol{e}}_3 = [\, 0 \quad 0 \quad 1 \,]^T$. The axes $\hat{\boldsymbol{y}}_V$ and $\hat{\boldsymbol{z}}_V$ can be oriented arbitrarily as long as the triad forms an orthogonal reference frame. Fig. 3.1 illustrates the definition of the V-frame along with the actual and commanded delta-V's.

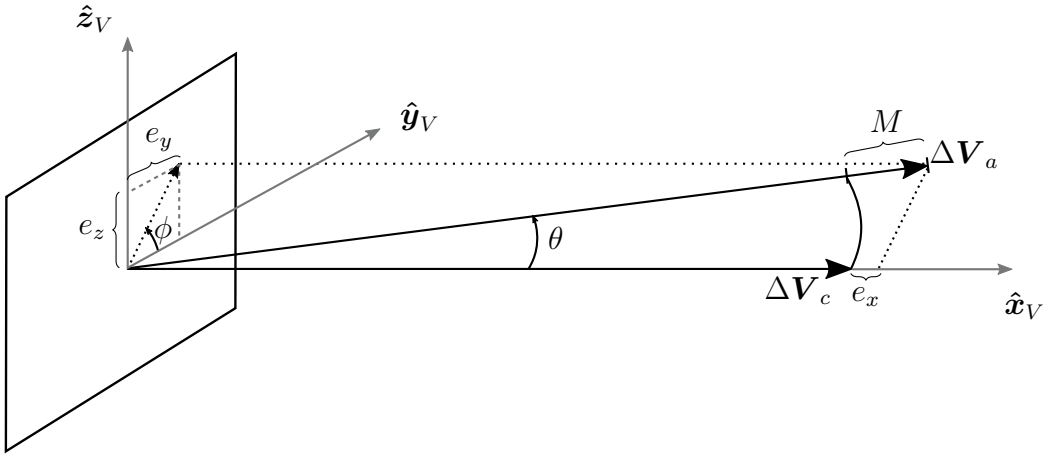

Figure 3.1: Definition of the V-frame. Reproduced from [98].

The maneuver's amplitude error is represented by M and the pointing error by the angles ϕ and θ. The projection of the actual delta-V on the V-frame is thus

$$\Delta \boldsymbol{V}_a = \begin{bmatrix} (\Delta V_c + M)\cos\theta \\ (\Delta V_c + M)\sin\theta\cos\phi \\ (\Delta V_c + M)\sin\theta\sin\phi \end{bmatrix} \tag{3.6}$$

with $\Delta V_c = \|\Delta \boldsymbol{V}_c\|$. It is now assumed that M follows a Gaussian distribution with mean $\mu_M = 0$ and standard deviation σ_M, ϕ a uniform distribution between 0 and

π, and θ a Gaussian distribution with mean $\mu_\theta = 0$ and standard deviation σ_θ. The corresponding probability density functions are

$$p_M(M) = \frac{1}{\sqrt{2\pi\sigma_M^2}} \exp\left(-\frac{M^2}{2\sigma_M^2}\right), \quad -\infty < M < \infty \tag{3.7}$$

$$p_\theta(\theta) = \frac{1}{\sqrt{2\pi\sigma_\theta^2}} \exp\left(-\frac{\theta^2}{2\sigma_\theta^2}\right), \quad -\infty < \theta < \infty \tag{3.8}$$

$$p_\phi(\phi) = \begin{cases} \frac{1}{\pi}, & 0 \leq \phi \leq \pi \\ 0, & \text{elsewhere} \end{cases} \tag{3.9}$$

Using these functions, the expected value of the actual delta-V, Eq. (3.6), can be computed [98]:

$$E\{\Delta \boldsymbol{V}_a\} = \begin{bmatrix} \Delta V_c \exp\left(-\frac{\sigma_\theta^2}{2}\right) \\ 0 \\ 0 \end{bmatrix} \tag{3.10}$$

Since the exponential term in the above equation is always smaller than one, this result shows that whenever a delta-V is commanded, the actual impulse provided by the thrusters tends to undershoot the commanded value. Hence, if the desired delta-V is

$$\Delta \boldsymbol{V}_d = \begin{bmatrix} \Delta V_d \\ 0 \\ 0 \end{bmatrix} \tag{3.11}$$

a slightly larger burn of

$$\Delta \boldsymbol{V}_c = \begin{bmatrix} \Delta V_d \exp\left(\frac{\sigma_\theta^2}{2}\right) \\ 0 \\ 0 \end{bmatrix} \tag{3.12}$$

should be commanded such that the expected value of the actual delta-V delivered by the thrusters corresponds to the desired amplitude:

$$E\{\Delta \boldsymbol{V}_a\} = \begin{bmatrix} \Delta V_d \\ 0 \\ 0 \end{bmatrix} \tag{3.13}$$

In the simulations presented in this chapter, the desired delta-V is determined using Eq. (2.272) and the commanded burn is computed from Eq. (3.12). The actual delta-V used for the orbital propagation is obtained by adding random perturbations to the magnitude and direction of the commanded value, each perturbation being drawn from its respective distribution function (Eqs. (3.7)-(3.9)). Algorithm 4 details the computation process to get the commanded delta-V as well as the actual delta-V used for the simulations.

Algorithm 4: Commanded and actual delta-V's

Input : $\Delta \boldsymbol{V}_d$, σ_M, σ_θ
Output: $\Delta \boldsymbol{V}_c$, $\Delta \boldsymbol{V}_a$

`/* Compute the V-frame transformation matrix */`

$\hat{\boldsymbol{e}}_3 \longleftarrow \begin{bmatrix} 0 & 0 & 1 \end{bmatrix}^T$

$\hat{\boldsymbol{x}}_V \longleftarrow \Delta \boldsymbol{V}_d / \|\Delta \boldsymbol{V}_d\|$

$\hat{\boldsymbol{y}}_V \longleftarrow (\hat{\boldsymbol{x}}_V \times \hat{\boldsymbol{e}}_3) / \|\hat{\boldsymbol{x}}_V \times \hat{\boldsymbol{e}}_3\|$

$\hat{\boldsymbol{z}}_V \longleftarrow \hat{\boldsymbol{x}}_V \times \hat{\boldsymbol{y}}_V$

$\mathbf{C} \longleftarrow \begin{bmatrix} | & | & | \\ \hat{\boldsymbol{x}}_V & \hat{\boldsymbol{y}}_V & \hat{\boldsymbol{z}}_V \\ | & | & | \end{bmatrix}$

`/* Generate random numbers */`

$M \longleftarrow \mathcal{N}(0, \sigma_M)$

$\theta \longleftarrow \mathcal{N}(0, \sigma_\theta)$

$\phi \longleftarrow \mathcal{U}(0, \pi)$

`/* Compute outputs */`

$\Delta \boldsymbol{V}_c \longleftarrow \mathbf{C} \begin{bmatrix} \|\Delta \boldsymbol{V}_d\| \exp(\sigma_\theta^2/2) & 0 & 0 \end{bmatrix}^T$

$\Delta \boldsymbol{V}_a \longleftarrow \mathbf{C}\mathbf{R}_1(\phi)\mathbf{R}_3(\theta) \begin{bmatrix} \|\Delta \boldsymbol{V}_c\| + M & 0 & 0 \end{bmatrix}^T$

In the scenarios presented in Section 3.2, the standard deviation of the amplitude errors is set to $\sigma_M = 1$ mm/s and the pointing error to $\sigma_\phi = 2$ deg.

The relative state knowledge uncertainties and the thrusting errors introduced in this section impact the accuracy with which formations can be established. In the following section, the accuracy is assessed for different magnitudes of these uncertainties as well as the different parameters of the control algorithm.

3.1.3 Formation Establishment Accuracy

The accuracy of formation establishment depends on many factors. Orbital perturbations, time interval between two waypoints, bounds on the maneuvers' amplitude, relative state knowledge uncertainties, and thrust errors all influence how close a spacecraft can track the reference trajectory. In order to assess the accuracy with which a formation can be established and maintained, the distance between the true position and the target position is computed:

$$err(t) = \|\boldsymbol{r}^{\text{LVLH}}(t) - \boldsymbol{r}_t^{\text{LVLH}}(t)\| \tag{3.14}$$

where the true position $\boldsymbol{r}^{\text{LVLH}}$ is the difference between the inertial state of the chief and the inertial state of the deputy obtained via numerical propagation and transformed into the LVLH frame, and the target position $\boldsymbol{r}_t^{\text{LVLH}}$ is obtained by converting the set of target ROEs into LVLH Cartesian coordinates:

$$\boldsymbol{\rho}_t(t) = \begin{bmatrix} x_{rt} & y_{rt} & a_{rt} & E'_{r0} + \Delta E_{rt} + nt & A_{zt} & \gamma_t \end{bmatrix}^T \rightarrow \boldsymbol{r}_t^{\text{LVLH}}(t) \tag{3.15}$$

For this analysis, the target relative orbit is a 50 m radius CRO centered on the chief and the deputy targets an angular separation $\Delta E_{rt} = -50°$ with respect to a virtual leader with $E'_{r0} = 0°$. The set of ROEs describing this relative orbit is

$$\boldsymbol{\rho}_t(0) = \begin{bmatrix} 0 \text{ m} & 0 \text{ m} & 50 \text{ m} & -50° & 43.3 \text{ m} & -90° \end{bmatrix}^T$$

The physical properties of the spacecraft are the same as in Section 2.4.2 and are described in Table 2.8. The initial conditions of the chief in terms of classical orbital elements are

$$a = R_\oplus + 500 \text{ km} \qquad e = 0 \qquad i = 30^\circ \qquad \Omega = 0^\circ \qquad \omega = 0^\circ \qquad M = 0^\circ$$

and the deputy's initial conditions are

$$\boldsymbol{\rho}_0 = \begin{bmatrix} -100 \text{ m} & -500 \text{ m} & 1400 \text{ m} & -20^\circ & 200 \text{ m} & 130^\circ \end{bmatrix}^T$$

The trajectory followed by the deputy is shown in Fig. 3.2 for a duration of 12 hours.

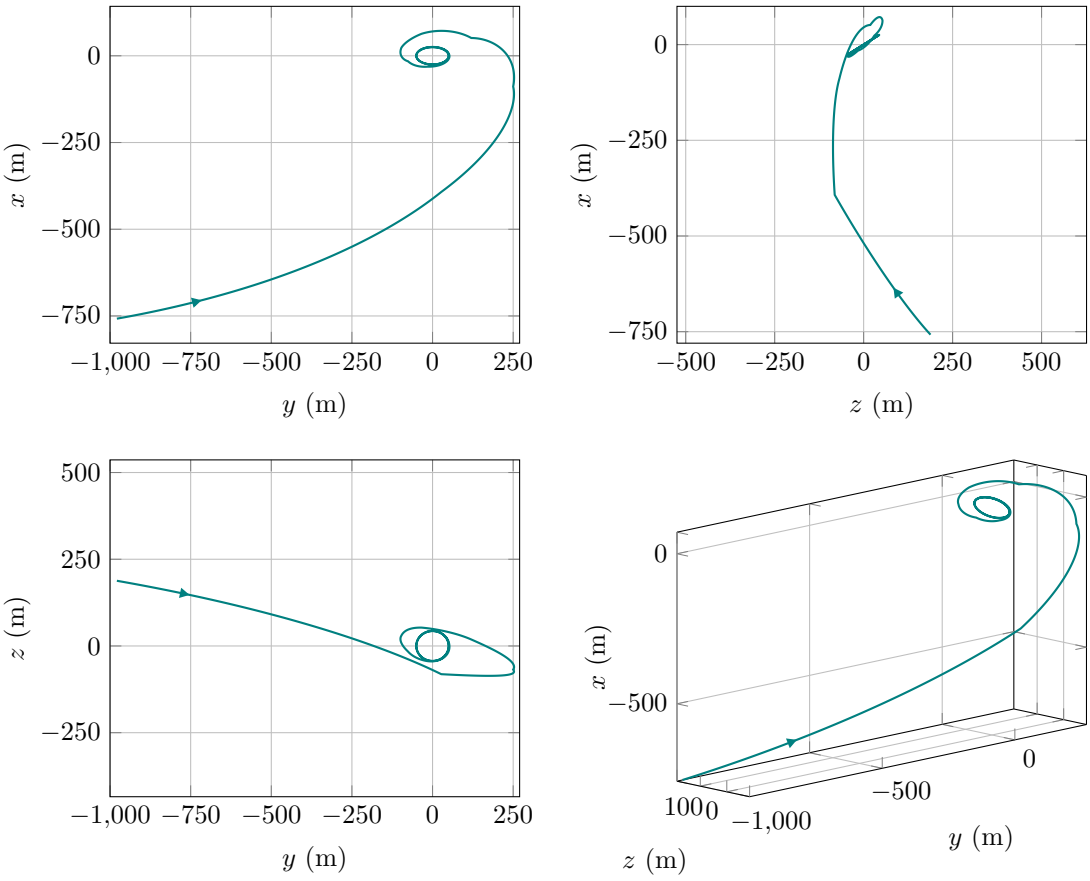

Figure 3.2: Relative trajectory followed by the deputy.

The effect of the orbital perturbation on the accuracy of the formation establishment is first analyzed. For this case, it is assumed that the maneuvers are unbounded, the spacecraft has perfect knowledge of its relative state, and no thrust errors occur. The time interval between two maneuvers is set to 30 minutes. Fig. 3.3 shows the time evolution of the accuracy of the formation establishment when the different orbital perturbations act on the spacecraft. We see in Fig. 3.3 that the error between

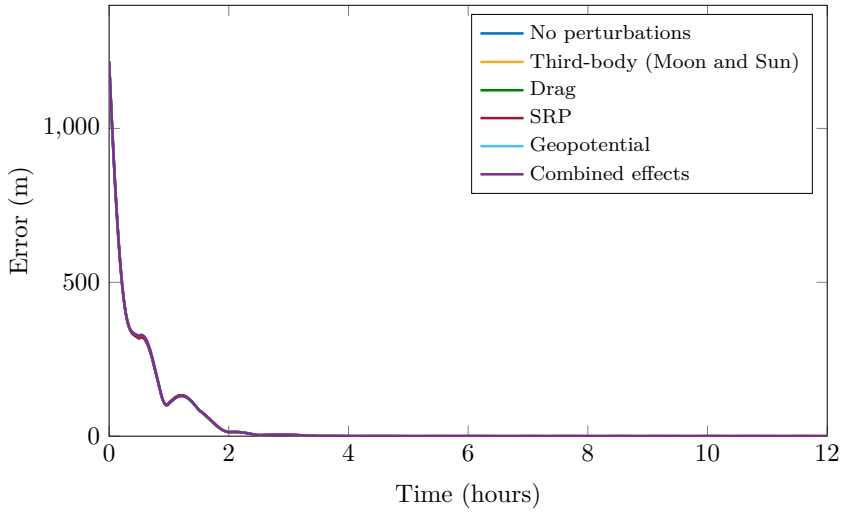

Figure 3.3: Accuracy of the formation establishment when different orbital perturbations act on the spacecraft.

the actual state and the target state quickly decreases during the first three hours of simulation, and the impact of the orbital perturbations is barely visible at that scale. A close up view of the accuracy between 4 and 12 hours is presented in Fig. 3.4.

As can be seen in Fig. 3.4, the dominant effect comes from the non-spherical geopotential with an error oscillating between about 10 and 70 centimeters. This result agrees with the significantly higher order of magnitude of the differential acceleration found in Section 2.4.1. The effect of the other perturbations is negligible since the resulting error is similar to the error without perturbations.

The accuracy for different time intervals between the maneuvers, T_m, is considered next. The same assumptions as before are made and the trajectories are propagated using the fully perturbed model. Fig. 3.5 shows the time evolution of the error for

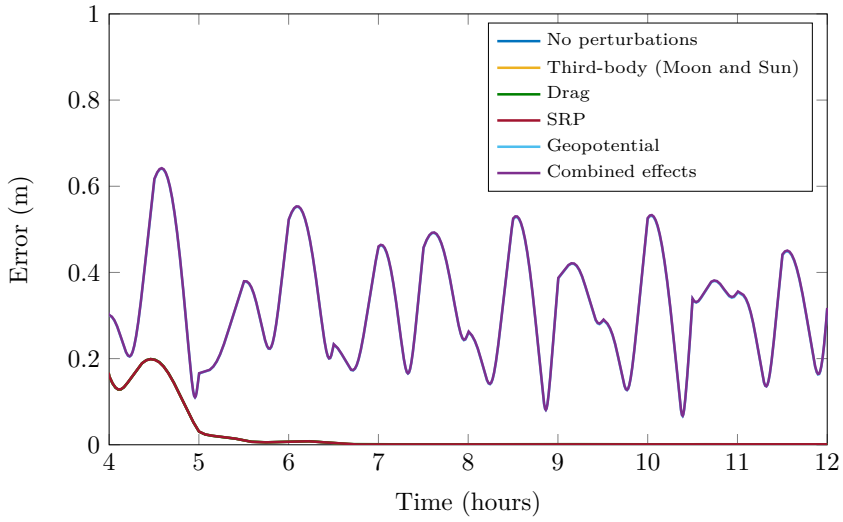

Figure 3.4: Zoom on the accuracy of the formation establishment when different orbital perturbations act on the spacecraft.

different T_m. At the beginning of the simulation, the spacecraft moves toward the

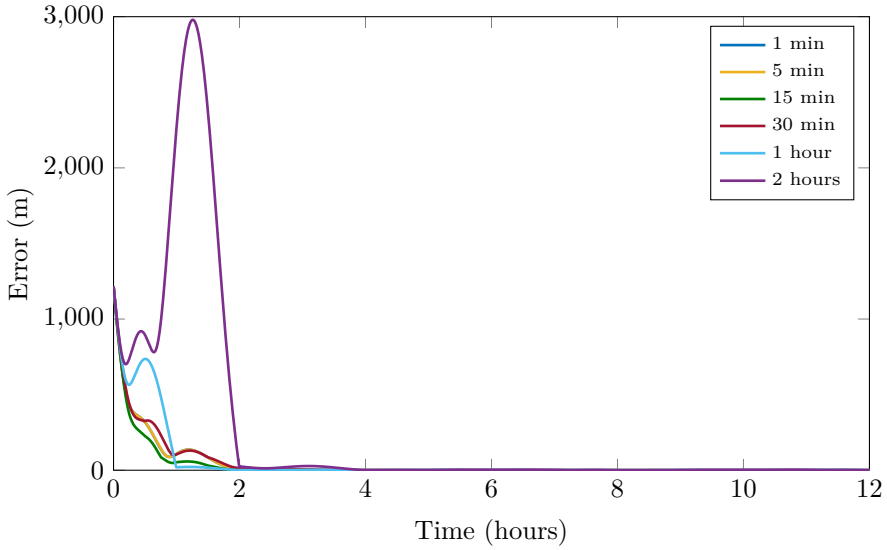

Figure 3.5: Accuracy of the formation establishment for different time intervals between the attractive maneuvers.

target orbit thus reducing the error. We see that for the two largest time intervals, the error grows considerably during the coast between two maneuvers. After two hours,

however, the error has significantly decreased but still fluctuates before stabilizing around 4 hours. Looking at Fig. 3.6, we see that the accuracy with which the deputy is able to track the reference varies with T_m. Even with a relatively long time interval of two hours, the error lies within 20 cm to 3.8 m. A sub-meter accuracy is reached for intervals of 30 minutes and shorter. For $T_m = 5$ minutes, the deputy stays within 10 cm of the target and this value falls below the centimeter mark for $T_m = 1$ minute.

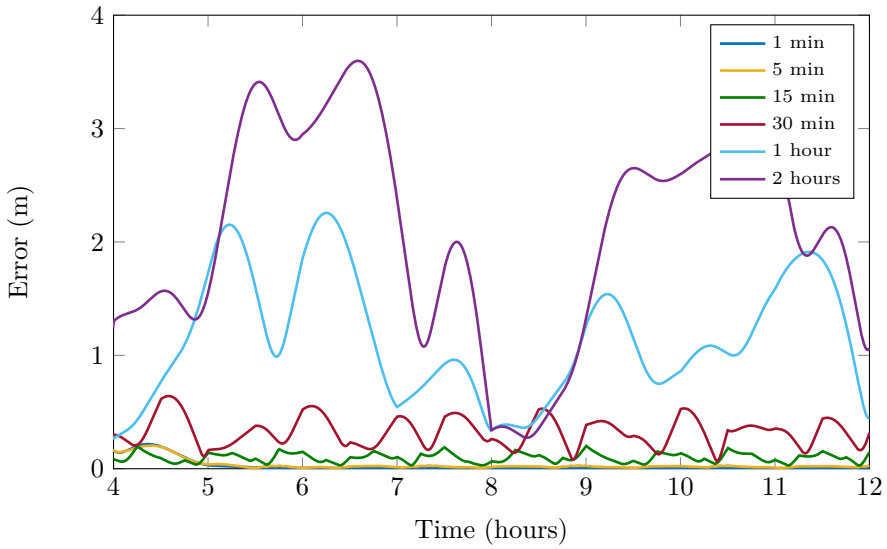

Figure 3.6: Zoom on the accuracy of the formation establishment for different time intervals T_m.

The influence of the lower bound on the maneuvers' amplitude is now studied. For this case, perfect knowledge of the relative state is assumed with no thrust errors and $T_m = 30$ minutes. We see in Fig. 3.7 that at the beginning of the simulation, the error is similar for all bounds. Since the spacecraft is quite far from the target, larger maneuvers are required which are not impacted by the lower bound. When the spacecraft is closer to the targeted CRO, smaller maneuvers are commanded to finely adjust its relative position and the lower bound on the magnitude prevents some maneuvers to be executed. A closer look at the error between 4 and 12 hours reveals that this parameter has a significant impact on the accuracy that can be reached,

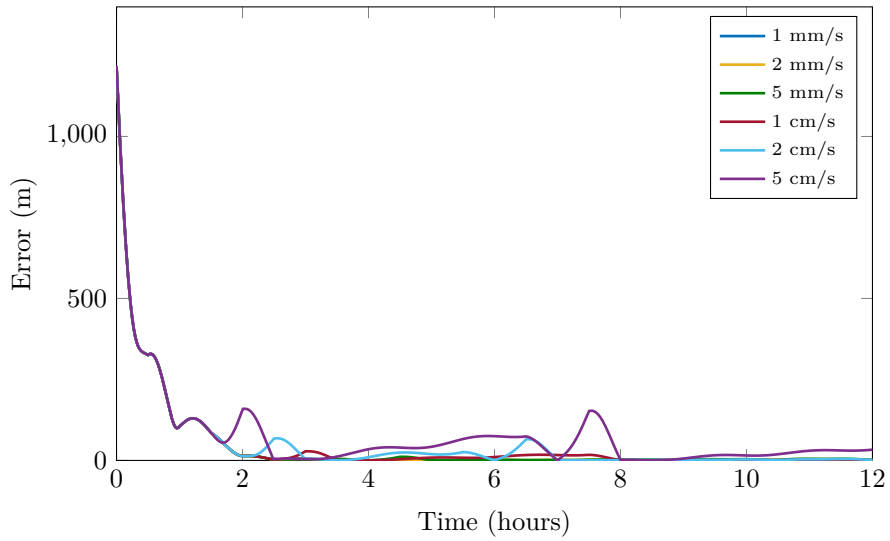

Figure 3.7: Accuracy of the formation establishment for different lower bounds on the maneuvers' amplitude.

Fig. 3.8. As can be seen in this figure, the error for $\Delta V_{min} = 2$ cm/s and $\Delta V_{max} = 5$ cm/s is very large and goes as high as 150 m. In Fig. 3.9, the two largest ΔV_{max} have been removed for a better view of the smallest bounds. We see in both Fig. 3.8 and 3.9 how the error builds up before the maneuver required to reduce it becomes larger than the lower bound and is thus applied.

The analysis of the effect of relative state knowledge on the accuracy is conducted by assuming that the relative velocity is known exactly and varying the mean μ of the relative position. The standard deviation of the uncertainties on the position is set to $\sigma = 0.7$ cm. We see in Fig. 3.10 that when the uncertainties have a large mean value of 1 m, the error oscillates between 5 and 8 meters. It is slightly lower for $\mu = 50$ cm and oscillates around 3 meters. For smaller μ values, the error between the actual position and the target position falls within one meter.

If perfect knowledge of the relative position is now assumed and the mean of the uncertainties on the relative velocity is varied, the error evolves as shown in Fig. 3.11. The standard deviation of the relative velocity has been set to $\sigma = 0.4$ mm/s. The violet line reveals that a mean uncertainty of 5 mm/s leads to an error of the relative

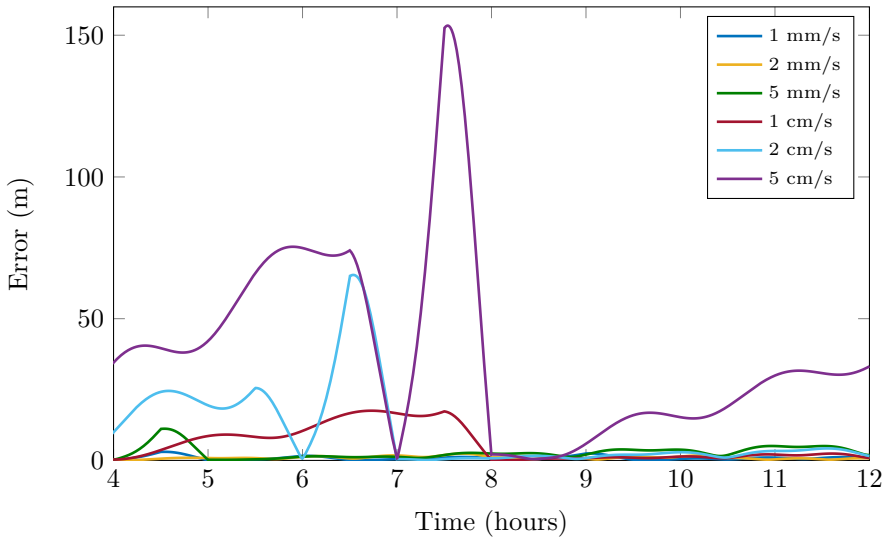

Figure 3.8: Zoom on the accuracy of the formation establishment for different lower bounds on the maneuvers' amplitude.

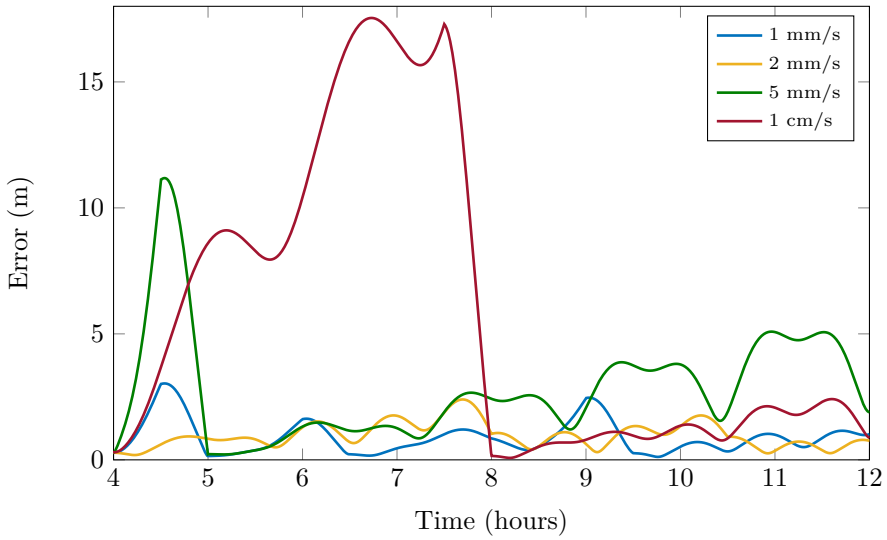

Figure 3.9: Accuracy of the formation establishment after four hours of simulation for a selection of ΔV_{min} values.

position with respect to the target between 20 and 30 meters. If the relative velocity is known with greater accuracy, the error falls within 10 meters. It oscillates around 6 meters for $\mu = 1$ mm/s and becomes as low as about 2 meters for 0.05 and 0.01

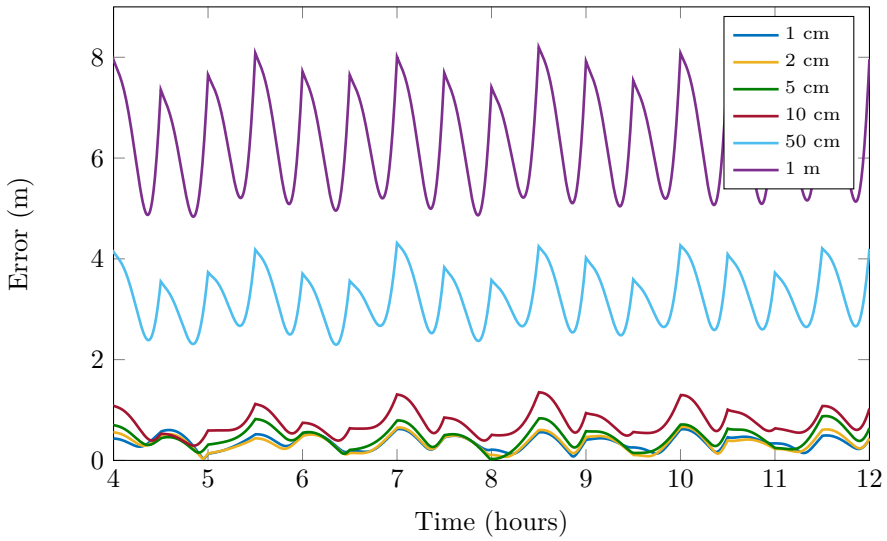

Figure 3.10: Accuracy of the formation establishment after four hours of simulation for different values of the mean error on the relative position determination.

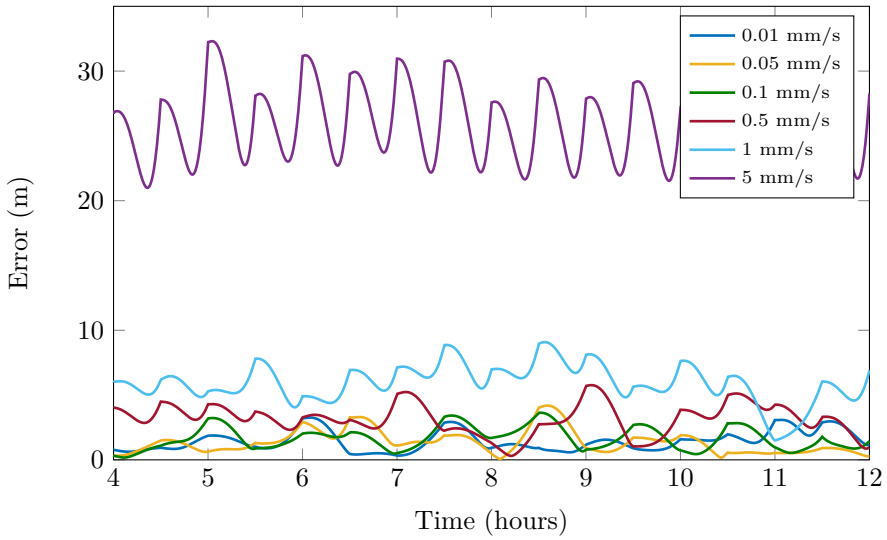

Figure 3.11: Accuracy of the formation establishment after four hours of simulation for different values of the mean error on the relative velocity determination.

mm/s. These results indicate that a precise determination of the relative velocity is required to get a low error.

Finally, a study of the effect of thrust errors on the formation establishment accuracy is presented. For this analysis, perfect knowledge of the relative state and

unbounded maneuvers amplitude are assumed. The effect of the magnitude error is first assessed in Fig. 3.12 for zero pointing error. As can be seen in that figure,

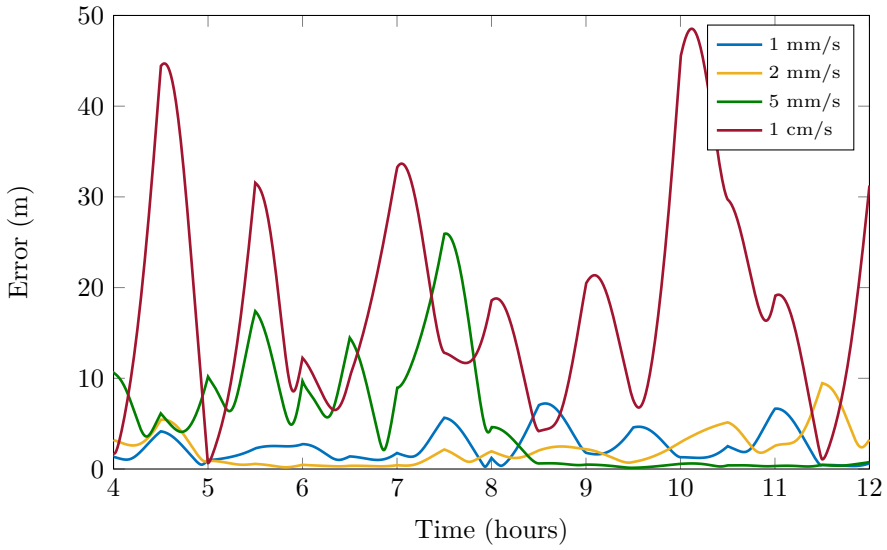

Figure 3.12: Accuracy of the formation establishment after four hours of simulation for different values of the standard deviation of the maneuvers amplitude errors.

a standard deviation of 1 cm/s for the error on the amplitude results in a tracking error that goes as high as 50 meters. If that standard deviation is reduced by half, the error falls to within 30 meters. For a propulsion system capable of delivering a delta-V with a standard deviation of 1 or 2 mm/s, the spacecraft is able to stay within 10 meters of the target. The effect of the pointing error is shown in Fig. 3.13. Interestingly, the formation establishment accuracy is not very sensitive to the thrust pointing errors. The error stays below two meters when a standard deviation of 10 degrees is considered and falls below one meter for smaller standard deviations. This indicates that even when a relatively large pointing error is present, a good targeting accuracy can be achieved.

This concludes the analysis of the formation accuracy for different perturbations, uncertainties and errors introduced in the model. Based on these results, the propulsion system plays an important role in the accuracy that can be reached especially with the smallest delta-V that can be delivered and the error on the maneuvers' am-

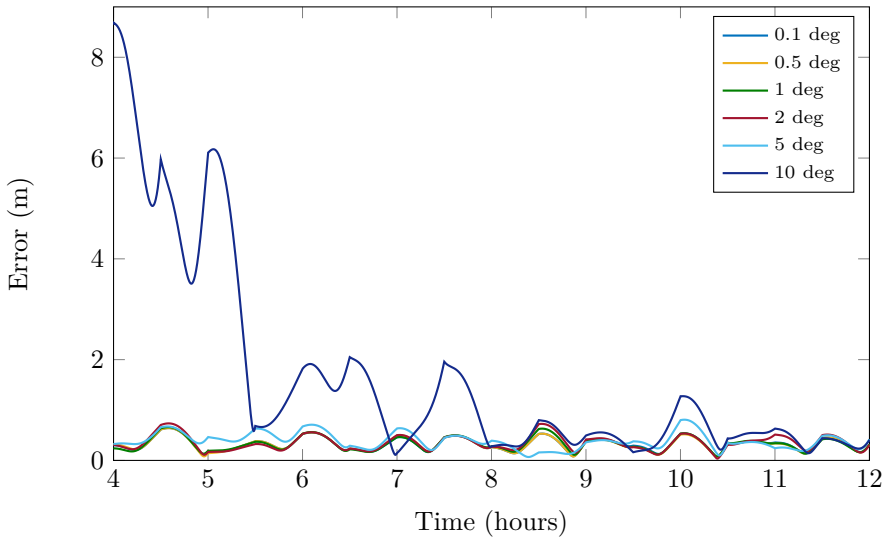

Figure 3.13: Accuracy of the formation establishment after four hours of simulation for different values of the standard deviation of the thrust pointing errors.

plitude. A proper selection of the parameters of the model results in an accuracy of a few meters for this specific set of chief's orbit, initial conditions, and target elements as shown in Fig. 3.14. This result was obtained with $T_m = 900$ s, $\Delta V_{min} = 2$ mm/s, $\sigma_M = 1$ mm/s, $\sigma_\theta = 2°$, and the state uncertainties of Table 3.3, and demonstrates that the algorithm is capable of accurately tracking the reference trajectory.

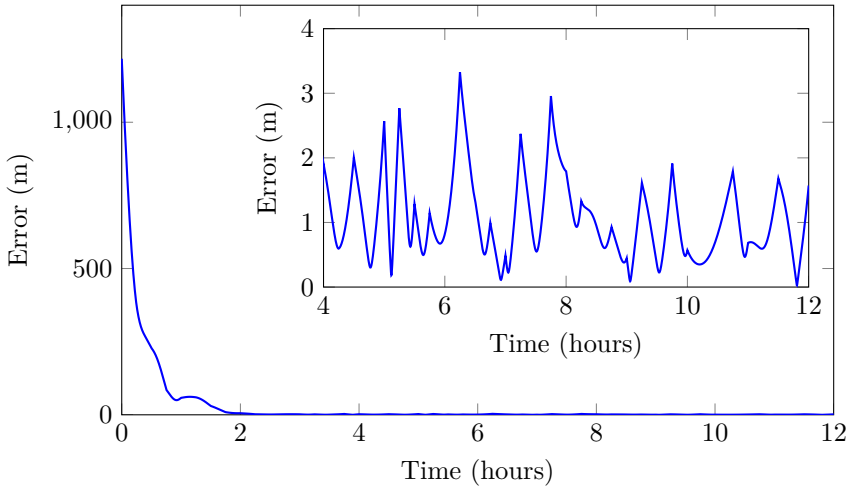

Figure 3.14: Accuracy of the reference tracking for a given set of parameters.

3.2 Scenarios

The establishment of four formations using the control algorithm introduced in this work is now presented. The first two formations contain a large number of agents and are designed using the ROEs. The third formation design illustrates the use of the GROEs for the visual inspection of an on-orbit structure, and in the last simulation, results of the establishment of a formation where one agent has a fixed position in the cross-track plane are presented.

3.2.1 Triangular Lattice

In this first scenario, the establishment of a 10-spacecraft triangular lattice is considered. This formation is characterized by two concentric CROs containing six and three spacecraft respectively and one spacecraft positioned at the origin of the LVLH frame. The radius of the inner CRO defines the inter-spacecraft distance and is the only design parameter of the formation. Fig. 3.15 illustrates the desired formation geometry.

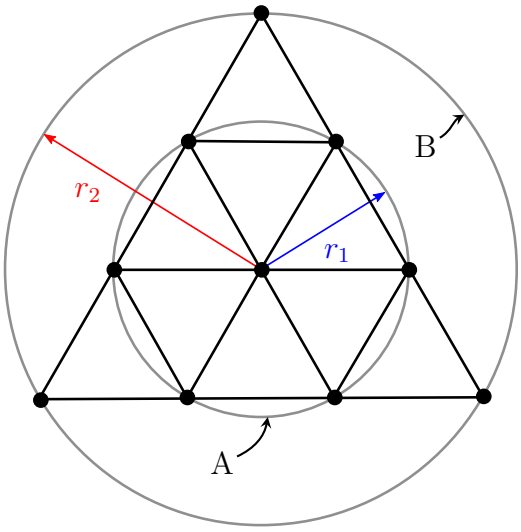

Figure 3.15: Triangular lattice geometry.

If the radius of the inner orbit A is r_1, then in order to have a similar distance between every adjacent spacecraft, the radius of the outer orbit B must be

$$r_2 = \sqrt{3} r_1 \tag{3.16}$$

For this simulation, a radius $r_1 = 100$ m has been chosen, leading to the following sets of ROEs:

Table 3.4: Target ROEs for the triangular lattice.

Orbit	x_r (m)	y_r (m)	a_r (m)	A_z (m)	γ (°)
Origin	0	0	0	0	n/a
A	0	0	100	86.6	-90
B	0	0	173.21	150	-90

The phase angle γ has been arbitrarily set to $-90°$ but could have been set to $90°$ as well. The angular separation between the agents is enforced by targeting relative eccentric anomaly differences with respect to a virtual leader. For orbit A, each spacecraft targets a separation which is a multiple of $60°$ with respect to a virtual leader characterized by an initial relative eccentric anomaly $E'_{r0} = 0°$. For orbit B, a multiple of $120°$ is targeted by each agent with respect to a leader initially located at $E'_{r0} = 30°$.

The spacecraft are assumed to be released along a hypothetical launch trajectory passing in the vicinity of the origin of a chief on a 500 km altitude circular orbit with a $30°$ inclination. The initial position of the agents has been randomly generated within a spheroid centered on $x = -100$ m, $y = 800$ m, and $z = -300$ m. The ellipsoid of revolution is oriented such that its major axis is aligned with the launch trajectory and has a length of 200 meters. The minor axis has a length of 60 meters. The initial velocities have been drawn from a Gaussian distribution with mean 5 cm/s and standard deviation 0.2 cm/s in the direction along the trajectory and mean 2 cm/s and standard deviation 0.5 cm/s in the direction orthogonal to the launch

trajectory. The initial positions of the spacecraft are generated such that the agents are guaranteed to be at least 20 meters apart. The initial conditions of each agent are listed in Table A.1 in the appendix and illustrated in Fig. 3.16.

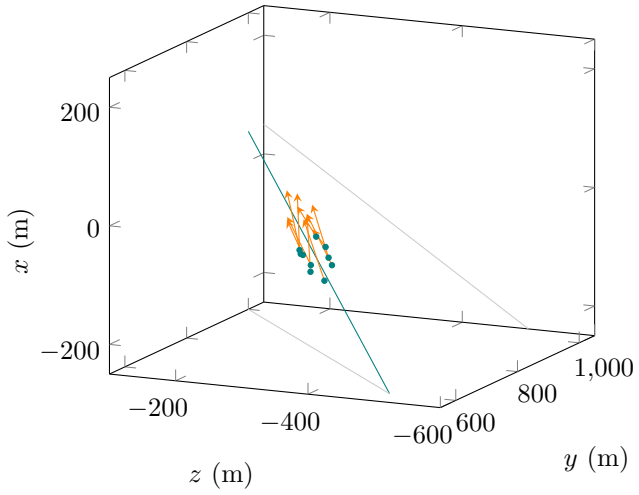

Figure 3.16: Initial conditions for the triangular lattice geometry along with the launch trajectory. Velocities are not to scale.

The controller is designed with the parameters shown in Table 3.5. The time

Table 3.5: Parameters of the controller for the establishment of the triangular lattice.

$T_m = 15$ min
$\tau_c = 4$ h
$d_c = 5$ m
$T_c = 5$ s
$r_s = 0.35$ m
$r_{\text{SOI}} = 20$ m
$p = 0.01$
$\upsilon = 3$

interval between two maneuvers is 15 minutes and has been chosen based on the accuracy analysis of Section 3.1.3. The autonomous computation of k_a assumes a convergence time of four hours and convergence threshold of five meters. Collision checks are preformed every five seconds and the obstacles are assumed to fit within a

sphere of radius 0.35 m. The sphere of influence around the obstacle has a radius of twenty meters and the value of the potential on its surface is one percent the values at r_s. Lastly, the semi-major axis of the repulsive ellipsoid is three times as large as the semi-minor axis.

All spacecraft are assumed to be identical and are characterized by the physical properties printed in Table 3.6. For this scenario, the thrust is bounded between

Table 3.6: Spacecraft properties for the triangular lattice.

$m_{\text{wet}} = 30$ kg	$A = 0.16$ m^2
$C_d = 2.1$	$A_{\odot} = 0.16$ m^2
$C_r = 1.5$	$I_{sp} = 220$ s

$F_{max} = 60$ N and $F_{min} = 0.06$ N. From Eq. (3.1), these bounds correspond to $\Delta V_{max} = 2$ m/s and $\Delta V_{min} = 2$ mm/s at the beginning of the simulation. As propellant is used and the mass of the spacecraft decreases, ΔV_{max} and ΔV_{min} will slightly increase over time. The standard deviations of the magnitude and pointing errors are set to $\sigma_M = 0.06$ N and $\sigma_\theta = 2°$. The time evolution of the formation establishment is shown in Fig. 3.17 for five hours[1].

The spacecraft are released slightly ahead of the chief (Fig. 3.17a) and start moving in the positive x and negative y direction (Fig. 3.17b). They quickly converge toward the origin of the LVLH frame (Fig. 3.17c) and establish a loose formation (Fig. 3.17d and 3.17e). The precise positioning of each agent is attained within five hours of deployment (Fig. 3.17f).

The delta-V used by each spacecraft is printed in Table 3.7. With a minimum of 1.58 m/s for agent B1 and a maximum of 13.82 m/s for agent A1, we see that the delta-V needed by each spacecraft varies considerably if collision avoidance maneuvers are performed.

[1]An animation of the formation establishment is available at `https://purr.purdue.edu/publications/3389/1`.

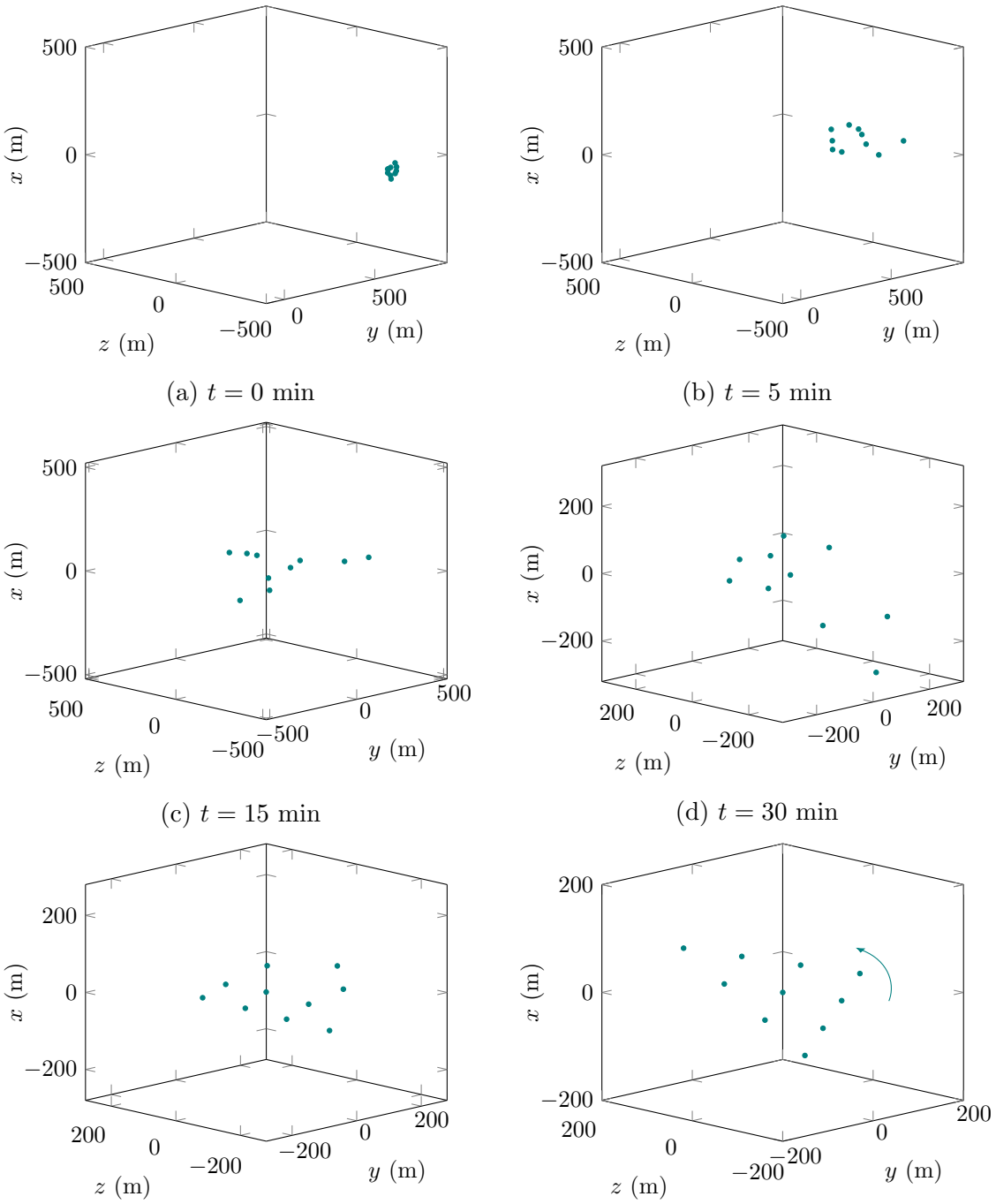

Figure 3.17: Formation establishment of the triangular lattice.

The time history of the maneuvers applied by spacecraft A6 is shown in Fig. 3.18. We see in that figure that most maneuvers are applied at the beginning of the simu-

Table 3.7: Delta-V consumption for the triangular lattice establishment.

Spacecraft	Delta-V (m/s)	Spacecraft	Delta-V (m/s)
Central	2.08	A5	9.09
A1	13.82	A6	11.34
A2	1.87	B1	1.58
A3	10.39	B2	6.19
A4	2.34	B3	8.37
Mean: 6.71 m/s		Std: 4.53 m/s	

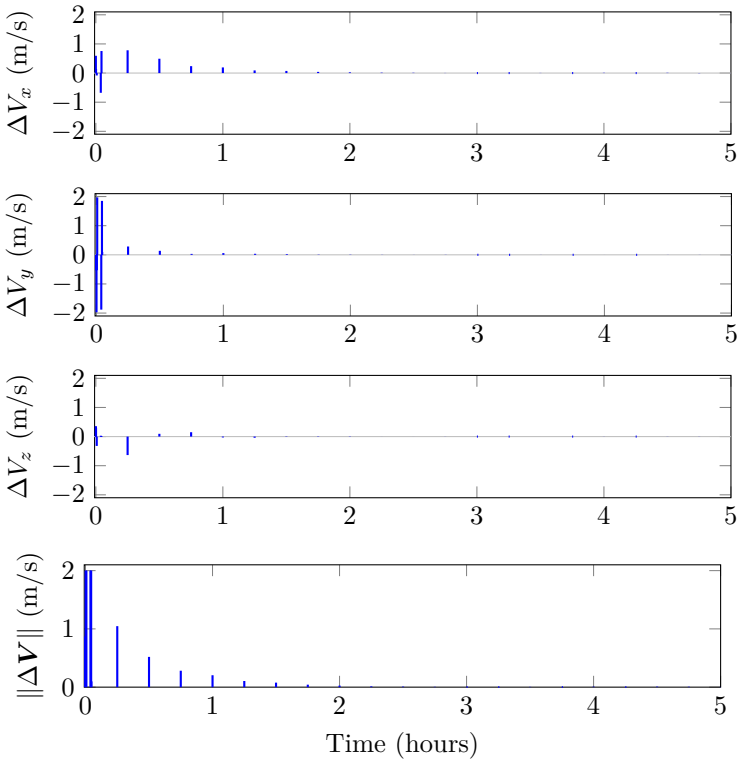

Figure 3.18: Delta-V history of spacecraft A6.

lation, suggesting that some CAMs occur during the first minutes after deployment. It can be seen from the last plot in this figure that the amplitude of the maneuvers decreases over time and becomes very small when the spacecraft has reached its target. A closer look (Fig. 3.19) reveals that maneuvers of a few centimeters per second

are applied in order to counter the perturbations and maintain the spacecraft on its relative orbit.

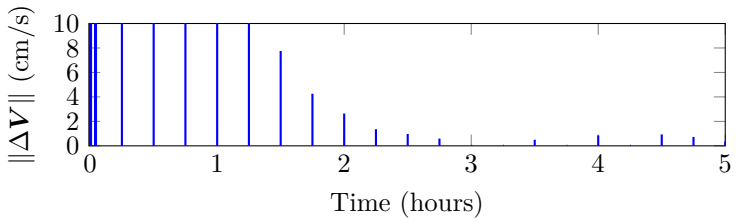

Figure 3.19: Zoom on the small maneuvers applied to maintain the spacecraft on its relative orbit.

Fig. 3.20 shows the positions and trajectories of the spacecraft 30 minutes after deployment, along with some collision avoidance maneuvers (red boxes). The sharp

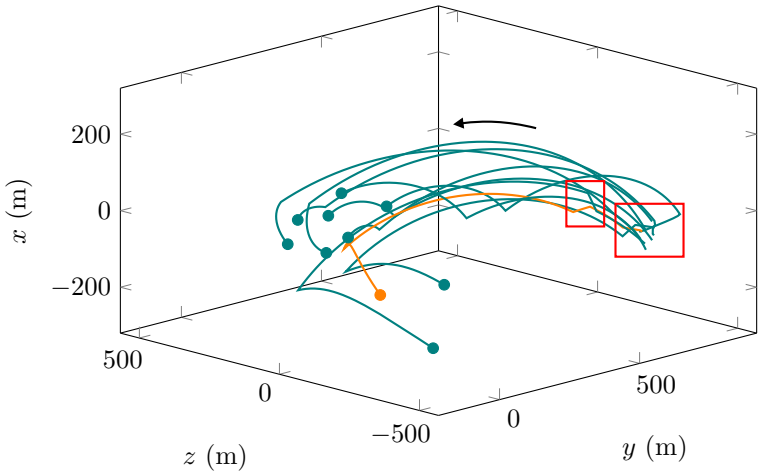

Figure 3.20: Positions, trajectories, and collision avoidance maneuvers 30 minutes after deployment.

changes in trajectory visible in the right red box indicates that many CAMs occur at the beginning of the simulation as previously suggested by the delta-V history of spacecraft A6. At that time, the spacecraft are relatively close to each other. The first attractive maneuver that they perform is likely to make them enter the sphere of influence of another spacecraft which might trigger a CAM. The left box highlights another CAM that occurs between two spacecraft later in the simulation, when the

two agents are coasting toward the next attractive waypoint. At least two CAMs are performed by spacecraft A6 (orange trajectory), which explain the high delta-V that this agent requires to track its reference.

The minimum distance between each pair of spacecraft is displayed in Table 3.8.

Table 3.8: Minimum distance between each pair of spacecraft, in meters.

	Central	A1	A2	A3	A4	A5	A6	B1	B2
A1	34.93								
A2	47.55	46.7							
A3	30.57	14.18	27.14						
A4	28.19	26.57	75.59	39					
A5	24.96	23.85	36.5	17.52	47.21				
A6	36.13	15.9	61.63	42.01	26.49	35.74			
B1	89.46	59.86	29.61	51.81	97.14	45.48	72.21		
B2	67.83	31.88	29.41	39.72	73.72	12.28	38.93	32.22	
B3	60.1	24.69	44.57	34.69	51.79	34.51	20	49.41	38.49

As can be seen in that table, a minimum distance of 12.28 m is reached between spacecraft A5 and B2. In order to increase this distance, a larger sphere of influence could be set or the repulsive potential could be tuned by modifying the p coefficient which influences the magnitude of the repulsive potential at r_{SOI}. The computation of the collision avoidance by each agent is performed using state estimates and the uncertainties that come with these estimates should be kept in mind when designing the repulsive potential.

The time evolution of the ROEs of spacecraft A6 is shown in Fig. 3.21. The ROEs move quickly toward the target value at the beginning of the simulation and then slowly adjust to closely align with the desired value. The CAM that occurs shortly after deployment is also visible with jitters occurring for each element.

The oscillations of the relative eccentric anomaly that happen during the first hour of reconfiguration can be explained by looking at the position of the spacecraft with respect to the instantaneous center of motion. Fig. 3.22 shows the time evolution of

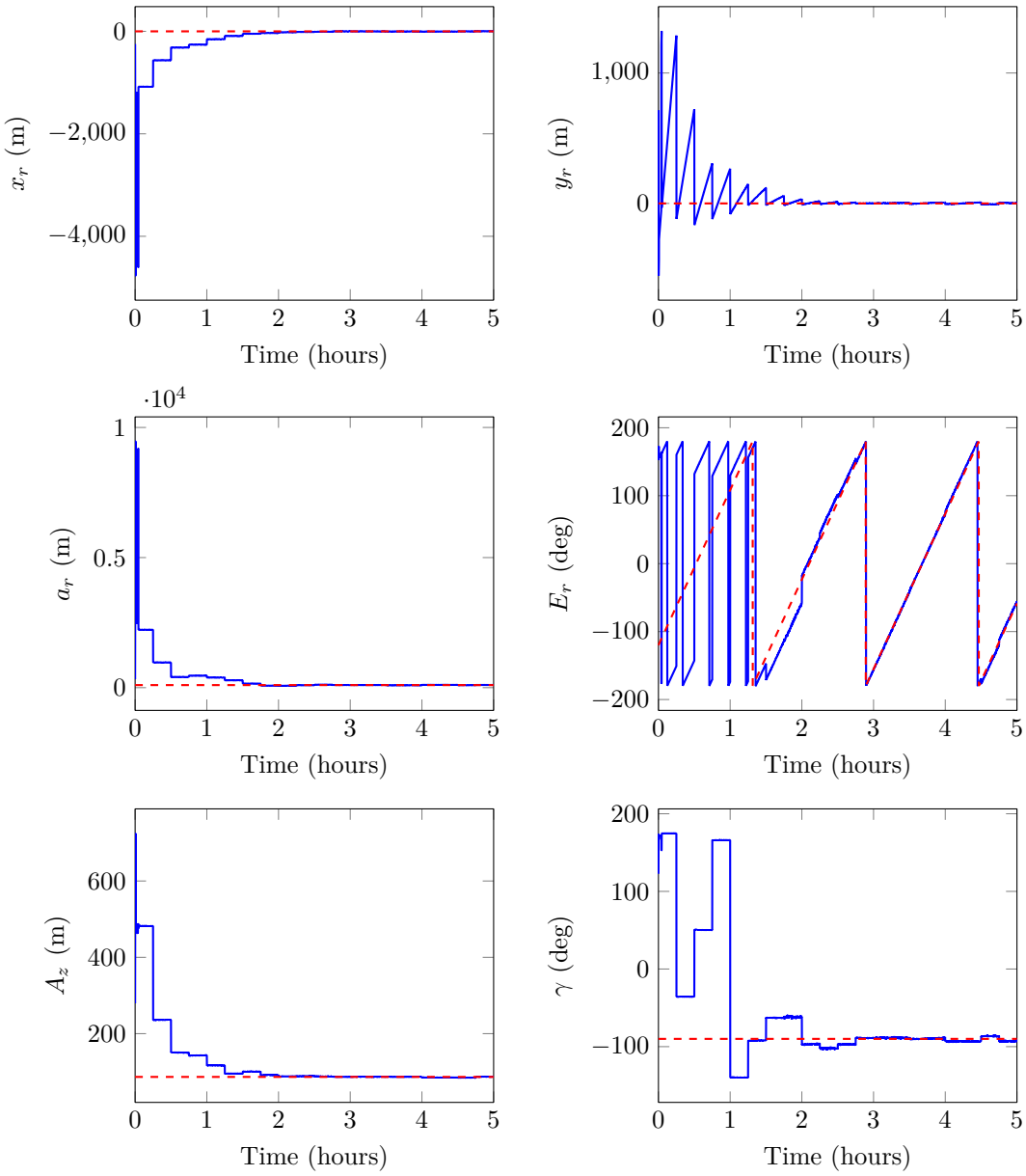

Figure 3.21: Time evolution of the relative orbital elements of spacecraft A6 together with the target values (red, dashed).

the in-plane position of the spacecraft and the position of the instantaneous center of motion (x_r, y_r). During the initial phase of the reconfiguration, the radial component of the spacecraft, x, is higher than the x_r component of the instantaneous center of motion while the along-track component y and y_r are very close. This results in

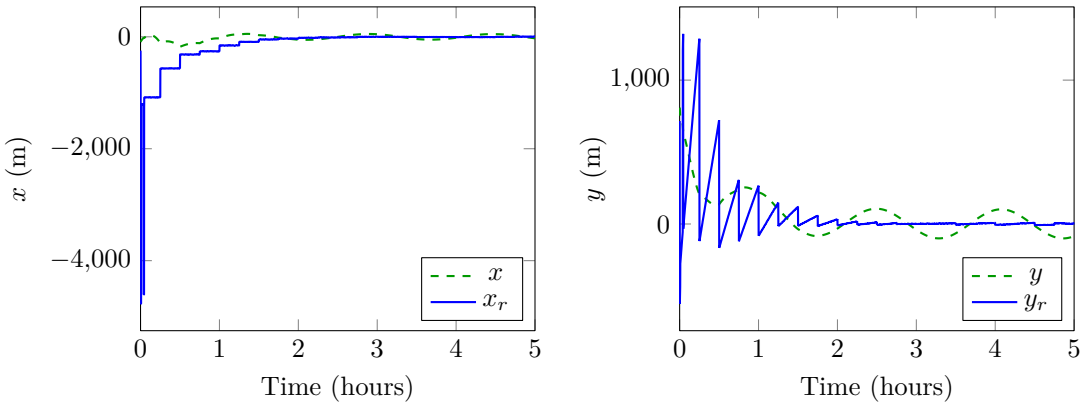

Figure 3.22: Time evolution of the in-plane position of spacecraft A6 and the position of the instantaneous center of motion.

the spacecraft being located directly above the instantaneous center of motion which leads to a relative eccentric anomaly of about 180°. After about an hour, x_r is much closer to x and the targeting of E_r becomes more effective.

The accuracy of the formation establishment is computed and displayed in Fig. 3.23. The error between the true position and the target position rapidly decreases during the first two hours of reconfiguration and stabilizes between 0 and 5 meters. A better accuracy could be attained by having a smaller T_m, allowing lower minimal delta-V's, or increasing the precision of the relative state estimate and thrust vector.

The results obtained with the APF-based controller are now compared with the formation establishment using a model predictive control (MPC) method that tracks a reference trajectory $\boldsymbol{r}_{\text{ref}}$ while minimizing the fuel consumption. The cost function for the MPC accounts for the error between the actual state and the reference as well as the delta-V consumption and is defined as

$$\begin{aligned} J = &\sum_{\kappa=k}^{N-1} \left[(\boldsymbol{r}(\kappa) - \boldsymbol{r}_{\text{ref}}(\kappa))^T \mathbf{Q} (\boldsymbol{r}(\kappa) - \boldsymbol{r}_{\text{ref}}(\kappa)) + \boldsymbol{u}(\kappa)^T \mathbf{R} \boldsymbol{u}(\kappa) \right] \\ &+ (\boldsymbol{r}(N) - \boldsymbol{r}_{\text{ref}}(N))^T \mathbf{P} (\boldsymbol{r}(N) - \boldsymbol{r}_{\text{ref}}(N)) \end{aligned} \tag{3.17}$$

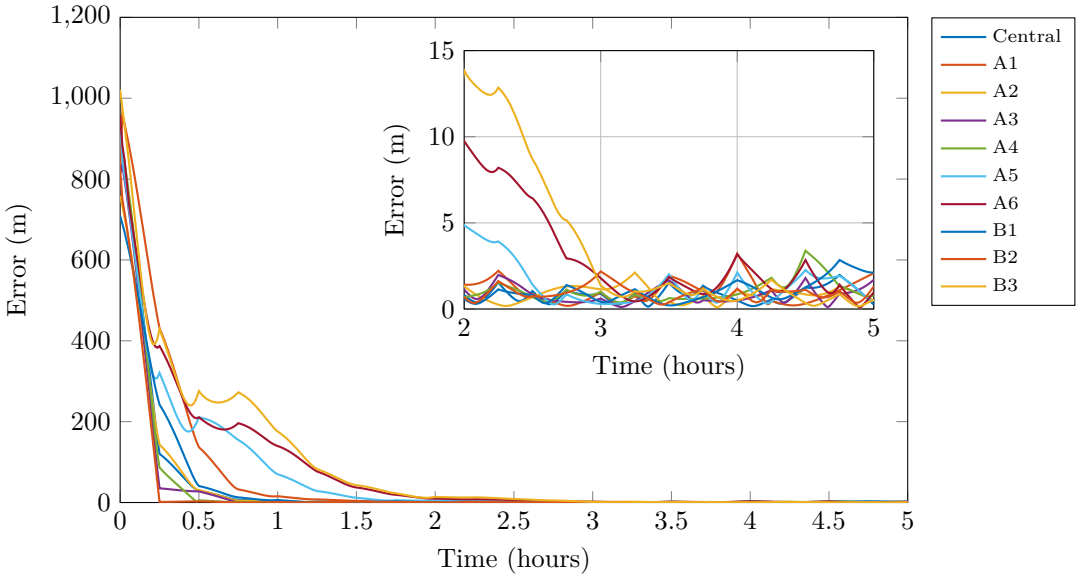

Figure 3.23: Accuracy of the triangular lattice formation establishment.

where k is the current time step and N is the horizon. Three weight matrices need to be defined: $\mathbf{Q}$ contains the weights which reflect the relative importance of closely following the reference, $\mathbf{R}$ the weights penalizing the use of large control inputs, and $\mathbf{P}$ the weight coefficients which reflect the relative importance of being close to the reference at the horizon. $\boldsymbol{r}(\kappa)$ is the relative state at step κ expressed in LVLH coordinates and the design variable $\boldsymbol{u}(\kappa)$ is the control input corresponding to an impulsive delta-V in this case. The reference trajectory is generated from the set of target ROEs. The relative eccentric anomaly targeted by each spacecraft is computed using Eq. (2.183):

$$E_{rt}(t) = \Delta E_{rt} + E_{r0}^{'} + n(t - t_0) \tag{3.18}$$

The set of target ROEs is then converted into the corresponding LVLH state using Eqs. (2.96)-(2.101). At each time step, the optimal control resulting from the minimization of the cost function, $\boldsymbol{u}^*$, is applied and the state is propagated using the fully perturbed, nonlinear model of the dynamics. The time interval between two

impulsive maneuvers is the same as before: $T_m = 15$ minutes. The parameters of the cost function have been set to

$$N = 10 \qquad \mathbf{Q} = 10^{-4} \cdot \mathbf{I}_6 \qquad \mathbf{R} = 10^{2} \cdot \mathbf{I}_6 \qquad \mathbf{P} = 10^{4} \cdot \mathbf{I}_6$$

where $\mathbf{I}_6$ denotes the 6-by-6 identity matrix. These parameters have been tuned to get a convergence time of the same order as the one obtained with the APF-based controller. The simulation was run with no collision avoidance and with the same bounds on the maneuvers' amplitude as previously (i.e. $\Delta V_{min} = 2$ mm/s, $\Delta V_{max} = 2$ m/s) which are enforced by setting the control input to:

$$\boldsymbol{u}^* = \begin{cases} \mathbf{0} & \text{if } \|\boldsymbol{u}^*\| < \Delta V_{min} \\ \boldsymbol{u}^* & \text{if } \Delta V_{min} \leq \|\boldsymbol{u}^*\| \leq \Delta V_{max} \\ \frac{\boldsymbol{u}^*}{\|\boldsymbol{u}^*\|}\Delta V_{max} & \text{if } \|\boldsymbol{u}^*\| > \Delta V_{max} \end{cases} \tag{3.19}$$

Choosing to enforce the bounds by clipping the control input rather than adding constraints to the optimization problem together with the utilization of a linearized model for the state propagation within the MPC enables the computation of an explicit solution without relying on iterative numerical methods (see for instance [99]). The total delta-V's used by each spacecraft to establish the triangular lattice using the MPC controller are displayed in Table 3.9. In comparison, Table 3.10 shows the total delta-V required when the APF-based controller is used without collision avoidance.

As can be seen from these Tables, the mean delta-V resulting from the use of the MPC controller is about 2.39 times smaller than the one obtained with the APF-based controller which highlights the sub-optimality of the APF controller. The computational efficiency of both methods has been measured on a 2.6 GHz 6-Core Intel Core i7 in Matlab. The elapsed real time needed to compute a single control input using the MPC controller is 0.91 ms whereas the time needed by the APF-based

Table 3.9: Delta-V consumption for the triangular lattice establishment using an MPC controller.

Spacecraft	Delta-V (m/s)	Spacecraft	Delta-V (m/s)
Central	0.99	A5	1.14
A1	0.99	A6	1.15
A2	0.90	B1	0.95
A3	0.93	B2	0.99
A4	1.06	B3	1.35
Mean: 1.05 m/s		Std: 0.14 m/s	

Table 3.10: Delta-V consumption for the triangular lattice establishment using the APF-based controller with no collision avoidance.

Spacecraft	Delta-V (m/s)	Spacecraft	Delta-V (m/s)
Central	2.15	A5	3.33
A1	1.78	A6	3.29
A2	1.88	B1	1.65
A3	2.20	B2	2.23
A4	2.42	B3	4.17
Mean: 2.51 m/s		Std: 0.82 m/s	

controller is 0.22 ms. Hence, the computation using the APF method is about 4.16 times faster than the computation using the MPC method. It must also be noted that when constraints such as collision avoidance are added to the MPC formulation, no explicit solution can be computed but instead the optimization problem must be solved using iterative methods which will result in a higher computation time. The inclusion of collision avoidance in the APF formulation through the addition of a repulsive portion to the potential, however, results in a very slight increase and yields an elapsed real time of 0.32 ms. We therefore see that the APF controller with collision avoidance is still about 3 times faster than the MPC controller without collision avoidance in this specific test case.

3.2.2 Hexagonal Lattices

The second scenario is the establishment of a 37-node formation composed of two hexagonal lattices on two different planes. Six concentric CROs need to be defined for this geometry, three per lattice. Fig. 3.24 illustrates the desired hexagonal pattern of one of the lattices along with the position of the agents. Six spacecraft are placed on the innermost orbit (A), six on the intermediate orbit (B), and six on the outermost orbit (C). Each agent has an angular separation of 60° with its neighbors on all three orbits. The spacecraft located at the center of the formation is "shared" between the two lattices.

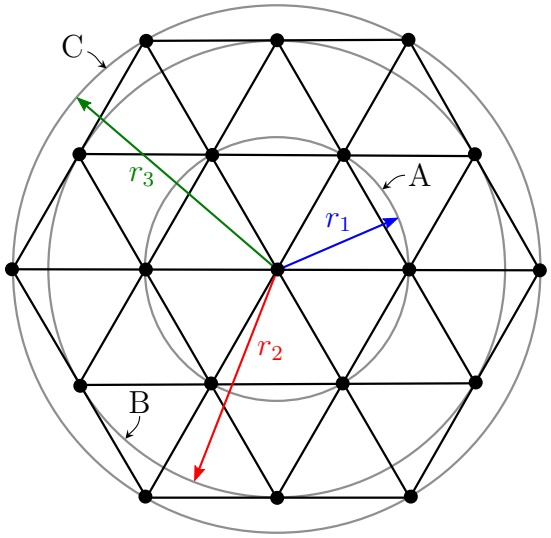

Figure 3.24: Hexagonal lattice geometry.

The only design parameter of this formation is the inter-spacecraft distance, which corresponds to the radius of the innermost CRO, r_1. An identical distance between each adjacent spacecraft is obtained by defining the radius of the intermediate orbit as

$$r_2 = \sqrt{3} r_1 \tag{3.20}$$

and the one of the outermost orbit as

$$r_3 = 2r_1 \tag{3.21}$$

Two such hexagonal lattices are constructed and oriented on two different planes such as to obtain the formation illustrated in Fig. 3.25. The formation is centered on the origin of the LVLH frame and the different orientations are obtained by defining different phase angles γ for each lattice. The first lattice, L_1, is characterized by $\gamma = 90°$, and the second one, L_2, by $\gamma = -90°$.

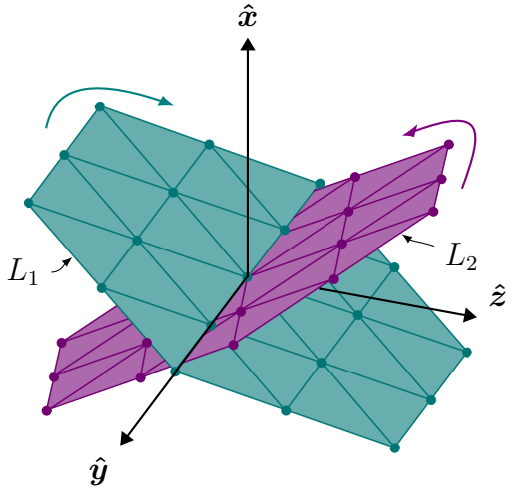

Figure 3.25: Formation composed of two hexagonal lattices.

The motion of the spacecraft on their respective relative orbit is imposed by orbital dynamics. A higher x coordinate means a higher altitude and therefore a lower orbital velocity in the along-track direction. The spacecraft with a positive x component will thus move in the negative y direction and vice versa for spacecraft at lower altitude.

In this scenario, an inter-spacecraft separation of 200 meters is chosen. The sets of relative orbital elements that describe the six relative orbits are shown in Table 3.11.

The angular separation between the agents is enforced by having each of them target a specific relative eccentric anomaly. For the first lattice, a virtual leader

Table 3.11: Relative orbital elements describing the CROs of the hexagonal lattices.

Orbit	x_r (m)	y_r (m)	a_r (m)	A_z (m)	γ (°)
Central	0	0	0	0	n/a
A	0	0	200	173.21	±90
B	0	0	346.41	300	±90
C	0	0	400	346.41	±90

with initial relative eccentric anomaly $E_{r0}^{'} = 0°$ is set and the agents target angular differences

$$\Delta E_{rt}^{(A_k^{(1)})} = (k-1) \cdot 60°,\ k = 1, .., 6 \tag{3.22}$$

where $A_k^{(1)}$ denotes spacecraft k of orbit A in lattice 1. Similar virtual leader and angular separations are used for the spacecraft on orbit C. For orbit B, the leader is characterized by $E_{r0}^{'} = 30°$ instead, and similar angular separations are targeted. As can be seen in Fig. 3.25, if the same initial values for the virtual leaders are used for both lattices, the spacecraft will reach the intersection of the two orbital planes at the same time, thus leading to many collision avoidance maneuvers. In order to prevent this from happening, the virtual leaders of the three CROs in the second lattice are shifted by 30°. Hence, a virtual leader with $E_{r0}^{'} = 30°$ is used for obits A and C of L_2 and $E_{r0}^{'} = 60°$ for orbit B. Even with this phase angle of 30°, the agents on the innermost orbit might come very close to each other depending on the radius of the CRO.

An expression to compute the minimum distance between two spacecraft targeting the same relative orbit and angular separation but on different lattices is now derived. This distance will be helpful to select an appropriate value for the sphere of influence in the design of the repulsive potential. It is assumed that the spacecraft are on two CROs with radius r and phase angle $\gamma = 90°$ and $\gamma = -90°$. Using Eq. (2.96)-(2.98)

and assuming that the orbits are centered on the chief, the LVLH relative position can be expressed in terms of ROEs as

$$\boldsymbol{r} = \begin{bmatrix} -\frac{1}{2}a_r \cos E_r \\ a_r \sin E_r \\ A_z \sin(\gamma + E_r) \end{bmatrix} \tag{3.23}$$

Hence, the relative position of the spacecraft on lattice L_1 is

$$\boldsymbol{r}_1 = \begin{bmatrix} -\frac{1}{2}r \cos E_r \\ r \sin E_r \\ \frac{\sqrt{3}}{2}r \sin(\frac{\pi}{2} + E_r) \end{bmatrix} \tag{3.24}$$

and the position of the one on L_2:

$$\boldsymbol{r}_2 = \begin{bmatrix} -\frac{1}{2}r \cos\left(E_r + \frac{\pi}{6}\right) \\ r \sin\left(E_r + \frac{\pi}{6}\right) \\ \frac{\sqrt{3}}{2}r \sin\left(-\frac{\pi}{2} + E_r + \frac{\pi}{6}\right) \end{bmatrix} \tag{3.25}$$

Taking the square of the norm of the difference results in

$$s = \|\boldsymbol{r}_1 - \boldsymbol{r}_2\|^2 = \frac{4+\sqrt{3}}{2}r^2 - 3r^2 \sin E_r \sin\left(E_r + \frac{\pi}{6}\right) \tag{3.26}$$

Computing the derivative of this equation with respect to E_r and setting it equal to zeros yields

$$\frac{ds}{dE_r} = -3r^2 \sin\left(2E_r + \frac{\pi}{6}\right) \triangleq 0 \tag{3.27}$$

which admits

$$E_r = \frac{(6n-1)\pi}{12},\ n = 0, 1, 2, \ldots \tag{3.28}$$

as solutions. Since a minimum is sought, the second derivative must be strictly positive

$$\frac{d^2s}{dE_r^2} = -6r^2 \cos\left(2E_r + \frac{\pi}{6}\right) > 0 \tag{3.29}$$

and therefore

$$E_r = \frac{(6n-1)\pi}{12},\ n = 1, 3, 5, \ldots \tag{3.30}$$

The evaluation of Eq. (3.26) at the minimum results in

$$s_{min} = \frac{2-\sqrt{3}}{4} r^2 \tag{3.31}$$

and it follows that the minimum distance between the two spacecraft is

$$d_{min} = \frac{\sqrt{2-\sqrt{3}}}{2} r \simeq 0.2588r \tag{3.32}$$

For a relative orbit radius of 100 meters, this distance would be $d_{min} = 25.88$ meters and for the selected radius of 200 meters, $d_{min} = 51.76$ meters. This result indicates that the baseline of the formation must be relatively large in order to avoid the spacecraft to come too close to each other when they cross the intersection of the two planes. This also means that if the radius of the sphere of influence is defined to be larger than d_{min}, every time a spacecraft on the innermost orbit reaches the intersection of the two planes, a collision avoidance maneuver will be performed. This would lead to unnecessary high propellant consumption and it is therefore best to select a value such that $r_{\mathrm{SOI}} < d_{min}$.

For this scenario, the same initial conditions as before are used for the chief and it is assumed that the spacecraft are released in two batches of 19 and 18 spacecraft respectively. The first batch is released around $x = -100$ m, $y = 800$ m, and $z = -300$ m within an ellipsoid of revolution with semi-major axis 100 m and semi-minor axis 25 m and oriented along the launch trajectory. The second batch is released within an identical ellipsoid but centered at $x = 200$ m, $y = 1200$ m, and $z = 100$ m. The initial distance between each spacecraft is at least 40 meters. The velocities are drawn from a Gaussian distribution with mean 5 cm/s and standard deviation 2 mm/s for the component along the trajectory and mean 2 cm/s and standard deviation 5 mm/s for the orthogonal component. The initial conditions are illustrated in Fig. 3.26 and are

printed in Table A.2 in the appendix. The spacecraft released at the first location will target lattice L_1 (green) and the ones released at the second location will target lattice L_2 (violet).

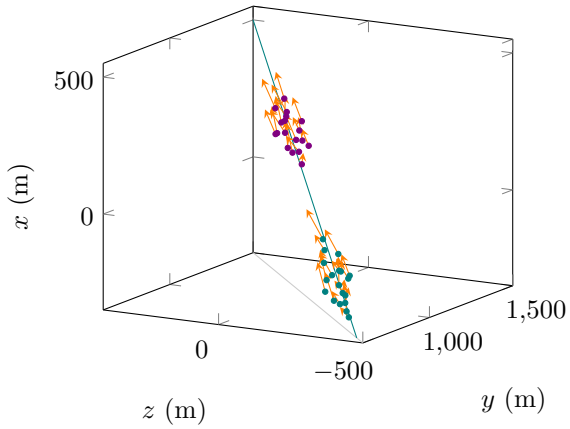

Figure 3.26: Initial conditions of the 37 spacecraft.

The parameters of the controller used to establish this formation are shown in Table 3.12. For this scenario, the same time intervals between attractive maneuvers

Table 3.12: Parameters of the controller for the hexagonal lattices.

$T_m = 15$ min
$\tau_c = 4$ h
$d_c = 5$ m
$T_c = 5$ s
$r_s = 0.35$ m
$r_{\text{SOI}} = 20$ m
$p = 0.001$
$\upsilon = 3$

and collision checks as before are used. The duration to obtain convergence in the autonomous computation of k_a is set to 4 hours with a threshold of 5 meters. The obstacles are defined with a radius of 0.35 meters and a 20 meters radius sphere of influence. The value of the repulsive potential at r_{SOI} is 0.1 percent its value at r_s and the semi-major axis of the ellipsoid is three times the semi-minor axis.

The same physical properties (Table 3.6) and maneuvers bounds as in the previous scenario are used. The formation reconfiguration is simulated for 6 hours. Fig. 3.27 shows the establishment of the two hexagonal lattices formation[2]. The 37 spacecraft are released in two batches slightly ahead of the chief (Fig. 3.27a). The spacecraft first disperse and move toward the origin of the frame (Fig. 3.27b). Collision avoidance maneuvers occur at the beginning of the simulation, which result in one of the agents being slightly behind the rest of the spacecraft as seen in Fig. 3.27c and 3.27d (violet dot at the top). One hour after deployment, a loose formation is already established (Fig. 3.27e) and the spacecraft continue to adjust their relative position during the following hours until they reach their final state as seen in Fig. 3.27f.

The total delta-V used by each spacecraft is presented in Table 3.13. We see in this table that the delta-V required to establish the formation ranges from 0.95 m/s for spacecraft L2A6 to 15.98 m/s for spacecraft L2B5 with a mean of 3.08 m/s and standard deviation of 2.81 m/s. If the simulation is run without collision monitoring, the mean delta-V is 2.26 m/s and the standard deviation 1.43 m/s. This shows that collision avoidance maneuvers account for a significant fraction of the total delta-V required to establish the formation. When the two batches are considered individually, a mean of 2.72 m/s for the establishment of lattice L_1 and a mean of 1.75 m/s for the establishment of lattice L_2 are obtained. This difference of about 1 m/s between the two lattices can be explained by the different release locations of the two batches. The spacecraft targeting the first lattice are released on a lower orbit than the chief with a velocity pointing in the positive y direction. Their natural tendency is therefore to move away from the chief and a higher delta-V is required to bring them back toward the origin of the LVLH frame. The spacecraft targeting the second lattice are released slightly above the chief, making them naturally moving along the negative y direction, toward the chief. The amount of delta-V required to bring them toward the origin of the frame is therefore lower than for the first batch. Fig. 3.28 shows

[2]An animation of the formation establishment is available at `https://purr.purdue.edu/publications/3389/1`.

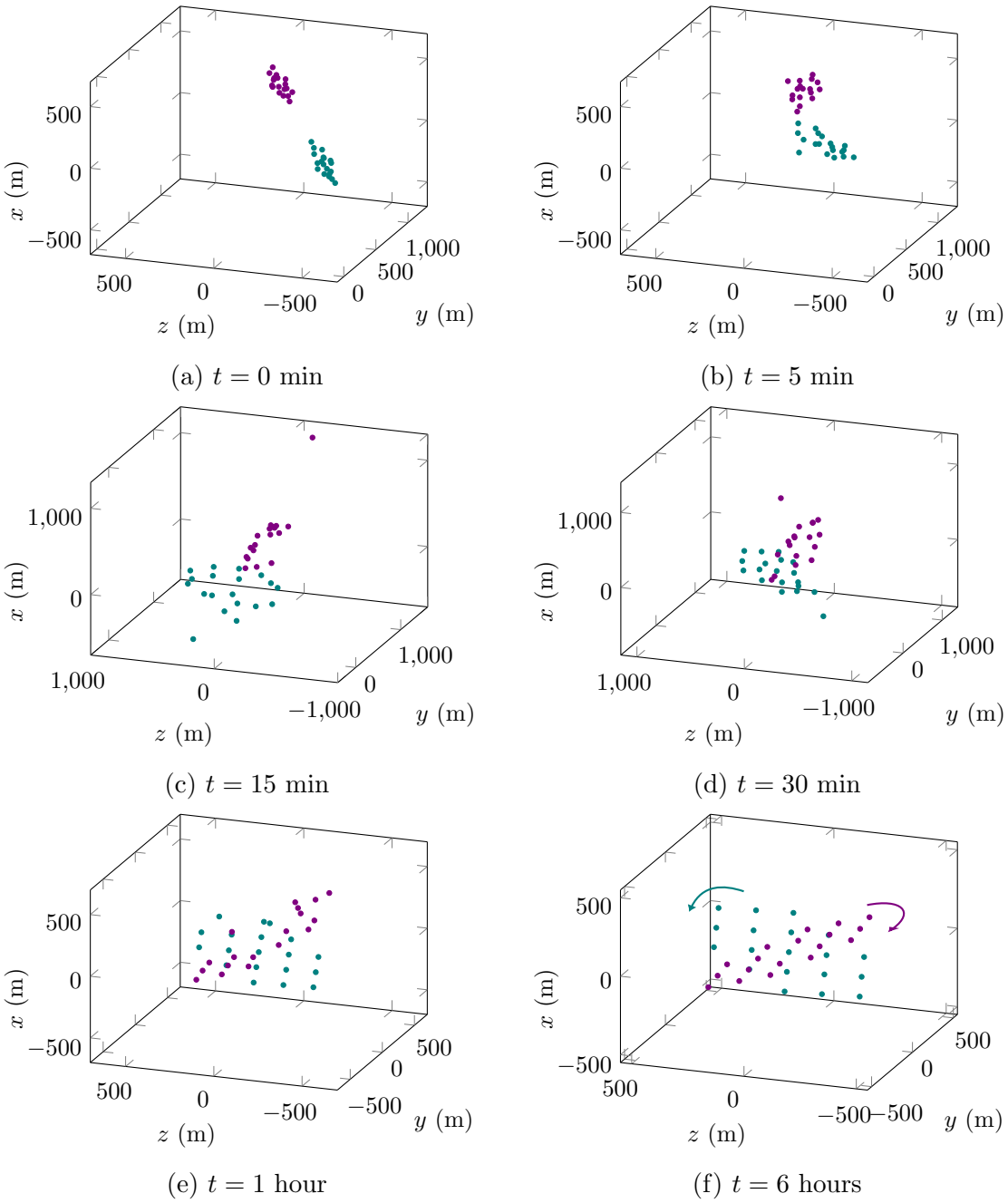

Figure 3.27: Formation establishment of the two hexagonal lattices.

the natural motion resulting from the propagation of the initial conditions over 30 minutes.

Table 3.13: Delta-V consumption for the establishment of the two hexagonal lattices formation.

Spacecraft	Delta-V (m/s)	Spacecraft	Delta-V (m/s)
Central	2.37	L2A1	1.03
L1A1	1.84	L2A2	1.23
L1A2	2.04	L2A3	2.36
L1A3	2.27	L2A4	1.98
L1A4	2.78	L2A5	2.67
L1A5	2.86	L2A6	0.95
L1A6	2.53	L2B1	1.21
L1B1	1.49	L2B2	1.41
L1B2	1.75	L2B3	7.70
L1B3	2.75	L2B4	1.48
L1B4	3.24	L2B5	15.98
L1B5	3.92	L2B6	1.09
L1B6	6.35	L2C1	6.01
L1C1	1.76	L2C2	1.50
L1C2	1.45	L2C3	2.29
L1C3	6.45	L2C4	3.29
L1C4	3.12	L2C5	1.43
L1C5	3.25	L2C6	1.01
L1C6	7.08		
Mean: 3.08 m/s		Std: 2.81 m/s	

The difference between the lowest and largest delta-V's observed in Table 3.13 is mainly due to collision avoidance maneuvers. Fig. 3.29 and 3.30 show the delta-V history of spacecraft L2A6 and L2B5 respectively.

As can be seen in Fig. 3.29, no collision avoidance maneuver occurs for spacecraft L2A6. The only maneuvers are to target attractive waypoints and follow the reference trajectory. The amplitude of the maneuvers decreases rapidly and two hours after deployment very small maneuvers of a few millimeters per second are sporadically applied to correct for orbital perturbations and maintain the spacecraft on its target orbit. In contrast, Fig. 3.30 shows that agent L2B5 performs many CAMs and

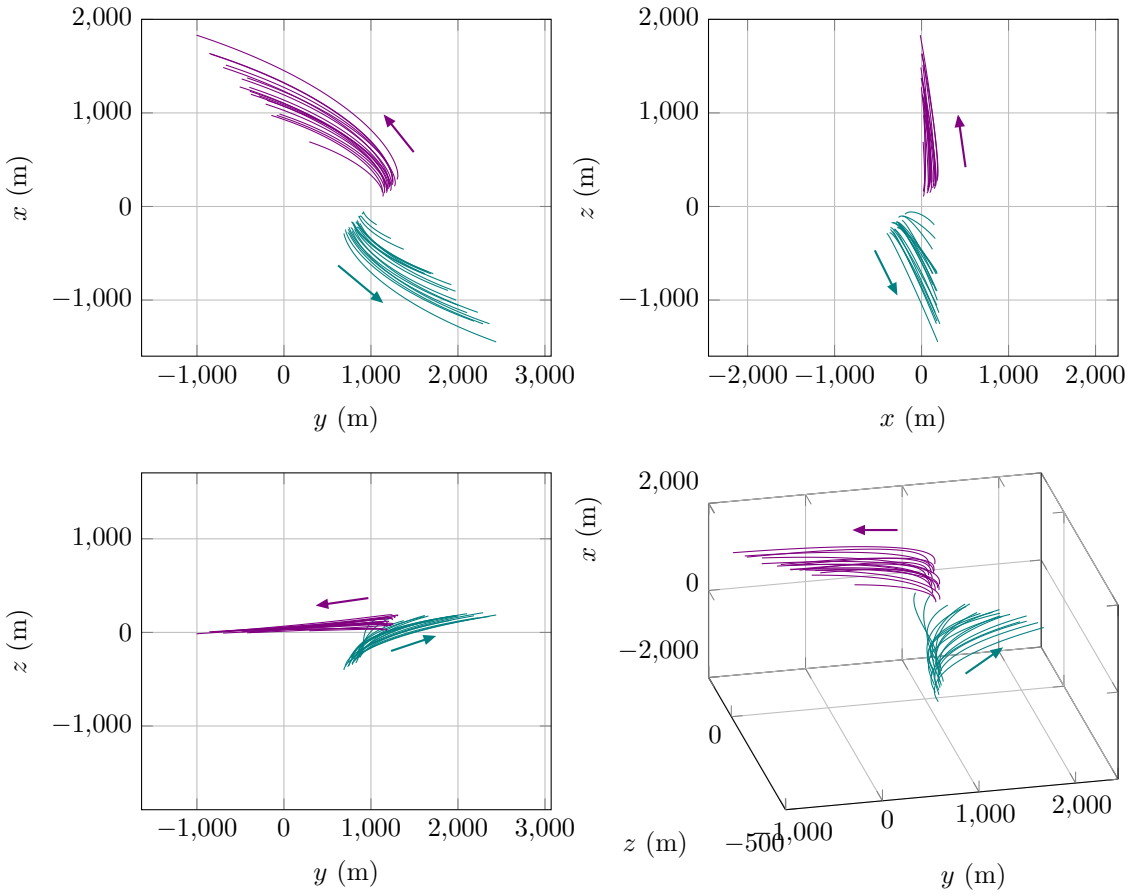

Figure 3.28: Free motion resulting from the initial conditions propagated for a duration of 30 minutes.

recovery maneuvers during the first hour after deployment. A few maneuvers saturate at the beginning of the simulation. We see that the spacecraft reaches its target orbit within two hours and small maneuvers are applied to maintain it on its orbit for the remainder of the simulation. Fig. 3.31 and 3.32 show the trajectory followed by each of these spacecraft together with the attractive (green circles) and repulsive (red circles) waypoints. As suggested by the delta-V history, agent L2A6 does not perform any collision avoidance maneuver during the reconfiguration and therefore only attractive waypoints are visible in Fig. 3.31. We see, however, that many CAMs occur for agent L2B5 (Fig. 3.32). The spacecraft performs four avoidance maneuvers early on in the reconfiguration process at $t = 120$ s, $t = 125$ s, $t = 130$ s, and $t = 140$

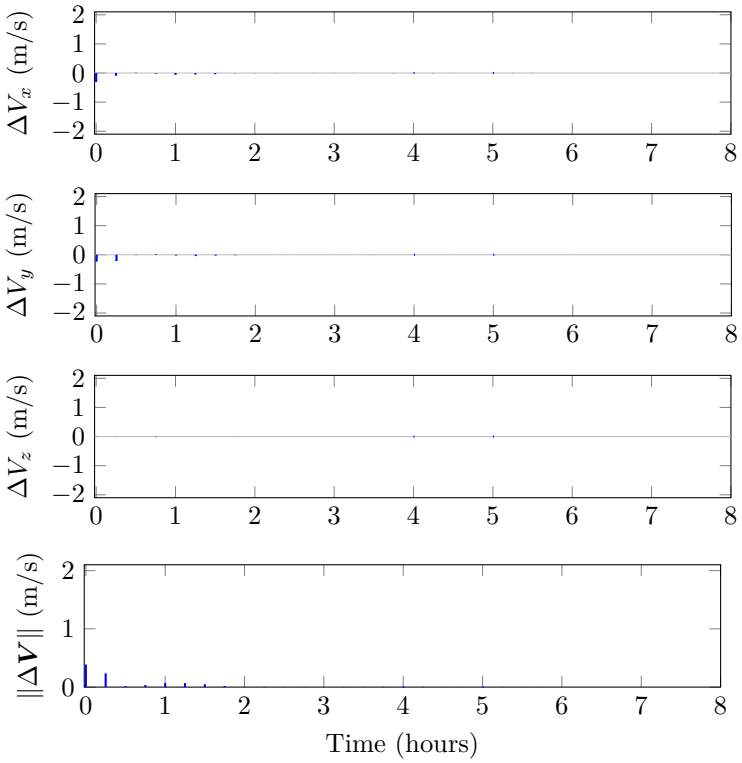

Figure 3.29: Delta-V history of spacecraft L2A6.

s. A fifth and last CAM is performed at $t = 28.75$ min. If we compare these five CAMs with the time history of the delta-V's (Fig. 3.30), we see that many maneuvers are applied to recover from these CAMs and place the spacecraft back on an arc that intercepts the next attractive waypoint. After the last avoidance maneuver has taken place, the agent follows the reference trajectory by targeting the attractive waypoints and reaches its target orbit within about 2 hours.

In this simulation, the closest approach between two agents is 15.40 meters and occurs between spacecraft L2B5 and L2C4. Table 3.14 shows the five closest approaches that happen during the formation establishment. These five closest approaches happen early on in the simulation, when the spacecraft have just been released and after they have performed a few maneuvers to target the first attractive waypoints. It is apparent from this table that no collision avoidance occurs when the second lattice "traverses" the first lattice after about 30 minutes. Spacecraft L2B5 being slightly

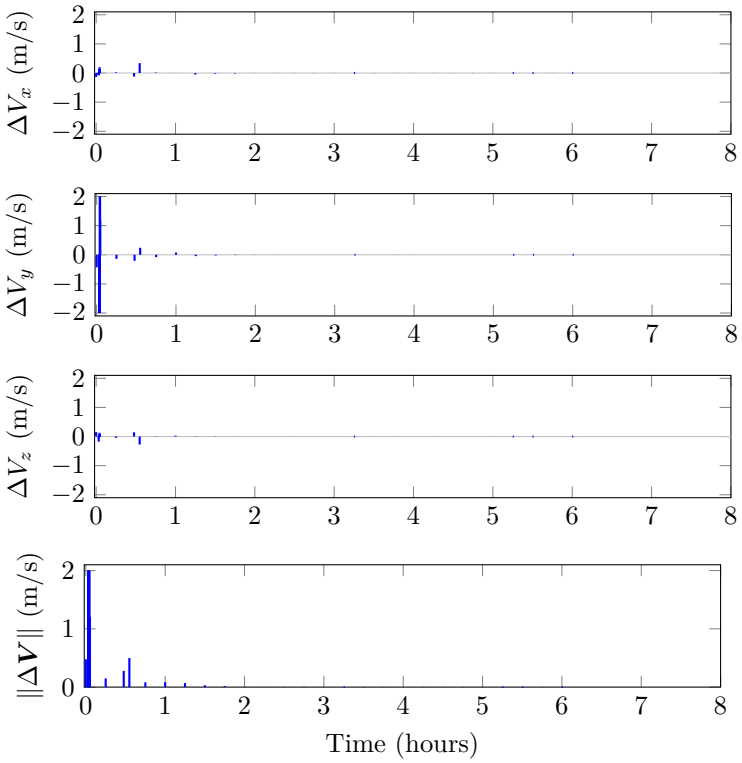

Figure 3.30: Delta-V history of spacecraft L2B5.

Table 3.14: Five closest approaches happening during formation establishment.

Distance (m)	Time (sec)	Spacecraft pair
15.40	135	L2B5 - L2C4
17.31	125	L2B5 - L2C1
18.34	60	L1B6 - L1C3
19.86	1720	L2A5 - L2B5
20.57	80	L2B2 - L2B5

behind the group at that time, the CAM performed by this agent at 28.75 min is not caused by the encounter of the two lattices.

Fig. 3.33 and 3.34 show the time evolution of the ROEs of spacecraft L2A6 and L2B5. The oscillations of the ROEs resulting from CAMs are clearly visible for all six elements for deputy L2B5 in Fig. 3.34. The value of x_r and a_r goes very far from the target value when maneuvers are executed. The time evolution of the ROEs also

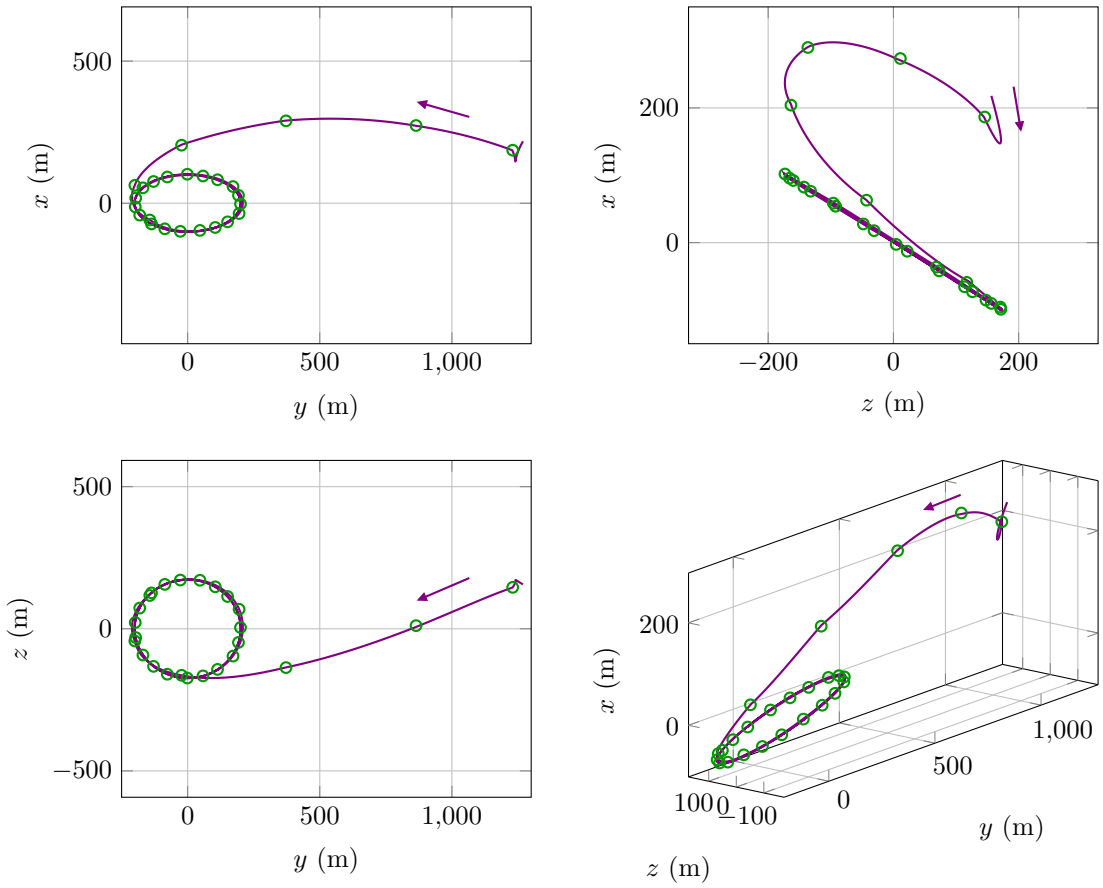

Figure 3.31: Trajectory and attractive waypoints for spacecraft L2A6.

shows that both agents have converged to their respective target orbit in about two hours. Since out of the six ROEs only y_r and E_r are time-varying, it is expected that in an unperturbed, linear environment, the value of the four other ROEs should remain constant between two maneuvers. The small variations that can be observed, especially in Fig. 3.33, are produced by nonlinearities and orbital perturbations.

It is interesting to note that even though the reference trajectory is computed by following the steepest descent of the APF, the ROEs do not monotonically decrease. This is due to the fact that only the relative position and not the relative velocity is tracked. In this case, since the unforced motion results in the targeted relative orbit, the relative velocity will converge to the velocity of the relative orbit by the only action of targeting the relative position. If the target orbit does not correspond

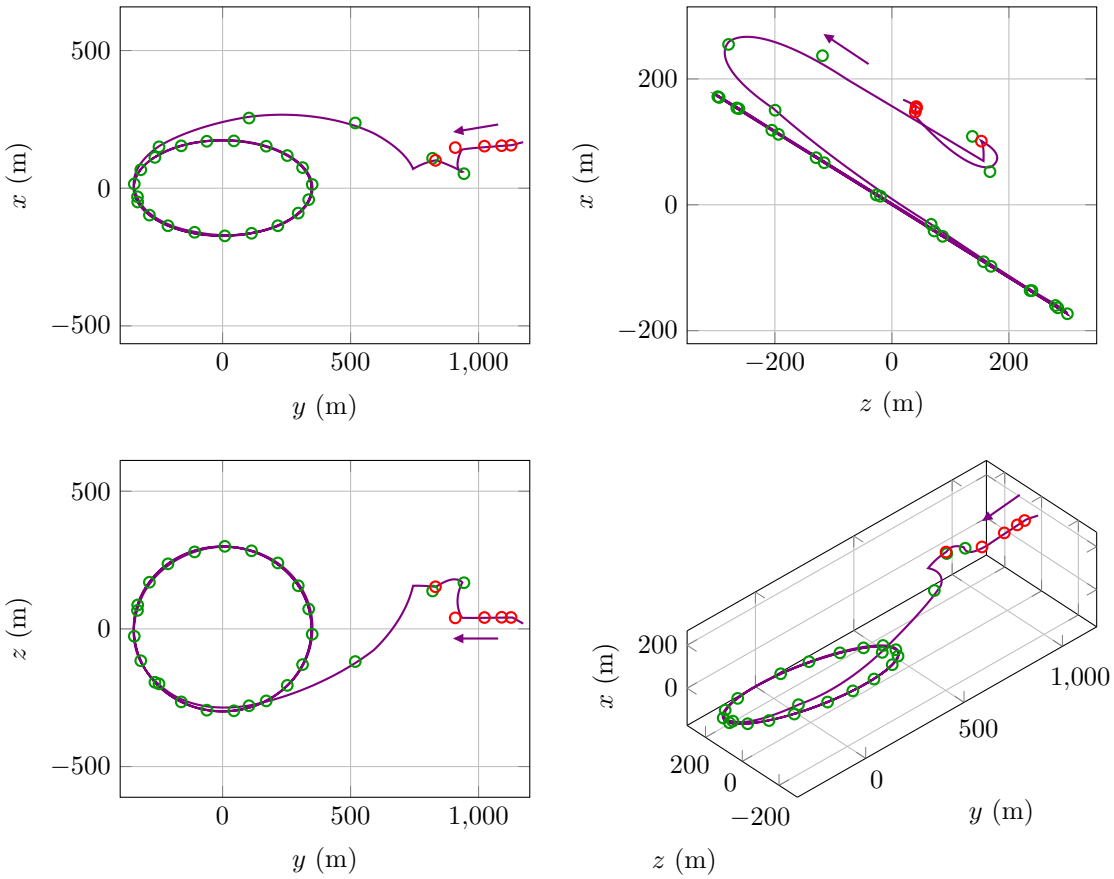

Figure 3.32: Trajectory, attractive waypoints (green), and repulsive waypoints (red) for spacecraft L2B5.

to the unforced motion, this will not be the case and the relative velocity of the deputy will not match that of the targeted relative orbit. When an unstable relative orbit is targeted, a small time interval between two attractive maneuvers must be selected to closely follow the reference trajectory and prevent the spacecraft to drift too far away. This behavior will be illustrated with the use of the GROEs in the next scenario. Fig. 3.35 shows the time evolution of the LVLH coordinates of agent L2B5 together with the LVLH coordinates of the target. We see that at the beginning of the reconfiguration, the velocity does not follow the target. Yet when the deputy reaches the targeted position, the velocity also closely aligns with the relative velocity of the target orbit.

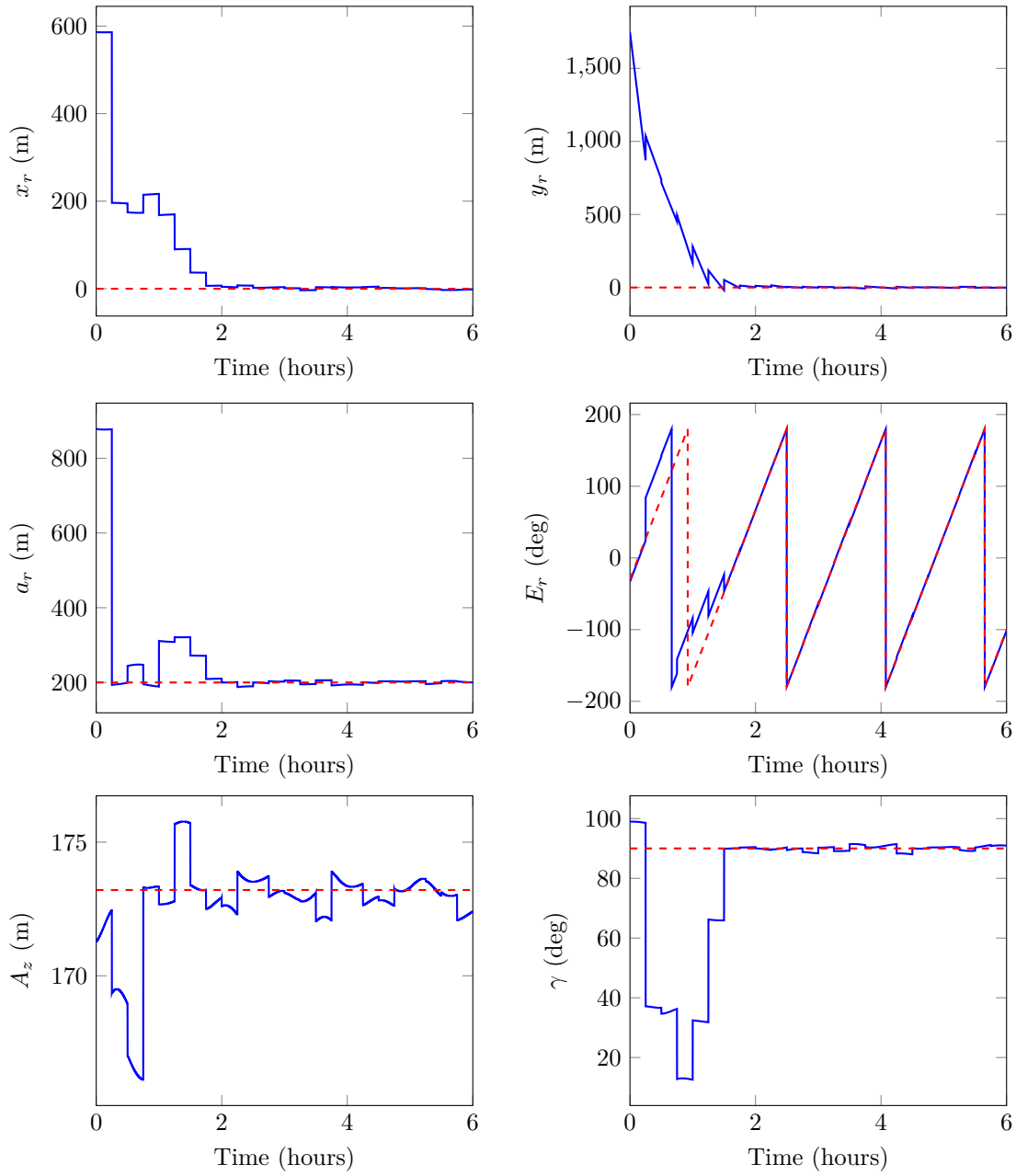

Figure 3.33: Time evolution of the relative orbital elements (blue) together with the target values (dashed red) of spacecraft L2A6.

The accuracy of the formation establishment is assessed by looking at the error between the true position of the spacecraft and the target position. Fig. 3.36 shows the time evolution of this error for each agent. As can be seen in that figure, the error

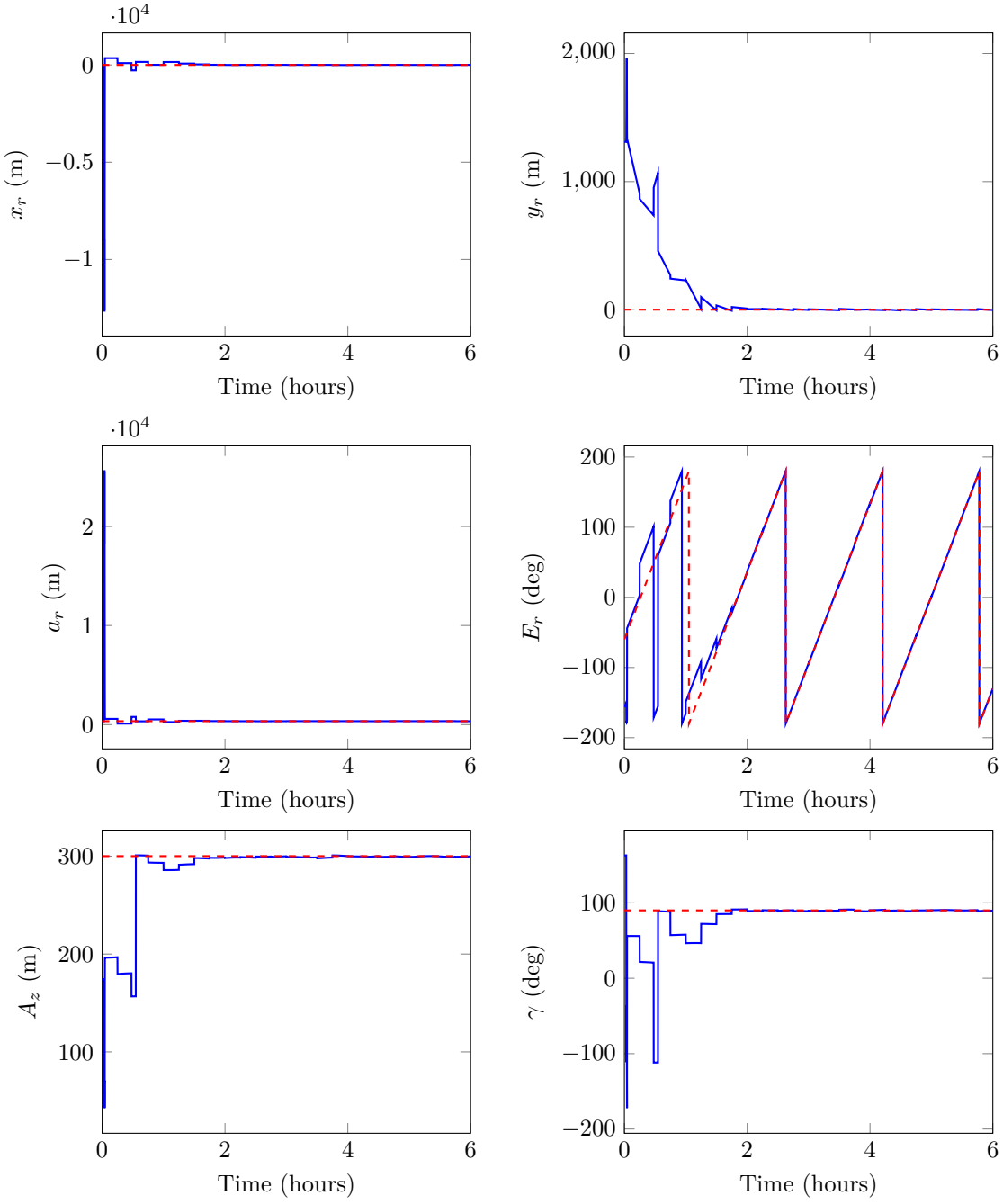

Figure 3.34: Time evolution of the relative orbital elements (blue) together with the target values (dashed red) of spacecraft L2B5.

quickly decreases during the first two hours of simulation before stabilizing within 5 meters. The error for one of the spacecraft, L2B3, takes slightly longer to decrease

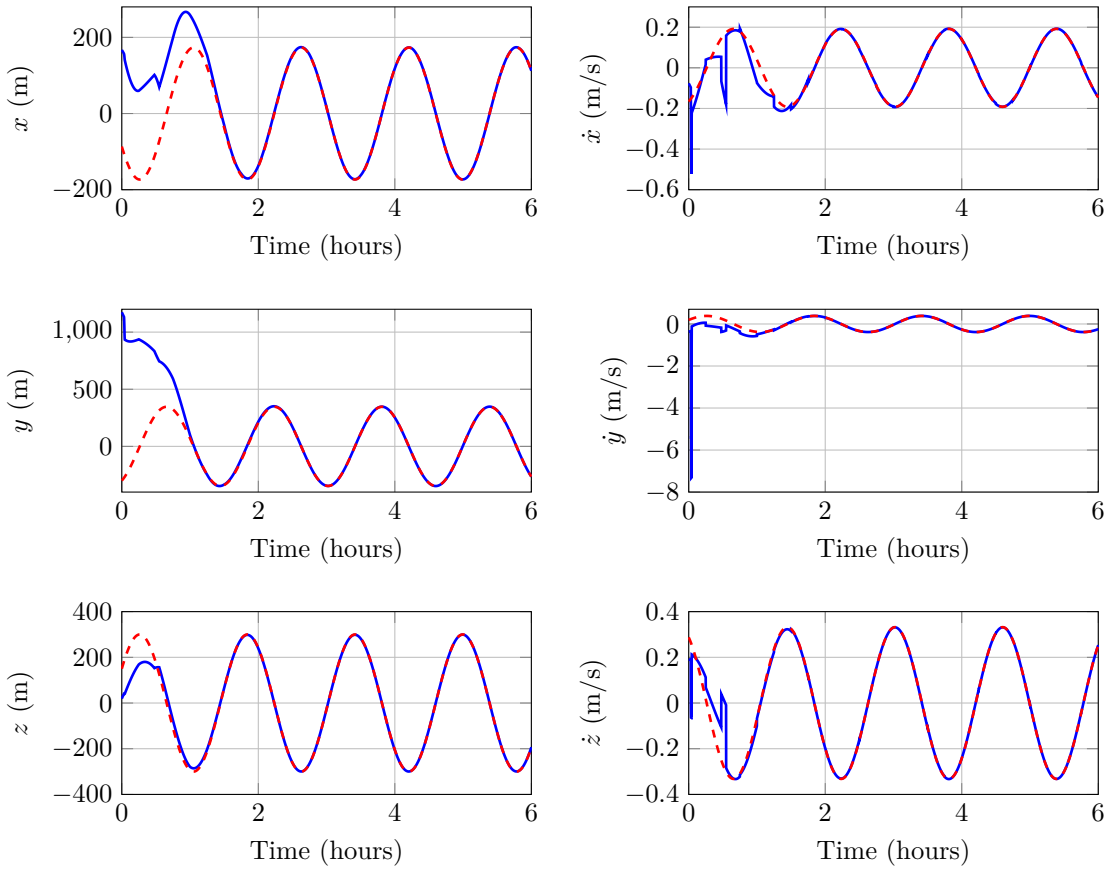

Figure 3.35: Time evolution of the LVLH coordinates (blue) and target orbit (dashed red) of spacecraft L2B5.

than the other ones. This is due to the combination of initial conditions and value of k_a for that specific agent.

3.2.3 Visual Inspection

In this third scenario, the visual inspection of a on-orbit structure by a spacecraft is simulated. The desired relative trajectory is to first establish a circular relative orbit at one end of the structure and then spiral along the main axis of the cylinder. The relative trajectory is illustrated in Fig. 3.37.

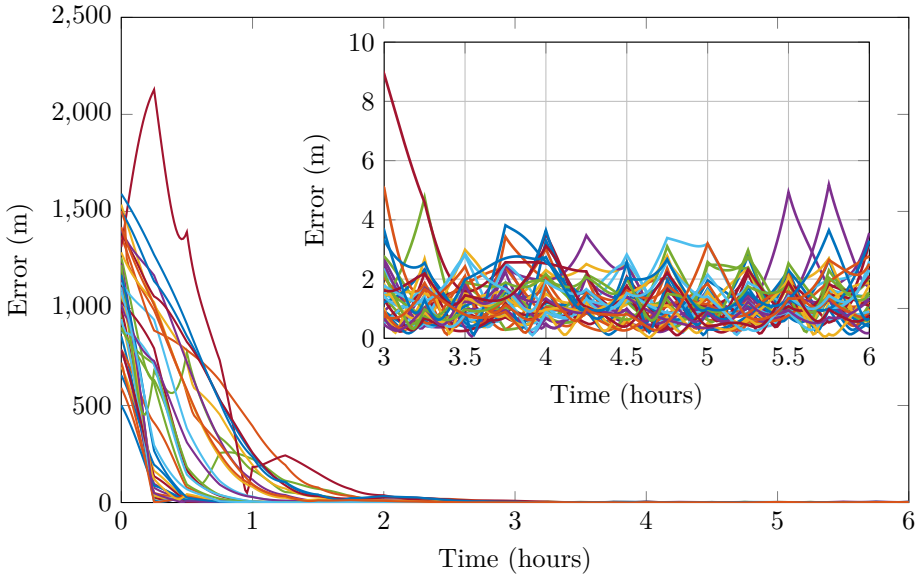

Figure 3.36: Accuracy of the two hexagonal lattices formation establishment.

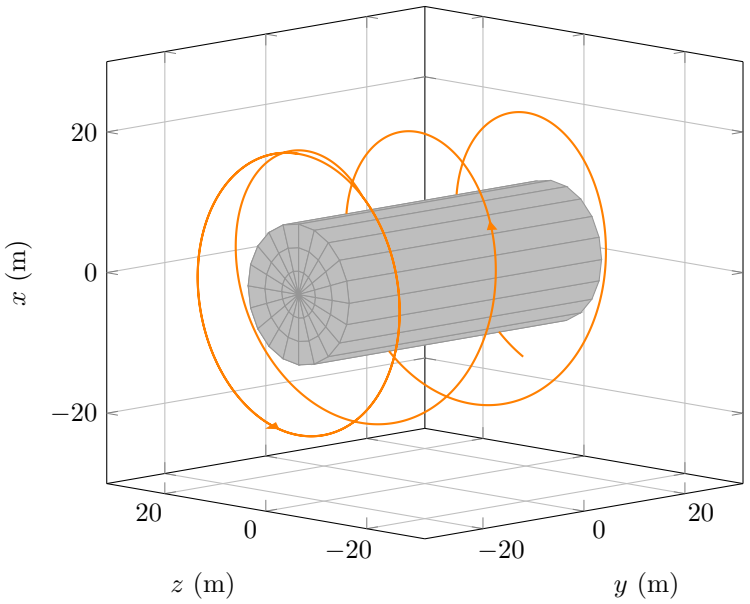

Figure 3.37: Desired trajectory for the visual inspection.

It is assumed that the structure is a 50 m long, 10 m radius cylinder with a fixed orientation along the y axis of the LVLH frame, and that it is on a near-polar orbit. The classical orbital elements describing the orbit of the structure (i.e. the chief) are

$$a = R_\oplus + 700 \text{ km} \qquad e = 0 \qquad i = 85^\circ \qquad \Omega = 45^\circ \qquad \omega = 0^\circ \qquad M = 60^\circ$$

If the circular relative orbit at the end of the structure is described in terms of ROEs, x_r and a_r should be set to zero which implies that x will always be null resulting in the spacecraft oscillating about the origin along the z-axis. This trajectory therefore cannot be described with ROEs and is designed with a set of GROEs instead. As a reminder, these elements are defined as

$$\boldsymbol{\rho} = \begin{bmatrix} x_c & y_c & a & e & c & \sigma & \Upsilon & \omega \end{bmatrix}^T$$

where x_c and y_c denote the position of the center of motion of the instantaneous relative orbit, a is the semi-major axis of the relative ellipse, e its eccentricity, c the central anomaly measuring the position of the spacecraft on the relative orbit, σ the slant, Υ the colatitude of the sinilaterating node, and ω the argument of pericenter, which is undefined for a CRO and can be set arbitrarily in this case.

The first part of the targeted trajectory is a circular relative orbit of radius 20 meters at the end of the structure located at $y = -25$ m. The location of the deputy on this relative orbit is arbitrarily set to target an angular separation of $\Delta c_t = 0°$ with respect to a virtual leader with $c_{r0}^{'} = 0°$. Hence, the set of elements describing this relative orbit is

$$\boldsymbol{\rho}_t = \begin{bmatrix} 0 \text{ m} & -25 \text{ m} & 20 \text{ m} & 0 & 0° & 90° & 0° & 0° \end{bmatrix}^T$$

where the fifth entry corresponds to Δc_t. Once the spacecraft has reached this CRO and stabilized, the y component of the instantaneous center of motion, y_c, is increased with time such that the spacecraft will start to spiral around the structure. If the spacecraft starts to spiral three hours after deployment and reaches the other end of the structure in four hours, y_{ct} can be defined as a function of time as follows:

$$y_{ct}(t) = \begin{cases} -25 \text{ m} & \text{if } t < 3 \text{ h} \\ \frac{55 \text{ m}}{4 \text{ h}}(t - 3 \text{ h}) - 25 \text{ m} & \text{if } t \geq 3 \text{ h} \end{cases} \tag{3.33}$$

Since the deputy will be targeting a moving target, it will be trailing slightly behind y_{ct} at all time, and a larger final value is thus targeted to ensure that the spacecraft reaches the end of the structure by the final time. Hence, $y_{ct}(t = 7 \text{ h}) = 30$ m whereas the end of the structure is located at $y = 25$ m. Note that the pitch of the helix can be adjusted by selecting a different duration for the helix portion of the trajectory. Also, the target set of GROEs in this example results in a left-handed helix. A right-handed helix can be obtained by setting $\Upsilon_t = 180°$ instead of $\Upsilon_t = 0°$.

It is assumed that the spacecraft is released behind the structure and slightly above it. The initial state is

$$\boldsymbol{s}_0 = \begin{bmatrix} 100 \text{ m} & -200 \text{ m} & 10 \text{ m} & -20 \text{ cm/s} & -20 \text{ cm/s} & -10 \text{ cm/s} \end{bmatrix}^T$$

and is illustrated in Fig. 3.38.

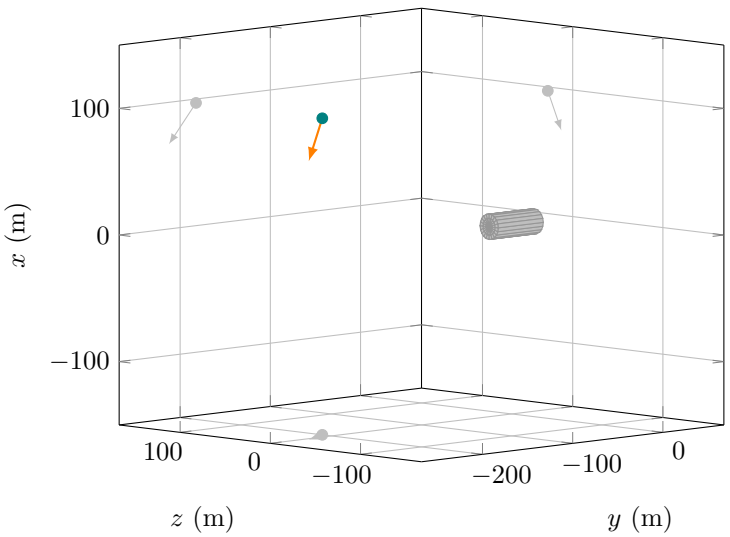

Figure 3.38: Initial state for the visual inspection. The velocity is not to scale.

Once the relative trajectory described by the GROEs is reached, the unforced motion of the spacecraft will result in a different relative orbit than the desired one. In order to maintain the spacecraft on the reference trajectory, frequent maneuvers are therefore required. For this reason, the time interval between two maneuvers is

set to $T_m = 5$ minutes. Collisions between the spacecraft and the structure are not monitored in this example.

It is assumed that the spacecraft is a 3U CubeSat with the properties listed in Table 3.15.

Table 3.15: Physical properties of the 3U CubeSat used for the visual inspection.

$m_{\text{wet}} = 3$ kg
$C_d = 2.1$
$C_r = 1.21$
$A = 0.03$ m^2
$A_\odot = 0.03$ m^2
$I_{sp} = 220$ s

For this scenario, the amplitude of the maneuvers is bounded between $\Delta V_{min} = 2$ mm/s and $\Delta V_{max} = 40$ cm/s. The scaling coefficient for the attractive potential is automatically computed using the process described in section 2.3.4. The result of the coefficient search is plotted in Fig. 3.39 where the selected value is $k_a = 10^{-3}$ (violet line).

The trajectory followed by the deputy spacecraft for a duration of 7 hours is shown in Fig. 3.40[3]. We see in that figure that the spacecraft first establishes the CRO at the end of the structure. Three hours after deployment and after about one orbit on the CRO, the y coordinate of the instantaneous center of motion, y_c, starts increasing, resulting in the helix trajectory. The total delta-V used to establish this relative trajectory is 2.76 m/s and the time history of the maneuvers is illustrated in Fig. 3.41. As can be seen in the figure, the amplitude of the first maneuver is close to the saturation limit of 40 cm/s. The subsequent maneuvers quickly decrease in magnitude and are mostly along the x and y components. Compared to the previous scenarios, the magnitude of the delta-V stays in the range of a few centimeters per second during the entire simulation. This shows that constant thrusting is necessary

[3]An animation of the formation establishment is available at `https://purr.purdue.edu/publications/3389/1`.

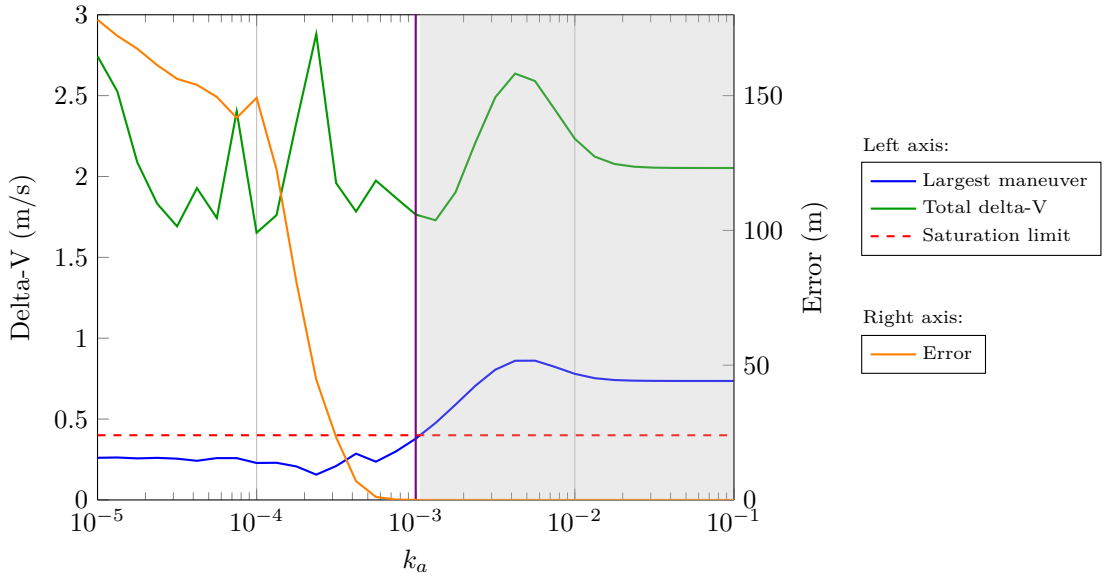

Figure 3.39: Autonomous k_a search for the visual inspection. The violet line corresponds to the selected value

to closely follow the desired relative trajectory. The spikes visible on the helix portion of the trajectory in Fig. 3.40 are also an indication of the frequent maneuvers.

The relative trajectory with the attractive waypoints is plotted in Fig. 3.42. If we look at the first and third waypoints, the effect of the orbital perturbations, state uncertainties, and thrust errors are clearly visible. We see that the spacecraft does not pass exactly through these waypoints but rather within a few meters of them. It can also be noticed that the distance between each waypoint decreases as the spacecraft approaches the target trajectory, yet the time interval between each of them is identical ($T_m = 5$ minutes). Fig. 3.43 shows the time evolution of the GROEs computed from the true LVLH state of the spacecraft. As expected, the GROEs computed from the actual state of the deputy do not converge to the targeted values. This is due to the fact that the designed trajectory requires frequent maneuvers and only the relative position is tracked but not the relative velocity. Thus, when the GROEs are computed from the actual LVLH coordinates of the deputy, they do not match with the target values. Fig. 3.44 shows the time evolution of the LVLH coordinates of the spacecraft along with the evolution of the LVLH coordinates of

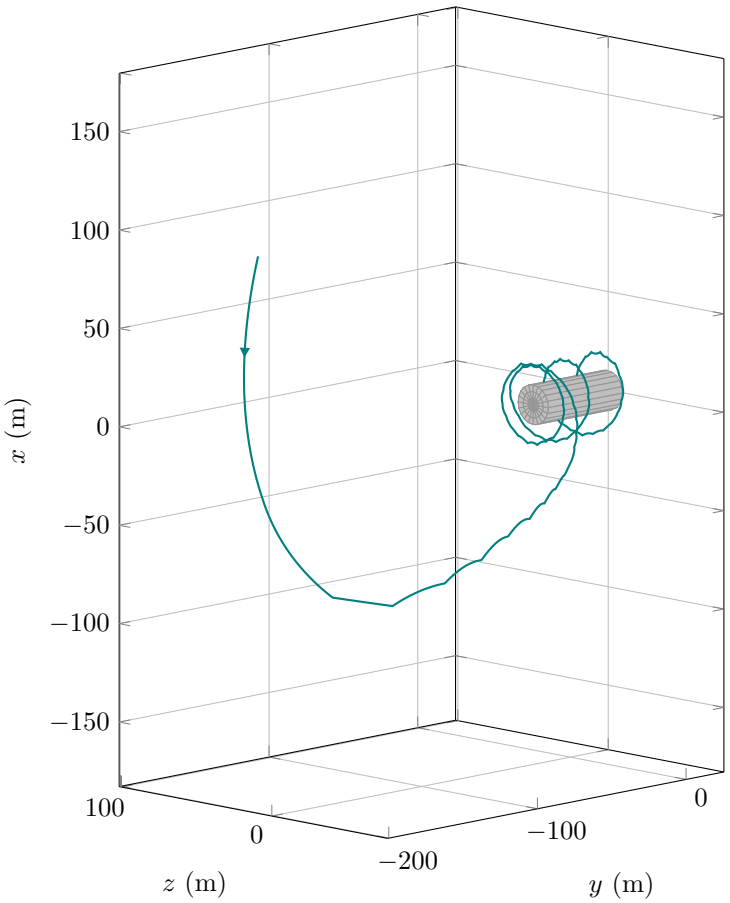

Figure 3.40: Relative trajectory of the deputy spacecraft.

the reference waypoints. As can be seen in that figure, the x, y, and z coordinates converge to the targeted values. The velocity however oscillates about the desired value and is constantly adjusted.

The accuracy of the tracking is shown in Fig. 3.45. The error between the actual position and the targeted one quickly decreases during the initial phase of the simulation. After two hours, the spacecraft is on the CRO and the error is lower than 2 meters, thanks to the short time interval between two maneuvers. When the position of the center of motion, y_c, starts to increase after three hours, the error slightly increases due to the fact that the spacecraft now tracks a moving target and is slightly trailing behind it. The error nevertheless stays below 6 meters.

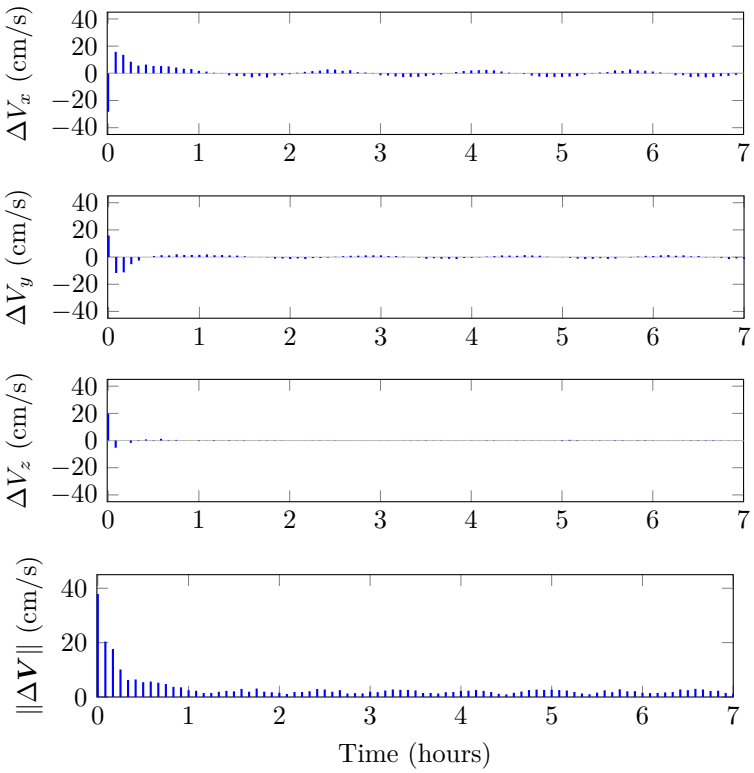

Figure 3.41: Delta-V history of the structure inspection.

The choice of the target value for the angular separation has been chosen arbitrarily for this example but the total delta-V required to track the reference trajectory can significantly vary depending on this value. Fig. 3.46 shows the dependency of the total delta-V in the targeted angular separation Δc_t. We see from this figure that the total delta-V ranges from 2.71 m/s for $\Delta c_t = -21.6°$ to 4.16 m/s for $\Delta c_t = -36°$. We also see that there is a large discontinuity between $\Delta c_t = -28.8°$ and $\Delta c_t = -21.6°$. If we compute the GROEs corresponding to the initial Cartesian state, we get

$$\boldsymbol{\rho}_0 = \begin{bmatrix} 22.7 \text{ m} & 177.3 \text{ m} & 408.6 \text{ m} & 0.84 & 156.54° & 155.70° & 98.27° & 9.72° \end{bmatrix}^T$$

Hence, the initial central anomaly is $c_0 = 156.54°$. One of the difficulties in targeting angular values is that since angles are cyclic, they can be targeted from above by decreasing the current value or below by increasing the current value. Fig. 3.47

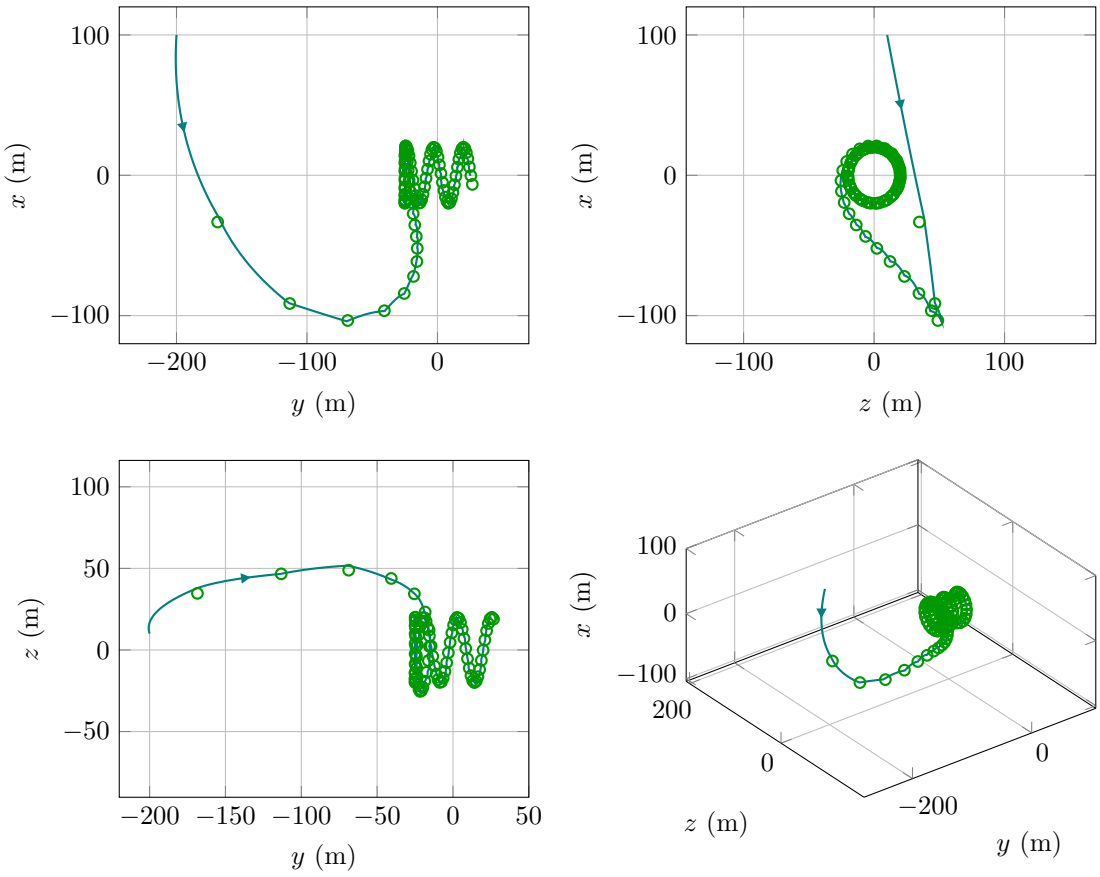

Figure 3.42: Relative trajectory and attractive waypoints.

illustrates this property for an initial angle of 120° and a target angle of −100°. The current implementation of the controller selects the path with the smallest angular separation. That is, when computing the gradient of the artificial potential with respect to the angle (E_r or c), the difference between the initial angle α_0 and target α_t is computed as

$$\Delta\alpha = [(\alpha_t - \alpha_0 + \pi) \bmod 2\pi] - \pi \tag{3.34}$$

where mod denotes the modulo operation and where α_0 and α_t must lie within $[-\pi, \pi)$. The initial central anomaly and the values next to the discontinuity in Fig. 3.46 are displayed in Fig. 3.48. We see in that figure that the path followed when angular separations of $\Delta c_t = -21.6°$ and $\Delta c_t = -28.8°$ are targeted is different. In the first case, the difference between the initial value and the target is shorter in the clockwise

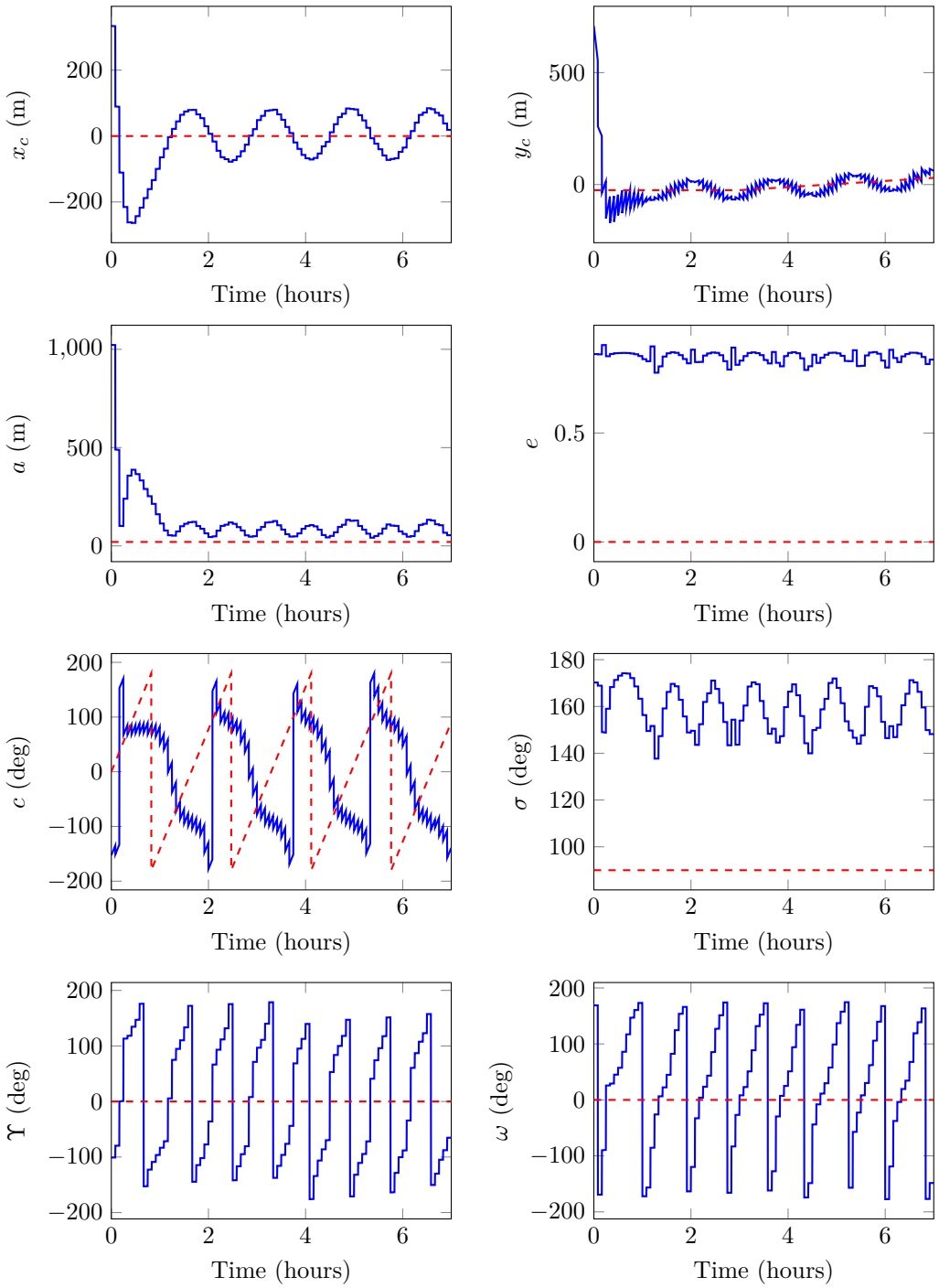

Figure 3.43: Time evolution of the GROEs (blue) together with the target values (dashed red).

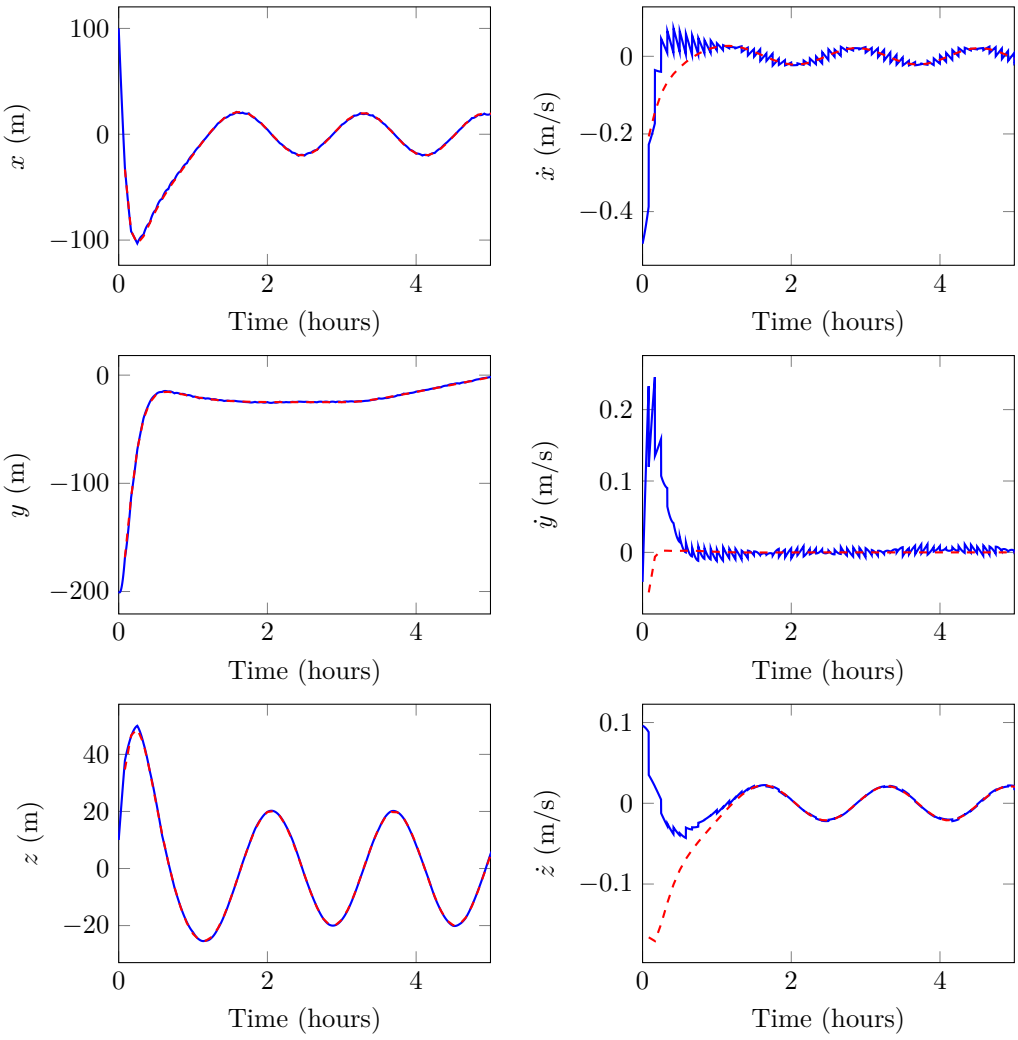

Figure 3.44: Time evolution of the LVLH coordinates of the spacecraft (blue) along with the LVLH coordinates of the reference waypoints (red).

direction, resulting in the algorithm decreasing the value of the central anomaly. In the second case, the path is shorter going counterclockwise, resulting in the central anomaly being increased to move toward the target.

Fig. 3.49 shows the two relative trajectories followed by the spacecraft when an angular separation of $-21.6°$ respectively $-28.8°$ is selected. The relative trajectory followed to reach the CRO at the beginning of the reconfiguration differs significantly between the two values. For $\Delta c_t = -21.6°$, the central anomaly decreases over time, leading to a relatively direct trajectory. For $\Delta c_t = -28.8°$, the central anomaly

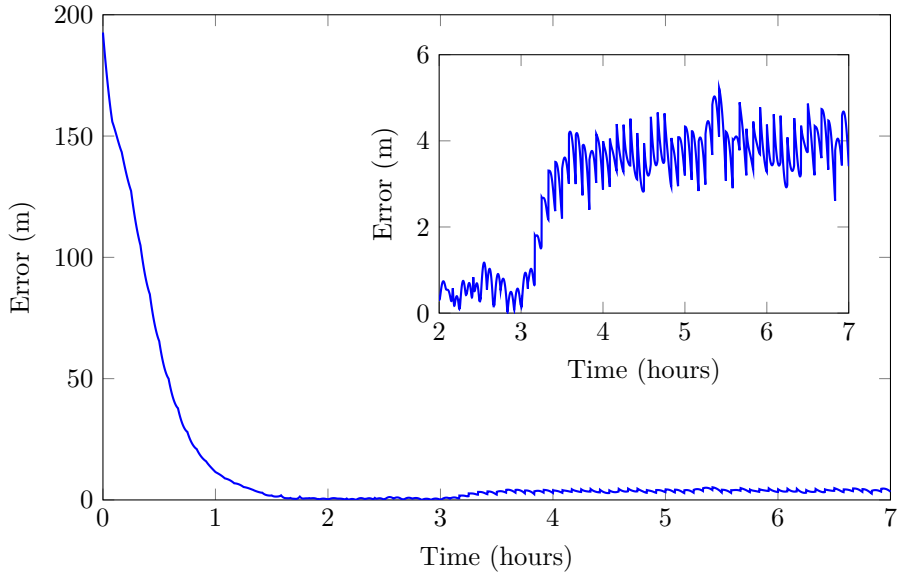

Figure 3.45: Accuracy of the reference trajectory tracking for the visual inspection.

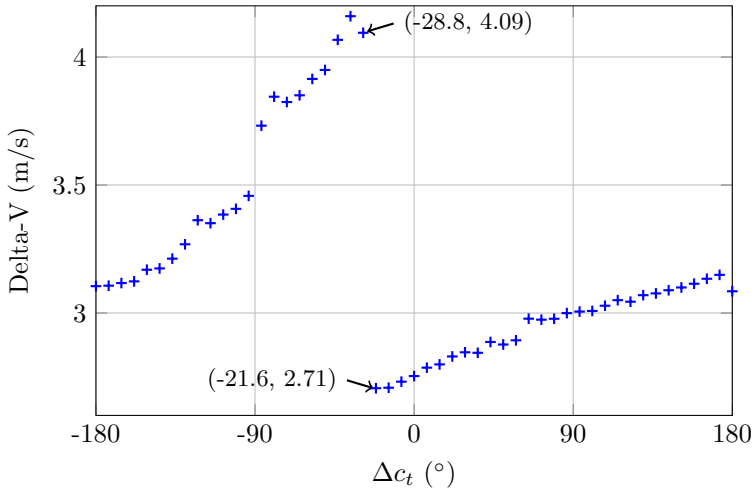

Figure 3.46: Total delta-V as a function of the targeted angular separation.

increases over time. The resulting trajectory leads the deputy to move on a lower altitude orbit that brings it ahead of the chief and then on a higher altitude orbit to move back to the extremity of the structure, on the targeted CRO. We also notice that the cross-track excursion is much larger for this trajectory. Once the spacecraft is on the CRO and spirals around the structure, both trajectories are very similar. Hence, we see that even if the desired angular separations are very close to each other,

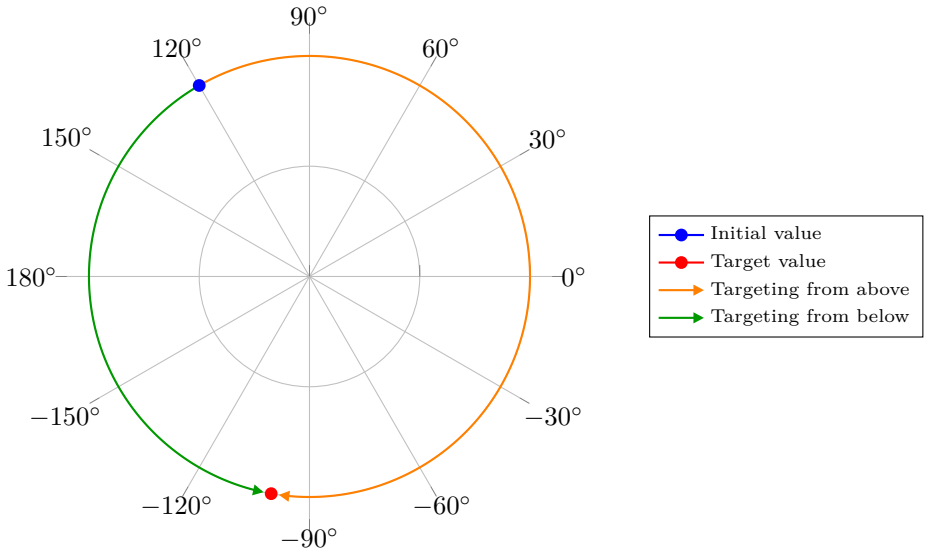

Figure 3.47: Targeting of an angle by increasing/decreasing the initial angle.

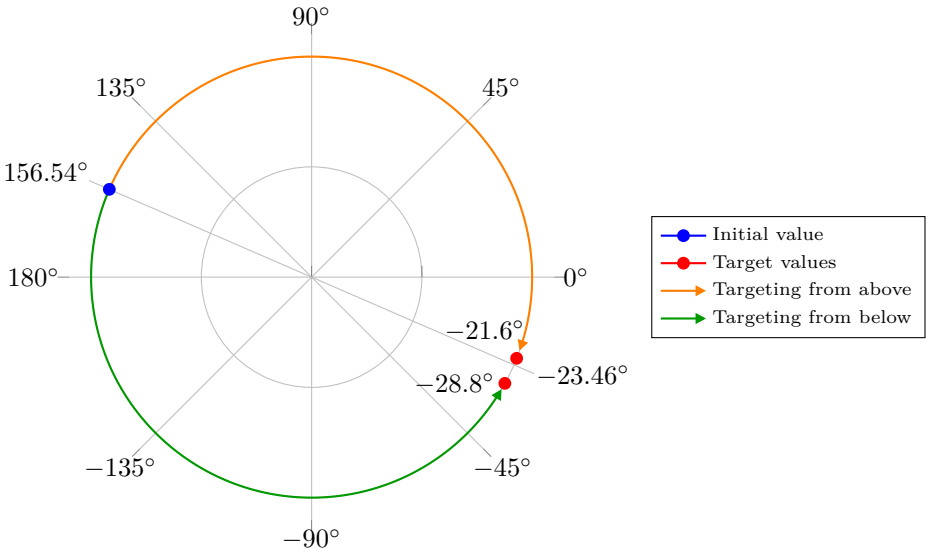

Figure 3.48: Path followed by the central anomaly for different targeted angular separations.

the path selected by the algorithm results in two very different relative trajectories, one of them requiring a significantly higher total delta-V than the other.

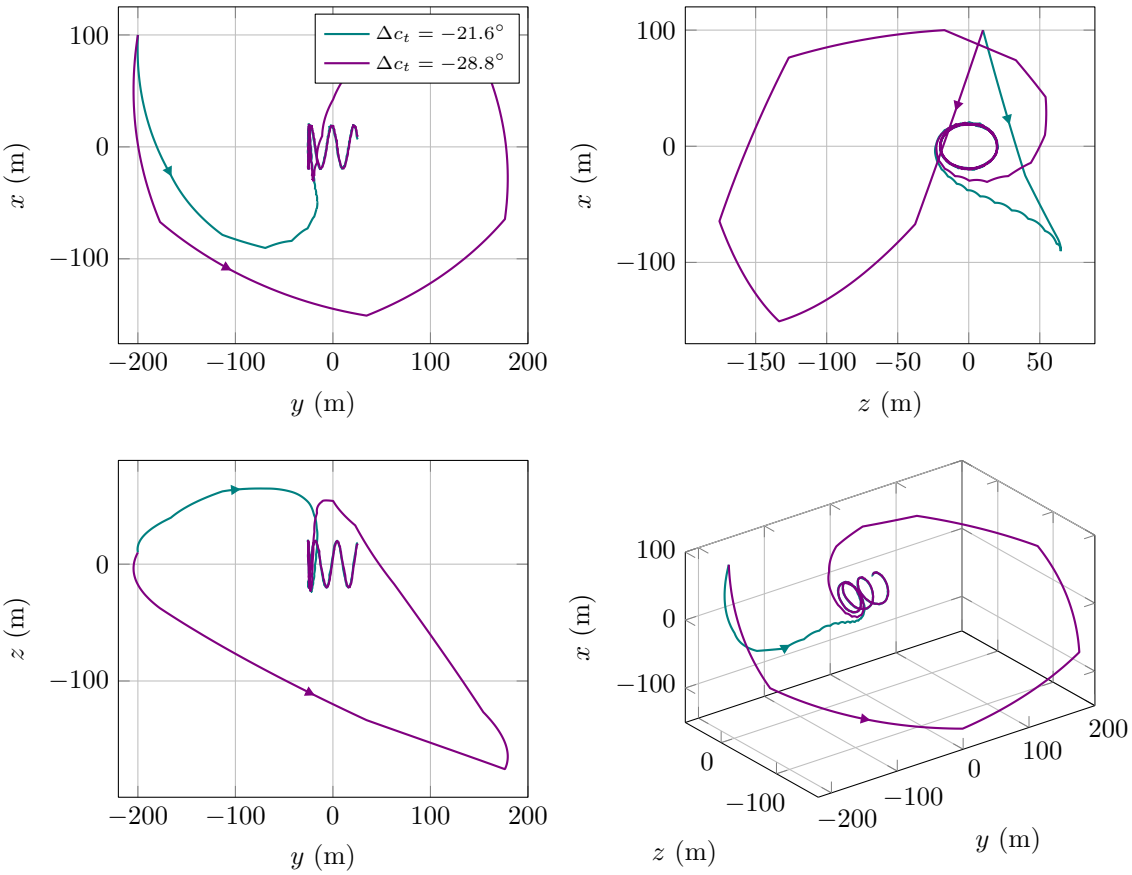

Figure 3.49: Relative trajectory for different Δc_t.

3.2.4 Tetrahedron

In this scenario, a tetrahedral formation composed of four spacecraft is designed. This geometry has been used for the Multiscale Magnetospheric Spacecraft (MMS) formation which collects data to study a process known as magnetic reconnection between the Earth's and the Sun's magnetic fields. The mission was launched in 2015 and is still operating as of 2020 [100]. The mission is divided in two phases: In Phase I, the formation evolves on a highly eccentric orbit characterized by a perigee of $r_p = 1.2R_\oplus$ and apogee $r_a = 12R_\oplus$ resulting in an eccentricity of 0.8182. The distance between each agent lies between 10 to 160 km. In that phase, science measurements are taken when the formation is further than $9R_\oplus$ from Earth and is within 30° of the Earth-Sun line on the sunward side. For Phase II, an orbit with $r_p = 1.2R_\oplus$ and

$r_a = 25R_\oplus$ is designed, resulting in an eccentricity of 0.9084, and the distance between each deputy is between 30 to 400 km. Science is conducted when the formation is at least $15R_\oplus$ away from the Earth and within 30-40° of the Earth-Sun line on the shadow side [101]. In both phases, the agents of the formation form a nearly perfect tetrahedron when they reach the apogee.

Since the control methodology is based on the circular orbit assumption, it is assumed that the chief is on a circular orbit for this scenario and a tetrahedron with a side length of one kilometer is maintained over the entire orbit. The desired formation geometry is shown in Fig. 3.50.

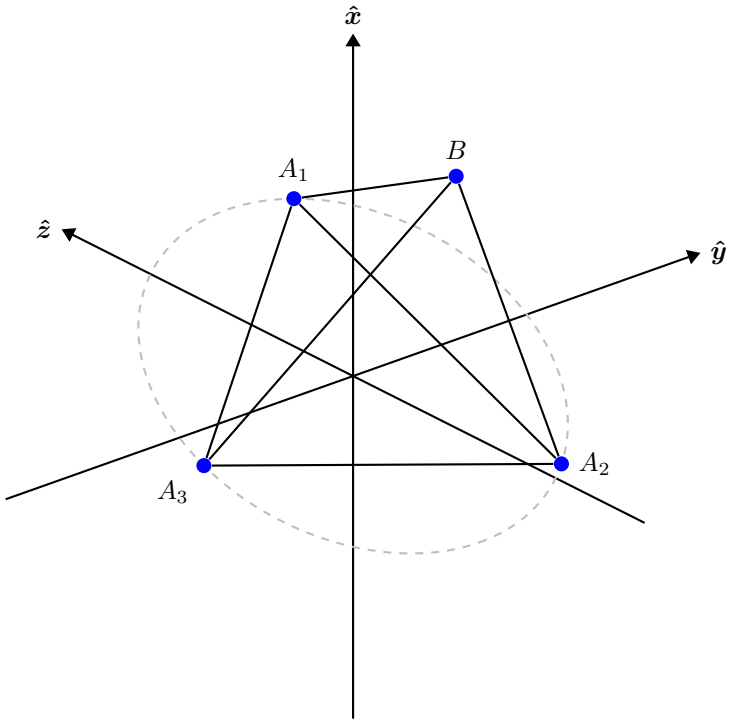

Figure 3.50: Tetrahedral geometry.

This geometry is designed by equally distributing three spacecraft on a CRO and positioning the fourth one in the x-z plane to complete the tetrahedron and such that all agents are equidistant to each other. The three spacecraft on the CRO will naturally stay on the relative orbit while the fourth one will require frequent maneuvers to maintain its fixed position. This formation is designed using ROEs

with a single design parameter, d, corresponding to the inter-spacecraft distance. For the CRO, a distance d between the spacecraft is obtained if the semi-major axis is set to

$$a = \frac{1}{\sqrt{3}} d \tag{3.35}$$

The position of the individual node, B, can be computed geometrically from Fig. 3.51.

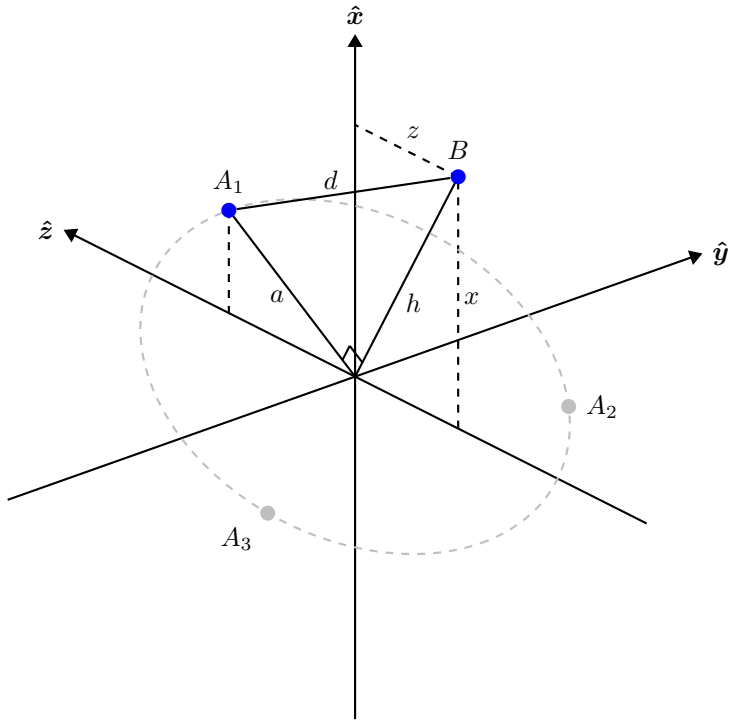

Figure 3.51: Position of the individual node B.

The distance between the vertex and the origin of the frame is given by

$$h = \sqrt{d^2 - a^2} = \sqrt{d^2 - \frac{1}{3} d^2} = \sqrt{\frac{2}{3}} d \tag{3.36}$$

and the position of the vertex in the LVLH frame is then

$$x = h\cos\frac{\pi}{6} = \frac{1}{\sqrt{2}}d \tag{3.37}$$

$$y = 0 \tag{3.38}$$

$$z = -h\sin\frac{\pi}{6} = -\frac{1}{\sqrt{6}}d \tag{3.39}$$

Since the spacecraft has to maintain a fixed position, its relative velocity must be null. This set of six LVLH Cartesian coordinates can be converted into the equivalent ROEs representation. For an inter-spacecraft separation of $d = 1$ km, the ROEs are

$$\boldsymbol{\rho}_t = \begin{bmatrix} 2.83 \text{ km} & 0 \text{ km} & 4.24 \text{ km} & 0^\circ & 0.41 \text{ km} & -90^\circ \end{bmatrix}^T$$

Hence, the sets of target elements for the CRO and the individual node are as displayed in Table 3.16. In addition to these elements, the agents on the CRO target

Table 3.16: Sets of target ROEs for the tetrahedron formation.

Orbit	x_r (km)	y_r (km)	a_r (km)	A_z (km)	γ (°)
CRO	0	0	0.58	0.5	-90
Individual node	2.83	0	4.24	0.41	-90

angular separations of $\Delta E_{rt} = 0^\circ, \pm 120^\circ$ and the individual node targets a constant relative eccentric anomaly of $E_{rt} = 0^\circ$. Since the individual node targets a fixed value for E_r, the recursive relations used to compute the attractive waypoints must be updated for that spacecraft. Eq. (2.256) defined in section 2.3.2 thus becomes

$$\tilde{E}_r(k) = (\tilde{E}_r(0) - E_{rt})(1 - k_a Q_{a4} dt)^k + E_{rt} \tag{3.40}$$

It is assumed that the spacecraft are released behind the chief on a slightly lower orbit. The initial states are listed in Table 3.17 and printed in Fig. 3.52.

Table 3.17: Initial states for the tetrahedron formation establishment.

Spacecraft	x_0 (m)	y_0 (m)	z_0 (m)	$\dot{x}_0$ (cm/s)	$\dot{y}_0$ (cm/s)	$\dot{z}_0$ (cm/s)
A1	-496.6	-2077.3	664.3	-8.76	22.65	15.89
A2	-412.3	-2195.2	491.9	-9.22	28.04	-3.07
A3	-705.9	-1754.4	690.8	-29.29	35.26	10.35
B	-322.5	-2409.2	517.8	-9.37	41.13	7.89

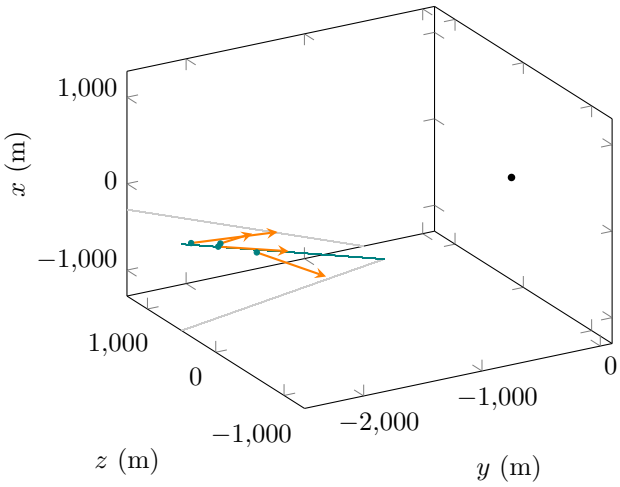

Figure 3.52: Initial relative positions and velocities (not to scale) for the tetrahedron formation establishment.

The four spacecraft in the formation are identical and have an octagonal shape of width 3.5 m and height 1.2 m. Their wet mass is 1,250 kg and they are equipped with 12 thrusters sized to be used for small orbit maintenance maneuvers as well as large reconfiguration maneuvers [100]. Based on these values, the physical properties shown in Table 3.18 along with maneuver's amplitude bounds of $\Delta V_{min} = 2$ mm/s and $\Delta V_{max} = 5$ m/s are assumed for the simulation.

The APFs are designed with the set of parameters shown in Table 3.19. The relatively small time interval between two attractive maneuvers is required to maintain the fixed relative position of spacecraft B.

Table 3.18: Spacecraft properties for the tetrahedron formation.

$m_{\text{wet}} = 1250$ kg
$C_d = 1.8$
$C_r = 1.5$
$A = 6.85$ m^2
$A_{\odot} = 6.85$ m^2
$I_{sp} = 220$ s

Table 3.19: Parameters of the APF used for the tetrahedron formation establishment.

$T_m = 5$ min
$\tau_c = 6$ h
$d_c = 5$ m
$T_c = 5$ s
$r_s = 2$ m
$r_{\text{SOI}} = 100$ m
$p = 0.01$
$\upsilon = 3$

The initial conditions of the chief expressed in terms of classical orbital elements are

$$a = R_{\oplus} + 1500 \text{ km} \qquad e = 0 \qquad i = 28^{\circ} \qquad \Omega = 0^{\circ} \qquad \omega = 0^{\circ} \qquad M = 0^{\circ}$$

The trajectories are propagated for 8 hours and are shown in Fig. 3.53[4].

We see in Fig. 3.53 that spacecraft B (violet) follows a rather direct trajectory, approaching its target from behind and from a higher altitude than the chief. Since the natural motion for a spacecraft above the chief would be to move in the negative y direction, we expect the delta-V used by spacecraft B to be large. The cumulative delta-V used by each agent is printed in Table 3.20. As can be seen in that table, the delta-V used by spacecraft B is much larger than the delta-V used by the other

[4]An animation of the formation establishment is available at `https://purr.purdue.edu/publications/3389/1`.

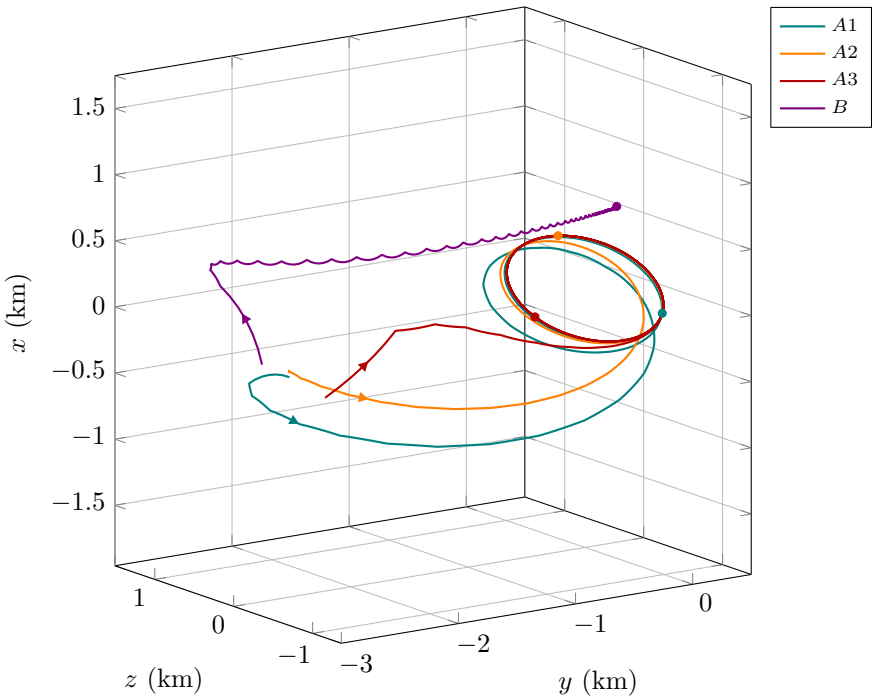

Figure 3.53: Trajectories of the tetrahedron formation establishment with the positions 8 hours after deployment (dots).

Table 3.20: Delta-V consumption for the tetrahedron formation establishment.

Spacecraft	Delta-V (m/s)
A1	7.66
A2	3.27
A3	5.81
B	59.25
Mean: 19.00 m/s	Std: 26.89 m/s

spacecraft. This can be explained by the approach trajectory followed during the initial phase of the reconfiguration as well as the requirement to constantly thrust to maintain a fixed relative position. This position being in the positive x and z planes, the natural tendency would be to move in the negative x and z directions, which must be counteracted. Fig. 3.54 shows the time history of the maneuvers performed by agent B. Many maneuvers are applied in the negative x direction in order to counter

the natural drift in the negative y direction and bring the spacecraft back to its target position.

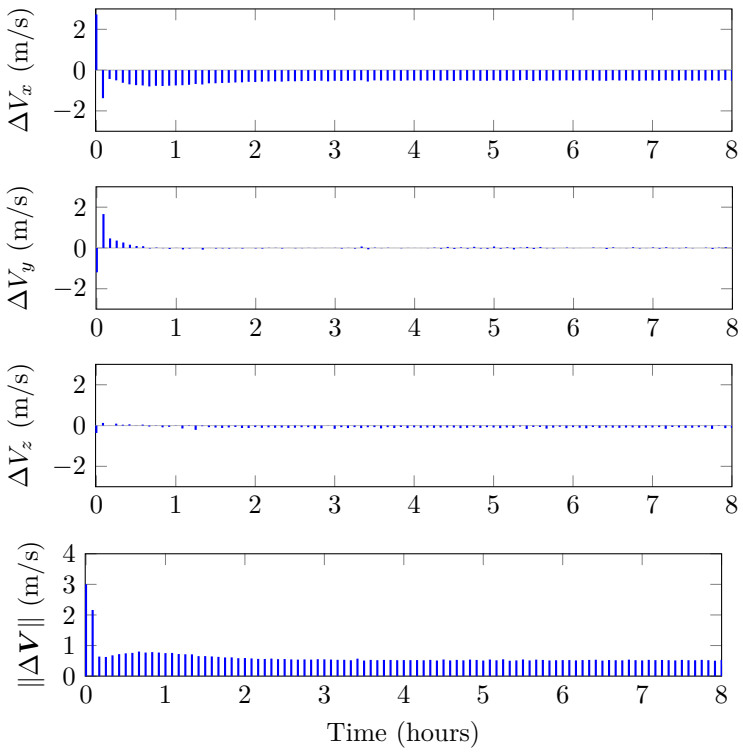

Figure 3.54: Time history of the maneuvers performed by spacecraft B.

The relative trajectory together with the waypoints computed for spacecraft B is displayed in Fig. 3.55. The first waypoint is nearly missed by the spacecraft due to the nonlinearities and orbital perturbations. A closer look at the target position (Fig. 3.56) reveals that the spacecraft has to constantly adjust its position to stay near the target. Even if the waypoints are not reached, the spacecraft stays within about 20 m from the target. Looking at the time evolution of the ROEs in Fig. 3.57, we see that the variations observed in Fig. 3.56 mostly translate into oscillations of the y_r and a_r elements around the target value. Since these two elements are the only time-varying ROEs, it is expected that they would drift if the deputy was not controlled.

The error between the actual position and the target position is printed in Fig. 3.58. The difference between the actual position and target position indicates that

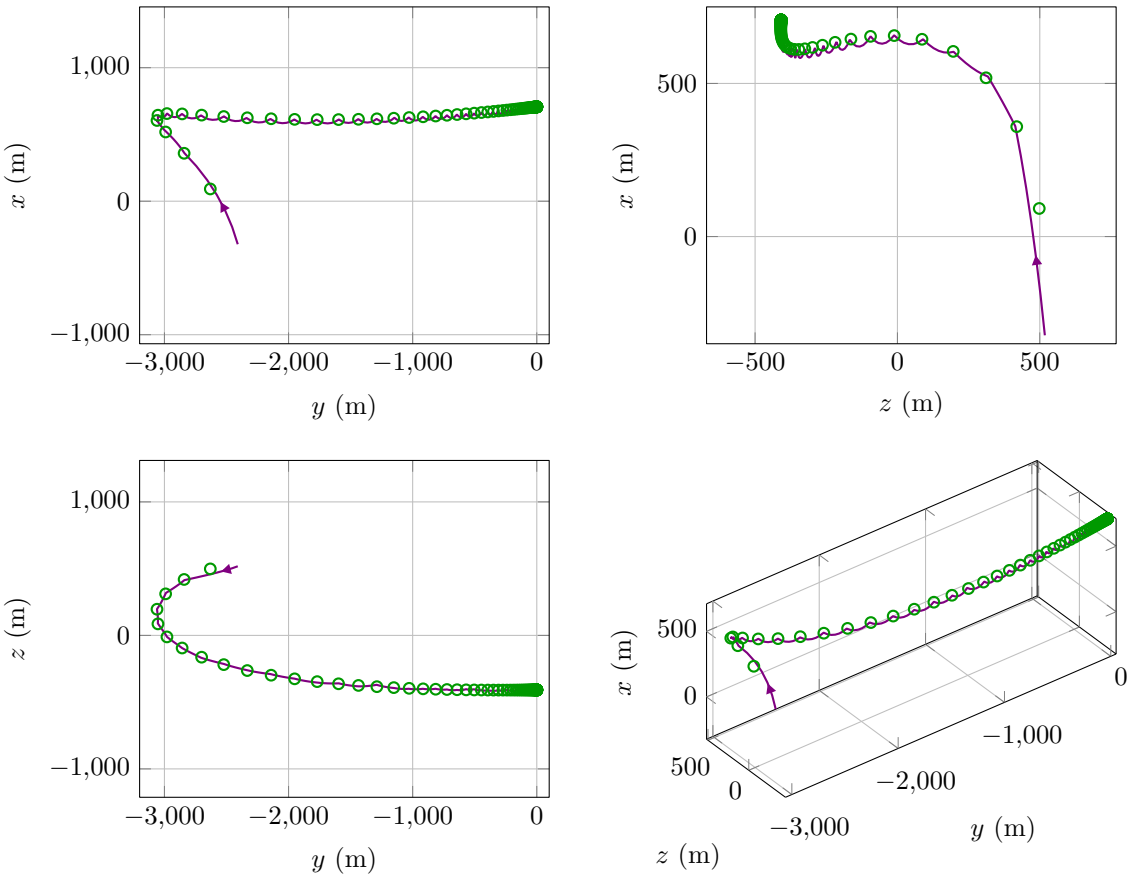

Figure 3.55: Projection of the relative trajectory together with the attractive waypoints of spacecraft B.

the three spacecraft on the CRO achieve a good accuracy with an error of a few meters only. For agent B, however, the error is larger and stays within 20 meters as previously suggested in Fig. 3.56. This metric gives an information on how well each agent is individually located but doesn't provide any insight into the "quality" of the tetrahedron. In order to assess this quality, two metrics called Glassmeier and Robert-Roux metrics [102–104] are used. The first parameter developed by Glassmeier is given by

$$Q_G = \frac{V}{V_{ideal}} + \frac{A}{A_{ideal}} + 1 \tag{3.41}$$

with V the volume of the tetrahedron, V_{ideal} the volume of a regular tetrahedron with edge length equal to the average of the six distances between the vertices, A the

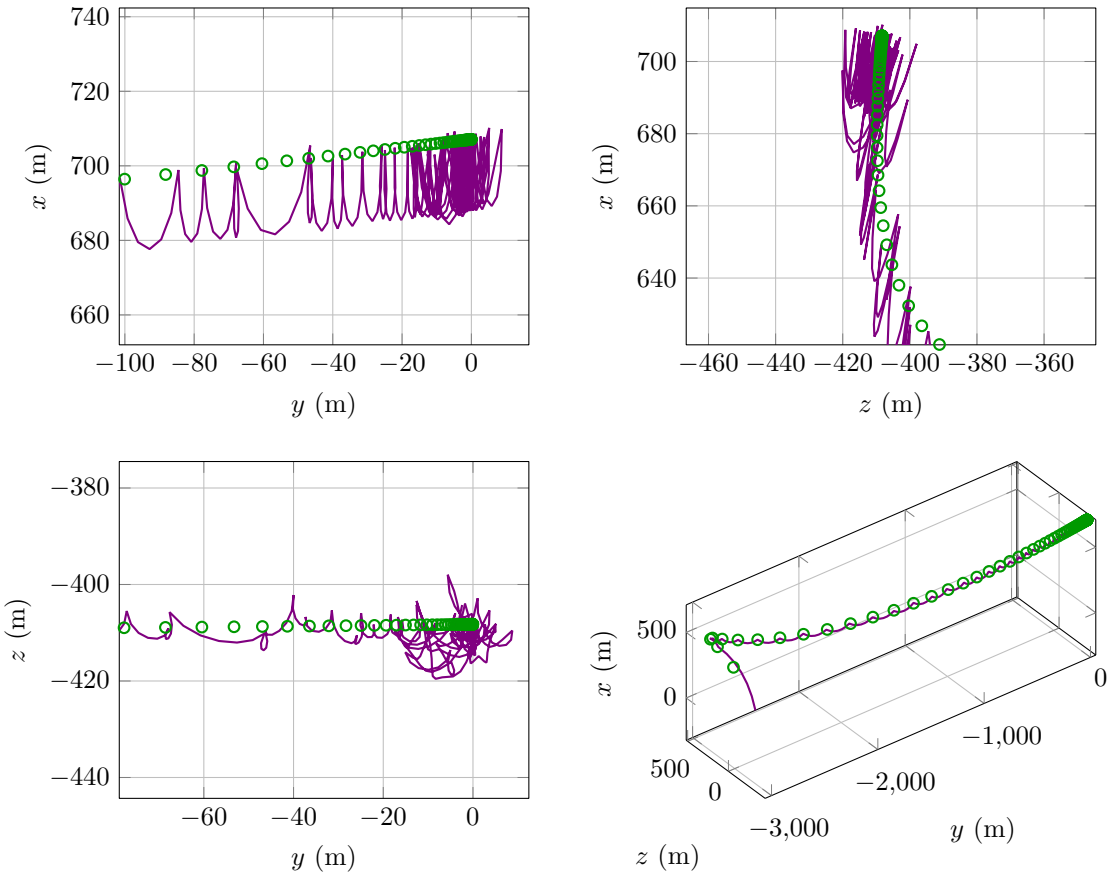

Figure 3.56: Zoom on the target position of spacecraft B.

surface area of the tetrahedron, and A_{ideal} the surface area of a regular tetrahedron with edge length equal to the average of the six distances. This parameter describes the dimensionality of the tetrahedron and takes a value between 1 and 3. A value of $Q_G = 1$ indicates that all four vertices are collinear, $Q_G = 2$ that all four vertices are coplanar, and $Q_G = 3$ that the four vertices form a regular tetrahedron. If $\boldsymbol{r}_i$, $i = 1, \ldots, 4$ are the coordinates of the four vertices of the tetrahedron (i.e. the LVLH relative positions of the four spacecraft), then the volume of the tetrahedron is

$$V = \frac{1}{6} \left| (\boldsymbol{r}_1 - \boldsymbol{r}_4) \cdot [(\boldsymbol{r}_2 - \boldsymbol{r}_4) \times (\boldsymbol{r}_3 - \boldsymbol{r}_4)] \right| \tag{3.42}$$

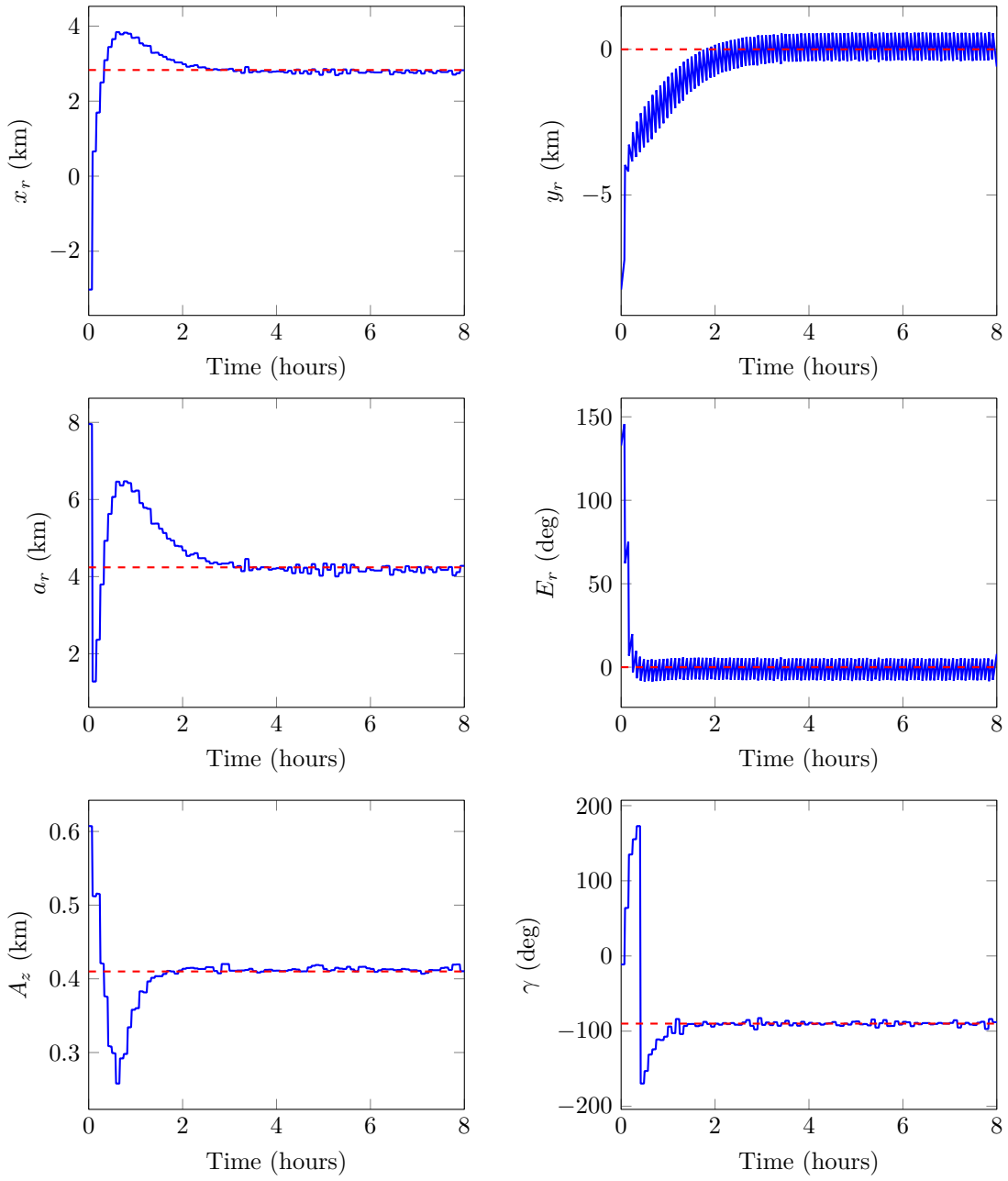

Figure 3.57: Time evolution of the ROEs (blue) and target values (dashed red) of spacecraft B.

The volume of the ideal tetrahedron is obtained by computing the average distance between the vertices:

$$\bar{d} = \frac{1}{6} \sum_{i=1}^{3} \sum_{j=i+1}^{4} \|\boldsymbol{r}_i - \boldsymbol{r}_j\| \tag{3.43}$$

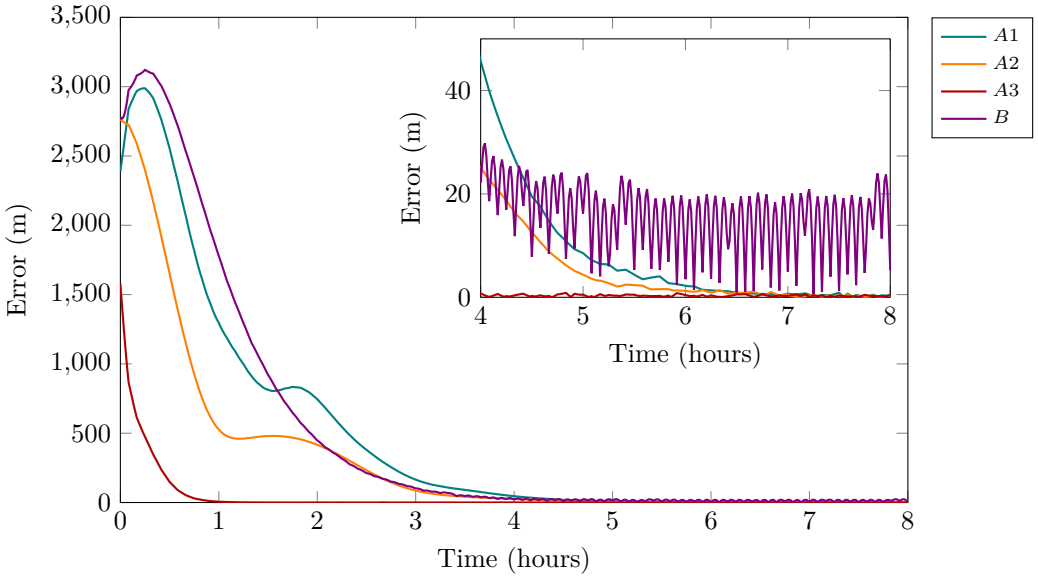

Figure 3.58: Targeting errors of the tetrahedron formation establishment.

and using this value to compute the ideal volume results in

$$V_{ideal} = \frac{\bar{d}^3}{6\sqrt{2}} \tag{3.44}$$

The surface area of the tetrahedron is computed using Heron's formula. For a triangle with sides of lengths a, b, and c, the surface area is given by

$$S = \sqrt{s(s-a)(s-b)(s-c)} \tag{3.45}$$

where $s = \frac{1}{2}(a+b+c)$ is the semi perimeter of the triangle. This formula is used to compute the surface area of each of the four faces which are then summed up to get the total surface of the tetrahedron:

$$A = \sum_{i=1}^{4} S_i \tag{3.46}$$

Lastly, the surface area of the ideal tetrahedron is computed with

$$A_{ideal} = \sqrt{3}\bar{d}^2 \tag{3.47}$$

The second parameter, the Robert-Roux parameter, measures the regularity of the tetrahedron and is given by

$$Q_R = \mathcal{N}\left(\frac{V}{V_{sphere}}\right)^{\frac{1}{3}} \tag{3.48}$$

where $\mathcal{N}$ is a normalization factor to make $Q_R = 1$ for a regular tetrahedron, V the volume of the tetrahedron given by Eq. (3.42), and V_{sphere} the volume of a sphere that circumscribes the tetrahedron, with all four vertices on the surface. The circumscribed sphere is found by computing the location of the point which is equidistant to all four vertices of the tetrahedron. If $\boldsymbol{r}_o$ is the center of the sphere, and r its radius, then

$$(\boldsymbol{r}_i - \boldsymbol{r}_o) \cdot (\boldsymbol{r}_i - \boldsymbol{r}_o) = r^2,\ i = 1, 2, 3, 4 \tag{3.49}$$

or equivalently

$$x_i^2 + y_i^2 + z_i^2 + ax + by + cz + d = 0,\ i = 1, 2, 3, 4 \tag{3.50}$$

with $a = -2x_0$, $b = -2y_0$, $c = -2z_0$, and $d = x_0^2 + y_0^2 + z_0^2 - r^2$. This system can be solved for a, b, c, and d using Cramer's rule. The radius of the circumscribed sphere is then

$$r = \frac{1}{2}\sqrt{a^2 + b^2 + c^2 - 4d} \tag{3.51}$$

and its volume

$$V_{sphere} = \frac{4}{3}\pi r^3 \tag{3.52}$$

For a regular tetrahedron of side length l, the volume is $V = \frac{l^3}{6\sqrt{2}}$ and the volume of the sphere $V_{sphere} = \frac{4}{3}\pi\left(\frac{\sqrt{6}}{4}l\right)^3$. Since $Q_R \triangleq 1$ for a regular tetrahedron, Eq. (3.48) is solved for $\mathcal{N}$ which yields

$$\mathcal{N} = \left(\frac{9\pi}{2\sqrt{3}}\right)^{\frac{1}{3}} \tag{3.53}$$

and therefore

$$Q_R = \left(\frac{9\pi}{2\sqrt{3}}\frac{V}{V_{sphere}}\right)^{\frac{1}{3}} = \frac{1}{r}\left(\frac{9\sqrt{3}}{8}V\right)^{\frac{1}{3}} \tag{3.54}$$

Fig. 3.59 shows the time evolution of these two metrics for the establishment of the tetrahedron formation. We see that the initial configuration of the formation is

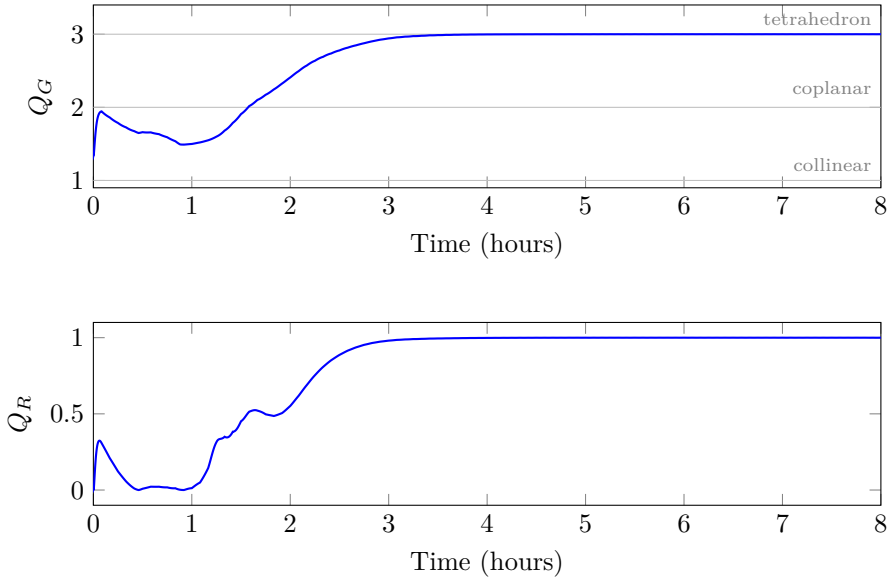

Figure 3.59: Glassmeier and Robert-Roux parameters for the tetrahedron formation establishment.

between collinear and coplanar. After the initial maneuvers, the spacecraft almost reach a coplanar configuration, go into a more disorganized state and then briefly transition into a coplanar configuration before reaching a tetrahedral arrangement about four hours after deployment. The regularity of the tetrahedron, Q_R, stays close to zero during the first hour of reconfiguration and then reaches a value close to

1 after about 4 hours. A closer look at these two metrics reveals oscillations of the metrics near the optimal values of $Q_G = 3$ and $Q_R = 1$, Fig. 3.60.

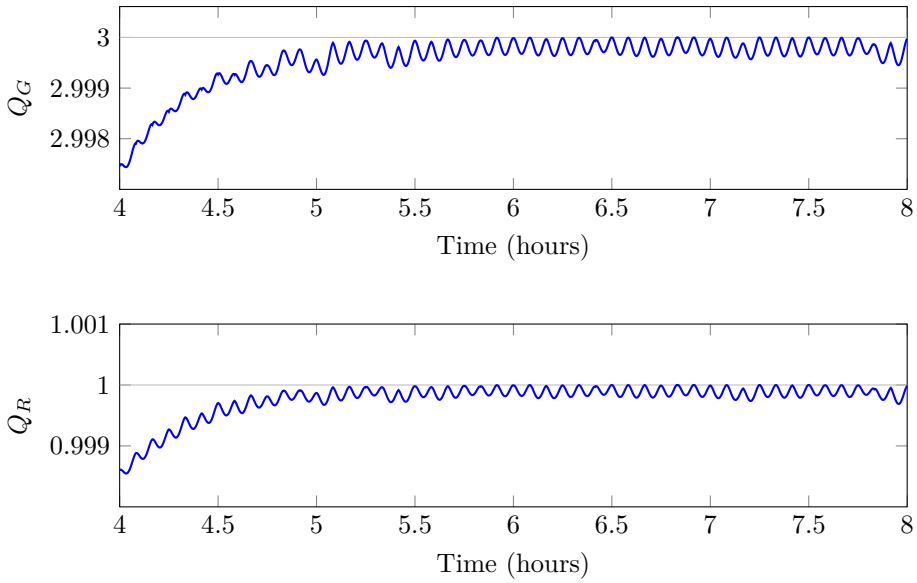

Figure 3.60: Oscillations of the dimensionality and regularity of the tetrahedron near the optimal values.

These oscillations are mostly due to the position of spacecraft B that requires constant actuation. If a larger time interval between the maneuvers, T_m, is used, the regularity of the tetrahedron will be lower. These results show that with the selected set of parameters, the control algorithm is able to maintain the formation in a nearly perfectly regular tetrahedron. A limitation of the control methodology when used with relative orbits that require frequent maneuvers is also illustrated with the high delta-V requirement to maintain spacecraft B on its target orbit.

4. CONCLUSIONS

In this work, a new control methodology has been presented to design and control spacecraft formations based on relative orbital element and artificial potential function formalisms. Different sets of relative orbital elements are used to describe the relative motion and enable the intuitive design of geometrically complex spacecraft formations. The computational efficiency of the artificial potential function methodology is leveraged to introduce a control algorithm able to continuously monitor the risk of collisions.

The formulation of an APF based on relative orbital element sets is introduced, enabling full control of the relative position and velocity of spacecraft. The inclusion of angular quantities in the formulation allows the targeting of specific positions on given relative orbits, thus allowing the control and establishment of spacecraft formations. The introduction of a total APF as the linear combination of an attractive quadratic potential for goal seeking and an ellipsoidal repulsive potential for obstacle avoidance results in autonomous collision detection and avoidance suitable for onboard applications. Any convergence issues that may be caused by the emergence of local minima and shift of the global minimum of the APF are mitigated by decoupling the maneuvers performed to target a goal from those performed to avoid collisions.

Different methods to automatically select the parameters of the model are presented. Considerations on fuel minimization allow the derivation of rules to compute the scaling parameters and some of the shaping coefficients of the attractive potential, and contribute to a significant reduction of the average delta-V consumption. These methods also replace some parameters with quantities having a stronger physical interpretation, thus facilitating intuitive tuning of the control algorithm.

The performance and limitations of the control algorithm are assessed using numerical simulations of four scenarios in a high-fidelity simulation environment that

accounts for geopotential perturbations, atmospheric drag, solar radiation pressure, and third-body effects. In the first scenario, a 10-spacecraft triangular lattice is designed and established. The cumulative delta-V of the formation establishment and the computational cost of the method are compared with a model predictive control algorithm. The sub-optimal nature of the APF methodology results in a cumulative delta-V which is about two and a half times larger for the APF-based method than for the MPC method. However, the computational efficiency of the method proposed in this work results in a computation time which is about four times shorter than the time required by the MPC method, demonstrating the suitability of the method for on-board applications. Next, the establishment of a formation composed of 37-spacecraft is presented. Two hexagonal lattices on two different relative orbital planes are designed with the definition of target relative orbits in terms of ROEs. The performance of the collision avoidance system is stressed with the high density of spacecraft in close proximity and preventive measures on the design of the formation are proposed to reduce the number of collision avoidance maneuvers. The convergence of the control algorithm is demonstrated and collision avoidance maneuvers happening during the reconfiguration are successfully handled. The third scenario illustrates the visual inspection of an on-orbit structure by a single spacecraft. The use of GROEs is illustrated and a method to target time-varying elements is proposed to create a helix trajectory around the structure. This simulation shows the successful targeting of a relative trajectory that requires frequent maneuvers and illustrates the flexibility of the control algorithm developed in this work. A limitation of the algorithm is also highlighted with the way angular values are targeted in the current implementation. Finally, in the last scenario, a tetrahedral geometry is established with a 1 km side length. The design of this formation requires one of the agents to maintain a fixed out-of-plane position, resulting in a large cumulative delta-V.

In summary, the control methodology introduced in this work enables the intuitive design and efficient control of spacecraft formations. The use of two different relative orbital element sets providing insight into the relative motion enables the

intuitive design of complex formation geometries. The formulation of an artificial potential function in terms of these elements allows the targeting of relative orbits and the straightforward integration of collision avoidance within the method. A computationally efficient algorithm is obtained as a result of the analytic nature of the control methodology and can be run on-board spacecraft to monitor collision risks in near real-time. The autonomous computation of several parameters of the algorithm developed in this manuscript facilitates the application of the method to different scenarios and contributes towards an increased level of autonomy in the control of spacecraft formations.

5. FUTURE WORK

The development of robust algorithms able to autonomously control spacecraft formations operating in a wide range of different situations still presents many challenges. The following paragraphs discuss several suggestions to improve the algorithm presented in this work.

The numerical simulation of the structure on-orbit visual inspection presented in section 3.2.3 illustrates some challenges of targeting angular values. The periodicity of these quantities makes it possible to target a value from above by decreasing the current angle or from below by increasing it. In the current implementation, the direction is selected such that the difference between the two angles is minimum. This direction, however, is not guaranteed to follow the natural time-evolution of the parameter and might therefore result in larger maneuvers than what would be achieved if the angle were moved in the direction of its natural time-evolution. Further investigation of the optimal angular targeting direction based on the relative state of the spacecraft and targeted value should be conducted to find a method that consistently results in a lower fuel consumption.

In the formulation of the quadratic function used for the attractive portion of the artificial potential, terms representing distances are summed up with terms representing angles. The addition of quantities having different dimensions should be avoided in order to keep a meaningful quantity but it is not harmful in this case since the components of the gradient of the APF still have the correct dimensions. Nonetheless, it would be interesting to investigate how the different scales of these values impact the convergence rate of the algorithm. The distances can take values from a few hundred of meters or even kilometers down to a few centimeters whereas the angles are bounded within 2π radians. Normalizing these quantities might help by having

each element converge at the same rate and equally contribute to the decrease of the artificial potential, which might result in a lower fuel consumption.

The analysis of the autonomous computation of the shaping coefficients for the attractive potential, $\mathbf{Q}_a$, led to a method to automatically select the coefficient associated with the relative eccentric anomaly. One of the difficulties in deriving rules to automatically compute these coefficients in the current formulation is that they are coupled through the relative velocity in the three directions. For instance, delaying the targeting of one of them might impact the convergence of some of the other elements which could result in the algorithm to diverge. A further investigation of the autonomous computation of the other coefficients might yield a method to further reduce the fuel consumption of formations establishment. It is important to realize that the trade-off between time of convergence and fuel minimization is most often driven by mission requirements and therefore at least one parameter reflecting this design decision will be required in the formulation of the control methodology.

The control algorithm presented in this work uses the ROEs and GROEs which are derived from the CW equations as well as a linear targeter also derived from the CW equations. Since the derivation of these equations is based on the assumption that the chief is on a circular orbit, the control methodology introduced in this work is limited to this assumption. Investigating the possibility to use a set of relative orbital elements valid for eccentric orbits together with the design of a targeter based on the Tschauner-Hempel or Yamanaka-Ankersen equations for instance, may result in the generalization of the proposed algorithm to eccentric orbits.

Finally, if the shape of the obstacle cannot be approximated as a point or a sphere such as in the example of visual inspection of a structure (Section 3.2.3), using a superquadric function for the repulsive potential might prove useful. This family of functions allows to represent various parametric geometries using relatively simple mathematical expressions, and can be incorporated within the APF methodology without increasing the computational cost too much. The formulation of an APF using superquadric functions for the repulsive potential has been studied in [69,70] but

it would be interesting to include it in the ROEs-based APF methodology presented in this work.

REFERENCES

[1] Jacqueline Le Moigne. Distributed Spacecraft Missions (DSM) Technology Development at NASA Goddard Space Flight Center. In *International Geoscience And Remote Sensing Symposium (IGARSS'2018)*, Valencia, Spain, 2018.

[2] A Poghosyan, I Lluch, H Matevosyan, A Lamb, C A Moreno, C Taylor, A Golkar, J Cote, S Pierotti, J Grave, J Narkiewicz, S Topczewski, M Sochacki, E Lancheros, H Park, A Camps, Thales Alenia Space, Politechnika Warszawska, and Universitat Politecnica De Catalunya. Unified Classification for Distributed Satellite Systems. *International Federated and Fractionated Satellite Systems Workshop*, pages 1–8, 2016.

[3] Daniel P. Scharf, Fred Y. Hadaegh, and Scott R. Ploen. A Survey of Spacecraft Formation Flying Guidance and Control (Part I): Guidance. In *Proceedings of the 2003 American Control Conference*, pages 1733–1739, Denver, CO, 2003.

[4] Kyle T. Alfriend, Srinivas R. Vadali, Pini Gurfil, Jonathan P. How, and Louis S. Berger. *Spacecraft Formation Flying*. Elsevier, 2010.

[5] O. Brown and P. Eremenko. Fractionated Space Architectures: A Vision for Responsive Space. In *4th Responsive Space Conference RS4-2006-1002*, Los Angeles, CA, 2006.

[6] Alessandro Golkar and Ignasi Lluch I Cruz. The Federated Satellite Systems Paradigm: Concept and Business Case Evaluation. *Acta Astronautica*, 111:230–248, 2015.

[7] W. H. Clohessy and R. S. Wiltshire. Terminal Guidance System for Satellite Rendezvous. *Journal of the Aerospace Sciences*, 27(9):653–658, 1960.

[8] J. Pieter De Vries. Elliptic Elements in Terms of Small Increments of Position and Velocity Components. *AIAA Journal*, 1(11):2626–2629, 1963.

[9] J. Tschauner and P. Hempel. Optimale Beschleunigungsprogramme für das Rendezvous-Manöver. *Astronautica Acta*, 10:296–307, 1964.

[10] Derek F. Lawden. *Optimal Trajectories for Space Navigation*. Butterworths, London, 1963.

[11] Derek F. Lawden. Fundamentals of Space Navigation. *British Interplanetary Society Journal*, 13:87–101, 1954.

[12] Thomas E. Carter. New Form for the Optimal Rendezvous Equations Near Keplerian Orbits. *Journal of Guidance, Control, and Dynamics*, 13(1):183–186, 1990.

[13] Koji Yamanaka and Finn Ankersen. New State Transition Matrix for Relative Motion on an Arbitrary Elliptical Orbit. *Journal of Guidance, Control, and Dynamics*, 25(1):60–66, 2002.

[14] Howard S. London. Second Approximation to the Solution of the Rendezvous Equations. *AIAA Journal*, 1(7):1691–1693, 1963.

[15] Maurice L. Anthony and Frank T. Sasaki. Rendezvous Problem for Nearly Circular Orbits. *AIAA Journal*, 3(9):1666–1673, 1965.

[16] Sesha S. Vaddi, Srinivas R. Vadali, and Kyle T. Alfriend. Formation Flying: Accommodating Nonlinearity and Eccentricity Perturbations. *Journal of Guidance, Control, and Dynamics*, 26(2):214–223, 2003.

[17] Matthew Willis, Alan Lovell, and Simone D'Amico. Second-Order Analytical Solution for Relative Motion on Arbitrarily Eccentric Orbits. In *29th AAS/AIAA Space Flight Mechanics Meeting*, Ka'anapali, HI, 2019.

[18] Kyle T Alfriend, Hanspeter Schaub, and Dong-Woo Gim. Gravitational Perturbations , Nonlinearity and Circular Orbit Assumption Effects on Formation Flying Control Strategies. In *AAS Guidance and Control Conference*, Breckenridge, CO, 2000.

[19] Mayer Humi and Thomas Carter. Rendezvous Equations in a Central-Force Field With Linear Drag. *Journal of Guidance, Control, and Dynamics*, 25(1):74–79, 2002.

[20] Thomas Carter and Mayer Humi. Clohessy-Wiltshire Equations Modified to Include Quadratic Drag. *Advances in the Astronautical Sciences*, 114 III(6):2025–2040, 2003.

[21] S. Schweighart and R. Sedwick. A Perturbative Analysis of Geopotential Disturbances for Satellite Cluster Formation Flying. *IEEE Aerospace Conference Proceedings*, 2, 2001.

[22] Samuel A. Schweighart and Raymond J. Sedwick. High-Fidelity Linearized J2 Model for Satellite Formation Flight. *Journal of Guidance, Control, and Dynamics*, 25(6):1073–1080, 2002.

[23] Srinivas R. Vadali. Model for Linearized Satellite Relative Motion About a J2-Perturbed Mean Circular Orbit. *Journal of Guidance, Control, and Dynamics*, 32(5):1687–1691, 2009.

[24] Hanspeter Schaub and Kyle T. Alfriend. J2 Invariant Relative Orbits for Spacecraft Formations. *Celestial Mechanics and Dynamical Astronomy*, 79(2):77–95, 2001.

[25] Daniel Morgan, Soon Jo Chung, Lars Blackmore, Behcet Acikmese, David Bayard, and Fred Y. Hadaegh. Swarm-Keeping Strategies for Spacecraft Under J2 and Atmospheric Drag Perturbations. *Journal of Guidance, Control, and Dynamics*, 35(5):1492–1506, 2012.

[26] Hanspeter Schaub and Kyle T. Alfriend. Hybrid Cartesian and Orbit Element Feedback Law for Formation Flying Spacecraft. *Journal of Guidance, Control, and Dynamics*, 25(2):387–393, 2002.

[27] Thomas Alan Lovell and Steven G. Tragesser. Guidance for Relative Motion of Low Earth Orbit Spacecraft Based on Relative Orbit Elements. In *AIAA/AAS Astrodynamics Specialist Conference and Exhibit*, Providence, RI, 2004.

[28] Hanspeter Schaub. Relative Orbit Geometry Through Classical Orbit Element Differences. *Journal of Guidance, Control, and Dynamics*, 27(5):839–848, 2004.

[29] N. Jeremy Kasdin, Pini Gurfil, and Egemen Kolemen. Canonical Modelling of Relative Spacecraft Motion via Epicyclic Orbital Elements. *Celestial Mechanics and Dynamical Astronomy*, 92(4):337–370, 2005.

[30] Simone D'Amico and Oliver Montenbruck. Proximity Operations of Formation-Flying Spacecraft Using an Eccentricity/Inclination Vector Separation. *Journal of Guidance, Control, and Dynamics*, 29(3):554–563, 2006.

[31] M C Eckstein, C K Rajasingh, and P Blumer. Colocation Strategy and Collision Avoidance for the Geostationary Satellites at 19 Degrees West. In *Presented at the CNES International Symposium on Space Dynamics*, Toulouse, France, November 1989.

[32] Oliver Montenbruck, Michael Kirschner, Simone D'Amico, and Srinivas Bettadpur. E/I-Vector Separation for Safe Switching of the GRACE Formation. *Aerospace Science and Technology*, 10(7):628–635, 2006.

[33] Simone D'Amico, Jean Sebastien Ardaens, and Sergio De Florio. Autonomous Formation Flying Based on GPS - PRISMA Flight Results. *Acta Astronautica*, 82(1):69–79, 2013.

[34] Jihe Wang and Shinichi Nakasuka. Optimal Cluster Flight Orbit Design Method For Fractionated Spacecraft Based On Relative Orbital Elements. In *AIAA Guidance, Navigation, and Control Conference*, Portland, August 2011.

[35] Quan He and Chao Han. Dynamics and Control of Satellite Formation Flying Based on Relative Orbit Elements. In *AIAA Guidance, Navigation, and Control Conference and Exhibit*, Honolulu, HI, 2008.

[36] Chao Han and Jianfeng Yin. Formation Design in Elliptical Orbit Using Relative Orbit Elements. *Acta Astronautica*, 77:34–47, 2012.

[37] Jianfeng Yin and Chao Han. Elliptical Formation Control Based on Relative Orbit Elements. *Chinese Journal of Aeronautics*, 26(6):1554–1567, 2013.

[38] Soung Sub Lee. *Dynamics and Control of Satellite Relative Motion: Designs and Applications*. Ph.d., Virginia Polytechnic Institute and State University, 2009.

[39] Arthur H. Ballard. Rosette Constellations of Earth Satellites. *IEEE Transactions on Aerospace and Electronic Systems*, AES-16(5):656–673, 1980.

[40] Yu Yao, Ruiqiang Xie, and Fenghua He. Flyaround Orbit Design for Autonomous Rendezvous Based on Relative Orbit Elements. *Journal of Guidance, Control, and Dynamics*, 33(5):1687–1692, 2010.

[41] Riccardo Bevilacqua and Thomas Alan Lovell. Analytical Guidance for Spacecraft Relative Motion Under Constant Thrust Using Relative Orbit Elements. *Acta Astronautica*, 102:47–61, 2014.

[42] Thomas A. Lovell and David A. Spencer. Relative Orbital Elements Formulation Based Upon the Clohessy-Wiltshire Equations. *Journal of the Astronautical Sciences*, 61(4):341–366, 2014.

[43] David A Spencer. *Automated Trajectory Control for Proximity Operations Using Relative Orbital Elements*. PhD thesis, Georgia Institute of Technology, 2015.

[44] David A. Spencer and Thomas A. Lovell. Maneuver Design Using Relative Orbital Elements. *The Journal of the Astronautical Sciences*, 62(4):315–350, 2015.

[45] Andrew J. Sinclair, Ryan E. Sherrill, and T. Alan Lovell. Geometric Interpretation of the Tschauner-Hempel Solutions for Satellite Relative Motion. *Advances in Space Research*, 55(9):2268–2279, 2015.

[46] G. Gaias, Simone D'Amico, and J.-S. Ardaens. Angles-Only Navigation to a Noncooperative Satellite Using Relative Orbital Elements. *Journal of Guidance, Control, and Dynamics*, 37(2):439–451, 2014.

[47] Liam M Healy and C Glen Henshaw. Trajectory Guidance Using Periodic Relative Orbital Motion. *Journal of Guidance, Control, and Dynamics*, 38(9):1714–1724, 2015.

[48] Trevor Bennett and Hanspeter Schaub. Continuous-Time Modeling and Control Using Nonsingular Linearized Relative-Orbit Elements. *Journal of Guidance, Control, and Dynamics*, 39(12):2605–2614, 2016.

[49] Joshua Sullivan, Sebastian Grimberg, and Simone D'Amico. Comprehensive Survey and Assessment of Spacecraft Relative Motion Dynamics Models. *Journal of Guidance, Control, and Dynamics*, 40(8):1837–1859, 2017.

[50] Oussama Khatib. Fonction Decision-Commande d'un Robot Manipulateur. Report 2/7'156, DERA/CERT, Toulouse, France, 1978.

[51] Oussama Khatib. Real-Time Obstacle Avoidance for Manipulators and Mobile Robots. *The International Journal of Robotics Research*, 5(1):90–98, 1986.

[52] R. Volpe and P. Khosla. Manipulator control with superquadric artificial potential functions: Theory and experiments. *IEEE Transactions on Systems, Man, and Cybernetics*, 20(6):1423–1436, Nov 1990.

[53] Elon Rimon and Daniel E. Koditschek. Exact Robot Navigation using Artificial Potential Functions. *IEEE Transactions on Robotics and Automation*, 8(5):501–518, 1992.

[54] Michael T. Wolf and Joel W. Burdick. Artificial Potential Functions for Highway Driving with Collision Avoidance. In *2008 IEEE International Conference on Robotics and Automation*, pages 3731–3736, Pasadena, CA, 2008.

[55] Ö Erkent and H Işil Bozma. Artificial Potential Functions Based Camera Movements and Visual Behaviors in Attentive Robots. *Autonomous Robots*, 32(1):15–34, 2012.

[56] Yuecheng Liu and Zhao Yongjia. A virtual-waypoint based artificial potential field method for uav path planning. In *2016 IEEE Chinese Guidance, Navigation and Control Conference (CGNCC)*, pages 949–953, Aug 2016.

[57] Colin R. McInnes. Autonomous proximity manoeuvring using artificial potential functions. *ESA Journal*, 17(2):159–169, January 1993.

[58] Colin R. McInnes. Autonomous Ring Formation for a Planar Constellation of Satellites. *Journal of Guidance, Control, and Dynamics*, 18(5):1215–1217, 1995.

[59] Ismael Lopez and Colin R. McInnes. Autonomous Rendezvous Using Artificial Potential Function Guidance. *Journal of Guidance, Control, and Dynamics*, 18(2):237–241, 1995.

[60] Frank B McQuade and Colin R. McInnes. Autonomous Control for On-Orbit Assembly Using Potential Function Methods. *The Aeronautical Journal*, 101(1006):255–262, 1997.

[61] Keisuke Sato. Deadlock-Free Motion Planning Using the Laplace Potential Field. *Advanced Robotics*, 7(5):449–461, 1993.

[62] Alexander B. Roger and Colin R. McInnes. Safety Constrained Free-Flyer Path Planning at the International Space Station. *Journal of Guidance, Control, and Dynamics*, 23(6):971–979, 2000.

[63] S.S. Ge and Y.J. Cui. Dynamic Motion Planning for Mobile Robots Using Potential Field Method. *Autonomous Robots*, 13(3):207–222, 2002.

[64] Andrew R. Tatsch and Norman Fitz-Coy. Dynamic Artificial Potential Function Guidance for Autonomous On-Orbit Servicing. In *Proceedings of the 6th International ESA Conference on Guidance, Navigation and Control Systems*, Loutraki, Greece, 2005.

[65] Andrew R. Tatsch. *Artificial Potential Function Guidance for Autonomous In-Space Operations*. PhD thesis, University of Florida, 2006.

[66] Veysel Gazi. Swarm aggregations using artificial potentials and sliding-mode control. *IEEE Transactions on Robotics*, 21(6):1208–1214, 2005.

[67] Chakravarthini M. Saaj, Vaios Lappas, and Veysel Gazi. Spacecraft Swarm Navigation and Control Using Artificial Potential Field and Sliding Mode Control. *Proceedings of the IEEE International Conference on Industrial Technology*, pages 2646–2651, 2006.

[68] Ender St.John-Olcayto, Colin R McInnes, and Finn Ankersen. Safety-Critical Autonomous Spacecraft Proximity Operations via Potential Function Guidance. In *2007 AIAA InfoTech at Aerospace Conference and Exhibit*, pages 1893–1902, Rohnert Park, CA, 2007.

[69] Ahmed Badawy and Colin R. McInnes. On-orbit assembly using superquadric potential fields. *Journal of Guidance, Control, and Dynamics*, 31(1):30–43, 2008.

[70] Ahmed Badawy and Colin R. McInnes. Small Spacecraft Formation Using Potential Functions. *Acta Astronautica*, 65(11-12):1783–1788, 2009.

[71] M. H. Mabrouk and C. R. McInnes. Solving the Potential Field Local Minimum Problem Using Internal Agent States. *Robotics and Autonomous Systems*, 56(12):1050–1060, 2008.

[72] Josue David Muñoz. *Rapid Path-Planning Algorithms for Autonomous Proximity Operations of Satellites*. PhD thesis, University of Florida, 2011.

[73] Sreeja Nag and Leopold Summerer. Behaviour Based, Autonomous and Distributed Scatter Manoeuvres for Satellite Swarms. *Acta Astronautica*, 82(1):95–109, 2013.

[74] Theodore Wahl and Kathleen C. Howell. Autonomous Guidance Algorithm for Multiple Spacecraft and Formation Reconfiguration Maneuvers. *Advances in the Astronautical Sciences*, 158:1939–1956, 2016.

[75] Theodore P. Wahl. *Autonomous Guidance Strategy for Spacecraft Formations and Reconfiguration Maneuvers*. PhD thesis, Purdue University, 2017.

[76] Theodore P. Wahl and Kathleen C. Howell. Autonomous Guidance Algorithms for Formation Reconfiguration Maneuvers. In *AAS/AIAA Astrodynamics Specialist Conference*, Stevenson, WA, 2017.

[77] David A. Spencer. Automated Trajectory Control Using Artificial Potential Functions to Target Relative Orbits. *Journal of Guidance, Control, and Dynamics*, 39(9):1–7, 2016.

[78] Jinfeng Sun, Haibing Chen, Kang Li, and Shuguang Zhang. A Decentralized and Autonomous Formation Planning Architecture for Large-Scale Spacecraft Swarm Using Artificial Potential Field and Bifurcation Dynamics. In *68th International Astronautical Congress*, Adelaide, September 2017.

[79] Zhaokui Wang, Yun Xu, Chao Jiang, and Yulin Zhang. Self-Organizing Control for Satellite Clusters Using Artificial Potential Function in Terms of Relative Orbital Elements. *Aerospace Science and Technology*, 84:799–811, 2019.

[80] Sylvain Renevey and David A Spencer. Spacecraft Formations Using Artificial Potential Functions and Relative Orbital Elements. In *29th AAS/AIAA Space Flight Mechanics Meeting*, Ka'anapali, HI, 2019.

[81] Sylvain Renevey and David A Spencer. Geometric Formations Using Relative Orbital Elements and Artificial Potential Functions. In *AAS/AIAA Astrodynamics Specialist Conference*, Portland, ME, 2019.

[82] Sylvain Renevey and David A. Spencer. Establishment and Control of Spacecraft Formations Using Artificial Potential Functions. *Acta Astronautica*, 162(September):314–326, 2019.

[83] David A. Vallado. *Fundamentals of Astrodynamics and Applications*. Macrocosm Press, Hawthorne, CA, 4 edition, 2013.

[84] Navigation and Ancillary Information Facility. *An Overview of Reference Frames and Coordinate Systems in the SPICE Context*, June 2019.

[85] Wigbert Fehse. *Automated Rendezvous and Docking of Spacecraft*. Cambridge University Press, Cambridge, UK, 2003.

[86] Erwin Kreyszig. *Advanced Engineering Mathematics*. Wiley, 2011.

[87] United Launch Alliance. *Delta IV Launch Services User's Guide*, June 2013.

[88] Nay Oo and Woon-Seng Gan. On Harmonic Addition Theorem. *International Journal of Computer and Communication Engineering*, 1(3):200–202, 2012.

[89] Oliver Montenbruck and Eberhard Gill. *Satellite Orbits*. Springer-Verlag, Berlin, Heidelberg, 4 edition, 2000.

[90] Anne C. Long, R. Pajerski, and R. Luczak. Goddard Trajectory Determination System (GTDS) Mathematical Theory (Revision 1). Technical Report FDD/552-89/001 and CSC/TR-89/6001, Goddard Space Flight Center: National Aeronautics and Space Administration, 1989.

[91] B. A. Archinal, M. F. A'Hearn, E. Bowell, A. Conrad, G. J. Consolmagno, R. Courtin, T. Fukushima, D. Hestroffer, J. L. Hilton, G. A. Krasinsky, G. Neumann, J. Oberst, P. K. Seidelmann, P. Stooke, D. J. Tholen, P. C. Thomas, and I. P. Williams. Report of the IAU Working Group on Cartographic Coordinates and Rotational Elements: 2009. *Celestial Mechanics and Dynamical Astronomy*, 109(2):101–135, 2011.

[92] William M Folkner, J. G. Williams, Dale H Boggs, Ryan S Park, and Petr Kuchynka. The Planetary and Lunar Ephemerides DE430 and DE431. Technical Report IPN Progress Report 42-196, Jet Propulsion Laboratory, 2014.

[93] NASA's GSFC Moon Facts. `https://nssdc.gsfc.nasa.gov/planetary/factsheet/moonfact.html`. Accessed: November 29, 2019.

[94] NASA's GSFC Earth Facts. `https://nssdc.gsfc.nasa.gov/planetary/factsheet/earthfact.html`. Accessed: November 29, 2019.

[95] Peter Z. Schulte and David A. Spencer. Development of an integrated spacecraft guidance, navigation, & control subsystem for automated proximity operations. *Acta Astronautica*, 118:168 – 186, 2016.

[96] David A. Spencer, Sean B. Chait, Peter Z. Schulte, Kevin J. Okseniuk, and Michael Veto. Prox-1 university-class mission to demonstrate automated proximity operations. *Journal of Spacecraft and Rockets*, 53(5):847–863, 2016.

[97] P Ferguson, F Busse, and J P How. Navigation Performance Predictions for the Orion Formation Flying Mission. In *International Symposium on Formation Flying: Missions and Technologies*, Toulouse, France, 2002.

[98] Vincent J. Chioma and Nathan A. Titus. Expected Maneuver and Maneuver Covariance Models. *Journal of Spacecraft and Rockets*, 45(2):409–412, 2008.

[99] E. F. Camacho and C. Bordons. *Model Predictive Control*. Springer-Verlag, 2007.

[100] Magnetospheric Multiscale Spacecraft mission description on NASA's website. `https://mms.gsfc.nasa.gov/index.html`. Accessed: November 08, 2019.

[101] MMS Magnetospheric Multiscale Mission, Southwest Research Institute's website. `http://mms.space.swri.edu/`. Accessed: December 30, 2019.

[102] R. vom Stein, K.-H. Glassmeier, and M. Dunlop. A Configuration Parameter for the Cluster Satellites. Technical Report 2/1992, Institut für Geophysik und Meteologie der Technischen Universität Braunschweig, 1992.

[103] Patrick Robert, Alain Roux, Christopher C. Harvey, Malcolm W. Dunlop, Patrick W. Daly, and Karl-Heinz Glassmeier. Tetrahedron Geometric Factors. In Gotz Paschmann and Patrick W. Daly, editors, *Analysis Methods for Multi-Spacecraft Data*, volume 1, chapter 13, pages 323–328. The International Space Science Institute, 1998.

[104] Daniel Chavez Clemente and Ella M. Atkins. Optimization of a Tetrahedral Satellite Formation. In *AIAA Guidance, Navigation, and Control Conference and Exhibit*, Providence, RI, 2004.

A. INITIAL CONDITIONS

Table A.1: Initial conditions for the triangular lattice.

Spacecraft	x_0 (m)	y_0 (m)	z_0 (m)	$\dot{x}_0$ (cm/s)	$\dot{y}_0$ (cm/s)	$\dot{z}_0$ (cm/s)
Central	-65.94	830.92	-281.46	5.18	4.97	3.32
A1	-87.53	791.89	-279.53	3.46	2.24	4.98
A2	-98.31	786.77	-325.81	7.44	7.74	5.97
A3	-92.63	808.55	-310.50	6.36	8.34	6.19
A4	-91.89	832.43	-255.54	3.37	6.50	7.62
A5	-78.47	819.82	-300.79	3.90	4.10	1.54
A6	-90.95	808.28	-268.52	5.12	6.49	8.57
B1	-119.77	766.37	-323.95	5.75	5.59	8.36
B2	-96.79	770.05	-301.67	5.36	3.87	6.58
B3	-116.90	799.61	-287.39	3.56	6.51	7.54

Table A.2.: Initial conditions for the two hexagonal lattices.

Spacecraft	x_0 (m)	y_0 (m)	z_0 (m)	$\dot{x}_0$ (cm/s)	$\dot{y}_0$ (cm/s)	$\dot{z}_0$ (cm/s)
Central	-229.09	744.47	-355.97	5.94	3.74	3.70
L1A1	-171.28	775.84	-291.87	6.91	4.58	6.00
L1A2	-241.75	807.97	-310.07	2.05	4.59	3.67
L1A3	-167.98	828.54	-285.93	5.22	4.58	1.89
L1A4	-290.28	688.22	-400.57	4.00	1.56	2.84
L1A5	-223.81	837.34	-280.41	5.29	8.71	7.72
L1A6	-178.41	783.14	-343.84	7.66	6.02	4.87
L1B1	-180.37	825.20	-324.28	7.09	7.33	5.17

continued on next page

Table A.2.: *continued*

Spacecraft	x_0 (m)	y_0 (m)	z_0 (m)	$\dot{x}_0$ (cm/s)	$\dot{y}_0$ (cm/s)	$\dot{z}_0$ (cm/s)
L1B2	-117.88	862.34	-263.48	9.17	7.78	5.97
L1B3	-283.27	732.25	-367.20	5.01	7.36	7.44
L1B4	-198.50	796.69	-260.82	4.46	4.11	7.19
L1B5	-82.66	899.87	-188.69	9.32	6.25	8.26
L1B6	-232.39	768.16	-272.56	6.40	6.42	8.43
L1C1	-268.00	780.27	-334.79	1.85	5.29	4.21
L1C2	-150.74	842.11	-225.44	2.45	1.99	4.06
L1C3	-251.39	736.07	-321.39	6.09	5.12	8.41
L1C4	-108.75	857.35	-218.60	5.02	2.73	4.35
L1C5	-251.08	704.22	-360.46	4.17	2.14	3.74
L1C6	-183.13	870.58	-267.57	1.85	4.20	2.53
L2A1	190.68	1199.48	143.21	5.06	5.54	7.87
L2A2	207.75	1208.59	71.43	5.43	5.48	2.90
L2A3	223.01	1227.45	144.48	5.39	5.85	7.61
L2A4	232.42	1242.24	82.26	8.29	8.81	5.62
L2A5	289.60	1297.62	175.08	8.45	9.55	6.45
L2A6	217.90	1268.87	156.38	4.34	7.68	6.86
L2B1	211.14	1149.58	86.75	7.61	4.25	6.28
L2B2	142.43	1148.30	60.42	6.19	6.87	8.28
L2B3	259.60	1240.08	133.26	9.68	7.66	6.96
L2B4	148.59	1176.68	93.04	4.64	6.67	7.85
L2B5	166.97	1174.22	19.17	6.22	6.58	3.88
L2B6	168.56	1221.16	68.02	5.94	7.88	5.92
L2C1	155.21	1126.83	25.47	6.88	4.04	3.90
L2C2	268.56	1238.94	172.24	8.06	6.04	8.31

continued on next page

Table A.2.: *continued*

Spacecraft	x_0 (m)	y_0 (m)	z_0 (m)	$\dot{x}_0$ (cm/s)	$\dot{y}_0$ (cm/s)	$\dot{z}_0$ (cm/s)
L2C3	255.33	1200.72	112.16	6.20	3.75	4.27
L2C4	108.38	1134.61	20.20	1.91	4.17	2.92
L2C5	181.10	1179.14	65.55	8.54	8.27	6.41
L2C6	199.23	1158.37	124.89	6.03	4.10	7.24

VITA

Sylvain Renevey graduated in 2015 from Ecole Polytechnique Fédérale de Lausanne in Switzerland with a Master of Science degree in Physics. He started his PhD in Aerospace Engineering at Purdue University in the Fall of 2016 and joined the Space Flight Projects Laboratory shortly after. His research focuses on spacecraft formation flying and proximity operations.